

THE MACHINABILITY OF RAPIDLY SOLIDIFIED
ALUMINIUM ALLOY FOR OPTICAL MOULD INSERTS

By

Timothy Otieno

Submitted in fulfilment of the requirements for the degree of Doctor
of Philosophy Engineering: Mechatronics at the Nelson Mandela
University

April 2018

Promoter/Supervisor: Prof. Khaled Abou-El-Hossein

Copyright Statement

The copy of this thesis has been supplied on condition that anyone who consults it understands and recognises that its copyright rests with the Nelson Mandela University and that no information derived from it may be published without the author's prior consent, unless correctly referenced.

Author Declaration

I, Timothy Otieno (student number 206035139), hereby declare that the thesis for PhD Engineering: Mechatronics is my own work and that it has not previously been submitted for assessment or completion of any postgraduate qualification to another University or for another qualification.

Timothy Otieno

Acknowledgements

My sincere gratitude and appreciation to my supervisor, Prof. Khaled Abou-El-Hossein for his guidance and support throughout this period. Particular thanks to the Technology Innovation Agency / Department of Science and Technology of South Africa, National Research Foundation of South Africa and the NMU Research Capacity & Development for the financial support provided for this research. The staff and my fellow colleagues at NMU who were always willing to assist with various matters whenever called upon, your kind support is greatly appreciated.

Thank you to my friends and family, you saw me through the entire process and always pushed me to work hard while continuously providing encouragement. An honourable mention to my parents, James and Sophie Otieno, for playing a major role in my life and in my work, without you none of this would be possible. I am truly grateful and will always do my best to make you proud.

Best Regards,

Timothy Otieno

Abstract

Ultra-high precision machining is a material removing process under the nanotechnology regime whereby the highest dimensional accuracies are attained. Critical components for optical devices and optical measuring systems are mainly produced through ultra-high precision machining. Their mass production is usually implemented by utilising optical moulds. Aluminium alloys have proven to be advantageous and very commonly used in the photonics industry for moulds. This ever-increasing use and demand within optics have led to the development of newly modified grades of aluminium alloys produced by rapid solidification in the foundry process. The newer grades are characterised by finer microstructures and improved mechanical and physical properties. The main inconvenience in their usage currently lies in their very limited machining database. This research investigates the machinability of rapidly solidified aluminium, RSA 905, under varying cutting conditions in single point diamond turning.

The machining parameters varied were cutting speed, feed rate and depth of cut. The resulting surface roughness of the workpiece and wear of the diamond tool were measured at various intervals. Acoustic emissions and cutting force were also monitored during machining. The results were statistically analysed and accurate predictive models were developed. Generally, very low tool wear, within 3 to 5 μm , and very low surface roughness, within 3 to 8 nm, was obtained. Acoustic emissions recorded were in the range of 0.06 to 0.13 V and cutting forces were in the range of 0.08 to 0.94 N. The trends of the monitored acoustic emissions and cutting force showed to have a linked representation of the tool wear and surface roughness results. Contour maps were generated to identify zones where the cutting parameters produced the best results. In addition, a range of machining parameters were presented for optimum quality where surface roughness and tool wear can be minimised. As the machining is of a nanometric scale, a molecular dynamics approach was

applied to investigate the underlying mechanisms at atom level. The nanomachining simulations were found to have a correlation to the actual machining results and microstructural nature of the alloy. This research proves that rapidly solidified aluminium is a superior alternative to traditional aluminium alloys and provides a good reference with room for flexibility that machinists can apply when using rapidly solidified aluminium alloys. Efficiency could be improved by reducing the required machining interruption through effective monitoring and performance could be improved by maintaining quality and extending tool life through parameter selection.

Table of Contents

	Page
Copyright Statement	i
Author Declaration.....	ii
Acknowledgements.....	iii
Abstract.....	iv
Table of Contents.....	vi
List of Figures	viii
List of Tables	xi
1. Introduction.....	1
1.1 Ultra-high Precision Machining.....	1
1.2 Problem Statement.....	2
1.3 Objective.....	3
1.4 Scope.....	3
1.5 Methodology.....	4
1.6 Outline.....	5
2. Literature Review.....	6
2.1 Single Point Diamond Turning	6
2.2 Tool Wear in Single Point Diamond Turning.....	9
2.3 Surface Finish	14
2.4 Forces in Single Point Diamond Turning	19
2.5 Acoustic Emissions in Ultra-high Precision Machining.....	22
2.6 Optical Grade Aluminium Alloys.....	25
2.7 Optical Moulding for Plastic Injection	30
2.8 Molecular Dynamics Simulation of Nanometric Machining.....	38
2.9 Past Work on Diamond Turning of Aluminium Alloys.....	48
3. Experimental Setup for Diamond Turning	54

3.1	Workpiece Material	54
3.2	Machining Setup	55
3.3	Response Surface Method and Box Behnken Design.....	59
4.	Surface Roughness Analysis.....	64
4.1	Surface Roughness Measurement Setup.....	64
4.2	Surface Roughness Results	66
4.3	Surface Roughness Statistical Analysis	73
4.4	Conclusion	86
5.	Tool Wear Analysis	88
5.1	Tool Wear Measurement Setup	88
5.2	Tool Wear Results.....	89
5.3	Tool Wear Statistical Analysis.....	103
5.4	Conclusion	115
6.	Cutting Force Analysis	116
6.1	Cutting Force Measurement Setup.....	116
6.2	Cutting Force Results.....	118
6.3	Cutting Force Statistical Analysis.....	125
6.4	Conclusion	131
7.	Acoustic Emission Analysis	132
7.1	Acoustic Emission Measurement Setup.....	132
7.2	Acoustic Emission Results.....	135
7.3	Acoustic Emission Statistical Analysis.....	142
7.4	Conclusion	148
8.	Machining Conditions Optimisation.....	149
8.1	Desirability and Numerical Optimisation	149
8.2	Fine Tuning and Graphical Optimisation	152
8.3	Conclusion	152

9. Molecular Dynamics Simulation	154
9.1 Microstructure Analysis	154
9.2 Molecular Dynamics Simulation Setup	159
9.3 Molecular Dynamics Simulation Results	165
9.4 Conclusion	178
References	180
Publications	188

List of Figures

Figure 2.1: Factors of ultra-high precision machining	7
Figure 2.2: Schematic representation of diamond turning process	9
Figure 2.3: Taylor tool life curve [8]	11
Figure 2.4: Wear regions on a cutting tool [11]	12
Figure 2.5: Surface texture [20]	15
Figure 2.6: Average surface roughness over sample length L [20]	16
Figure 2.7: Surface roughness, waviness and form	17
Figure 2.8: Forces acting on the chip (a) and on the tool (b) [8]	20
Figure 2.9: Features of an acoustic emission signal	24
Figure 2.10: Rapid solidification process [50]	28
Figure 2.11: Microstructure of conventional and modified aluminium alloy [50]	29
Figure 2.12: Injection moulding machine schematic [44]	32
Figure 2.13: Injection mould schematic	33
Figure 2.14: Plastic lens mould insert [57]	34
Figure 2.15: Processing steps of RSA 905 vs Ni-P plating in mould making [62]	35
Figure 2.16: Mould life comparison of RSA 905 vs copper alloys [62]	37
Figure 2.17: Injection-moulded octagon for laser barcode scanning application [44]	38
Figure 2.18: Injection-moulded ellipsoidal mirror [44]	38
Figure 2.19: Interatomic potential energy and force diagrams [68]	43
Figure 2.20: Molecular dynamics simulation of metal cutting [72]	45
Figure 3.1: Workpiece setup	55
Figure 3.2: Precitech Nanoform 250 Ultragrind	56
Figure 3.3: Diamond tool holder and insert	57
Figure 3.4: Diamond tool dimensions	57
Figure 3.5: Experimental setup	58
Figure 3.6: Cutting tool path viewed from top	58
Figure 3.7: Three factorial Box Behnken design	60

Figure 4.1: Form Talysurf PGI Optics 3D	65
Figure 4.2: Stylus probe measuring workpiece surface	66
Figure 4.3: Spiral cutting path comparison of cutting speed/feed rate combinations.....	69
Figure 4.4: Tool tip flattening and smoothening surface	70
Figure 4.5: Surface profile chart for Ra 3.2 nm	71
Figure 4.6: Surface profile chart for Ra 53.9 nm	71
Figure 4.7: Comparison between good surface finish and poor surface finish.....	72
Figure 4.8: Chips around tool during low cutting speeds	73
Figure 4.9: Chips collected after high speed cutting (left) and low speed cutting (right)	73
Figure 4.10: Box-Cox plot for R_a model.....	74
Figure 4.11: Normal probability plot for R_a model	77
Figure 4.12: Effect of cutting speed on inverse surface roughness model	78
Figure 4.13: Effect of feed rate on inverse surface roughness model.....	78
Figure 4.14: Effect of depth of cut on inverse surface roughness model	78
Figure 4.15: Surface roughness map for 5 μm depth of cut	79
Figure 4.16: Surface roughness map for 15 μm depth of cut	79
Figure 4.17: Surface roughness map for 25 μm depth of cut	80
Figure 4.18: Normal probability plot for 10 km surface roughness model	82
Figure 4.19: Effect of cutting speed on inverse surface roughness model 10 km	83
Figure 4.20: Effect of feed rate on inverse surface roughness 10 km.....	83
Figure 4.21: Effect of depth of cut on inverse surface roughness model 10 km	84
Figure 4.22: Surface roughness map for 5 μm depth of cut at 10 km	85
Figure 4.23: Surface roughness map for 15 μm depth of cut at 10 km	85
Figure 4.24: Surface roughness map for 25 μm depth of cut at 10 km	86
Figure 5.1: Joel JSM-6380.....	89
Figure 5.2: Tool tip wear	100
Figure 5.3: SEM image of tool edge.....	102
Figure 5.4: Box-Cox plot for tool wear model	103
Figure 5.5: Normal probability plot for tool wear model	106
Figure 5.6: Effect of cutting speed on inverse tool wear	106
Figure 5.7: Effect of feed rate on inverse tool wear	107
Figure 5.8: Effect of depth of cut on inverse tool wear	107
Figure 5.9: Wear map for 5 μm depth of cut	108
Figure 5.10: Wear map for 15 μm depth of cut	108
Figure 5.11: Wear map for 25 μm depth of cut	109
Figure 5.12: Normal probability plot for 10 km tool wear model	111
Figure 5.13: Effect of depth of cut on inverse tool wear model 10 km	111
Figure 5.14: Effect of feed rate on inverse tool wear model 10 km	112
Figure 5.15: Effect of cutting speed on inverse tool wear model 10 km	112
Figure 5.16: Wear map for 5 μm depth of cut at 10 km	113
Figure 5.17: Wear map for 15 μm depth of cut at 10 km	114

Figure 5.18: Wear map for 25 μm depth of cut at 10 km	114
Figure 6.1: Cutting force measurement schematic	116
Figure 6.2: Kistler force measurement equipment.....	117
Figure 6.3: Force sensor setup	118
Figure 6.4: Normal probability plot for cutting force model	127
Figure 6.5: Effect of cutting speed on cutting force	128
Figure 6.6: Effect of feed rate on cutting force.....	128
Figure 6.7: Effect of depth of cut on cutting force	129
Figure 6.8: Cutting force contour map for 5 μm depth of cut	130
Figure 6.9: Cutting force contour map for 15 μm depth of cut	130
Figure 6.10: Cutting force contour map for 25 μm depth of cut	131
Figure 7.1: Acoustic emissions measurement schematic.....	132
Figure 7.2: Acoustic emission measurement equipment	133
Figure 7.3: AE sensor setup.....	134
Figure 7.4: Labview acoustic data acquisition program display.....	134
Figure 7.5: Raw AE signals for experiment 7 and experiment 11	135
Figure 7.6: Normal probability plot for AE_{RMS} model	144
Figure 7.7: Effect of cutting speed on AE_{RMS}	145
Figure 7.8: Effect of feed rate on AE_{RMS}	145
Figure 7.9: Effect of depth of cut on AE_{RMS}	146
Figure 7.10: AE_{RMS} contour map for 5 μm depth of cut.....	147
Figure 7.11: AE_{RMS} contour map for 15 μm depth of cut.....	147
Figure 7.12: AE_{RMS} contour map for 25 μm depth of cut.....	148
Figure 8.1: Optimum solutions desirability map	151
Figure 8.2: Overlay plot of optimal region	152
Figure 9.1: Bright field TEM of FIB lamella.....	155
Figure 9.2: Area mapped with EDS.....	156
Figure 9.3: EDS results in the TEM.....	157
Figure 9.4: Sum spectrum for EDS mapped area	158
Figure 9.5: MD simulation setup	161
Figure 9.6: Morse potential plot for C-Al.....	164
Figure 9.7: Machining simulation progression at 0.5 nm depth of cut and 5 m/s cutting speed	165
Figure 9.8: Atom distribution during cutting process.....	166
Figure 9.9: Displacement vectors of workpiece atoms on y-z plane	167
Figure 9.10: Shear strain of workpiece atoms	168
Figure 9.11: Dislocation analysis of workpiece lattice	168
Figure 9.12: Bond representation of workpiece structure.....	168
Figure 9.13: Machining simulation with increasing depth of cut at 5.0 nm tool travel.....	169
Figure 9.14: Total energy at 5 m/s cutting speed and 0.5-1.5 nm depth of cut	170
Figure 9.15: Temperature at 5 m/s cutting speed and 0.5-1.5 nm depth of cut	170

Figure 9.16: Maximum total energy vs depth of cut.....	171
Figure 9.17: Maximum temperature vs depth of cut.....	171
Figure 9.18: Cutting forces at 5 m/s cutting speed and 0.5 depth of cut	172
Figure 9.19: Cutting forces at 5 m/s cutting speed and 1.0 depth of cut	173
Figure 9.20: Cutting forces at 5 m/s cutting speed and 1.5 depth of cut	173
Figure 9.21: Average forces vs depth of cut	174
Figure 9.22: Machining simulation with increasing cutting speed at 5.0 nm tool travel.....	174
Figure 9.23: Total energy at 1.0 nm depth of cut and 5-15 m/s cutting speed	175
Figure 9.24: Maximum total energy vs cutting speed.....	175
Figure 9.25: Temperature at 1.0 nm depth of cut and 5-15 m/s cutting speed	176
Figure 9.26: Maximum temperature vs cutting speed	176
Figure 9.27: Cutting forces at 10 m/s cutting speed and 1.0 depth of cut	177
Figure 9.28: Cutting forces at 15 m/s cutting speed and 1.0 depth of cut	177
Figure 9.29: Average forces vs cutting speed	178

List of Tables

Table 2.1: Aluminium temper designations and definitions [44]	27
Table 2.2: Comparative characteristics of aluminium alloy tempers [44].....	27
Table 2.3: Physical and mechanical properties of AA 6061, AA 6082 and RSA 905 [54-56]	30
Table 2.4: Chemical composition % of AA 6061, AA 6082 and RSA 905 [54-56]	30
Table 2.5: Comparison of material properties used in mould making [62]	36
Table 2.6: Nanometric cutting and conventional cutting comparison [65]	39
Table 2.7: Past work on surface roughness and tool wear of modified aluminium alloys	53
Table 3.1: Experiments machining parameters.....	60
Table 3.2: Experiments cutting parameters detail.....	63
Table 4.1: Surface roughness results	66
Table 4.2: Lack of Fit tests for R_a model	75
Table 4.3: Analysis of variance for R_a model.....	75
Table 4.4: Lack of fit tests for 10 km surface roughness model.....	81
Table 4.5: Analysis of variance for 10 km surface roughness model	81
Table 5.1: Tool wear results.....	89
Table 5.2: Lack of fit tests for tool wear model.....	104
Table 5.3: Analysis of variance for tool wear model.....	104
Table 5.4: Lack of fit tests for 10 km tool wear model.....	110
Table 5.5: Analysis of variance for 10 km tool wear model.....	110
Table 6.1: Cutting force results.....	119
Table 6.2: Lack of fit tests for cutting force model	125
Table 6.3: Analysis of variance for cutting force model	125
Table 7.1: Acoustic emission results	136

Table 7.2: Lack of fit tests for AE_{RMS} model.....	143
Table 7.3: Analysis of variance for AE_{RMS} model.....	143
Table 8.1: Optimisation constraints	150
Table 8.2: Optimum solutions.....	150
Table 9.1: EDS results in the SEM of % wt	159
Table 9.2: MD simulation conditions for nanomachining of RSA 905.....	162
Table 9.3: Tersoff parameters for SiC [96].....	162
Table 9.4: EAM parameters for AlCuNiFeMoMgTiZr [84]	163
Table 9.5: Morse parameters for C-AlCuNiFeMoMgTiZr.....	164

1. Introduction

1.1 Ultra-high Precision Machining

Ultra-high precision machining can be defined as the process by which the highest possible dimension accuracy is achieved [1]. The dimensions of parts produced can be of the order 1 nm with dimensional tolerances of the order 10 nm and a surface roughness as small as 1 nm. Satisfying such requirements requires machines with a resolution of 0.01 nm and repeatability in the order of 10 nm. Ultra-high precision machining processes fall under the nanotechnology regime. The following noteworthy processes are capable in achieving ultra-high precision [2]:

1. Single-point diamond and cubic boron nitride (CBN) cutting.
2. Multi-point abrasive cutting/burnishing such as diamond and CBN grinding.
3. Free abrasive processes such as lapping and polishing.
4. Chemical processes such as etch machining.
5. Energy beam processes such as laser cutting and lithography.

Ultra-high precision machining (UHPM) is used intensively in the photonics industry for the production of parts for optical devices and measuring systems. These systems are used in critical applications in a wide range of fields. Military applications include thermal imaging and night vision systems for surveillance equipment. The medical industry uses this technology in building surgical instruments such as laparoscopes. Photonics engineering employ ultra-high precision in the production of components such as lenses and mirrors for optical encoders, DVD players and laser projectors etc. [3,4].

Nickel-phosphorous (Ni-P) plated steels, copper alloys and optical aluminium alloys are among the materials used in making optical mould inserts for plastic injection. Aluminium alloys have proven to be advantageous and are most commonly used over other materials in

mould making. Aluminium alloys exhibit less tool wear and are relatively cheaper in comparison to Ni-P steels and copper alloys.

Recently, the increasing demands from optical systems have led to the development of newly modified grades of non-ferrous alloys characterised by finer microstructures and defined mechanical and physical properties that have become more sought after in optical mould making. These mainly include modified aluminium alloys and copper alloys, but their machining database is quite limited. More research is still required in the tool wear, surface quality and machining performance when these modified alloys are diamond turned.

1.2 Problem Statement

In ultra-high precision machining of optical mould inserts, one of the main challenges is to increase productivity while maintaining acceptable tool wear rates and desirable surface quality. Cutting conditions are vital in the machining performance to meet the end product requirements. The importance of achieving the desired surface finish cannot be overemphasised in ultra-high precision machining. Past research has highlighted the potential of modified aluminium alloys in diamond machining optical surfaces. However, none of the research has adequately addressed the surface quality and diamond tool wear corresponding with varying cutting conditions.

Wear and surface roughness maps and models have been developed and used for various precision processes and materials over the years but there are currently no existing maps for nano-level tool wear and surface roughness in single point diamond turning of modified aluminium alloys. Surface and wear data developed for machining at macro or micro level cannot be downscaled into the nano range due to scale effects [5], further increasing the need for this research data to be made available.

This research investigated the machinability of rapidly solidified aluminium (RSA 905) for the making of optical mould inserts for plastic injection by identifying cutting parameters that provide high surface quality while minimising tool wear. The ultimate significance of this investigation is to subsequently reduce manufacturing costs and increase production rates in the machining of RSA 905 for manufacture of optical components. This also contributes to current research efforts in rapidly solidified aluminium by establishing a machining reference.

1.3 Objective

The aim of this research is to investigate the machinability of ultra-high precision diamond turned rapidly solidified aluminium, RSA 905, for optical mould inserts by determining the associated surface quality, tool wear, cutting forces and acoustic emissions over a range of cutting parameters. The effects of these parameters were also studied to provide a guide for suitable machining ranges for desirable results.

1.4 Scope

The research provides a reference guide for the expected tool wear and surface quality in ultra-high precision machining of rapidly solidified aluminium and traditional aluminium alloy over a range of cutting parameters. The research had the following limitations:

- The machining was based on single point diamond turning.
- The material investigated was rapidly solidified aluminium 905.
- The workpiece surface was flat.
- The tool geometry was fixed.
- The cutting parameters varied were limited to cutting speed, feed rate and depth of cut.
- The cutting was intermittent by performing multiple passes to achieve the required cutting distance.

1.5 Methodology

The cutting parameters investigated were cutting speed, feed rate and depth of cut. The main responses investigated were surface roughness and tool wear. Statistical methods were applied to the parameters to create a design of experiments and investigate their effects to the responses. The tests were carried out on the Precitech Nanoform 250 Ultragrind machining centre, a high performance ultra precision machine designed for the most demanding turning and grinding applications. Cutting was carried out on a flat RSA 905 workpiece surface and the resulting surface quality and diamond tool wear measured. From the results, the effect of cutting parameters were identified, a predictive model was created, and a surface roughness map and corresponding tool wear map was developed to identify zones that provide the optimum results. In addition, acoustic emissions and the cutting force during machining was monitored and recorded. Based on past research, the following ranges of cutting parameters were selected:

- Cutting speed 500-3000 rpm
- Feed rate 5-25 mm/min
- Depth of cut 5-25 μm

The contour maps consist of shaded boundaries grouping areas with similar surface roughness and tool wear. The two results were also linked to allow a user to prioritise and/or compromise between tool wear and the associated surface roughness based on the application with the optimum solution being a minimised surface roughness and minimised tool wear. Additional provided information such as machining time could also be considered when making this compromise to maximise productivity.

1.6 Outline

The thesis begins with a chapter on the literature studied that covers the theoretical concepts relevant to the research. Theory on diamond turning, tool wear, surface roughness, forces in diamond turning, acoustic emissions, optical grade aluminium alloys, optical moulding and molecular dynamics are covered in Chapter 2. In addition, past work significant to this research is reviewed and summarised. Chapter 3 provides a detailed description of the experimental setup and statistical methods used. Chapter 4, 5, 6 and 7 illustrates and analyses the surface roughness, tool wear, cutting force and acoustic emission results obtained from the experiments, respectively. Chapter 8 discusses a list of solutions to optimise the machining process based on minimising surface roughness and tool wear. Chapter 9 covers the microstructure analysis of rapidly solidified aluminium and investigates the nanomachining process using the molecular dynamics simulation approach.

2. Literature Review

2.1 Single Point Diamond Turning

Precision turning processes involve the generation of high quality surfaces by movement of a cutting or abrasive contact point on a defined path with the highest possible accuracy. Ultra-high precision machining is made up of a number of factors as illustrated in Figure 2.1. The main factors are tool and material technology, environmental conditions, machining technology and inspection technology. The tool and material technology includes the material and geometry of the cutting tool and the workpiece material. The tool used can be diamond, ceramic, carbide or nitrides. The tool materials have varying physical and chemical properties that affect their wear rates. The tool geometry involves the rake angle, clearance angle and edge radius as different geometries directly affect the surface produced. The workpiece materials, from metal alloys to polymers, also have varying properties and affinity to the tool affecting the wear rates and finish produced.

Environmental control is very important in precision machining. The work area must be vibration free to avoid tool trajectory errors and produce a good surface finish. Control of temperature and humidity can be achieved by placing the machine in an air-conditioned room to avoid thermal growth and its effects.

Machining technology includes the machine configuration, machining planning, machining parameters, tool and workpiece setup. It is necessary to maximise stiffness and damping in a high precision machine while maintaining high control accuracy. Various design features are implemented to achieve this. The machine base is made up of a high rigidity granite block that absorbs any shock or vibration. The machine elements generally consist of hydrostatic or pneumatic bearing slides for carriage movement, optical encoders with nanometre resolution for axis positioning and air bearing or magnetic spindles. The drive systems are mostly run by

linear motors which have recently replaced the traditional ball-screw system. These features minimise friction and the related risks of heating and wear. The centring of the part is highly important to prevent spindle imbalance. The part centring and the tool adjustment to the spindle axis must be carried out to micrometre precision to avoid form inaccuracies. The entire system is controlled by an advanced PC-based CNC controller. Machining parameters are generally a cutting speed from 600 to 2000 rpm, feed rate from 5 to 25 mm/min, depth of cut from 5 to 20 μm [6].

Inspection technology involves the analysis of the results using machines such as profilometers, laser interferometers, white light interferometers and other high resolution microscopy techniques. The analysis mostly involves studying the surface roughness, surface profile, form accuracy and tool wear.

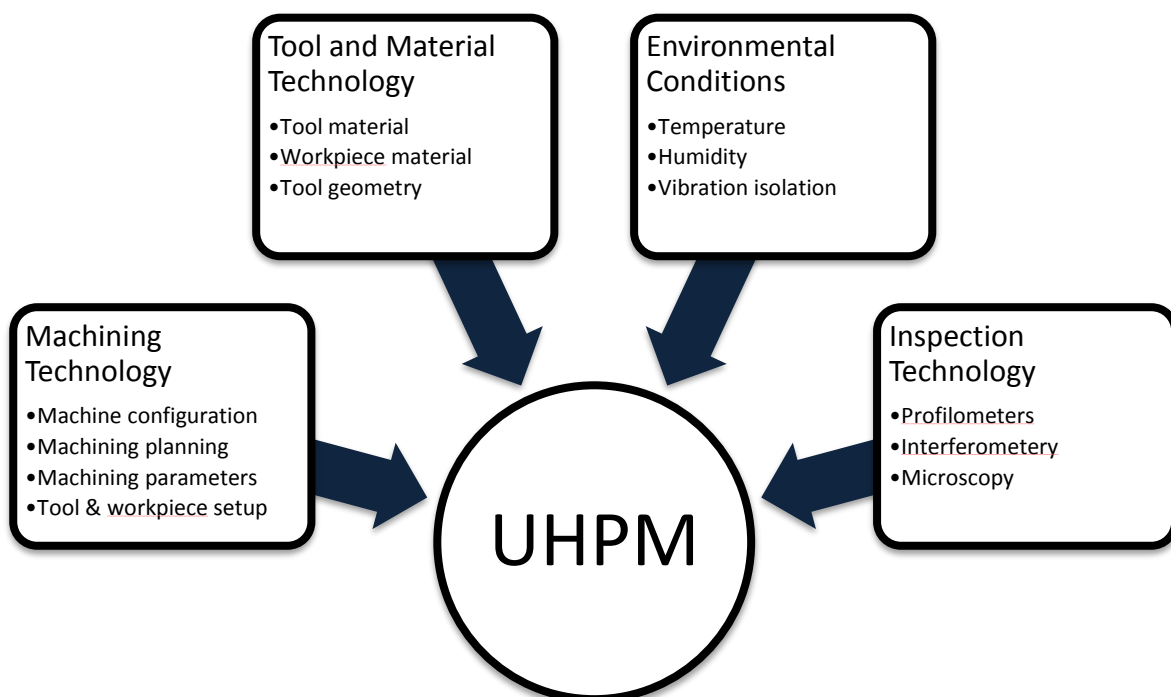


Figure 2.1: Factors of ultra-high precision machining

The tool, which is the last link in the machining elements, is of great importance and must be chosen with great care as it is in direct contact with the part. Single point diamond turning (SPDT) is the ultra-high precision machining technique used for the fabrication of optical components and precision surfaces from engineering materials. This technology employs high rigidity machine tools and extreme precision to produce nanometric surface finishes. Single crystal diamond is employed as the cutting tool in UHPM due to its high hardness, low tool-chip friction and high wear resistance. This results in a longer tool life than other tool materials such as carbides and oxides. Single crystal is preferred over polycrystal mainly due to the fact that its edge can have very low waviness producing a very high quality surface finish.

Single point diamond turning has numerous advantages over traditional grinding and polishing methods in achieving nano level surface finishes. SPDT has a higher material removal rate and automation capability resulting in relatively less machining time and higher accuracy than conventional machining methods. In addition, SPDT can produce spherical and flat surfaces as well as aspheric surfaces that are growing in usage in the optics field. SPDT is capable of achieving high dimensional accuracy and eliminates post-machining processes such as polishing required to achieve high surface finishes [7].

The main operating parameters in a turning operation are cutting speed V , feed rate f and depth of cut d . Figure 2.2 is a representation of the single point diamond turning process. During cutting, the tool's flank face penetrates a depth d into the work piece that rotates at the cutting speed V . The tool moves perpendicular to the rotation at feed rate f as the chips flow over the rake face. The cutting edge is the intersection between the flank face and rake face. The nose of the diamond tool is either very sharp or most commonly, has a very small radius. Optimising the cutting parameters produces high quality surface finishes.

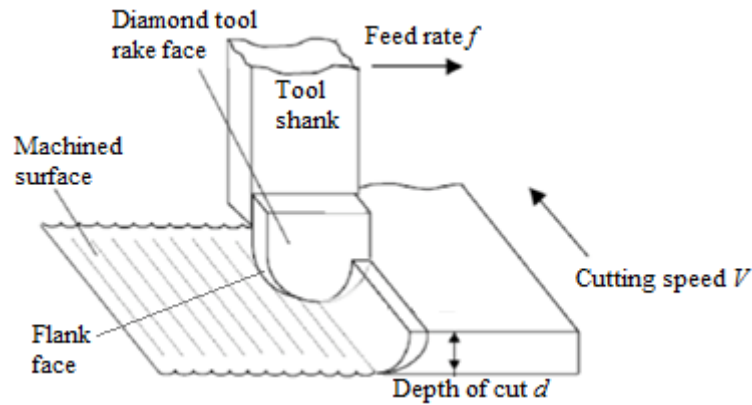


Figure 2.2: Schematic representation of diamond turning process

During the face turning operation, as the spindle speed is constant, the cutting speed varies from a maximum when the tool is at the edge of the disc to a minimum when at the centre due to the decreasing radius. Traditional machines counteract this effect by gradually increasing the spindle speed as the tool approaches the centre. This technique is avoided in precision turning as changes in the spindle speed while cutting creates unwanted features on the surface which adversely affect the surface roughness and profile at nano level.

2.2 Tool Wear in Single Point Diamond Turning

Diamond tools have the ability to retain their cutting edge for virtually most of their useful life and are capable of machining up to 100 times the number of parts than conventional high-speed steels or carbide tools [2]. Mono-crystalline diamond tool is generally used as they can be manufactured with sharper and more accurate cutting edge than polycrystalline diamond. The cutting edge is important for achieving high surface quality as well as tool life. Tool wear is a highly critical aspect in machining with respect to efficiency and surface quality, and the related costs.

During cutting, the tool material progressively diminishes leading to a change in the shape of the cutting edge and resulting workpiece attributes. Eventually the tool must be changed. Tool wear is mainly influenced by machining conditions, namely:

- Cutting parameters
- Tool geometry
- Tool material and workpiece material properties
- Coolant or lubricant properties
- Machine tool rigidity

Factors that influence tool wear have a direct effect on tool life. Taylor's equation provides a relationship between tool life expectancy and cutting speed that is widely adopted in various machining applications.

$$VT^n = C \quad (2.1)$$

where V is the cutting speed, T is the tool life, n is the exponent coefficient, C is the cutting speed that gives a lifetime of one. The effect of feed and depth of cut on tool life can be expressed in a similar manner.

The three tool wear categories established based on Taylor tool life curve are initial wear or break-in period, steady-state or uniform wear and failure or severe wear [8]. Figure 2.3 illustrates the tool life curve, which is a function of tool wear with time. There is an initial rise in tool material loss followed by a relatively slow increase and finally a sharp rise ultimately leading to catastrophic tool failure. There is a recognised international standard that relates the amount of tool wear to the status of the tool for macro and micro machining tools but nothing concrete exists for ultra-high precision diamond tools. In most UHPM applications the status of the tool is determined by monitoring the surface roughness obtained. A high deterioration of the surface roughness after cutting a known distance means a worn out cutting edge.

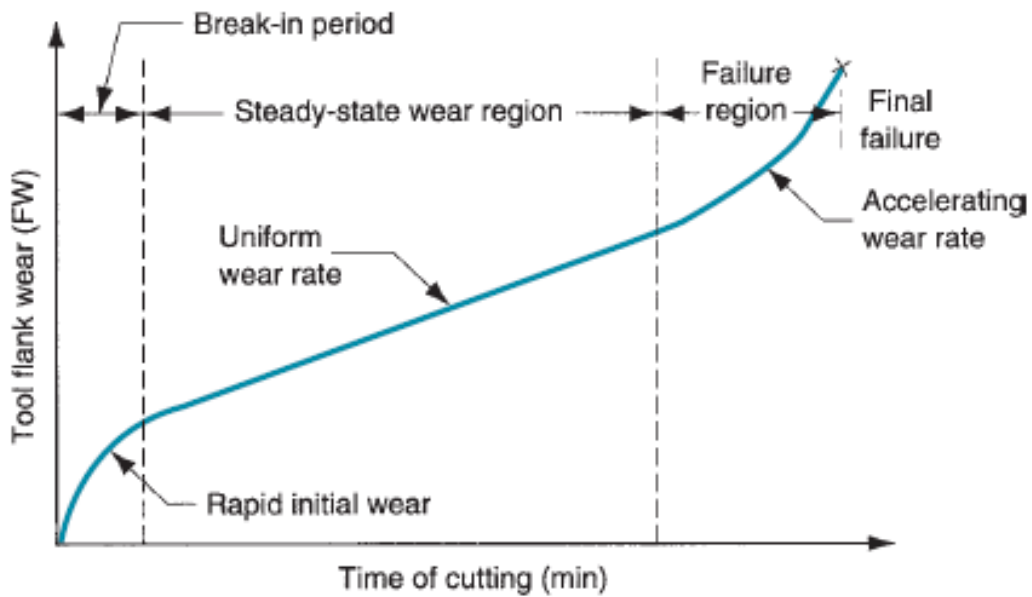


Figure 2.3: Taylor tool life curve [8]

There are various forms and mechanisms of wear that occur during machining. Common wear mechanisms include:

- Abrasion wear – contact and dissimilarity of hardness between the tool and workpiece material deteriorating the tool cutting edge.
- Adhesive wear – build-up or welding of the machined workpiece material on to the tool cutting edge weakening the tool.
- Attrition wear – impact of solid, liquid or gaseous particles on the tool surface causing gradual erosion of the tool.
- Diffusion wear – high temperatures and high friction cutting conditions causing the elements of the tool material to fuse with the elements of the workpiece material or vice versa.
- Corrosive wear – chemical affinity of the tool and workpiece elements caused by oxidation and accelerated by favourable chemical reactions conditions altering the material composition.
- Fatigue wear – cyclic loading and unloading during machining weakening the tool, mostly forming cracks.

- Fracture wear – constant interrupted machining leading to chipping and cracking of the tool surface.

The most common forms of wear are flank wear, crater wear, nose wear and notch wear. Figure 2.4 shows the forms of wear occurring on the tool surface. Flank wear is mainly caused by abrasive and adhesive wear mechanisms due to the rubbing of the clearance face and cutting edge with the workpiece. Nose wear occurs the tip of the cutting edge and is mainly caused by abrasive wear. Crater wear forms on the rake face away from the cutting edge and is caused by a combination of abrasive, adhesive, diffusion and corrosive mechanisms. Notch wear is a groove that is mainly caused by abrasion and adhesion wear mechanisms. Out of the common forms of wear, flank wear is usually selected as the measure for tool wear because it is usually the most dominant and has the highly affects the machining accuracy, surface finish and integrity [9,10].

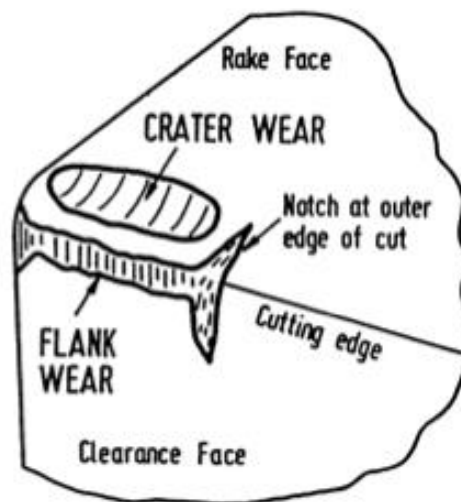


Figure 2.4: Wear regions on a cutting tool [11]

The wear rate R is calculated as the logarithmic ratio of the flank wear VB to the actual length of the cut l . The wear rate is expected to be negative. A higher negative numeric value the lower the flank wear [12].

$$R = \log \left(\frac{VB}{l} \right) \quad (2.2)$$

The tool wear mechanisms in diamond turning of engineering materials are mainly attributed to adhesion, abrasion and chemical wear. Adhesion occurs due to the formation of built-up edge (BUE) on the tool and is common when machining softer materials such as silicon or polymers. The work piece material builds up and sticks to the diamond tool. The BUE may become unstable causing fracture of the diamond tool. Abrasion and chipping is caused by impurities in the material's grain boundaries and the physical hardness property of materials such as copper and aluminium alloys. Chemical wear is due to the chemical affinity of diamond with elements in work piece. The carbon atoms in diamond break off from the lattice and diffuse into the work piece, graphitise and react to form carbon monoxide or carbon dioxide, or react with the work piece to form carbides. The heat generated when cutting metals may also accelerate carbide formation and cause thermal tool wear [13-15]. Tribo-electric tool wear was later discovered to also occur during diamond turning. This is dependent on the electrical conductivity of the work piece. Only work piece materials that are electrical insulators have shown to exhibit this behaviour since diamond is also an insulator and static electrification may occur. Thus, tribo-electric wear is not relevant when diamond machining metals [16,17]. During diamond machining multiple mechanisms may be in effect simultaneously but one mechanism is usually dominant for a given workpiece material. Determining and predicting tool wear behaviour is of high importance to the product quality which is a major factor in nano machining.

Wear maps are very useful in any machining process to identify an acceptable window of cutting conditions to achieve maximum performance. Wear maps are developed by determining the wear rate for various cutting parameters and grouping similar values to create a contour map. They present wear data in a user-friendly manner as an easy reference for

designers and engineers. Generally, the wear rate data are indicated as mild to severe wear. Predicted wear rates calculated from mathematical models are also included [18].

There are numerous wear maps for macro and micro machining processes and materials [5,12] but there are currently no existing wear maps for the ultra-high precision diamond turning of modified aluminium alloys. It is possible to combine published tool wear data and supplementary experiments using the framework created by Lim et al. [19] to generate wear maps, but differences in cutting tools, machining conditions and workpiece materials presents a lack of standardisation and inaccuracies. These differences have a more significant effect in UHPM compared to macro or micro level machining.

The reference provided by wear contour maps help minimise costs and increase production. Areas with the lowest tool wear rates are commonly referred to as safety zones [5]. Cutting variables that produce the least wear can be selected from wear maps. The close association between tool wear and surface quality make wear maps a very useful guide in determining performance and the expected results.

2.3 Surface Finish

The measurement and description of surface texture includes roughness, waviness, lay and flaw, as illustrated in Figure 2.5. Surface texture is generally analysed from a two-dimensional point of view. Surface roughness refers to the variations in the height of the surface relative to a reference plane. Roughness is characterised by short wavelengths with local maxima and minima of varying amplitude and spacing. Waviness is the surface fluctuations of relatively longer wavelengths. It is formed as a result of machine or work piece deflections, vibration or chatter. Lay is the direction of the predominant surface pattern as a result of the machining process. Flaws are unexpected and unintended disturbances in the surface texture [20].

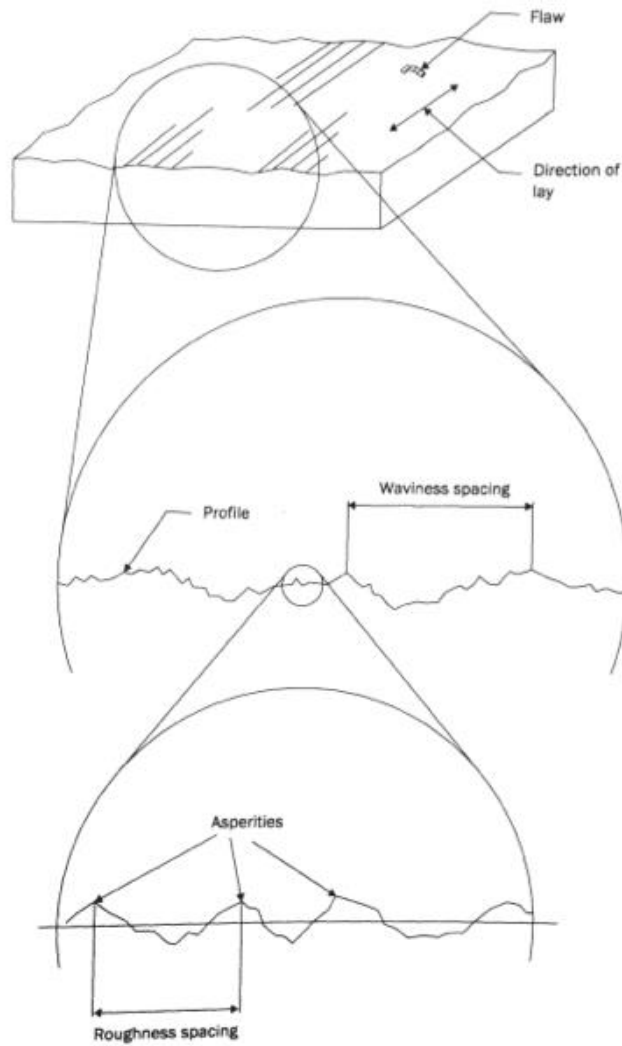


Figure 2.5: Surface texture [20]

Surface roughness is most commonly defined by average roughness R_a . This is the arithmetic mean deviation of the surface height from the mean line through the profile and is calculated as

$$R_a = \frac{1}{L} \int_0^L |Z(x)| dx \quad (2.3)$$

where $Z(x)$ is the height of the surface above the mean line at a distance x from the origin and L is the length of the profile as shown in Figure 2.6 [20].

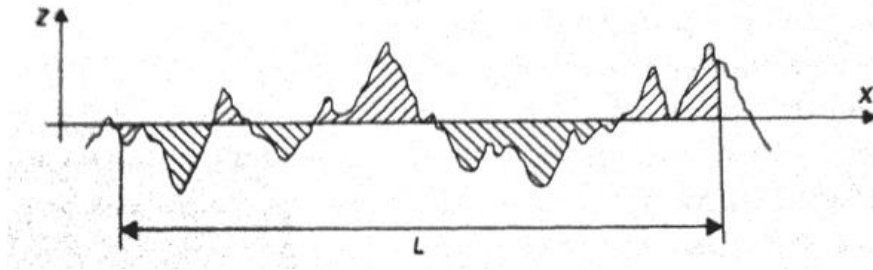


Figure 2.6: Average surface roughness over sample length L [20]

Another important parameter to describe surface roughness is the root mean square (RMS) roughness R_q . This parameter represents the standard deviation of the distribution of the surface heights. It is defined as the root mean square deviation of the profile from the mean line calculated as [20]

$$R_q = \sqrt{\frac{1}{L} \int_0^L |Z(x)|^2 dx} \quad (2.4)$$

R_a is mostly utilised in general engineering and automotive components while R_q is more suited for optical or electronic components due to its sensitivity to spurious peaks and valleys. Peak amplitude parameters may also be useful in roughness measurements. R_p is the maximum height while R_v is the maximum depth of the profile from the mean line, and they indicate the extreme peak and valley of the profile, respectively.

The cutting action of the tool also leaves a spiral profile of finely spaced peaks and valleys or feed marks on the surface. In ideal machining conditions, these feed marks create a surface roughness that can be defined theoretically using the tool radius r and feed per revolution f as [21]

$$R = \frac{f^2}{8r} \quad (2.5)$$

In an ideal machining process, the feed marks are a periodic tool trace on the surface. In practice, however, these roughness values will always be higher as the cutting process is

never ideal and there are several other factors in play such as vibration and chatter. For a single point tool, the mean line is 1/8 from the bottom of the profile and hence the theoretical average roughness is calculated as [22]

$$R_a = 0.032 \frac{f^2}{r} \quad (2.6)$$

Surface profile form factor is the measurement of the accuracy of the shape. The mean deviation of the actual surface shape from the ideal shape is the profile form error. Distance, radius and angle are some of the main aspects of form measurements. Peak to valley parameters are related to a mean line. The least squares line is used which bisects the profile such that the areas above and below this line are equal and are kept to a minimum. The form error of a machined part is compared to the specification tolerance and a pass/fail determination made. Single point diamond turning can achieve various optical surface forms from planar, spherical and aspheric to surfaces with structures such as diffractive, lenslet arrays and Fresnel facets. The resulting surface finish is mainly due to how the cutting tool reacts with the material. This brings variables such as tool shape, cutting parameters and built-up edge into play. Figure 2.7 illustrates the differences between surface parameters.

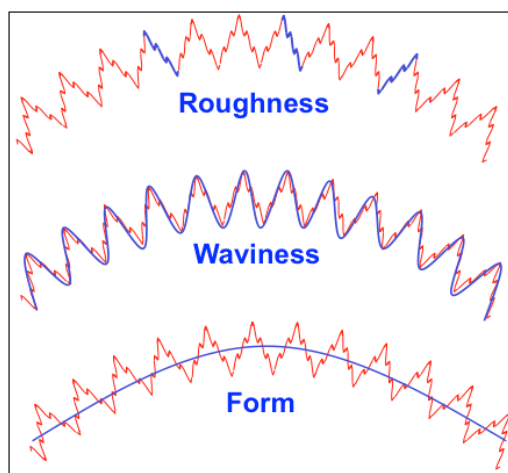


Figure 2.7: Surface roughness, waviness and form

Hybrid parameters such as the arithmetic mean slope R_{da} and RMS slope R_{dq} provide a means of determining the characteristic of the surface for given applications. This is the mean of the local peaks and valleys slope angle along the surface profile. Similar to roughness, RMS slope is preferred for optical components where surfaces are smooth and small changes need to be highlighted. The significance of the slope values in relation to the component property is as follows [23]:

- Friction – higher slope, higher friction.
- Reflectivity – higher slope, less reflective the surface.
- Elasticity – higher slope, more likely to deform under load.
- Wear – higher slope, greater rate of wear.
- Vibration – lower slope, less vibration/more quiet.
- Adhesion – higher slope, better adhesion/less shearing.

Irregularities on the surface of a machined component develop from various factors or conditions. For example, instable cutting may cause excessive waviness or noise indicating faulty machining. Too many peaks may cause premature surface breakdown, while deep valleys may experience crack propagation. However, the desired surface characteristics are directly dependent on the component application. Components that need to be well lubricated must have sufficient valleys for oil retention, components that must be adhesive require sufficient peaks, and components requiring high reflectivity or reduced noise must be smooth.

The main factors considered when measuring surface finish are [23]:

- Material microstructure
- Cutting tool action
- Instability of the cutting process
- Errors in machine tool guideways
- Deformations due to stress patterns on the component

Numerous measurement methods are available for performing surface analysis. Direct measurement techniques, such as using a mechanical profilometer, involve dragging a stylus probe over the surface whose displacement provides proportional amplified electric signals that can be fed into a chart recorder to produce a profile. Profilometers have the advantages of being highly accurate and being able to measure large surfaces. However, they have the disadvantage of marking or damaging the surface in ductile materials resulting in distorted readings. This effect can be minimised by adjusting the pressure of the stylus while still maintaining sufficient contact to take a valid measurement [20].

Non-contact measurement techniques involve interferometry by optical instrumentation such as a scanning electron microscope (SEM) or laser interferometer. Interferometry uses the principle of interference of light to produce patterns of bright and dark bands that indicate the departure of the surface from a desired reference. Interferometers produce images of the surface that are transferred into a computer program to calculate roughness parameters. In addition, metallurgical properties like grain structure can also be examined. Most roughness measurement methods have a vertical resolution of the order of 0.1 nm [20].

The sharp cutting edge of the diamond tool produces a very fine surface finish with high dimensional accuracy. Surface quality is dependent on the cutting tool condition and cutting parameters, hence the importance of investigating tool wear and the associated surface roughness. Modification of cutting parameters is the easiest and most conventional method of improving surface quality.

2.4 Forces in Single Point Diamond Turning

Mechanical machining, such as turning and grinding, is essentially applying forces on a workpiece using a cutting tool to generate the desired shape. This makes cutting force a fundamental parameter in most aspects of machining processes from design to manufacture.

Determining the cutting force in UHPM, as in any other machining process, is important in understanding the mechanism and the associated effects of the machining process. Cutting forces in diamond turning can usually range from 1 N to as small as tens of micron Newtons [24,25].

Cutting forces in diamond turning share the same fundamental principles as orthogonal cutting. The orthogonal cutting model is simpler and well suited to research investigations as many of the independent variables can be eliminated [26,25,27]. Several forces relationships are in effect during cutting as shown in Figure 2.8. The forces can be divided into the forces acting on the chip and the forces acting on the tool. The forces on the chip are a result of plastic deformation along shear plane orientated at an angle ϕ with the workpiece surface. The direction of chip flow follows the tool rake angle α as the chip grows in thickness along the shear plane until it falls off. The total force acting on the tool can be conveniently resolved into normalised components. The thrust force F_t in the direction of the feed and the cutting force F_c in the primary direction of cutting or chip removal. The cutting force constitutes to approximately 80% of the total force [28].

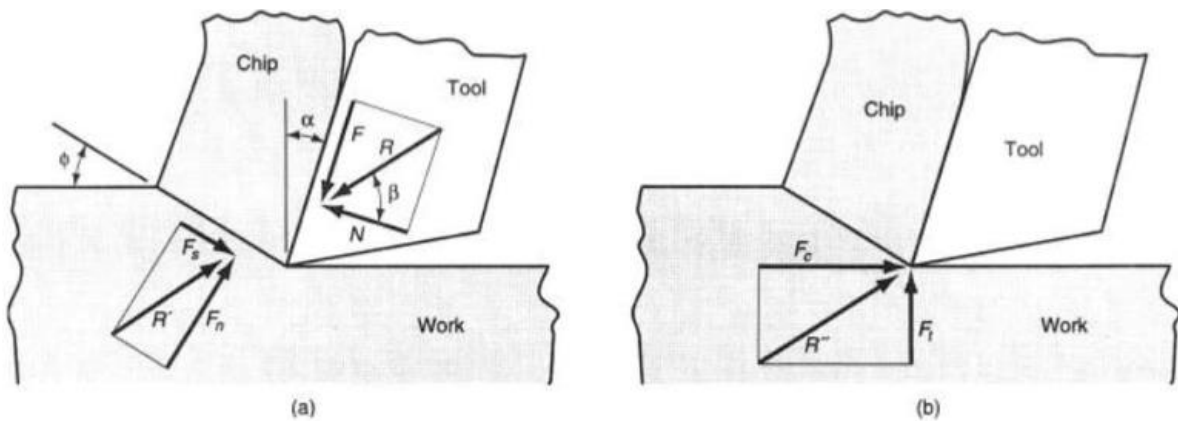


Figure 2.8: Forces acting on the chip (a) and on the tool (b) [8]

Using the Merchant's model, the force relationship can be described as

$$\tau_s = \frac{F_c \cos\phi - F_t \sin\phi}{(t_0 w / \sin\phi)} \quad (2.7)$$

where τ_s is the shear stress, t_0 the undeformed chip thickness, w the width of the workpiece, F_c cutting force, F_t the thrust force, and ϕ the shear angle [8].

The use of Merchant's model is based on the assumptions that the deformation is two-dimensional, the shear stresses are evenly distributed, the tool tip is perfectly sharp and the resultant forces on the tool-chip interface are equal, collinear and opposite [29].

Cutting force is primarily affected by cutting conditions (cutting speed, feed rate, depth of cut), cutting tool geometry and properties of work material. Cutting conditions provide the simplest means to vary and control cutting force. Generally, increase in cutting speed reduces cutting force, while increases in feed rate or depth of cut leads to an increase in cutting force [28]. Cutting force is a significant factor in the resultant surface quality and tool wear in machining and hence effective monitoring is very useful in SPDT.

Past work has shown that cutting force has a greater effect in nanomachining than in higher level machining. This has been labelled as the size effect, where the force per unit depth of cut increases significantly as the depth of cut is decreased below approximately 20 μm [30,31]. Gao et. al [25] employed piezoelectric force transducers and measured the cutting force and thrust force in nanomachining. They employed a two-dimensional cutting model by likening the diamond turning to orthogonal cutting. The findings showed an increase in cutting force with increase in depth of cut. The cutting force profile also showed a sharp increase in the early stages then gradually decreased during cutting as the distance increased.

2.5 Acoustic Emissions in Ultra-high Precision Machining

Acoustic emissions can be defined as elastic waves emitted from sources inside a material as a result of the sudden release of energy during material deformation [32]. Acoustic emissions are utilised in various industries, with applications ranging from leak detection in pipe systems to structural monitoring in pressure vessels to fracture testing in electronic circuits. Acoustic emissions (AE) signals have proved to be viable in monitoring the behaviour of machining operations, such as tool wear detection and non-destructive testing. The main advantage of using AE signals is that ambient noises and vibrations are excluded due to the much higher frequency range of the elastic waves and sensors (typically 100 kHz to 1 MHz), thus the received signal is focused on the cutting process [33].

During machining, the material reaches yield stress and as structural deformation occurs, energy is released in the form of elastic waves. These elastic waves are naturally generated ultrasound travelling through the material. There are several sources of acoustic emission during machining, namely [34]:

- Tool approach, entry and exit
- Deformation of work material
- Tool chipping, breakage and fracture
- Chip breakage and collision

The sensing of acoustics is usually done through a piezoelectric transducer that generates electric signals as a result of applied mechanical force. This phenomenon is known as the piezoelectric effect, and the material that is usually employed is lead zirconate titanate (PZT).

The electric field generated is expressed as

$$T = C \times E \left(\frac{\Delta L}{L} \right) \quad (2.8)$$

where E is the material's Young's modulus (58.5 GPa for PZT), L its length, C the piezoelectric stress constant (24.4×10^{-3} V m/N for PZT) [35].

The elastic waves apply mechanical forces on the sensor face that are converted into a corresponding voltage. This voltage is given as [35]

$$V = C \times E \times \Delta L \quad (2.9)$$

There are two types of AE signals generated during metal cutting, transient signals and continuous signals [34]. Transient signals are generally bursts or sharp spikes that result from tool fracture, chip breakage and collisions. Continuous signals are generally constant as a result of material deformation and shear or sliding of the tool and chip. A raw acoustic emission signal has several features as shown in Figure 2.9. The ring-down count is the number of times the signal exceeds the reference threshold. The time elapsed from the first point the signal crosses the threshold to the last point is the duration. The rise time is the time required to reach peak amplitude from the point the signal first crosses the threshold. The peak amplitude gives a measure of the intensity of the AE source [33].

From the raw AE signal, various statistical signal processing methods can be applied from time domain analysis based on the generated signal over time to frequency domain analysis based on the power spectrum. Collecting all the features of an AE signal is impractical in terms of time, cost and accuracy. The root mean square (RMS) of the acoustic emission signal is the best representation of the signal energy. It is directly related to the amount of work done by the signal source and is calculated as

$$AE_{RMS} = \frac{1}{T} \int_0^T V^2(t) dt \quad (2.10)$$

where $V(t)$ is the signal function and T is the time period [33].

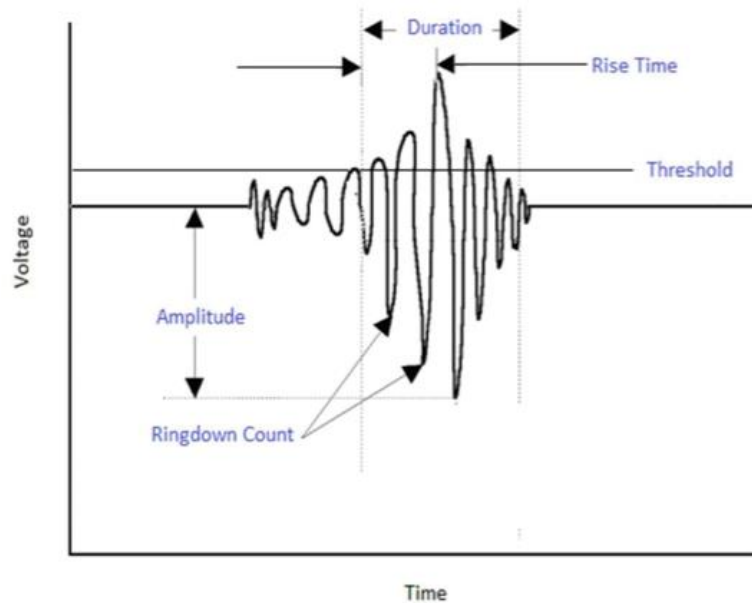


Figure 2.9: Features of an acoustic emission signal

The use of acoustic emissions has been extensively used in macro machining for online monitoring of tool wear and catastrophic tool failure detection. Various researchers have performed investigations using the time domain and frequency spectrum of AE signals to identify tool and chip behaviour. Lan and Dornfeld [36] reported the burst signals generated during tool fracture and that the RMS is dependent upon fracture area. Emel and Kannatey-Asibu [37] used features of the AE frequency spectra for identification of tool wear, chip noise and tool breakage by applying pattern recognition to a calibrated normalised AE spectrum. Inasaki and Yonetsu [38] proposed an algorithm to detect chipping using AE signals. They also found that tool fracture created an increase in the AE signal amplitude that was attributed to the increase in contact area between the tool and the workpiece. Lee et al. [39] performed online tool breakage detection by combining an AE sensor and a force sensor. They reported that AE signal burst is generated at tool fracture followed by a drop in cutting

force. This combination is highly significant in differentiating between the different sources of the AE burst signals.

There is very limited research on the applicability of monitoring AE signals in ultra-high precision machining. The viability of transferring the macro machining acoustic monitoring methods to nano-level machining has not been extensively investigated. Tool wear is progressively minimal in comparison with macro machining so the detection of significant signal changes with time and various cutting parameters needs to be studied for nanomachining as well. The most published work on the use of AE signal in ultra-precision machining was for contact detection [40]. Min et al. [40] successfully used acoustic emission to precisely determine when the tool made contact with the workpiece to improve tool/work setup error and time. This allowed for an accelerated approach feed rate before slowing down for contact with the workpiece. An accurate tool/work setup allows flexible tool changes and improves the resulting surface finish and form.

Acoustic emission sensing provides a means of monitoring that would be suited to ultra-high precision machining due to its high signal to noise ratio. Thus, allowing the ability to monitor micro level mechanisms in a relatively noisy machining environment.

2.6 Optical Grade Aluminium Alloys

Aluminium alloys are commonly used in the production of optical and structural components of optical systems from ultra-high precision machining. Traditional grades of aluminium alloys, such as AA 6061, are produced through conventional foundry processes that involve slow solidification. Hence, they are made up of a coarse microstructure and relatively large grain sizes. Diamond turned AA 6061 results in surface roughness values of approximately 5-8 nm [13]. To achieve lower surface roughness values, the machined aluminium alloy must be plated with either high purity aluminium (AlumiPlate) or nickel and diamond turned again.

AlumiPlate produces a surface roughness of 2-4 nm while nickel plating produces a surface roughness of 1-2 nm. In addition to having this added process, AlumiPlate and nickel plating have other disadvantages. AlumiPlate is relatively soft making chip removal and cleaning of the finished surface very difficult. The large difference in the coefficient of thermal expansion between nickel and aluminium makes nickel plated surfaces susceptible to bi-metallic bending in low temperature applications. AlumiPlate has a similar coefficient of thermal expansion to aluminium alloys thus it is less affected by thermal effects, but nickel is harder than AlumiPlate making it more scratch-resistant and easier to polish [41]. The added production steps, namely applying the coating and another diamond turning process to achieve the desired surface roughness on the coated workpiece, increases throughput times and production costs. Machining material with smaller grain sizes would be advantageous in achieving lower surface roughness values without additional production steps and the use of expensive and vulnerable plating.

Aluminium alloy 6061 is one of the most commonly used traditional aluminium alloy. It offers medium to high strength, good corrosion resistance and very good weldability [6]. Aluminium alloy 6082 has gained popularity over AA 6061, as this grade of traditional aluminium alloy offers similar physical characteristics but higher mechanical properties when tempered. The higher strength has been attributed the higher amount of manganese present in AA 6082 [42]. AA 6082 offers good weldability, brazeability, corrosion resistance, formability and machinability with very good finishing characteristics [43]. The common aluminium alloy temper designations and definitions are shown in Table 2.1. The standard tempers are defined based on the process used in the alloy heat treatment. Table 2.2 compares the characteristics of the tempers for AA 6061 and AA 6082. Each characteristic in the table is graded with A being the highest and D being the lowest as represented by the Aluminium

Association [44]. T6 tempers are favoured for optical machining applications as they provide the best machinability and highest strength producing better surface finishing.

Table 2.1: Aluminium temper designations and definitions [44]

Standard Tempers	Definition
F	As fabricated.
O	Annealed, to obtain the lowest strength temper.
T4	Solution heat-treated and naturally aged.
T5	Cooled from an elevated temperature shaping process and artificially aged.
T6	Solution heat-treated and artificially aged.

Table 2.2: Comparative characteristics of aluminium alloy tempers [44]

Alloy	Temper	Formability	Machinability	Corrosion Resistance	Weldability	Brazeability
6082	O	A	D	B	A	A
	T4	B	C	B	A	A
	T5	C	B	B	A	A
	T6	C	B	B	A	A
6061	O	A	D	B	A	A
	T4	B	C	B	A	A
	T5	C	B	B	A	A
	T6	C	B	B	A	A

The newly developed modified aluminium alloys, namely rapidly solidified aluminium (RSA), are produced through rapid solidification during foundry, resulting in fine microstructures with enhanced mechanical and physical properties [45-48]. Melt spinning is qualitatively the best method in rapid solidification, providing highest cooling rate (10^6 K/s) and the finest microstructure [49]. Figure 2.10 illustrates the steps in the rapid solidification process. Firstly, the alloy is prepared by melting and combining the elements. This melt is then poured into a very high speed spinning copper wheel to create a rapidly solidified ribbon. The ribbon is chopped into flakes and collected in a vessel where they are degassed

and subjected to hot isostatic pressure processing, creating consolidated material in the form of billets. The billets can then be extruded or forged into the required dimensions.

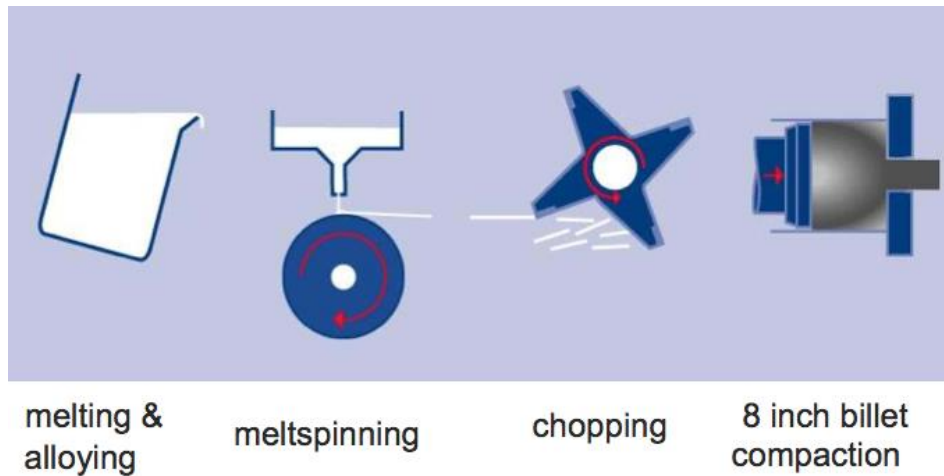


Figure 2.10: Rapid solidification process [50]

Figure 2.11 shows the microstructure of conventional aluminium alloy compared to the rapidly solidified aluminium alloy at 500x magnification. It can clearly be seen that rapidly solidified aluminium has a superiorly finer grain structure. The grain size in rapidly solidified aluminium is approximated to be in the range of 1 μm . As seen in Figure 2.11 the RSA grains are not clearly visible using conventional high resolution microscopy. Higher resolution techniques such as transmission electron microscopy (TEM) would be required to provide a clearer image of the RSA ultra-fine crystalline structure.

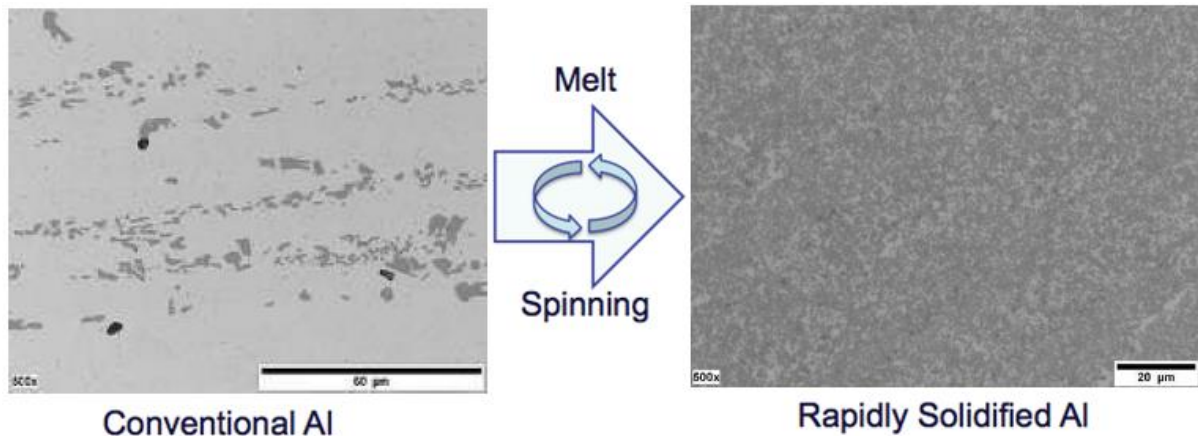


Figure 2.11: Microstructure of conventional and modified aluminium alloy [50]

The mechanical properties and chemical composition of rapidly solidified aluminium (RSA 905) and traditional optical grade aluminium alloys (AA 6061-T6 and AA 6082-T6) are compared in the Table 2.3 and Table 2.4. From the tables it is seen that RSA 905 exhibits better mechanical and physical properties compared to traditional aluminium alloys. RSA 905 has a higher ultimate tensile strength and hardness, reasonable ductility, and a relatively lower thermal expansion rate. These properties make RSA 905 a suitable alternative material for making optical mould inserts for plastic injection. The chemical composition of RSA 905, shows the absence of silicon (Si) and a small presence of magnesium (Mg). This eliminates the presence of Mg_2Si compounds that form from the slow solidification of aluminium alloys causing accelerated tool deterioration and shortens tool life [51]. However, the presence of iron (Fe) and nickel (Ni) elements in RSA 905 have a high chemical affinity to the carbon in diamond. The iron and nickel particles are highly brittle and possess sharp edges. This may cause powerful impacts on the cutting edge and work piece surface finish when diamond machined due to breaking under combined shear and compression effect [52]. These effects are reduced due to the rapid solidification process that produces small sizes of iron and nickel particles. Copper (Cu) content substantially increases strength and facilitates precipitation hardening. Cu also improves the machinability by increasing matrix hardness. Manganese

(Mn) improves strain hardening enhancing tensile strength. The presence of zirconium (Zr) reduces grain growth or re-crystallisation [53].

Table 2.3: Physical and mechanical properties of AA 6061, AA 6082 and RSA 905 [54-56]

	AA 6061	AA 6082	RSA 905
Physical Properties			
Density (g/cm ³)	2.7	2.7	2.95
Thermal expansion (10 ⁻⁶ /K)	23	24	19
Thermal conductivity (W/m.K)	166	180	100
Modulus of elasticity (GPa)	70	70	91
Mechanical Properties			
Ultimate tensile strength (MPa)	310	340	600
Yield strength (MPa)	270	290	480
Elongation (%)	12	6	6
Hardness	100	95	180

Table 2.4: Chemical composition % of AA 6061, AA 6082 and RSA 905 [54-56]

Element	Fe	Si	Ni	Cu	Mn	Mg	Mo	Cr	Zr	Zn	Ti
AA 6061	0.7	0.4-0.8	-	0.15-0.4	0.15	0.8-1.2	-	0.04-0.35	-	0.25	0.15
AA 6082	0.5	0.7-1.3	-	0.1	0.4-1.0	0.6-1.2	-	0.25	-	0.2	0.1
RSA 905	2.5	-	5.0	2.5	1.0	0.6	0.8	-	0.8	-	0.6

2.7 Optical Moulding for Plastic Injection

There are three main application areas for aluminium alloys in the optical industry:

1. Diamond machined mirrors
2. Polished mirrors
3. Mould insert applications

Moulding plays an important role in manufacturing industries as it provides an efficient means of rapidly reproducing a product. It is widely adopted in plastic and glass lens production, automobile and aerospace industries. Optical design using moulded optics provides additional variables, such as aspheric and diffractive surface coefficients, compared to standard optical design [3].

In optics, no single material caters for all design problems. The selection of either glass or plastic optics depends on a number of factors ranging from optical characteristics, manufacturing precision levels, volume and packaging to environmental concerns. Plastic optics are generally favoured due to their low unit costs, ability to achieve complex geometries and consistency in moulding quality [44]. There are three typical moulding techniques used in optics, namely, injection moulding, compression moulding and injection-compression moulding.

The plastic injection moulding process is carried out in a machine consisting of a fixed platen, a moving platen, a clamping unit and an injection unit, as shown by the schematic in Figure 2.12. The upper mould half is attached to the fixed platen on the injection side and the lower mould half is attached to the moveable platen on the ejector side. The moveable platen moves forward closing the mould inserts and the high pressure clamp holds it closed. Plastic pellets are fed into the injection barrel from the hopper. The injection barrel has heater bands that melt the plastic for injection. The plastic is heated and a predetermined amount is injected into the mould. The injection of the molten plastic generates pressures in the range of thousands of kilos per square centimetre, requiring the clamping to have a higher pressure capacity to hold the mould closed. The clamping force is provided by hydraulics, although, the electrical servo mechanisms are becoming more favoured for their superior control and repeatability. The plastic takes the shape of the insert cavity as it cools and solidifies. The mould then opens once cooling is complete and an ejection mechanism releases the produced optic from the mould. Injection moulding is capable of running single and multi cavity moulds (producing several parts per cycle). Moulding machines are rated by their maximum clamping force. They typically range from 5 to 2500 tonnes. Injection moulding machines specifically for optics typically run in the range from 10 to 50 tonnes [3].

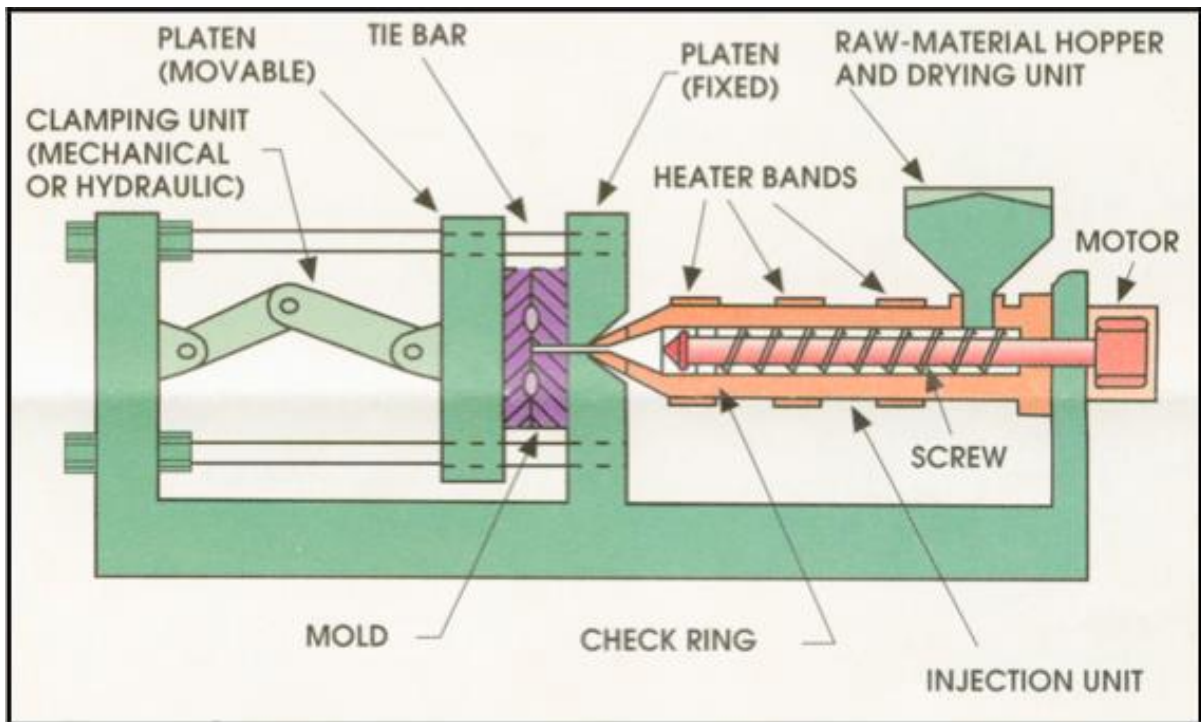


Figure 2.12: Injection moulding machine schematic [44]

In compression moulding, the plastic is introduced into the mould in pellet or sheet form and pressed between heated platens. The platens are temperature cycled during the pressing to form the moulded optic part. This method is used to manufacture Fresnel and lenticular moulds with extremely fine depth grooves and tight angular tolerances [44].

Injection-compression moulding is the hybrid process where a plastic is injected into the clamped mould between temperature-controlled platens. Unlike the standard injection process where the mould is clamped shut in a fixed position, pressing moves the mould against the injected plastic. This allows for the production of higher-level features, such as wide, thin parts, parts with large thickness variations and parts requiring tighter tolerances, such as prisms [3].

Optical mould inserts are manufactured as negatives of the final component shape. The inserts are generally spherical or planar shapes. Improvements in diamond turning technology over the years has led to the production of aspheric, diffractive, non-symmetric and freeform

surfaces. Optical moulds are typically made out of materials of high hardness in order to maintain a surface finish that will not degrade under the heat and pressures of the moulding process. The inserts are fabricated by diamond turning or diamond grinding producing high quality surface finishes. The mould is made up of two halves, with one being attached to the fixed platen and the other to the moveable platen. Figure 2.13 is a schematic of an injection mould showing the fixed half on the right and the moveable half on the left of the diagram.

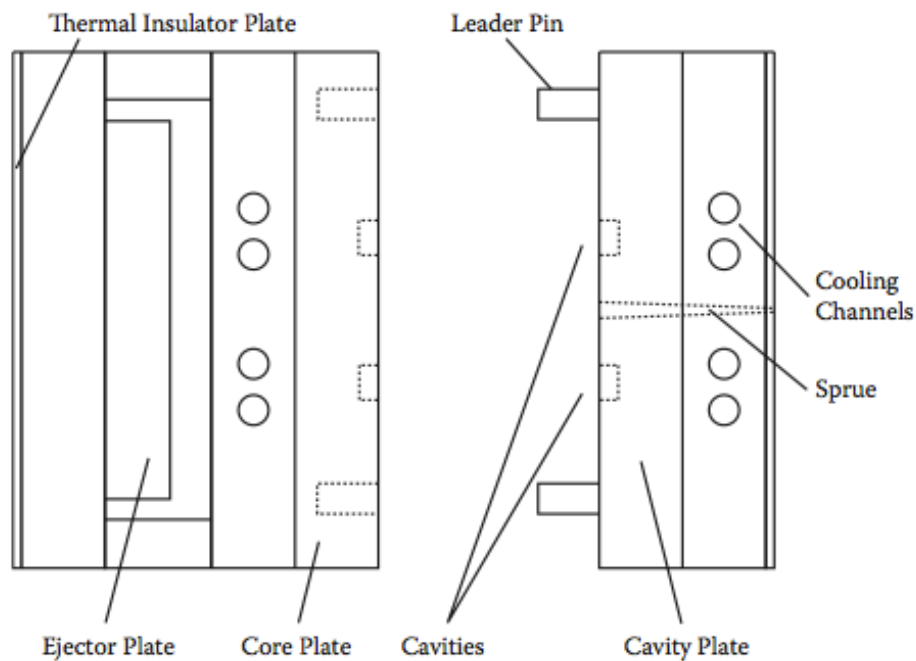


Figure 2.13: Injection mould schematic

The area where the two halves separate is called the parting line. This is the area where the injected molten plastic flows. The thermal insulator plate on the outside of each half insulates the moulds from the heated platens. The cooling channels on both halves are connected to hoses that feed oil into the mould to help cool and harden the plastic. In addition, vents are also present to allow air to escape when the plastic is injected. This is essential in preventing air getting trapped during injection, which may cause the mould to burn due to the high pressure or may form air bubbles, in both cases ruining the part. The cavity plate on the fixed mould half contains inserts that form the surface of the moulded part. The cavity plate can

hold multiple inserts making it possible for multiple copies of the same part to be created in one cycle. This reduces manufacturing time for a given number of parts and lowers cost. The core plate on the moving mould half holds the other half of the insert that completes the component shape. The ejector plate is responsible for the removal of the finished part from the mould. A series of pins are connected to the ejector plate running forward to the core plate. When the ejector plate pushed forward, the pins move forward and push the part off the core plate insert. Figure 2.14 shows an example of an optical mould insert fabricated by Zhong et al [57]. One half of the insert was a spherical convex core and the other half a spherical concave cavity for moulding plastic lenses. The main shapes were machined using a CNC machine and the spherical surfaces were machined by single point diamond turning to produce a shiny and smooth surface finish. The insert surface finish is of very high importance as it has a direct impact on the surface of the final moulded part.



Figure 2.14: Plastic lens mould insert [57]

Electroless nickel-phosphorous plated mould steels, optical aluminium alloys and copper alloys are among the materials used in making optical mould inserts [58]. The turning of Ni-P steels have exhibited accelerated tool wear, affecting the final surface quality, and requiring additional processes to obtain the desired optical quality surface [59-61]. Aluminium alloys and copper alloys have gained popularity over Ni-P steel in the making of optical moulds due to these major technical disadvantages. Figure 2.15 illustrates the processing steps of RSA

905 in comparison to Ni-P plating in the production of moulds. It can be seen that using RSA 905 greatly reduces cycle time.

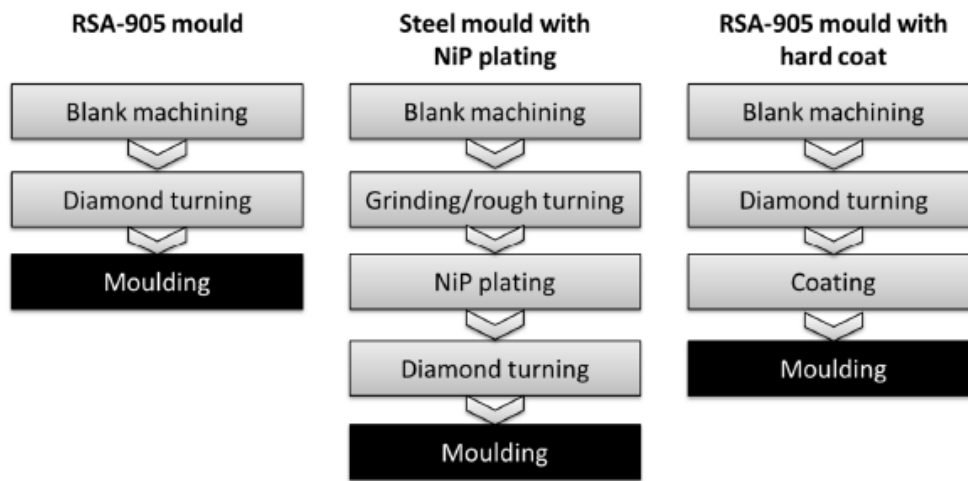


Figure 2.15: Processing steps of RSA 905 vs Ni-P plating in mould making [62]

Table 2.5 is an overview comparison of properties and achievable surface finishes between the materials commonly used in making optical moulds. Conventional aluminium alloys, such as AA-7075, are limited by their low maximum operating temperature and tendency to suffer from pull-outs during diamond turning, making mould processing at high temperatures difficult and reducing tool life, respectively. RSA 905 has a high hardness and high operating temperature (in the same range as Ni-P plating/steel) making it suitable for high temperature mould processes, such as the making of polycarbonate lenses which are typically injected at 310°C [62].

Table 2.5: Comparison of material properties used in mould making [62]

	RSA-905	Copper alloy	Steel + NiP	NiP plating	AA-7075
Principal elements	Al, Ni, Fe, Cu	Cu, Ni, Si, Cr	Cr Mo Steel		Cu, Mg, Zn
Density (g/cm³)	2,95	8,72	7,8		2,85
Mechanical properties					
Young modulus (GPa)	90	131	205		70
YS (MPa)	480	510	895		525
UTS (MPa)	600	662	1020		565
Elongation (%)	6	13	20		10
Brinell Hardness (HB)	180	210	301	480	160
Thermal properties					
CTE (µm/m/K)	19	17,5	12,1	13	24,7
Conductivity (W/m/k)	115	208	29		160
Heat capacity (J/kg/K)	849	381	460		844
Diffusivity (mm ² /s)	46	63	8		67
Volumetric thermal stability (m ² K/s)	2,4	3,6	0,7		2,7
Max. operating temperature (°C)	380	482	400	400	125
Surface characteristics					
Diamond turnable	Good	Medium (large crystals)	Steel bad NiP good	Good	Medium (large crystals; pull-outs)
Surface roughness Sq (nm)	2	5-10	2	2	5-10

Generally, Ni-P steels are used in large series moulding of up to several million operations while copper alloys are used in smaller series moulding of up to several thousand operations. The disadvantage of copper alloys is excessive tool wear which in turn quickly degrades the surface quality. This can be improved by coating the copper with Ni-P but this again this is an additional step that lengthens the lead time. Gubbels et al. [62] performed an injection moulding test comparing copper alloy, Ni-P plated copper alloy and RSA 905 moulds. Polycarbonate lenses were moulded with a mould temperature of 115°C and 300°C using mould inserts for biconvex lenses with a diameter of 12 mm. Figure 2.16 is a chart showing of the results. The copper alloy mould performed poorly in comparison due to deterioration from corrosion by the polymer. The Ni-P plating improve the life of the copper alloy mould but this was still outperformed by the RSA 905 mould. It is clear from the tests that RSA 905 provides a longer mould life and would be a viable alternative to copper alloys and the Ni-P

steels which are time consuming to produce. More research is still required in the diamond turning process of RSA 905 to further understand and maximise its potential.

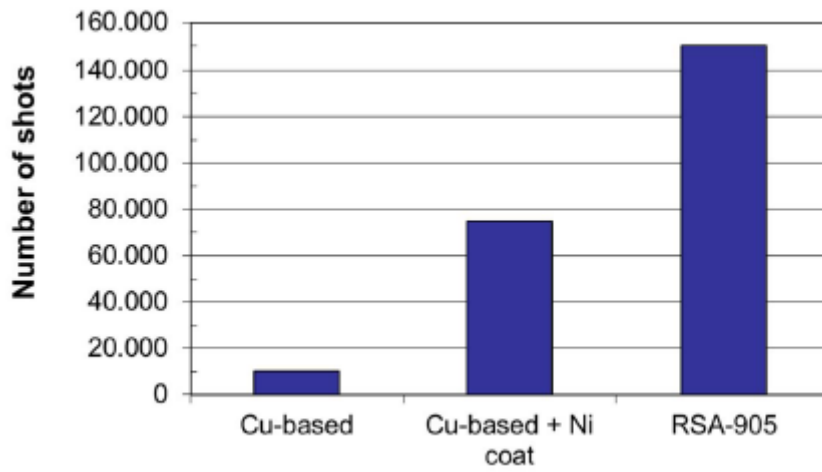


Figure 2.16: Mould life comparison of RSA 905 vs copper alloys [62]

Figure 2.17 and Figure 2.18 are examples of injection-moulded components produced by Accu-Sort Systems, Inc.



Figure 2.17: Injection-moulded octagon for laser barcode scanning application [44]

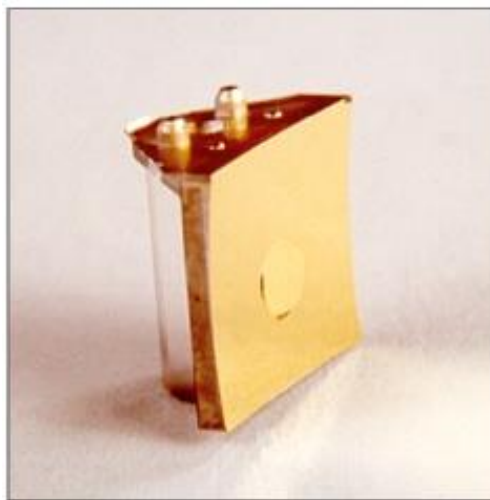


Figure 2.18: Injection-moulded ellipsoidal mirror [44]

2.8 Molecular Dynamics Simulation of Nanometric Machining

Ultra-high precision machining involves material removal at a nanometric level that results in high form and a superior surface finish. It is difficult to fully observe the machining phenomena occurring at micro and nano scale. Conventionally, finite element methods (FEM) are used in modelling machining processes. FEM has successfully modelled machining at macro level and micro level providing information on cutting temperature, cutting forces, chip formation and stress distribution [63,64]. Macro and micro scales of machining assume the cutting to be a continuous process, but once the cutting reduces to the nanoscale it is assumed to be a discrete process. Discrete atomistic simulations are a suitable

method to investigate the material behaviour down at nanoscale. The physics of the cutting mechanism at nano level is different from that at the macro/conventional level. Table 2.6 compares nanometric and conventional cutting mechanics.

Table 2.6: Nanometric cutting and conventional cutting comparison [65]

	Nanometric Cutting	Conventional Cutting
Fundamental Cutting Principles	Discrete molecular mechanics	Continuum mechanics
Workpiece Material	Heterogeneous	Homogeneous
Cutting Physics	Atomic cluster model	Shear plane model
Energy Consideration	Interatomic potential function	Shear/friction power
Cutting Force	Interatomic forces	Plastic deformation
Chip Formation	Inner crystal deformation	Inter crystal deformation
Deformation and Stress	Discontinuous	Continuous
Tool Edge Radius	Significant	Ignored
Tool Wear	Cutting face and edge	Rake face

Molecular dynamics (MD) is a computer simulation technique used in the study of the motions of a set of particles [66]. The MD method involves solving equations of motion for interacting atoms and determining their positions, velocities and accelerations with time. Classic MD simulation utilises Newton's second law of motion by which the force F acting on each atom is

$$F = m a \quad (2.11)$$

where m is the mass of the atom and a is the acceleration of the atom.

MD simulation can be outlined in the following steps [67]:

1. Select the model (2D/3D).
2. Select an interatomic potential.
3. Select the algorithm for integrating equations of motion.
4. Initialise the model.
5. Relax the model from its initial state to a dynamically equilibrium condition.
6. Run the simulation and analyse the results.

One of the most important steps of MD simulation is selecting the appropriate interatomic potential. The forces on the atoms are calculated as the gradient of the potential function, hence the interatomic potential is a key factor in the resulting accuracy of the simulation. The forces of the atoms are calculated as

$$F_i = -\frac{\partial}{\partial r_i} V(r_i \dots r_n) \quad (2.12)$$

where $V(r_i \dots r_n)$ represents the potential energy of the system with $(r_i \dots r_n)$ describing the coordinate position of the atoms [67].

There are various potential functions that are commonly used to model various materials, namely:

- Lennard-Jones
- Morse
- Tersoff
- Born-Meyer
- Embedded-Atom Method

Lennard-Jones (LJ) is mostly suited for rare gases and is defined by the equation

$$V_{ij} = 4\varepsilon \left[\left(\frac{\sigma}{r} \right)^{12} - \left(\frac{\sigma}{r} \right)^6 \right] \quad (2.13)$$

where ε and σ are constants which are dependent on the physical properties of the material [67].

The Morse potential is suited for cubic metals and is defined by the equation

$$V_{ij} = D \{ \exp[-2\alpha(r_{ij} - r_e)] - 2\exp[-\alpha(r_{ij} - r_e)] \} \quad (2.14)$$

where r_{ij} and r_e are instantaneous and equilibrium distances between atoms i and j respectively, α and D are constants based on the material properties [67].

The Tersoff potential is suited for covalently bonded materials like silicon atoms and is defined by the equation

$$V_{ij} = V_r(r_{ij}) - B_{ij}V_a(r_{ij}) \quad (2.15)$$

where V_r and V_a are the potentials due to repulsive and attractive forces between atoms i and j and B_{ij} is a parameter that provides the information for the direction and the length of the bond [67].

The Born-Meyer potential is suited for Group III-V semiconductors and ceramics and is defined by the equation

$$V_{ij} = A\{exp[-2\alpha(r_{ij} - r_0)]\} \quad (2.16)$$

where A and r_0 are constants dependent on the material properties [67].

The Embedded-Atom Method (EAM) potential is suited for a wide range of metals and is defined by the equation

$$V_{ij}(R) = U_{ij}(R) + 2G'_i(\bar{\rho}_i)\rho_j^a(R) + G''_i(\bar{\rho}_i)\left(\rho_j^a(R)\right)^2 \quad (2.17)$$

Where U_{ij} is the electrostatic interaction between two atoms, G is the embedding energy, ρ is the constant background density, ρ^a is the average atomic electron density, and R is the separation of the atoms [67]. The EAM potential incorporates an approximation for the many-atom interactions neglected by other potential schemes. EAM can be modified to include the directionality of the bonding or bond angle. This extension of EAM is known as Modified Embedded-Atom Method (MEAM) potential and it accommodates covalent

systems by explicitly handling the bond angle. MEAM is suited for metals and alloys with FCC, BCC, HCP and cubic structures, and covalent materials such as silicon and carbon. Generally, EAM and MEAM should be used for metals, Tersoff and MEAM for covalent materials, and LJ and Morse for interactions of materials where suitable potentials are not available [67]. The interatomic potential can be plotted as a function of energy against atomic distance providing an illustration of various energy aspects of the bond. Figure 2.19 shows a typical profile of an interatomic potential function and its characteristics along with a related force curve. This potential energy well profile provides information on bonding energies which are directly related to physical properties such as melting point, elastic modulus and thermal coefficient. For example, a deeper well represents strong interatomic interactions, meaning more energy is required to break these bonds and thus a high melting temperature and low thermal coefficient.

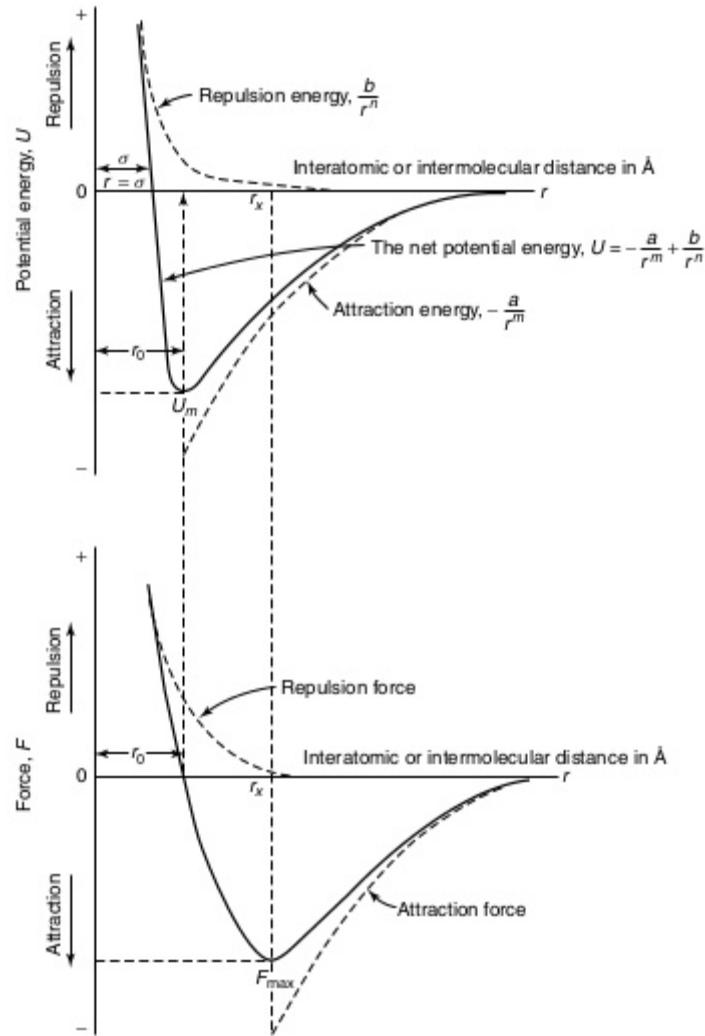


Figure 2.19: Interatomic potential energy and force diagrams [68]

Once the appropriate potential is selected, an algorithm for the integration of Newton's equations of motions is chosen. This involves solving for the positions and velocities at a time t and at a later time $t + \Delta t$. The integration schemes approximate the positions, velocities and accelerations using a Taylor series expansion. A number of algorithms have been developed for the integration such as the Verlet algorithm, the predictor-corrector algorithm and the Beeman's algorithm. These algorithms are usually already implemented within the MD software. The time steps used in MD simulations are mostly within a few femto (10^{-15}) seconds [69].

Following the selection of the integration scheme for the equations of motion, the model is initialised. This involves defining the MD control volume and assigning the initial position and velocities of the atoms. Crystal structures may be used to define the positions and velocities can be randomised. The model is then relaxed from its initial state to a dynamically equilibrium condition. This is done by running the MD program under a constant temperature for a pre-determined time steps, allowing the system to gradually reach a natural state of dynamic equilibrium at the specified temperature [70]. The simulation can then be run and the results recorded and analysed. Machining parameters and/or conditions can easily be adjusted using MD simulations and their resulting effects analysed. The properties of materials and cutting tools can also be adjusted and the effects studied. The results obtained from MD simulations include cutting forces, cutting temperature, kinetic and potential energies, and pressure. These results are indicative of machining process and the effects on the workpiece and tool. For example, low cutting forces mean less vibration of the tool and as a result improved surface roughness [71].

The images obtained also provide information on the chip formation. Figure 2.20 shows a typical MD simulation of a machining process. The simulation space involves two sets of bodies, the workpiece and the cutting tool, made up of a group of atoms. The cutting tool atoms collide with the workpiece atoms at a specified speed and depth simulating the cutting process.

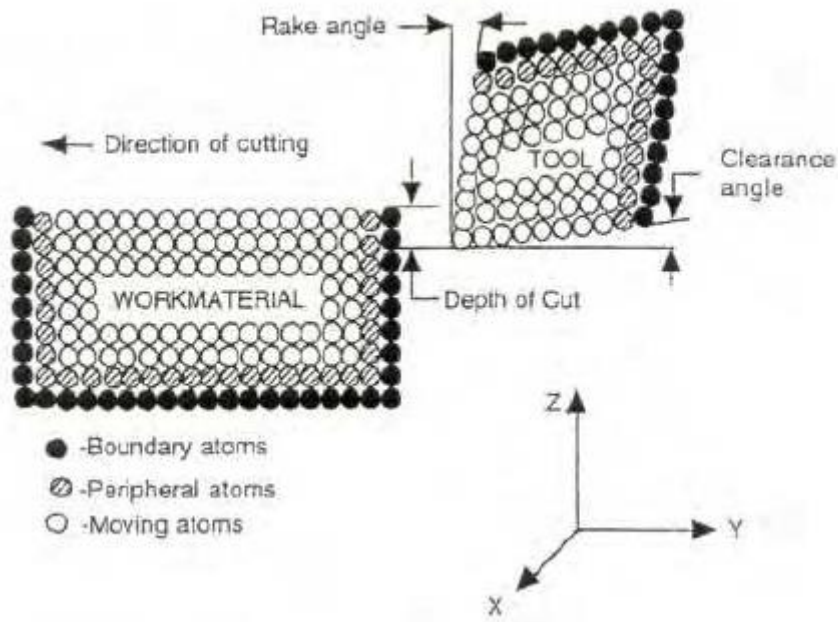


Figure 2.20: Molecular dynamics simulation of metal cutting [72]

The material lattice structure is made up of three types of atoms: boundary atoms, thermostat atoms and Newtonian atoms. The boundary atoms are fixed to reduce edge effects, the thermostat atoms conduct the heat generated from cutting and the Newtonian atoms are the moving atoms that follow Newton's equation of motion. Most models of nanometric simulations are 2D as this saves a vast amount of computation time but there is a significant loss of quality in material representation. Simulations using 3D models are becoming increasingly utilised and the increased computational requirement is compensated by applying parallel computation systems or developing smaller models of small width. Smaller models also means less atoms need to be generated reducing computational time. Another effort to reduce the computational requirements in nanometric machining simulations is the use of extremely high cutting speeds, in the range of 200 to 500 m/s compared to conventional speeds of 2 to 5 m/s. The use of higher spec workstations and parallel computing can bring the simulation cutting speeds down to a more realistic level. The tool itself is usually modelled as a rigid body, hence disregarding workpiece interaction and tool wear.

Belak et al. [73] pioneered the MD simulation of nanomachining. They simulated the cutting of copper to investigate chip formation, mechanisms of plastic deformation, flow of material and the flow of energy into the chip and workpiece. EAM potential was used to model the copper workpiece and LJ potential was used for the tool-workpiece interface. Since then numerous researchers have used MD simulation to model nanomachining. There has been a significant amount of work in modelling the effect of the cutting conditions. Promyoo et al. [74] simulated the nanometric diamond cutting of single-crystal copper to investigate the cutting forces and mechanism of chip formation. The EAM potential was employed for the workpiece (Cu atoms) and Morse potential was employed for the workpiece to diamond tool interaction (Cu-C atoms). The cutting tool was considered as a rigid body due to the high hardness of diamond. The cutting tool rake angle was varied from 0° to 45° and the depth of cut varied from 0.724 nm to 2.172 nm. It was concluded that the cutting force, thrust force and ratio of thrust force to cutting force decreased with increasing rake angle. The forces were found to be independent of depth of cut. The chip thickness was found to decrease with an increase of rake angle. Komanduri et al. [75,76] performed extensive research on the effects of machining parameters on the performance of nanomachining using MD simulation. They performed various work investigating the effects of machining parameters, such as cutting speed, depth of cut, width of cut, crystal orientation, rake angle, on chip formation and cutting force development. MD simulations have also been used to research how the workpiece material properties affect the nanomaching performance. Huang et al. [77] performed MD simulations to investigate the influence of material properties on the nanometric cutting of copper and aluminium. EAM potential was used to model the workpiece (Cu-Cu atoms and Al-Al atoms) and Morse potential for the tool-workpiece interactions. The diamond tool was treated as a rigid body. The results showed significant differences in the cutting forces, surface quality and chip morphology between the two

materials, proving the material properties have a strong influence in nanometric cutting. MD simulations have also been used to model the performance of the tool by investigating tool wear. Cheng et al. [78] performed various investigations on diamond tool wear using MD. They discovered that cutting temperature has an effect on diamond tool wear as heat generation decreases the cohesiveness between carbon atoms. Narulkara et al. [79] discovered that iron has an anisotropic influence on graphitisation, an important aspect that directly affects the chemical wear in diamond tool.

It is important to generate an accurate atomistic model of the material being analysed. Most research on MD simulation of nanomachining employs monocrystalline structures as the work material. However, most engineering materials exist in polycrystalline form presenting a new challenge when it comes to MD modelling. Shi and Verma [80] performed a preliminary study by simulating nanomachining of polycrystalline copper and comparing it to monocrystalline copper. They discovered that for various cutting conditions, smaller cutting forces were produced for the polycrystalline structure. This was linked to the existence of more grain boundaries (regarded as defects) that leads to easier chipping. Shi et. al [81] performed an extensive study on the nanoscale machining of polycrystalline copper by focusing on the effect of grain size and machining parameters. The machining speed, depth of cut, rake angle and grain size were varied. The results showed increase in cutting forces with increase in machine speed and with increase in depth of cut, but less significant with change in depth of cut. The cutting forces was found to decrease with increase in rake angle. Also, an increase in grain size resulted in higher cutting forces, and monocrystalline copper that was used as a benchmark produced higher forces than all the polycrystalline copper experiments.

Another challenge that exists in the MD modelling of alloys is brought about by the presence of multiple elements. The atomistic structure has to be well represented and an accurate

potential function assigned for the interactions between the different types of atoms. If there is a heavy presence of multiple elements, phases and/or intermetallic interactions within the alloy structure, selecting a suitable potential function to model the material can become difficult. Libraries of accurate alloy EAM potentials exist for some intermetallic interaction (such as Cu-Au, Al-Ni, Cu-Al-Zr), but these are very limited. EAM potential files can mostly be found in established online repositories such as the NIST Interatomic Potentials Repository Project [82]. Developing new and accurate potential for alloys can be a time-consuming and exhaustive process. Ward et al. [83] have developed a procedure to generate accurate binary potentials by combining already-existing single-element potentials to form multi-component alloy potentials. This could be a very useful tool for modelling metal alloys but the database is currently limited to Ag, Al, Au, Cu, Ni, Ti and Zr. Similarly, a method developed by Zhou et al. [84] also exists to create EAM files for alloy systems, but this is also limited to Cu, Ag, Au, Ni, Pd, Pt, Al, Pb, Fe, Mo, Ta, W, Mg, Co, Ti and Zr. This method offers more elemental metals combinations and produces potentials well fitted to material properties that have been successfully implemented in studies [85,86].

There are currently no related studies carried out on molecular dynamics simulations of rapidly solidified aluminium alloys. The lack of past studies in this area can be attributed to the lack of sufficient data on the newly-developed RSA crystal structure and interatomic potential limitations.

2.9 Past Work on Diamond Turning of Aluminium Alloys

Detailed extensive research on diamond machining of modified aluminium alloys is very limited. Precision machining of traditional aluminium alloys has been investigated by various researchers [14,87-90]. Revel et al. [88] performed diamond turning of traditional aluminium alloys of varying hardness. The alloys selected were Al 5083, AU4G and Fortal, which were

also compared to pure aluminium. The varying hardness was due to the element crystals or precipitates present in the alloy. Fortal was the hardest with the most precipitates present, AU4G was less hard with fewer precipitates and Al 5083 was the softest with the least precipitates. The workpieces were 35 mm diameter disks of 6 mm thickness. The first set of tests involved varying the cutting speed and the second set of tests involved varying the feed rate. Depth of cut was kept constant and the aim was to determine the optimum cutting speed and feed rate. Varying the cutting speed with constant feed rate and depth of cut showed a trend of lower surface roughness values for higher cutting speeds. Varying the feed rate with constant feed rate and depth of cut showed a trend of lower surface roughness values for lower feed rates. Based on these tests, the cutting speed was selected as 1200 rpm, the feed rate as 10 $\mu\text{m}/\text{rev}$ and the depth of cut was maintained at 15 μm . The specimens were cut using a single crystal diamond tool with a 5° rake angle. Al 5083 achieved a surface roughness of 5 nm, AU4G 8 nm and Fortal 15 nm. Pure aluminium had the lowest roughness value of 4 nm. They concluded that the surface roughness produced was a function of the presence of precipitates and their hardness. This proved that microstructural properties directly affect the roughness of a diamond machined surface.

Zhong et al. [57] compared the performance of rapidly solidified aluminium with beryllium copper and aluminium alloy 6061 in the making of mould inserts. The moulds were made up of a spherical convex core insert and a spherical concave cavity insert that were used to mould plastic lenses. The inserts were diamond machined at a depth of cut of 6 μm , cutting speed of 2000 rpm and feed rate of 5 $\mu\text{m}/\text{rev}$. They found that high precision SPDT of RSA produced a finer surface quality compared to traditional AA 6061 and BeCu. They did not measure the surface finish of the mould inserts but of the lenses produced from them instead. The performance of the mould inserts was evaluated using an injection moulding machine to produce 1500 plastic lenses from each insert. RSA performed much better than AA 6061 and

slightly better than BeCu as mould inserts. The surface roughness of the lenses produced was measured in intervals through the production and the average calculated. The lenses produced from the AA 6061, BeCu and RSA had an average surface roughness of 45 nm, 35 nm and 25 nm, respectively. The lenses produced from the AA 6061 insert showed a deteriorating surface quality over increasing mould operations while the BeCu and RSA inserts maintained a fairly constant surface quality. This was attributed to the hardness and wear rates of the insert materials. BeCu, being the hardest, has the lowest wear rate and thus a longer mould insert lifespan, followed by RSA then AA 6061 which is the softest with the highest wear rate. Harder insert materials are better in maintaining a constant surface quality of the produced lenses over subsequent operations. BeCu produced very good results but beryllium is known to be a toxic element that poses health risks and must be handled with extreme caution. It was concluded that RSA is a suitable replacement to BeCu.

Gubbles et al. [41] investigated the diamond machinability of AA 6061, nickel plated RSA 6061 and melt spun RSA 6061. Flat samples 40 mm in diameter were turned with diamond tool of 0.5 mm nose radius and zero rake angle. The machining parameters were kept constant at 3000 rpm cutting speed, 5 mm/min feed rate and 5 μ m depth of cut. The resulting surface roughness obtained from AA 6061 was 3.8 nm, 1.7 nm from Ni plated 6061 and 2.3 nm from melt spun RSA 6061. The high hardness of nickel facilitates polishing behaviour allowing very low surface roughness to be achieved, but nickel plating means an additional manufacturing process. The results showed the high performance of RSA by achieving surface roughness values lower than traditional AA 6061 and close to Ni plated 6061 without the need for additional processing steps.

Horst et al. [91] performed diamond turning and polishing tests on AA 6061, RSA 6061 and RSA 905 to compare the surface roughness achievable. The samples were 60 mm in diameter

and were machined under the same conditions; a cutting speed of 2500 rpm, feed rate of 2 mm/min and depth of cut of 4 μm . AA 6061 achieved an average surface roughness of 5 nm, RSA 6061 and RSA 905 approximately 3.5 nm. In addition, different heat treated samples of these alloys were diamond turned and compared, billet and extrusion. It was discovered that the extruded samples performed slightly better than the billet samples under these machining conditions. The machining conditions were then optimised using statistical methods to determine the effect of various parameters on the resulting surface roughness. The following factors were investigated: machine, operator, tool wear, spindle speed, feed rate, diamond crystal orientation, tool nose radius, plano/spherical workpiece, lubricant application pressure, lubricant quantity, rake angle of the tool and material. It was found that tool angle, tool sharpness, speed, feed and machine were the only ones that were statistically relevant. For minimum surface roughness, the tool should be sharp and have a 0° rake angle. These are fixed settings and one should select the best machine, tool configuration and tool sharpness. However, the spindle speed and feed rate can be tuned to achieve the optimum result. An optimising ratio of feed rate to spindle speed was calculated as 1.3 $\mu\text{m}/\text{rev}$ to achieve minimum surface roughness. Under the optimised machining conditions, a surface roughness within 1 nm was then achieved for RSA 6061 and approximately 2 nm for RSA 905. There was no difference in surface roughness between billet and extruded samples under the optimised machining conditions. All the samples were diamond turned with the same tool for a total distance of approximately 35 km under these optimal conditions and no significant tool wear was noticed. The non-optimised resulting samples were polished and a surface roughness of approximately 1 nm was obtained from both the conventional and the modified alloys. However, the AA 6061 required more polishing time.

Shi et al. [43] used electron-beam-induced deposition (EBID) and scanning electron microscopy (SEM) to measure diamond tool wear. A hydrocarbon line was deposited by

EBID across the flank face and rake face of the diamond tool allowing for direct observation in the SEM images. An aluminium 6061 disk of 100 mm diameter was orthogonally cut using a flat nose (0° rake angle) diamond tool with a 6° clearance angle. The cutting conditions were kept constant at 500 rpm cutting speed and $2\ \mu\text{m}$ depth of cut. The 6061 disk was cut for a distance of 10 km and resulted in a tool wear of $4.5\ \mu\text{m}$.

Abou-El-Hossein et al. [13] looked into diamond tool wear when precision machining RSA 905 while varying the feed rate. The workpieces were machined to produce convex surfaces of 100 mm convexity radius. The diamond inserts had a negative rake angle of 5° and clearance of 5° . The feed rate used was 5, 15 and 25 mm/min. The cutting speed and depth of cut were kept constant at 2000 rpm and $25\ \mu\text{m}$, respectively. The machining tests were stopped after cutting a distance of 17 km. In addition, the wear on the diamond inserts and resulting chips were analysed using scanning electron microscopy. The tool wear mechanism observed was identical for the three feed rates. Tool wear of $3\ \mu\text{m}$, $12\ \mu\text{m}$ and $10\ \mu\text{m}$ were observed for the three feed rates, respectively. It was discovered that the abrasive effect on the diamond edge was the dominant wear mechanism when machining RSA. The abrasion was found to be less at lower feed rates and less harmful. The SEM analysis showed uniform wear and absence of chipping and grooving mechanisms. A lack of notch wear was also observed showing that RSA was almost free from built-up edge chip formation. The chips produced from all three feed rates were continuous indicating they were flowing smoothly during cutting. This can be attributed to the ultra-fine microstructure of RSA. These results show that RSA has better tool wear performance compared to AA 6061 used by Shi et al. [43], considering more severe cutting conditions were employed here.

As seen, most of these studies focused on the surface quality with very little attention given to the wear of the diamond tool. Also, none of them adequately studied the machinability of

the materials over a range of cutting parameters. However, it is important to note that all the results show a trend of improved surface roughness for modified aluminium alloys compared to traditional aluminium alloys. The relevant past work is summarised in Table 2.7. This research thesis aims to close this gap by studying the effects of cutting parameters on surface quality and tool wear to establish a suitable machining reference for achieving more efficient results. Furthermore, the cutting forces, acoustic emissions and material behaviour was examined and correlated to provide more insight into the surface results obtained.

Table 2.7: Past work on surface roughness and tool wear of modified aluminium alloys

Author	Material	Cutting speed (rpm)	Feed rate (mm/min)	Depth of cut (μm)	Cutting distance (km)	Roughness (nm)	Tool wear (μm)
Revel et al. [88]	Pure Al Al 5083 AU4G Fortal	1200	12	15	-	4 5 8 15	-
Zhong et al. [57]	BeCu AA 6061 RSA 905	2000	10	6	-	35 45 25	-
Gubbles et al. [41]	AA 6061 Ni-plated RSA 6061	3000	5	5	-	3.8 1.7 2.3	-
Horst et al. [91]	AA 6061 RSA 6061 RSA 905	2500	2	4	-	5 3.5 3.5	-
Shi et al. [43]	AA 6061	500	-	2	10	-	4.5
Abou-El-Hosseini et al. [13]	RSA 905	2000	5 15 25	25	17	-	3 12 10

3. Experimental Setup for Diamond Turning

3.1 Workpiece Material

The workpiece material used was RSA 905 produced by RSP Technology Ltd. The RSA 905 underwent the melt spinning solidification process at a rate of 10^6 K/s producing an ultra fine microstructure composition. It is a very robust and universal alloy that exhibits superior mechanical and physical properties in comparison to other optical grades of aluminium. No heat treatment is required to realise its properties. It has very high stiffness, high strength, high fatigue and is corrosion resistant. The RSP alloy boasts the following properties [54]:

- Density 2.95 g/cm^3
- Thermal expansion $19 \cdot 10^{-6}/\text{K}$
- Thermal conductivity 100 W/m.K
- Modulus of elasticity 90 GPa
- Ultimate tensile strength 600 MPa
- Yield strength 475 MPa
- Elongation 7%
- Hardness 180 HB

The RSA 905 workpiece was a 60 mm diameter disk as shown in Figure 3.1. The workpiece was fitted in an adapter designed for easy spindle attachment/detachment and centring.



Figure 3.1: Workpiece setup

3.2 Machining Setup

The experiments were performed on the Precitech Nanoform 250 Ultragrind machining centre shown in Figure 3.2.



Figure 3.2: Precitech Nanoform 250 Ultragrind

The Nanoform 250 had the following key features:

- 4 axes (X, Y, Z and B)
- 1 nm accuracy
- Up to 7000 rpm spindle speed
- Vacuum chuck
- Turning and grinding capabilities

Mono-crystalline diamond was used as the cutting tool. The diamond tool inserts manufactured by Contour Fine Tooling (shown in Figure 3.3 and Figure 3.4) are commonly used in optics manufacturing and had the following features:

- Non-controlled waviness
- 0.5 mm nose radius
- -2.5° rake angle
- 5° clearance angle



Figure 3.3: Diamond tool holder and insert

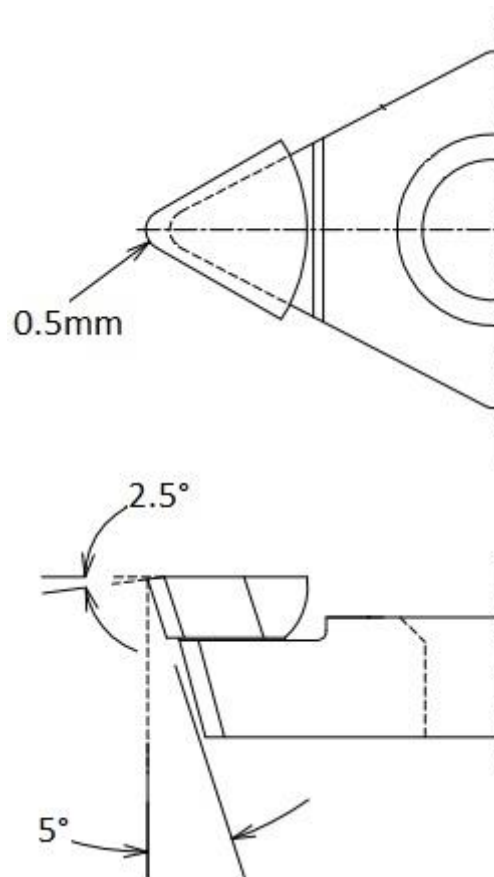


Figure 3.4: Diamond tool dimensions

The inserts were mounted on a horizontal 0° tool holder. A new diamond insert was used for each experiment number. Odourless kerosene mist was used as coolant. The force sensor and acoustic sensor were mounted on the tool holder. The data from the sensors was collected simultaneously for each experiment. The final setup is shown in Figure 3.5.

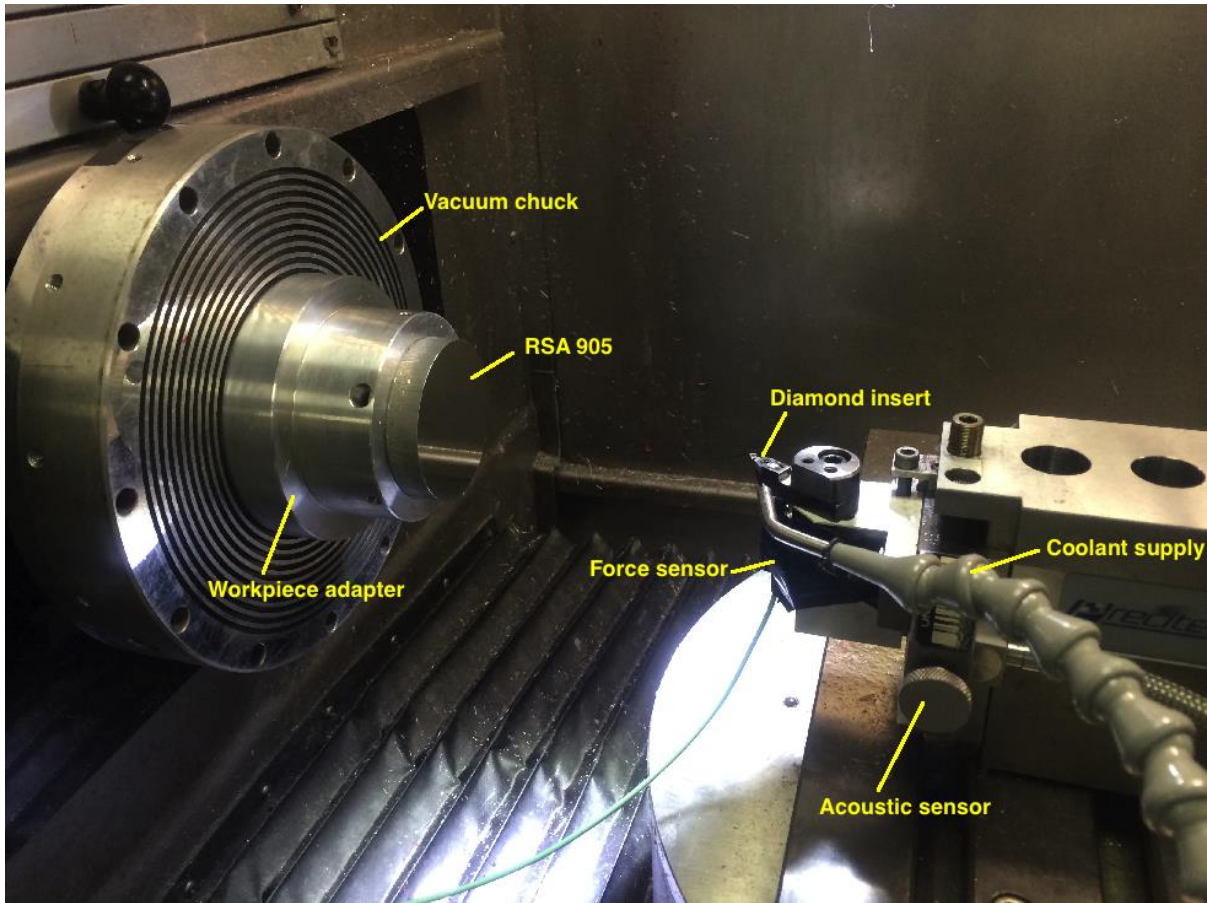


Figure 3.5: Experimental setup

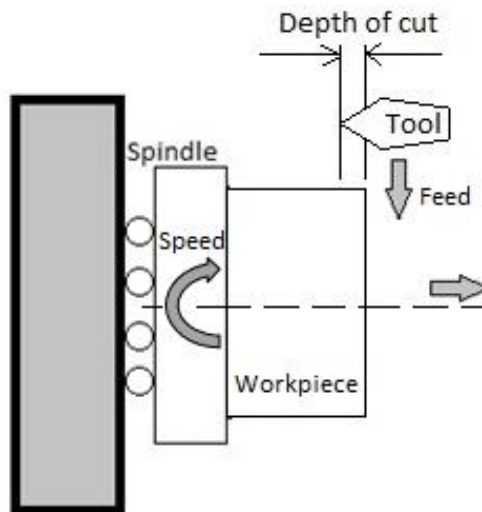


Figure 3.6: Cutting tool path viewed from top

The face turning tool path is illustrated in Figure 3.6 as viewed from the top. The tool nose engaged the workpiece at a set depth of cut moving towards the centre where it disengaged,

while the workpiece rotated on its own axis. The machining tool path was repeated to reach the required cutting distance by performing multiple passes.

3.3 Response Surface Method and Box Behnken Design

Response surface methodology (RSM) is a mathematical/statistical technique that is utilised for modelling the relationship between input variables and output responses. The cutting conditions, cutting speed, feed rate and depth of cut, were the input parameters. The output responses were surface roughness, tool wear, acoustic emission RMS and force. RSM also provides a means of determining the most influential input parameter and the effect of the interactions of the parameters on the response. RSM reduces the required number of experiments for analysis saving time and cost.

The Box Behnken method was used to create a design of experiments [92]. This method is favoured in machining research due to the fact that it requires minimal tests. It was selected as it is efficient (fewer runs), almost rotatable (precision depends on distance to the origin), and has no corner points (no extreme conditions). It is generally used in non-sequential experimentation and offers efficient evaluation for first and second order models. The input variables were selected at three levels as the end points and centre points of the ranges: cutting speed 500, 1750 and 3000 rpm, feed rate 5, 15 and 25 mm/min, depth of cut 5, 15 and 25 μm . The parameter ranges were selected to cover reasonable extremes of commonly used cutting conditions in machining aluminium alloys based on previous work as described in Section 2.9. The design, shown on Figure 3.7 and Table 3.1, produced 13 different experiment combinations with the centre point being replicated twice (to minimise error) giving a total of 15 experiments to be run. The number on each node on Figure 3.7 correlates with the standard order in Table 3.1.

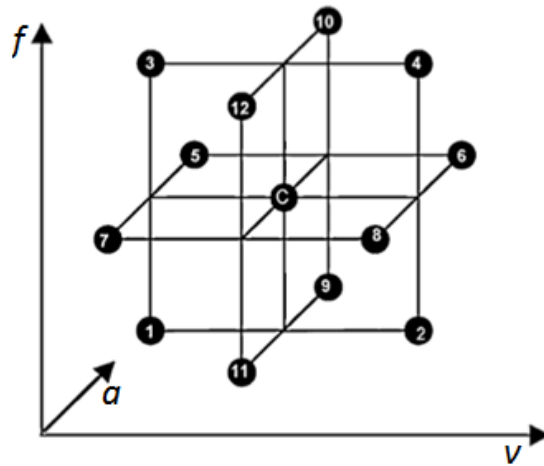


Figure 3.7: Three factorial Box Behnken design

Table 3.1: Experiments machining parameters

Standard Order	Experiment No.	Cutting Speed v (rpm)	Feed Rate f (mm/min)	Depth of Cut a (μ m)
12	1	1750	25	25
10	2	1750	25	5
2	3	3000	5	15
13	4	1750	15	15
15	5	1750	15	15
11	6	1750	5	25
7	7	500	15	25
4	8	3000	25	15
8	9	3000	15	25
3	10	500	25	15
6	11	3000	15	5
1	12	500	5	15
9	13	1750	5	5
14	14	1750	15	15
5	15	500	15	5

From the results, the effect and dominance of the cutting parameters on the response were identified and a model was created to predict resulting surface roughness and tool wear. A second order model was considered as it provides an understanding into the second order effect of each variable and the two-way interaction between these variables. The second order model was represented in the form

$$\hat{y}'' = y'' - \varepsilon = b_0x_0 + b_1x_1 + b_2x_2 + b_3x_3 + b_{11}x_1^2 + b_{22}x_2^2 + b_{33}x_3^2 + b_{12}x_1x_2 + b_{13}x_1x_3 + b_{23}x_2x_3 \quad (3.1)$$

where y is the response experimental value and \hat{y} is the response predicted value, while $x_0, x_1, x_2, x_3, \varepsilon$ are dummy variable ($x_0 = 1$), cutting speed, feed rate, depth of cut, and experimental error, respectively, and b_0, b_1, b_2, b_3 are the model parameters. The adequacy of the models was verified using analysis of variance (ANOVA). A surface roughness and tool wear models were charted to illustrate the performance of the aluminium alloys with varying cutting parameters and identify zones that provide the optimum results.

Equation 3.2 – 3.7 were used for parameter conversions to determine the number of passes required for each experiment to achieve the desired distance as well as the material removal rate. The results were tabulated in Table 3.2.

Cutting speed:

$$v_{m/s} = \frac{v_{rpm} \times \pi \times d}{60} \quad (3.2)$$

where $v_{m/s}$ is the cutting speed in metres per second, v_{rpm} is the cutting speed in revolutions per minute and d is the diameter of the workpiece in metres.

$$v_{rpp} = v_{rpm} \times t_p \quad (3.3)$$

where v_{rpp} is the cutting speed in revolutions per pass, v_{rpm} is the cutting speed in revolutions per minute and t_p is the time per pass.

Feed rate:

$$f_{\mu m/rev} = f_{mm/min} \times \frac{1000}{v_{rpm}} \quad (3.4)$$

where $f_{\mu m/rev}$ is the feed rate in micrometres per revolution, $f_{mm/min}$ is the feed rate in millimetres per minute and v_{rpm} is the cutting speed in revolutions per minute.

Time:

$$t_p = \frac{d}{2f_{mm/min}} \quad (3.5)$$

where t_p is the time per pass in seconds, d is the diameter of the workpiece in metres, $f_{mm/min}$ is the feed rate in millimetres per minute.

Distance:

$$s_p = \pi \times \frac{d}{2} \times v_{rpp} \quad (3.6)$$

where s_p is the distance per pass in metres, d is the diameter of the workpiece in metres and v_{rpp} is the cutting speed in revolutions per pass.

Material removal rate:

$$MRR = v_{m/s} \times 60 \times 1000 \times \frac{f_{\mu m/rev}}{1000} \times \frac{a}{1000} \quad (3.7)$$

where $v_{m/s}$ is the cutting speed in metres per second, $f_{\mu m/rev}$ is the feed rate in micrometres per revolution and a is the depth of cut in micrometers.

Table 3.2: Experiments cutting parameters detail

Exp	Cutting Speed			Feed Rate		Depth of Cut	Workpiece Diameter		Time per Pass	Distance per Pass	Total Distance	Total Passes	Total Time	Material Removal Rate
	No.	rpm	m/s (max)	rev/pass	mm/min		μm/rev	μm						
1	1750	5.50	2100.00	25	14.29	25	60	0.06	1.20	197.92	4.0	20	24	117.81
2	1750	5.50	2100.00	25	14.29	5	60	0.06	1.20	197.92	4.0	20	24	23.56
3	3000	9.42	18000.00	5	1.67	15	60	0.06	6.00	1696.46	4.0	2	14	14.14
4	1750	5.50	3500.00	15	8.57	15	60	0.06	2.00	329.87	4.0	12	24	42.41
5	1750	5.50	3500.00	15	8.57	15	60	0.06	2.00	329.87	4.0	12	24	42.41
6	1750	5.50	10500.00	5	2.86	25	60	0.06	6.00	989.60	4.0	4	24	23.56
7	500	1.57	1000.00	15	30.00	25	60	0.06	2.00	94.25	4.0	42	85	70.69
8	3000	9.42	3600.00	25	8.33	15	60	0.06	1.20	339.29	4.0	12	14	70.69
9	3000	9.42	6000.00	15	5.00	25	60	0.06	2.00	565.49	4.0	7	14	70.69
10	500	1.57	600.00	25	50.00	15	60	0.06	1.20	56.55	4.0	71	85	70.69
11	3000	9.42	6000.00	15	5.00	5	60	0.06	2.00	565.49	4.0	7	14	14.14
12	500	1.57	3000.00	5	10.00	15	60	0.06	6.00	282.74	4.0	14	85	14.14
13	1750	5.50	10500.00	5	2.86	5	60	0.06	6.00	989.60	4.0	4	24	4.71
14	1750	5.50	3500.00	15	8.57	15	60	0.06	2.00	329.87	4.0	12	24	42.41
15	500	1.57	1000.00	15	30.00	5	60	0.06	2.00	94.25	4.0	42	85	14.14

4. Surface Roughness Analysis

4.1 Surface Roughness Measurement Setup

Surface quality can be regarded the most important property of a precision machined product. This is mainly due to the fact that precision machining is used when a very high surface quality is required. The cutting action of the diamond tool produces a roughness profile on the workpiece surface. A direct measurement technique was employed to measure this surface roughness. A profilometer was used to measure the mean deviation of the surface height from the mean profile line giving average roughness R_a values.

The profilometer used was the Form Talysurf PGI Optics 3D by Taylor Hobson (Figure 4.1) and it had the following features:

- Form measurement capability of better than $0.1 \mu\text{m}$
- Measurement of high numerical apertures - slopes greater than 85°
- Automated set-up, measurement and analysis routines
- 3D aspheric measurement, analysis and surface astigmatism display
- Large working envelope - from 1 mm up to 200 mm



Figure 4.1: Form Talysurf PGI Optics 3D

The Form Talysurf setup has a user-friendly interface with a fully automated calibration and operation. This allows for accurate and efficient measurements. Based on the cutting parameters from the Box Behnken design, the surface roughness of the RSA 905 workpiece was measured at various intervals for each experiment. The machined workpiece was placed on the high precision air-bearing spindle on the profilometer table (Figure 4.2) and the automated probe dragged along the surface giving roughness measurements. The measurement was taken parallel to the direction of the feed.

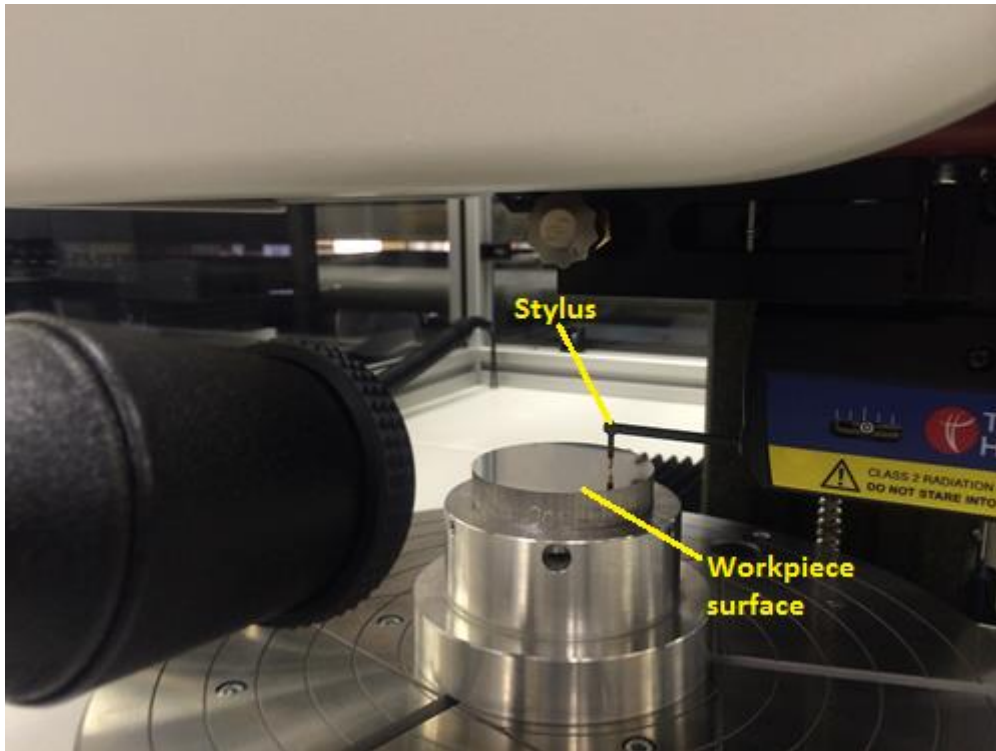


Figure 4.2: Stylus probe measuring workpiece surface

4.2 Surface Roughness Results

Table 4.1 shows the average roughness results of each experiment at various distances up to 10 km.

Table 4.1: Surface roughness results

Experiment No.	Cutting Speed v (rpm)	Feed Rate f (mm/min)	Depth of Cut a (μm)	Distance (km)	Roughness R_a (nm)
1	1750	25	25	0.4	8.9
				4.0	7.0
				10.0	10.9
2	1750	25	5	0.6	7.3
				4.0	6.6
				10.0	6.7
3	3000	5	15	4.0	3.9
				10.0	2.6
4	1750	15	15	0.7	4.6
				4.0	3.6
				10.0	4.3
5	1750	15	15	0.7	4.4
				4.0	3.7
				10.0	4.5
6	1750	5	25	2.0	3.1
				4.0	3.2
				10.0	4.3

7	500	15	25	0.2	50.4
				1.0	31.9
				1.9	21.8
				2.9	31.4
				4.0	53.9
				10.0	73.0
8	3000	25	15	0.7	5.0
				4.0	4.2
				10.0	4.7
9	3000	15	25	1.1	4.1
				4.0	3.7
				10.0	6.0
10	500	25	15	0.1	130.1
				0.3	124.3
				0.6	116.8
				1.6	79.4
				2.8	42.9
				4.0	31.2
				10.0	51.0
11	3000	15	5	1.1	4.6
				4.0	4.6
				10.0	8.4
12	500	5	15	0.6	4.6
				4.0	4.1
				10.0	5.3
13	1750	5	5	2.0	4.0
				4.0	3.3
				10.0	3.5
14	1750	15	15	0.7	4.6
				4.0	4.2
				10.0	4.7
15	500	15	5	0.2	47.9
				1.7	25.1
				2.9	24.3
				4.0	34.5
				10.0	85.0

The diamond tool interaction with the material, the tool shape, the cutting parameters and the built-up edge all had an effect on the resulting surface finish. The results showed a common trend of minimal decrease to surface roughness with increasing cutting distance. This showed the consistency of RSA 905 and the ultra-high precision cutting process. However, this only held true to a given point, thereafter the surface roughness increased with distance as other effects such as tool wear came into play. This was found to occur between 4 km and 10 km

cutting distance. The effect of each cutting parameter on the surface roughness remained constant with increase in cutting distance.

Large differences in surface roughness occurred with changes in cutting speed. Experiment 11 and experiment 15 that had the same feed rate 15 mm/min and depth of cut 5 μm , showed drastic differences in roughness. Experiment 11 with the higher cutting speed 3000 rpm had a much lower surface roughness of 4.6 nm compared to experiment 15 with the lower cutting speed of 500 rpm and a surface roughness of 34.5 nm after 4 km.

Changes in feed rate suggested that lower feed rates produced finer surfaces. Experiment 1 and Experiment 6, both at 1750 rpm cutting speed and 25 μm depth of cut, resulted in 7 nm roughness for 25 mm/min feed rate and 3.2 nm roughness for 5mm/min feed rate after 4 km. Also comparing experiment 2 and experiment 13, at 1750 rpm and 5 μm , the higher feed rate had R_a 6.6 nm while the lower feed rate had R_a 3.3 nm after 4 km.

Changes in depth of cut between 5 μm and 25 μm seemingly had a small effect on the surface roughness results. Experiment 1 and experiment 2 that had the same cutting speed 1750 rpm and feed rate 25 mm/min but varying depth of cut produced similar results within 7 nm after 4 km. Similarly, experiment 9 with 25 μm depth of cut and experiment 11 with 5 μm depth of cut, both at cutting speed 3000 rpm and feed rate 15 mm/min, produced roughness values with less than 1 nm difference.

Low cutting speeds combined with high feed rates produced the poorest results. Experiment 10 at 500 rpm cutting speed and 25 mm/min feed rate gave the highest initial surface roughness measurement of 130.1 nm. High cutting speeds combined with low feed rates produced the best results. Experiment 6 at 1750 rpm and 5 mm/min gave the lowest initial surface roughness of 3.1 nm. The combination of a high feed rate and low cutting speed could possibly have not allowed the tool to thoroughly cut the workpiece during each pass. Figure

4.3 illustrates how the spiraling cutting path is widened creating a surface profile with spaced grooves or peaks and valleys, thus increasing the average surface roughness. It should be noted that the spiral spacing in the figure have been exaggerated for comparison purposes.

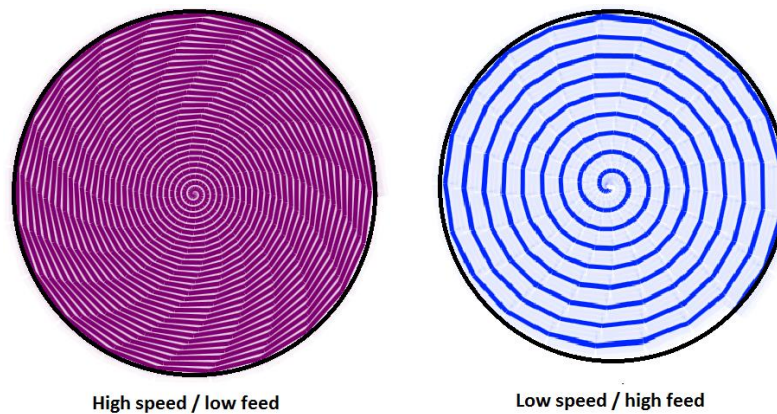


Figure 4.3: Spiral cutting path comparison of cutting speed/feed rate combinations

It was interesting to note that changes in depth of cut had a small effect on the average surface roughness. This could be attributed to the cutting tool tip dimensions, mainly the nose radius and rake angle which were sufficiently large enough for nanomachining depths of cut while maintaining a sharp contact point. The depth of cut would not have a significant effect on the surface finish within the selected range (5 – 25 μm) unless increased to a point where the tool engagement is deep enough to be classified as a “rough” cut. This meant that within the selected depth of cut range, high material removal rates could be achieved with very little compromise to the desired optical surface quality, especially when combined with high cutting speeds. A sharper tool tip might provide a better surface finish but this flexible cutting depth range might become more limited. Further statistical analysis was applied to determine the effect of each parameter.

The surface roughness improving and/or maintaining fairly consistent values with increasing distance could be linked to the manner in which the tool is wearing. The tool has a large nose radius in comparison to the contact area and the tool engages the workpiece from the side at

the desired depth. As the cutting edge wears, a newer, flatter contact surface with sharp end edges is created that will engage the workpiece on the next pass. This means a sharp tool engagement point with every pass and the flattening out of irregularities on the workpiece surface thus improving/maintaining the surface roughness as seen with most of the experiments. This effect is prevalent due to the workpiece surface being flat, illustrated in Figure 4.4. When machining a workpiece where form accuracy is critical, such as a concave surface, this would not apply as the surface roughness and form accuracy would most likely be seen to deteriorate. However, the tool wears to a point where the newly sharp edges also wear down and the surface roughness then deteriorates, as seen with the 10 km readings. This created the surface roughness trend of improvement followed by deterioration with increased cutting distance. This effect is further seen when the total number of passes are high, such as experiment 10 and experiment 15.

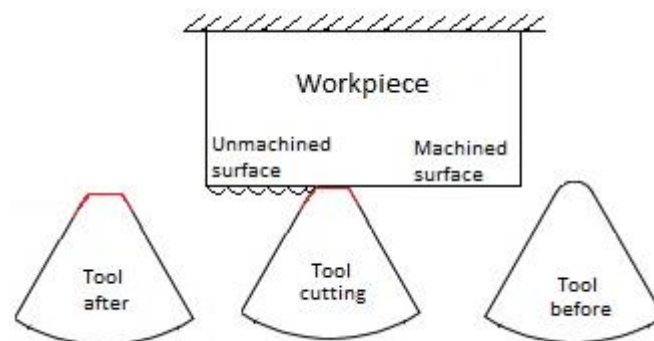


Figure 4.4: Tool tip flattening and smoothing surface

Figure 4.5 shows the lowest R_a result obtained from the profilometer after 4 km of 3.2 nm, where the parameters were cutting speed 1750 rpm, feed rate 5 mm/min and depth of cut 25 μm (experiment 6).

The surface profile charts showed that higher R_a values produced more periodic profiles with higher amplitudes than lower R_a values. As R_a decreased, amplitude peaks increased and became more closely packed, but their magnitude decreased. Figure 4.7 shows the workpiece comparison between a good surface finish and a poor surface finish, where the superior finish is clearly seen to be characterised with a smoother and more reflective surface.

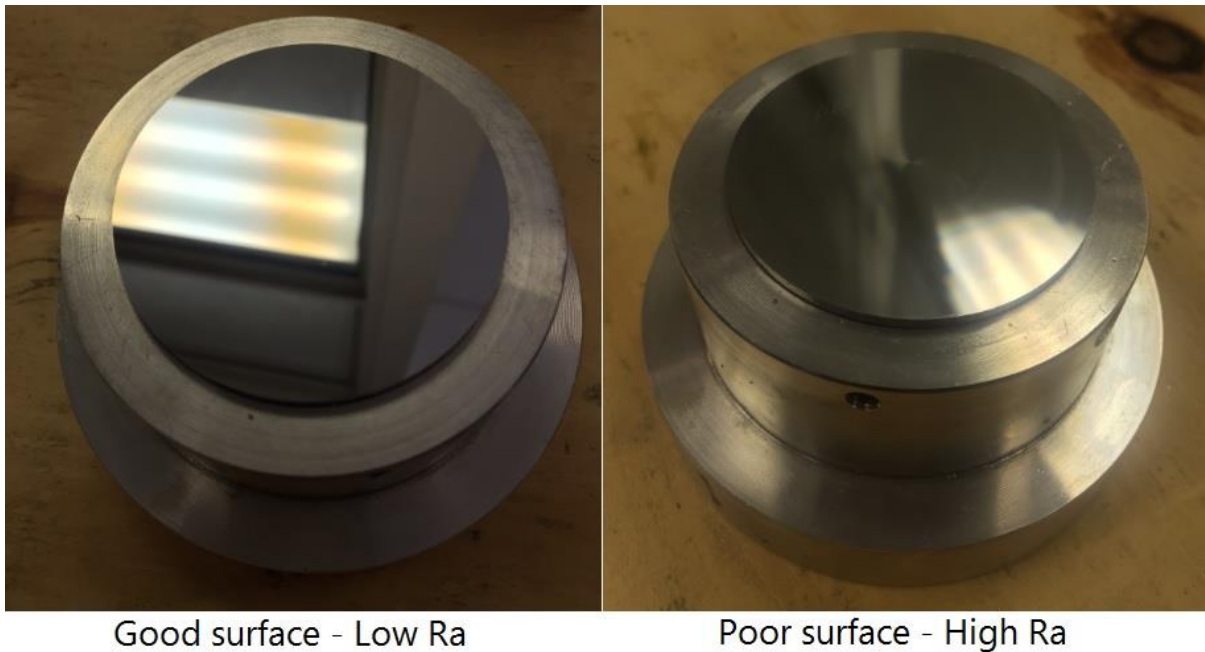


Figure 4.7: Comparison between good surface finish and poor surface finish

A tendency of the chips to collect and coil around the tool and workpiece (Figure 4.8) was observed during experiments with slower cutting speeds. At low cutting speeds and feeds, the chips became longer and tangled around the tool reducing the efficiency of the coolant at the cutting zone. This effect made the cutting more abrasive and deteriorated the surface quality and the tool as well (as seen in the next chapter). The collecting chips constantly rubbing on the workpiece consequently influenced the resulting surface roughness as these experiments had higher R_a values. The chips were generally long and stringy for slower speeds and very fine/powdery for higher speeds (Figure 4.9). Higher cutting speeds did not allow for this

tangling and build-up to occur producing fine segmented chips and better surface quality as a result.



Figure 4.8: Chips around tool during low cutting speeds

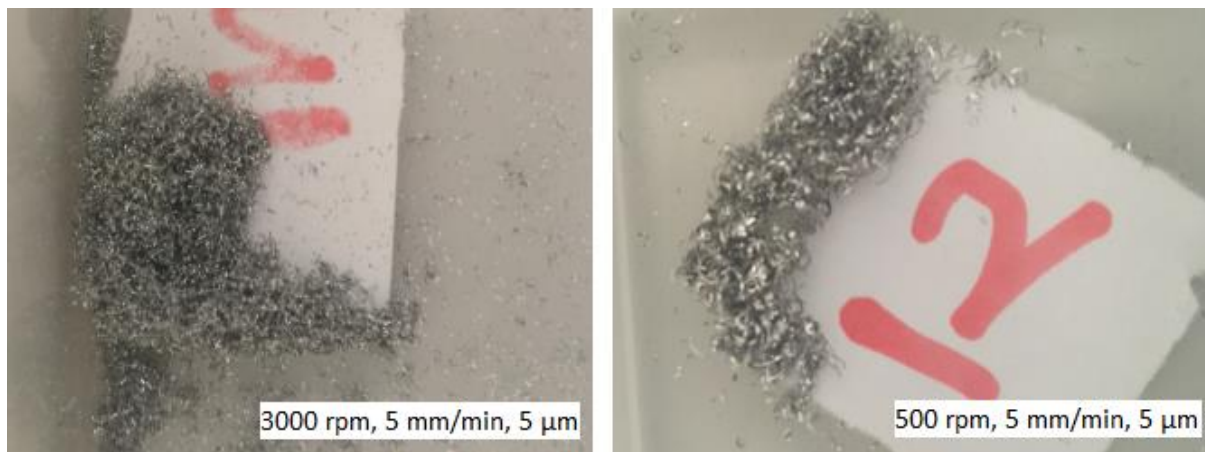


Figure 4.9: Chips collected after high speed cutting (left) and low speed cutting (right)

4.3 Surface Roughness Statistical Analysis

The measurements of the surface roughness from each experiment were entered into the Box Behnken design in Design Expert software. The response surface method was applied to

create and evaluate the model. The selection of a suitable polynomial equation was done by performing lack of fit tests. The surface roughness results ranged from 3.2 nm to 53.9 nm. The ratio of maximum to minimum was 16.84. The initial model failed the lack of fit tests and an inverse transformation was applied based on the Box-Cox plot (Figure 4.10) to produce a model of the form

$$y' = \frac{1}{y+k} \quad (4.1)$$

Design-Expert® Software
1.0/(Surface Roughness)

Lambda
Current = -1
Best = -1.01
Low C.I. = -1.86
High C.I. = -0.34

Recommend transform:
Inverse
(Lambda = -1)

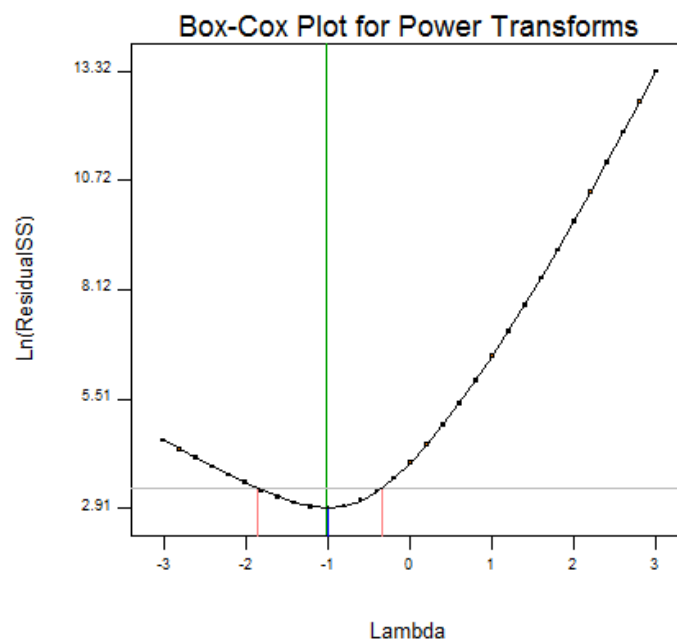


Figure 4.10: Box-Cox plot for R_a model

The Box-Cox plot shows the minimum error point and the software suggests the power transform required. The lack of fit tests produced the results shown in Table 4.2. The lack of fit should be insignificant ($p\text{-value} > 0.05$). Table 4.2 shows that a quadratic model should be selected as it was insignificant and had the highest $p\text{-value}$.

Table 4.2: Lack of Fit tests for R_a model

Source	Sum of Squares	DF	Mean Square	F-Value	P-Value
Linear	0.050153814	9	0.005572646	12.54018109	0.0760
2FI	0.039705512	6	0.006617585	14.89161847	0.0643
Quadratic	0.007388356	3	0.002462785	5.542030712	0.1567
Cubic	0	0			
Pure Error	0.000888766	2	0.000444383		

The adequacy of the model was evaluated through ANOVA as shown in Table 4.3. Table 4.3 revealed the relevant terms at 95% confidence level that had a significant effect (P-value < 0.05) on surface roughness. The insignificant terms were eliminated to produce a reduced model for surface roughness. The results show the model was significant and lack of fit was insignificant.

Table 4.3: Analysis of variance for R_a model

Source	Sum of Squares	DF	Mean Square	F-Value	P-Value
Model	0.133599005	6	0.022266501	17.98610823	0.0003
A-Cutting Speed	0.054231589	1	0.054231589	43.80639915	0.0002
B-Feed Rate	0.037994794	1	0.037994794	30.6908791	0.0005
C-Depth of Cut	0.000233907	1	0.000233907	0.188942027	0.6753
AB	0.009364059	1	0.009364059	7.563962748	0.0250
A ²	0.025272219	1	0.025272219	20.41402362	0.0020
C ²	0.008424832	1	0.008424832	6.805287479	0.0312
Residual	0.009903866	8	0.001237983		
Lack of Fit	0.0090151	6	0.001502517	3.381128124	0.2458
Pure Error	0.000888766	2	0.000444383		
Cor Total	0.143502871	14			

The final model to determine surface roughness was thus defined as Equation 4.2 below.

$$R_a = (0.082276 + 0.00019258v - 0.013665f + 0.014828a + 0.00000387vf - 0.00000005v^2 - 0.000476259a^2)^{-1} \quad (4.2)$$

where v is the cutting speed in rpm, f is the feed rate in mm/min, a is depth of cut in μm , and R_a is the surface roughness in nm.

The model shows that increase in cutting speed would decrease surface roughness but when significantly increased, the cutting speed squared term with a negative coefficient would come into effect and increase the surface roughness. The feed rate increasing would directly increase the surface roughness. Increase in depth of cut would have a similar effect on the surface roughness as cutting speed but its squared term would come into effect much sooner (at lower values). This means depth cut would initially decrease surface roughness to a point then lead to an increase in surface roughness. These effects could be seen in the results recorded in Table 4.1. Experiments with higher cutting speeds had lower surface roughness values. Cutting speeds of 1750 rpm and 3000 rpm had low results while 500 rpm had very high results in comparison. This suggests that the lowest surface roughness attainable is within 1750-3000 rpm and slowly deteriorates thereafter. Experiments with higher feed rates generally had higher surface roughness values and this was fairly proportional. Depth of cut showed similar surface roughness results for 5 μm and 25 μm (i.e. experiment 1 and experiment 2) while most experiments (i.e. experiment 4) with 15 μm had lower surface roughness values suggesting the roughness initially decreased with increasing depth of cut thereafter roughness increased. The effect of a single factor may not hold true for all experiments as the three factors all play a role in the determining the result. The model was analysed further to provide a better understanding and verification on the effect of the factors.

The normal probability plot in Figure 4.11 shows normality of residuals and close proximity to the probability line supporting the adequacy of the model.

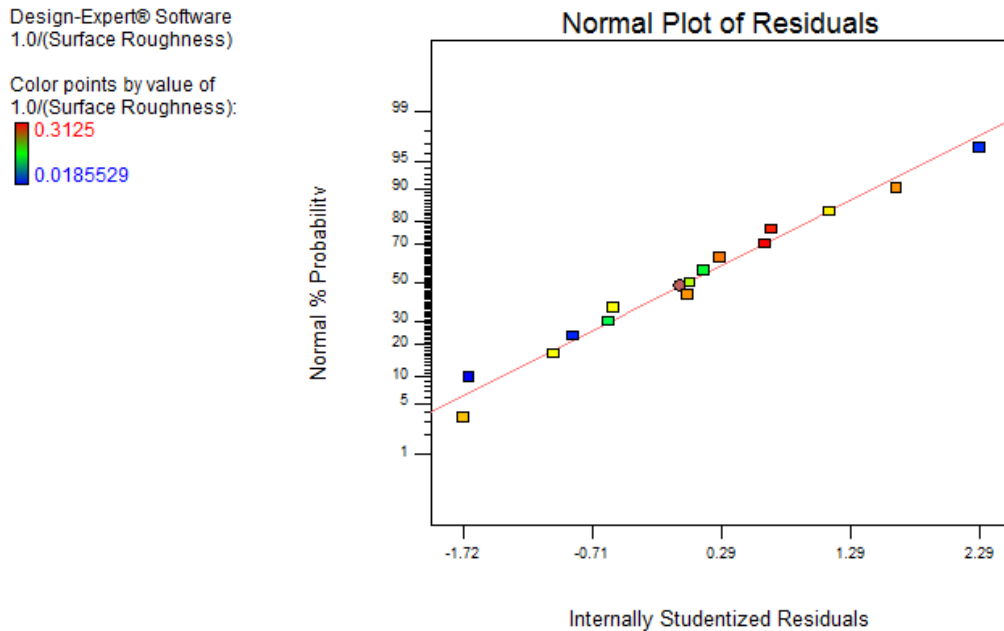


Figure 4.11: Normal probability plot for R_a model

The impact of each variable was assessed by plotting the inverse surface roughness term against each variable. Figure 4.12 shows cutting speed has a square curve relationship with surface roughness. As the cutting speed increases, the inverse surface roughness increases in a curved manner, peaking at approximately 2300 rpm before slowly decreasing. Hence, surface roughness decreases with increase in cutting speed to an optimum point before increasing. Figure 4.13 shows feed rate has a linear relationship with inverse surface roughness. As the feed rate increases, the inverse surface roughness decreases in a linear manner and hence surface roughness increases. Figure 4.14 shows depth of cut has an almost flat curve with the best surface roughness achieved at 15 μm depth of cut. From the plots it can be seen that cutting speed has the greatest impact on surface roughness while depth of cut has the least impact.

Design-Expert® Software
Transformed Scale
1.0/(Surface Roughness)

◆ Design Points

X1 = A: Cutting Speed

Actual Factors
B: Feed Rate = 15.00
C: Depth of Cut = 15.00

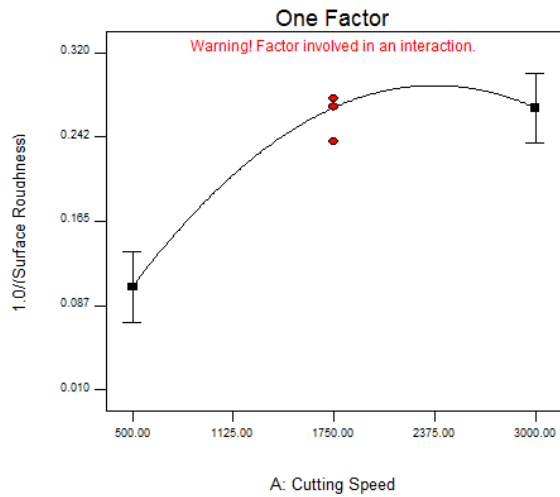


Figure 4.12: Effect of cutting speed on inverse surface roughness model

Design-Expert® Software
Transformed Scale
1.0/(Surface Roughness)

◆ Design Points

X1 = B: Feed Rate

Actual Factors
A: Cutting Speed = 1750.00
C: Depth of Cut = 15.00

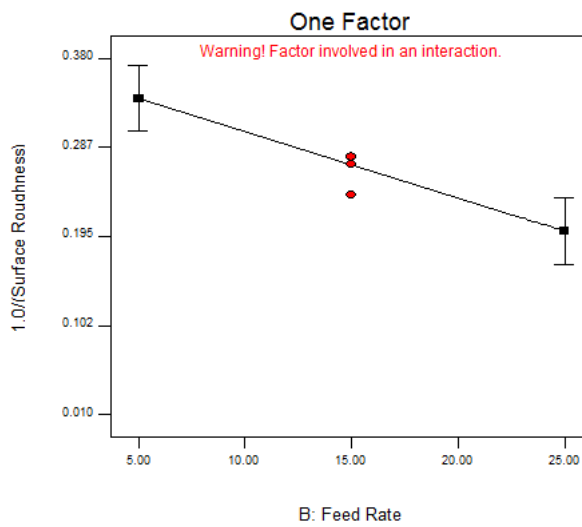


Figure 4.13: Effect of feed rate on inverse surface roughness model

Design-Expert® Software
Transformed Scale
1.0/(Surface Roughness)

◆ Design Points

X1 = C: Depth of Cut

Actual Factors
A: Cutting Speed = 1750.00
B: Feed Rate = 15.00

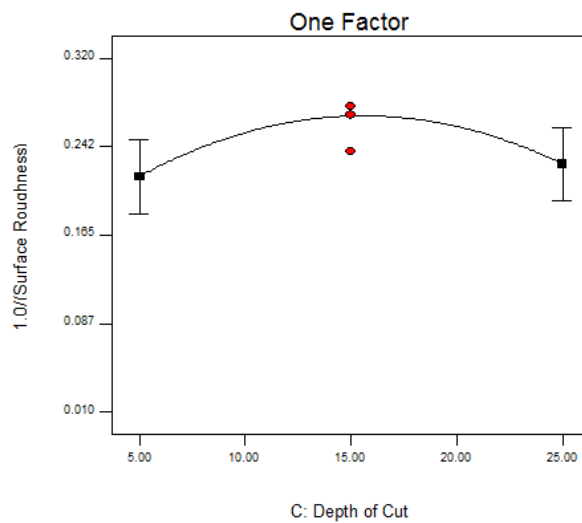


Figure 4.14: Effect of depth of cut on inverse surface roughness model

The developed model was used to plot contour maps of inverse surface roughness at the three levels of depth of cut. Figure 4.15-Figure 4.17 were surface roughness maps generated from the model at 5 μm , 15 μm and 25 μm depth of cut, respectively, after 4 km of machining. The ideal cutting parameters would maximise the inverse surface roughness.

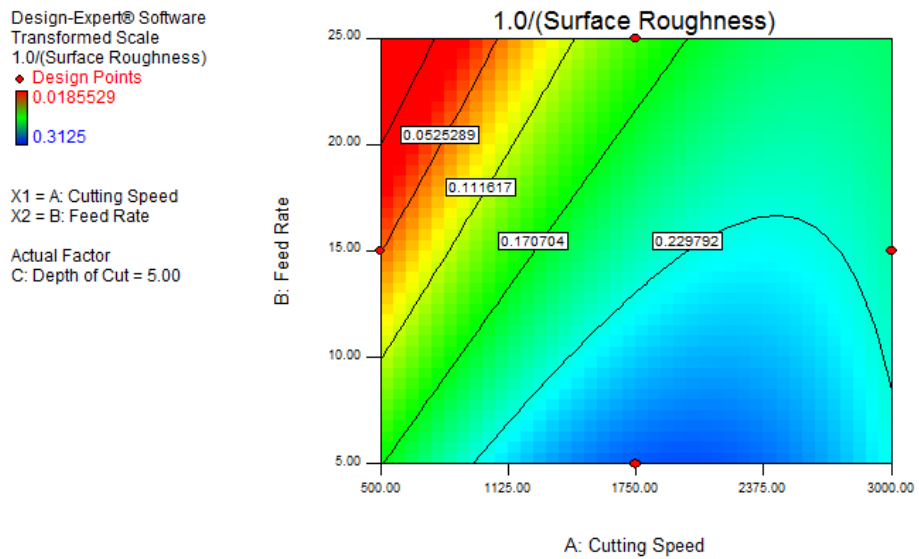


Figure 4.15: Surface roughness map for 5 μm depth of cut

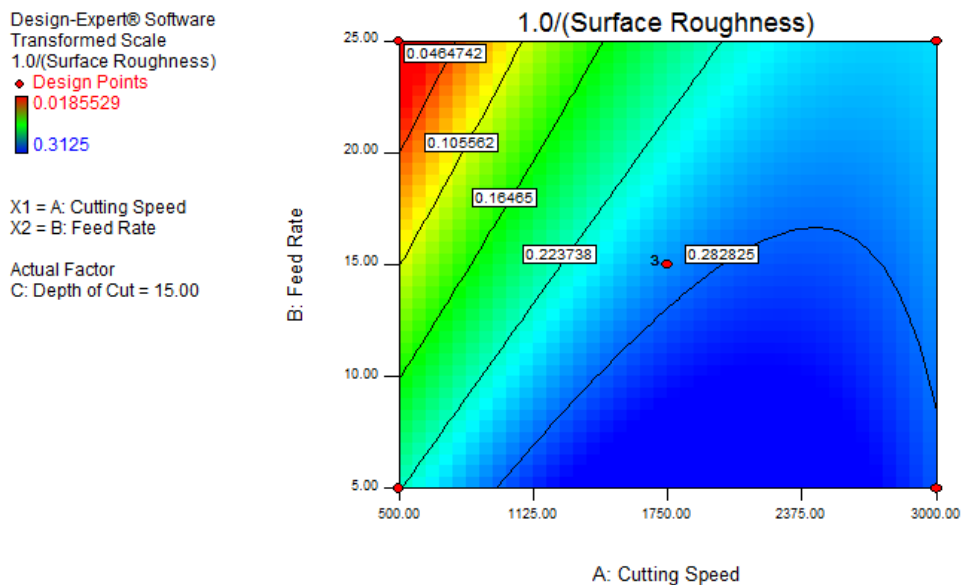


Figure 4.16: Surface roughness map for 15 μm depth of cut

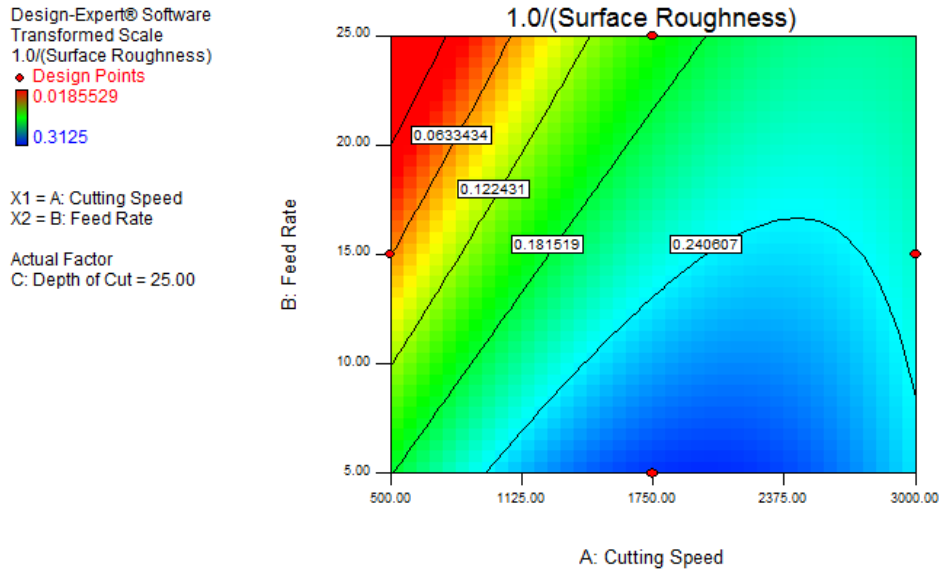


Figure 4.17: Surface roughness map for 25 µm depth of cut

The surface roughness maps show the lowest surface roughness was associated with higher cutting speeds and lower feed rates. The maps also show that depth of cut had a small influence on the surface roughness as the three generated maps are similar. The 15 µm depth of cut chart shows a wider area of very low surface roughness showing that this cutting depth provides the best flexibility of cutting speed and feed rate range.

As the cutting distance increased to 10 km, the inverse model was maintained and the lack of fit tests (Table 4.4) also maintained that the quadratic equation would produce the best fit. The 10 km surface roughness model was defined as:

$$R_{a10} = (0.03222110 + 0.00021403v - 0.02136614f + 0.0226842a - 0.00000004v^2 + 0.00045462f^2 - 0.0007816a^2)^{-1} \quad (4.3)$$

where v is the cutting speed in rpm, f is the feed rate in mm/min, a is the depth of cut in µm and R_{a10} is the surface roughness in nm after 10 km of cutting.

Table 4.4: Lack of fit tests for 10 km surface roughness model

Source	Sum of Squares	DF	Mean Square	F-Value	P-Value
Linear	0.054116128	9	0.006012903	61.35796936	0.0161
2FI	0.053587675	6	0.008931279	91.138199	0.0109
Quadratic	0.00579021	3	0.00193007	19.69517345	0.0487
Cubic	0	0			
Pure Error	0.000195994	2	9.79971E-05		

The ANOVA results (Table 4.5) and the normal probability plot (Figure 4.18) show the significant terms and adequacy of the model. The model was significant and the lack of fit was insignificant.

Table 4.5: Analysis of variance for 10 km surface roughness model

Source	Sum of Squares	DF	Mean Square	F-Value	P-Value
Model	0.14874133	6	0.02479022	30.44239974	< 0.0001
A-Cutting Speed	0.05270615	1	0.05270615	64.72316892	< 0.0001
B-Feed Rate	0.04777085	1	0.04777085	58.66261897	< 0.0001
C-Depth of Cut	0.00046686	1	0.00046686	0.57330652	0.4707
A ²	0.01635809	1	0.01635809	20.08774216	0.0021
B ²	0.00763133	1	0.00763133	9.37128187	0.0156
C ²	0.02255649	1	0.02255649	27.69937981	0.0008
Residual	0.00651466	8	0.00081433		
Lack of Fit	0.00631866	6	0.00105311	10.74634176	0.0876
Pure Error	0.00019599	2	0.00009800		
Cor Total	0.15525598	14			

Design-Expert® Software
 1.0/(Surface Roughness 10km)

Color points by value of
 1.0/(Surface Roughness 10km):
 0.384615
 0.0117647

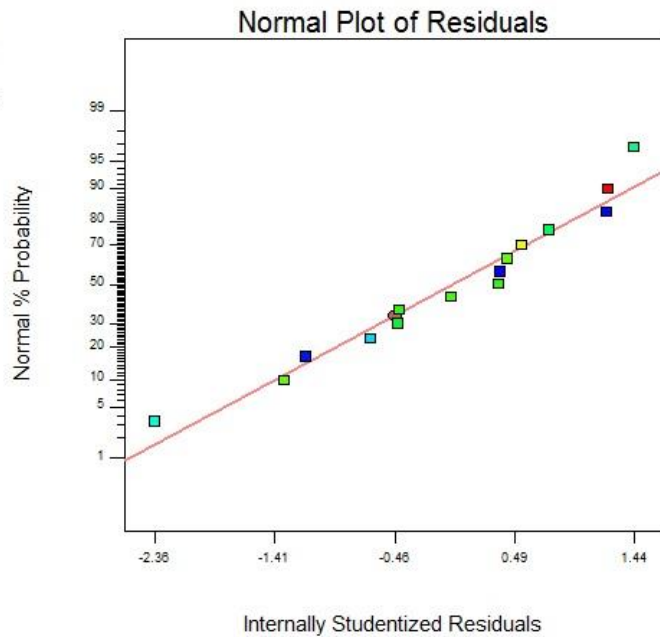


Figure 4.18: Normal probability plot for 10 km surface roughness model

The presence of square terms in the model suggests a curved profile for each of the cutting parameters as the distance increased to 10 km. The effect of each parameter remained the constant with distance as seen in Figure 4.19-Figure 4.21. The only difference being the feed rate having a slightly curved profile where increase in feed rate led to an increase in surface roughness but at a declining rate. Although the effect of depth of cut increased with distance, cutting speed and feed rate were still the dominant parameters on the surface roughness result.

Design-Expert® Software
Transformed Scale
1.0/(Surface Roughness 10km)

◆ Design Points

X1 = A: Cutting Speed

Actual Factors

B: Feed Rate = 15.00

C: Depth of Cut = 15.00

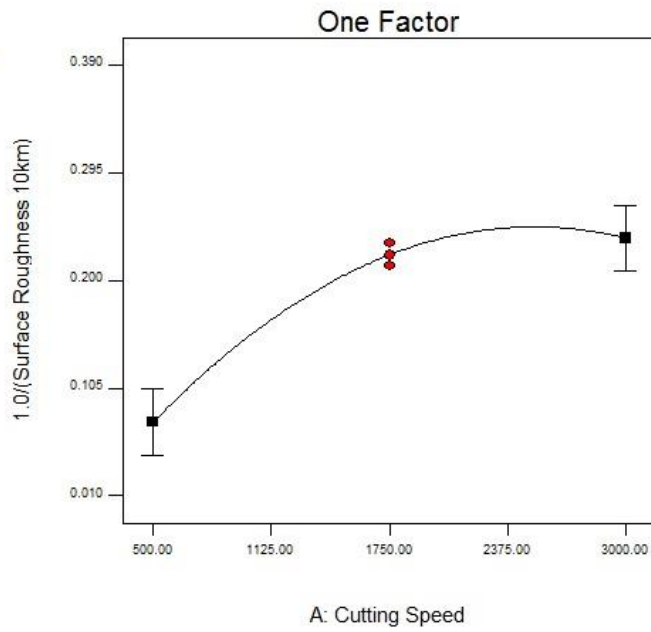


Figure 4.19: Effect of cutting speed on inverse surface roughness model 10 km

Design-Expert® Software
Transformed Scale
1.0/(Surface Roughness 10km)

◆ Design Points

X1 = B: Feed Rate

Actual Factors

A: Cutting Speed = 1750.00

C: Depth of Cut = 15.00

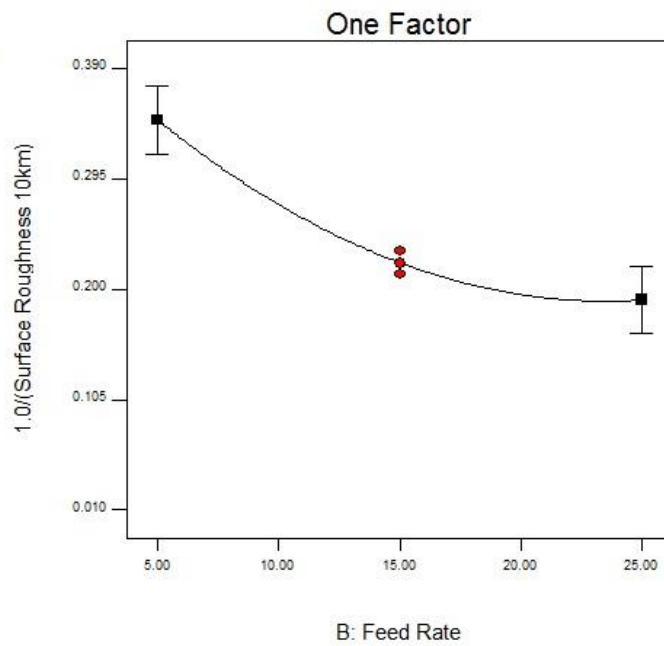


Figure 4.20: Effect of feed rate on inverse surface roughness 10 km

Design-Expert® Software
Transformed Scale
1.0/(Surface Roughness 10km)

◆ Design Points

X1 = C: Depth of Cut

Actual Factors

A: Cutting Speed = 1750.00

B: Feed Rate = 15.00

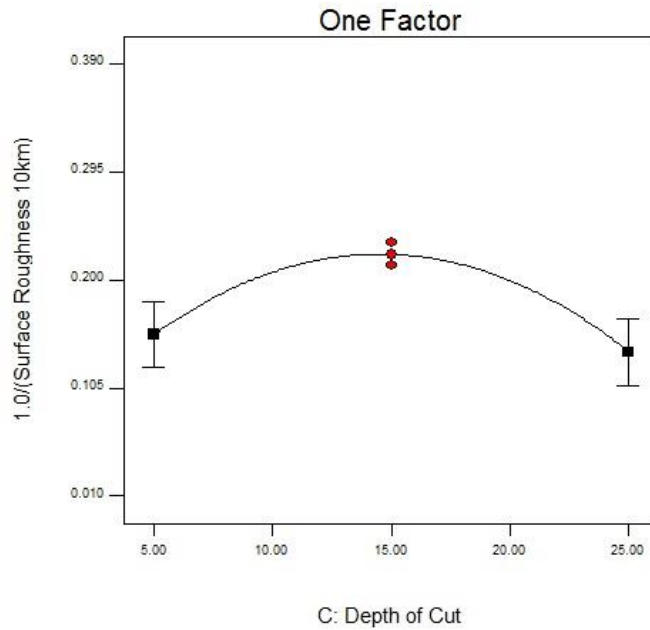


Figure 4.21: Effect of depth of cut on inverse surface roughness model 10 km

The profiles of the surface roughness maps did not change with increased distance, as seen by Figure 4.22-Figure 4.24 being similar to the 4 km maps, but the surface roughness values increased. This could be seen by the larger presence of the orange/red regions in the maps. The model maintained that high cutting speed, low feed rate and low-to-moderate depth of cut produced the best surface roughness. This further proved that the surface quality and the effect of its contributing factors were fairly consistent. This was attributed to the ultra-fine grain microstructure coupled with the hardness of the diamond tool which provided consistent surface finishes.

Design-Expert® Software
 Transformed Scale
 1.0/(Surface Roughness 10km)
 ♦ Design Points
 0.0117647
 0.384615

X1 = A: Cutting Speed
 X2 = B: Feed Rate

Actual Factor
 C: Depth of Cut = 5.00

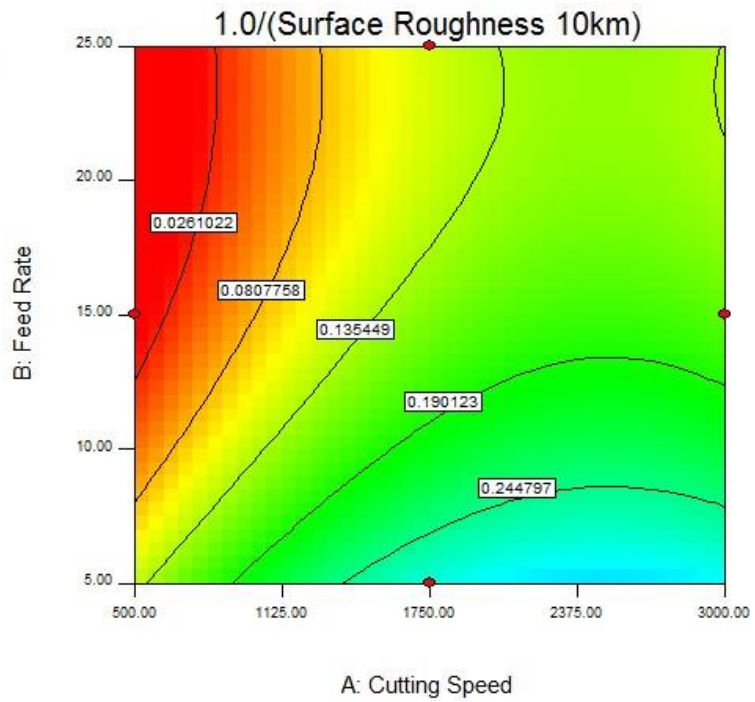


Figure 4.22: Surface roughness map for 5 µm depth of cut at 10 km

Design-Expert® Software
 Transformed Scale
 1.0/(Surface Roughness 10km)
 ♦ Design Points
 0.0117647
 0.384615

X1 = A: Cutting Speed
 X2 = B: Feed Rate

Actual Factor
 C: Depth of Cut = 15.00

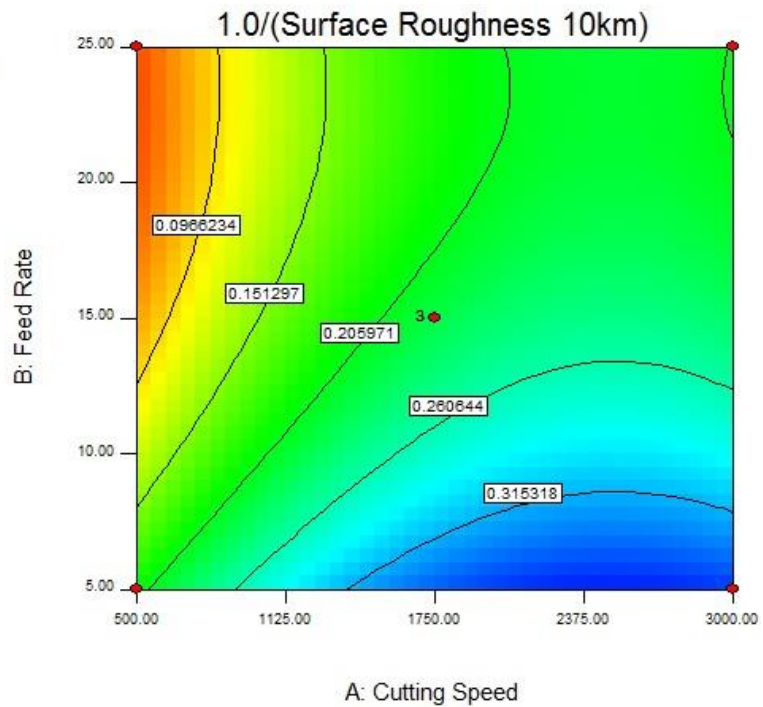


Figure 4.23: Surface roughness map for 15 µm depth of cut at 10 km

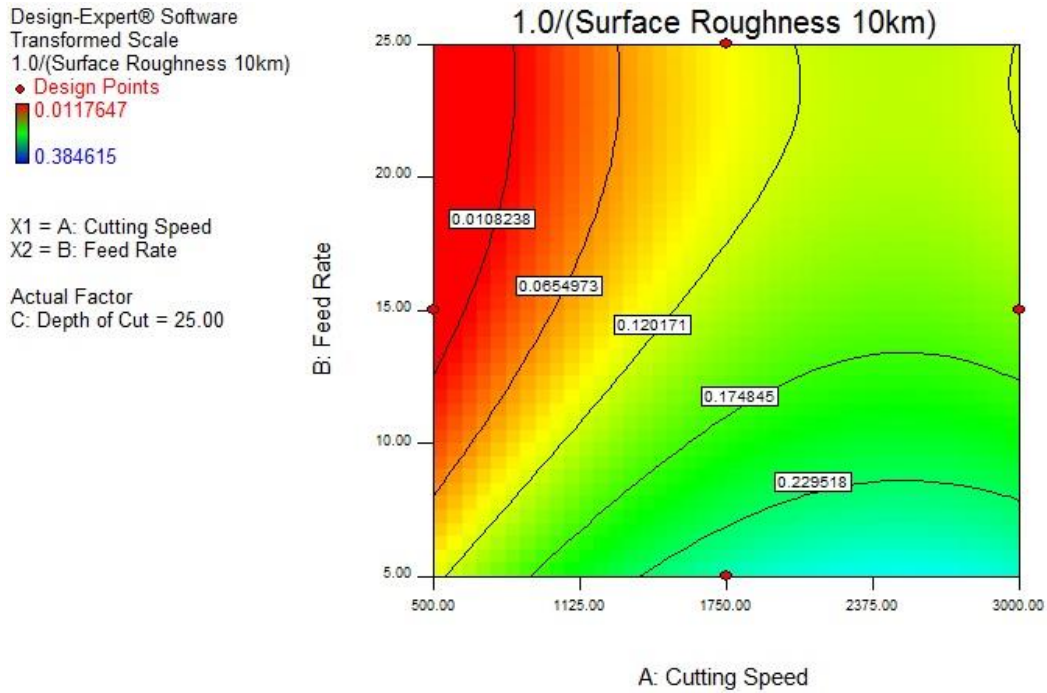


Figure 4.24: Surface roughness map for 25 μm depth of cut at 10 km

4.4 Conclusion

The Box-Behnken method was implemented and the surface roughness for 15 combinations of cutting parameters was measured using a profilometer in stages up to a cutting distance of 4 km and 10 km. The ANOVA method was used to create a model to predict the surface roughness at 4 km and 10 km. The results showed two main trends. One based on the cutting distance and the other based on the effect of each cutting parameter. The surface roughness was seen to slightly decrease then sharply increase with cutting distance. As the cutting distance increased the surface roughness remained fairly constant and slowly decreased. This was attributed to the tool edge flattening and smoothing out the workpiece surface fluctuations that make up the roughness. As the distance increased, the flattened edge became irregular and this directly led to increase in surface roughness. The cutting parameters various effects on the surface roughness. Increase in cutting speed led to a decrease in surface roughness. Low cutting speeds were seen to create strands of chip that would accumulate around the tool and directly rub against the workpiece, resulting in poor surface finishes.

Increase in feed rate led to an increase in surface roughness while depth of cut had a minimal effect on the surface roughness. The best surfaces would be achieved with a combination of high cutting speed of 1750-3000 rpm and low feed rate of 5 mm/min, resulting in an average surface roughness of 3-5 nm.

5. Tool Wear Analysis

5.1 Tool Wear Measurement Setup

Tool wear performance is critical in UHPM as it directly affects the resulting surface quality. As the tool wears, the cutting edge progressively changes shape affecting the workpiece attributes. The diamond inserts for each experiment were examined using scanning electron microscopy after multiple pass cutting of 4 km and 10 km. The wear land on the cutting edge was measured for each experiment.

The SEM machine used was the Jeol JSM-6380 (Figure 5.1). This high-performance scanning electron microscope is equipped with the following features:

- Super conical lens
- Resolution 3 nm
- Magnification x5-300 000
- Maximum specimen size 5” (full 360 coverage)
- Computer controlled 5-axis motor drive

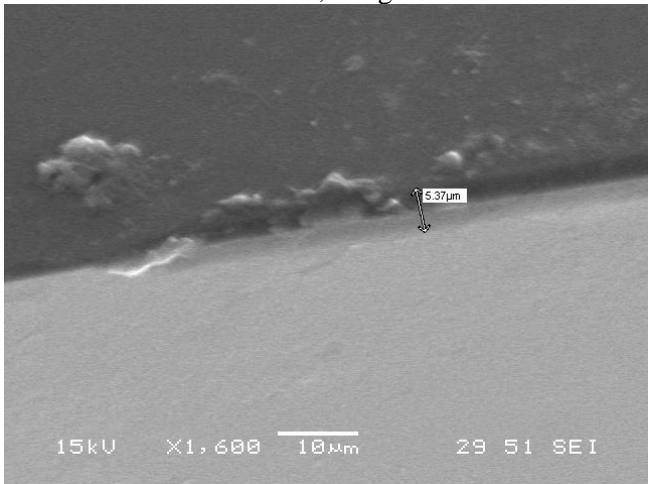


Figure 5.1: Joel JSM-6380

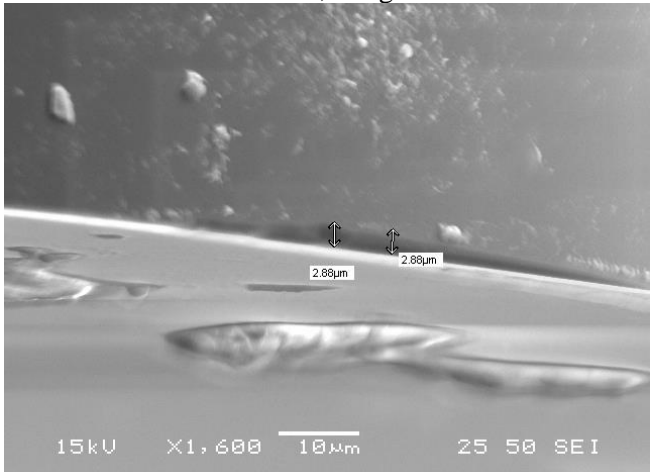
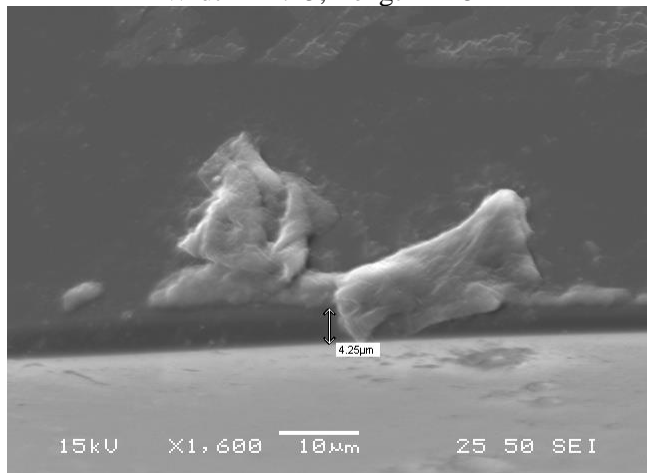
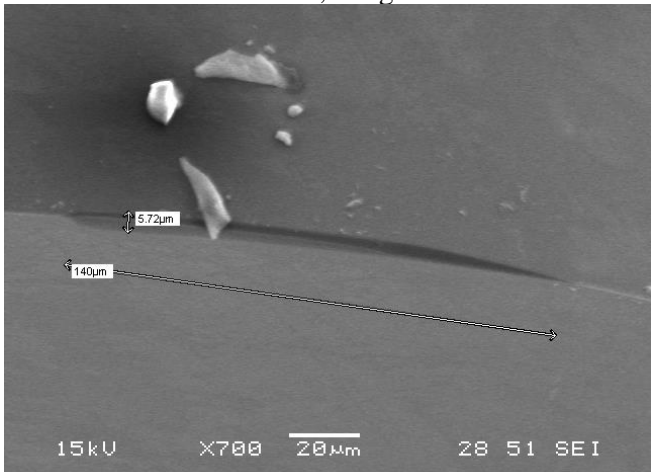
5.2 Tool Wear Results

Table 5.1 shows the results from the measured tool wear of each experiment as well as the length of the wear land.

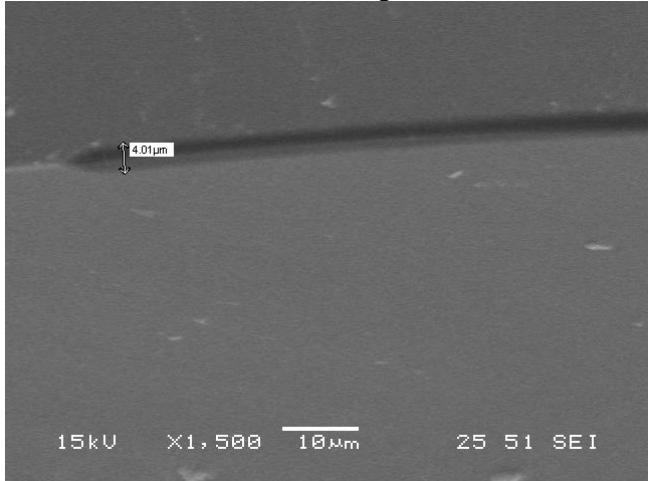
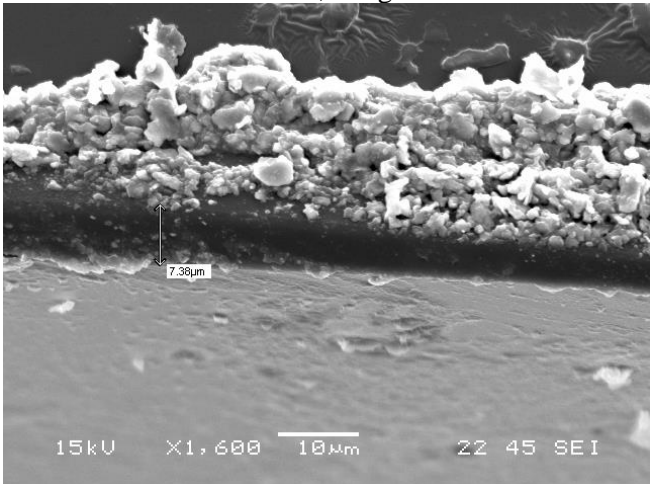
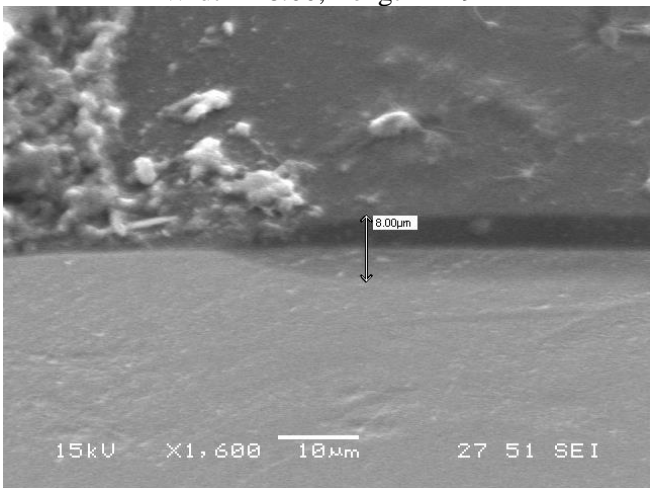
Table 5.1: Tool wear results

No.	v (rpm)	f (mm/min)	a (μm)	Distance (km)	Wear (μm)
1	1750	25	25	4.0	Width = 5.37, Length = 188 

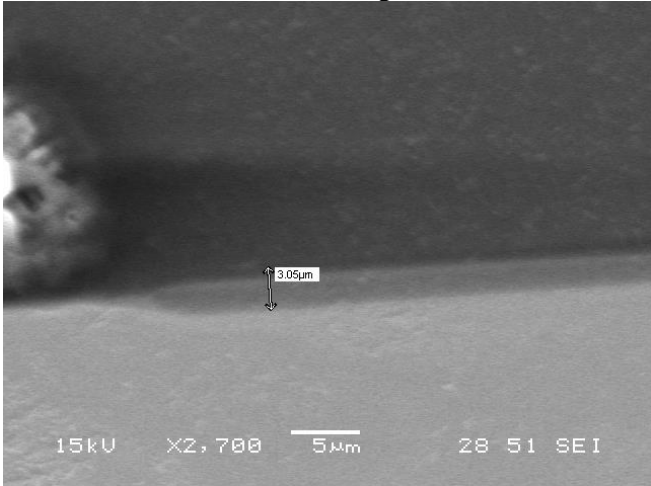
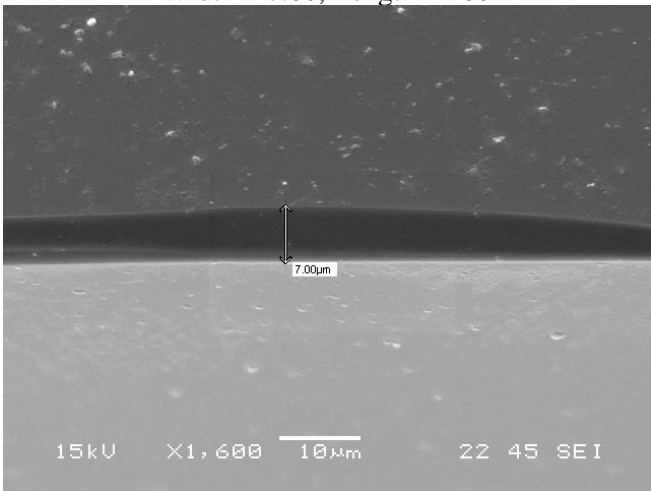
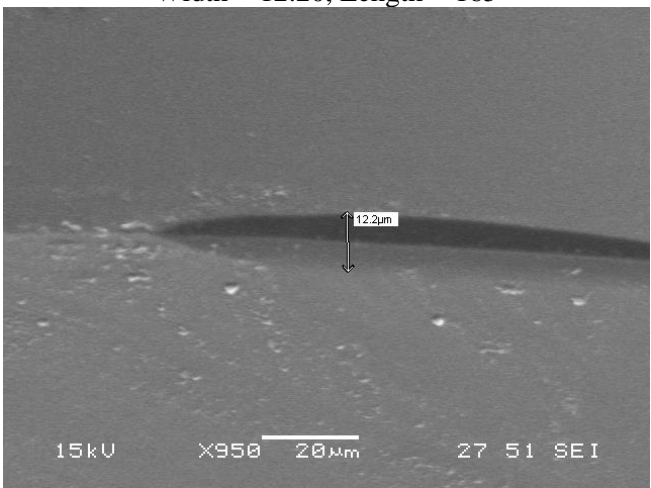
				10.0	<p>Width = 9.13, Length = 200</p>
2	1750	25	5	4.0	<p>Width = 5.07, Length = 75.4</p>
				10.0	<p>Width = 6.00, Length = 87.3</p>

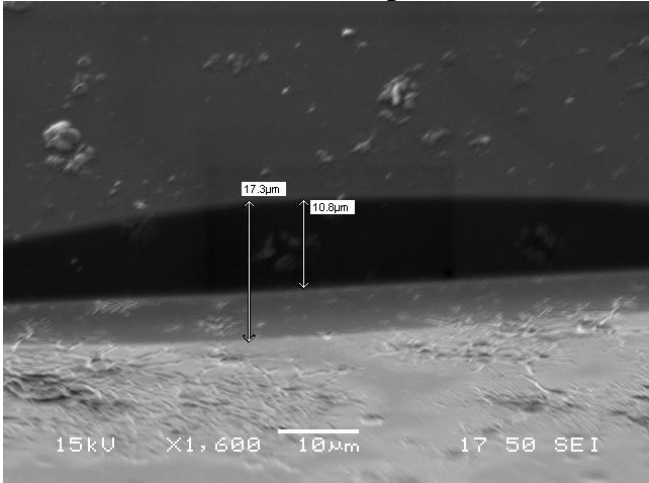
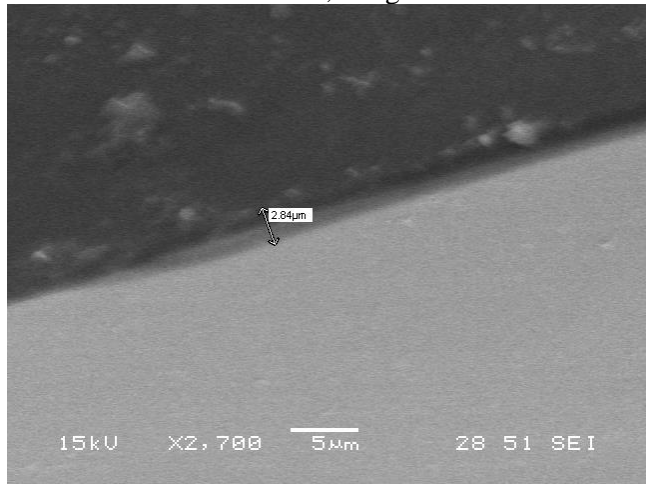
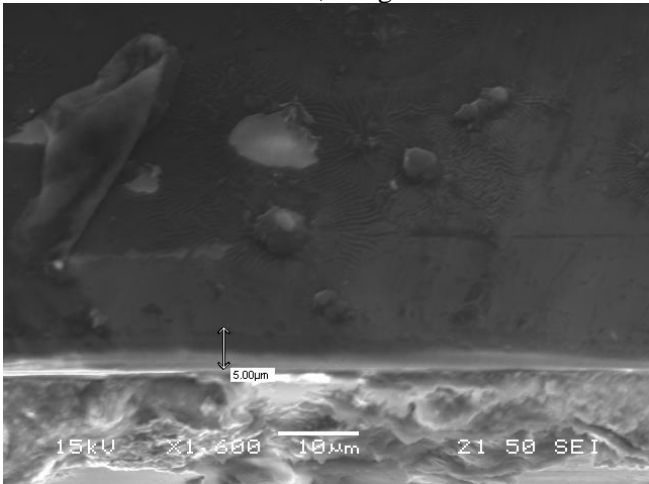
3	3000	5	15	4.0	<p>Width = 2.88, Length = 135</p> 
				10.0	<p>Width = 4.25, Length = 151</p> 
4	1750	15	15	4.0	<p>Width = 5.72, Length = 140</p> 

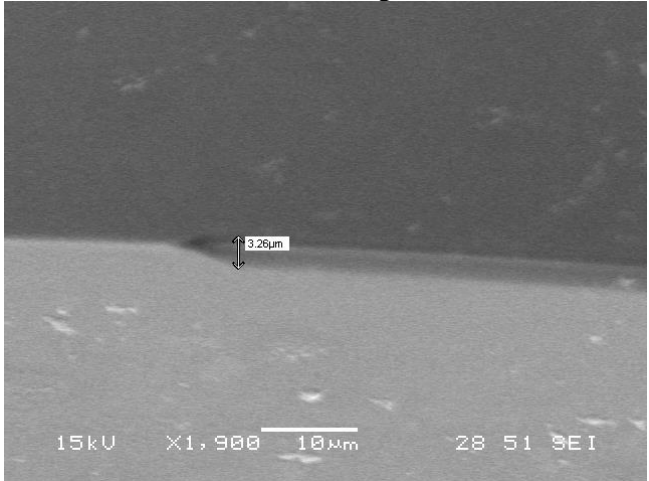
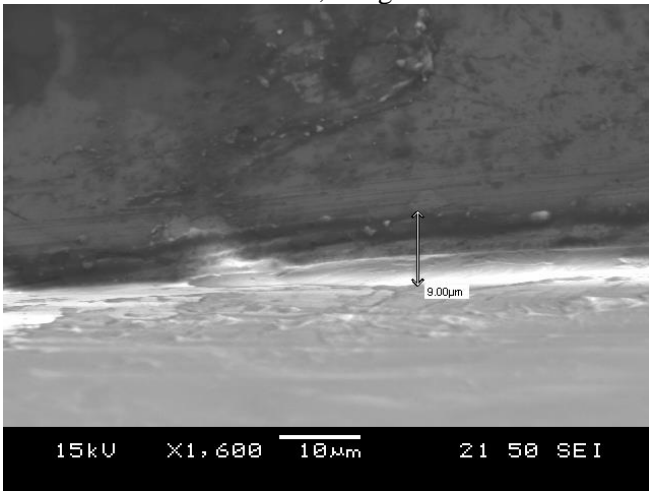
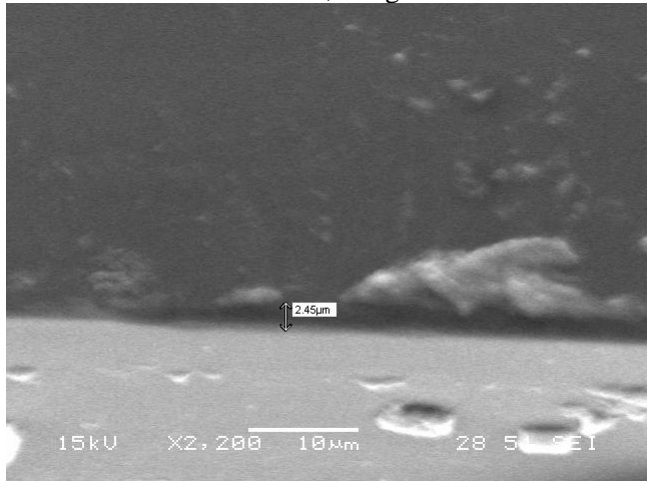
				10.0	<p>Width = 6.50, Length = 145</p>
5	1750	15	15	4.0	<p>Width = 5.72, Length = 140</p>
				10.0	<p>Width = 6.50, Length = 145</p>

6	1750	5	25	4.0	<p>Width = 4.01, Length = 174</p> 
				10.0	<p>Width = 7.38, Length = 200</p> 
7	500	15	25	4.0	<p>Width = 8.00, Length = 191</p> 

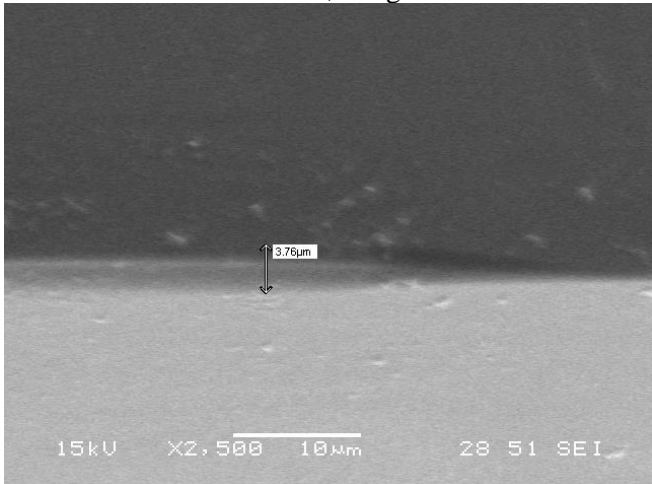
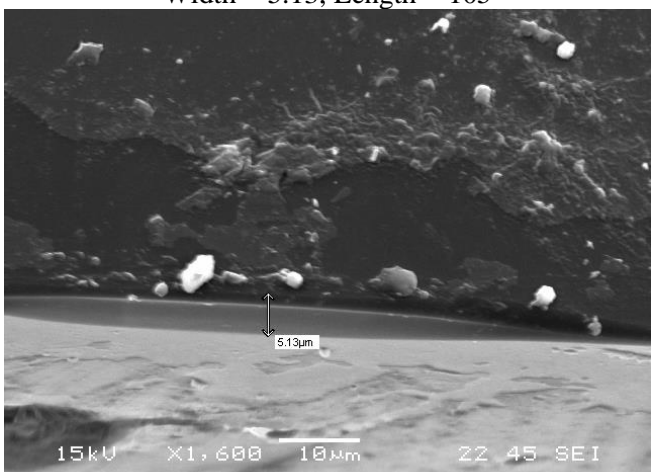
				10.0	<p>Width = 8.88, Length = 226</p>
8	3000	25	15	4.0	<p>Width = 3.36, Length = 139</p>
				10.0	<p>Width = 4.75, Length = 141</p>

9	3000	15	25	4.0	<p>Width = 3.05, Length = 180</p> 
				10.0	<p>Width = 7.00, Length = 180</p> 
10	500	25	15	4.0	<p>Width = 12.20, Length = 165</p> 

				10.0	<p>Width = 17.30, Length = 190</p> 
11	3000	15	5	4.0	<p>Width = 2.84, Length = 90</p> 
				10.0	<p>Width = 5.00, Length = 108</p> 

12	500	5	15	4.0	<p>Width = 3.26, Length = 137</p> 
				10.0	<p>Width = 9.00, Length = 164</p> 
13	1750	5	5	4.0	<p>Width = 2.45, Length = 99</p> 

				10.0	<p>Width = 3.63, Length = 119</p>
14	1750	15	15	4.0	<p>Width = 5.72, Length = 140</p>
				10.0	<p>Width = 6.50, Length = 145</p>

15	500	15	5	4.0	<p>Width = 3.76, Length = 96</p> 
				10.0	<p>Width = 5.13, Length = 105</p> 

The tool wear progression occurred as illustrated in Figure 5.2. The tool edge flattened as cutting progressed with majority of affected area being on the flank face. This dimension was considered as the main wear measurement and was recorded as the width. The extent of the wear across the tool edge was taken as the length. The tool wear (width) was generally low (within 3-5 μm) after cutting for 4 km. The length of the wear land varied from 75 μm to 191 μm . The overall tool wear was seen to considerably increase as the cutting distance reached 10 km. The wear increased to a range of 5 to 17 μm and the length of the wear land to a range of 87 to 226 μm . The trends of the wear length progression followed that of the wear width.

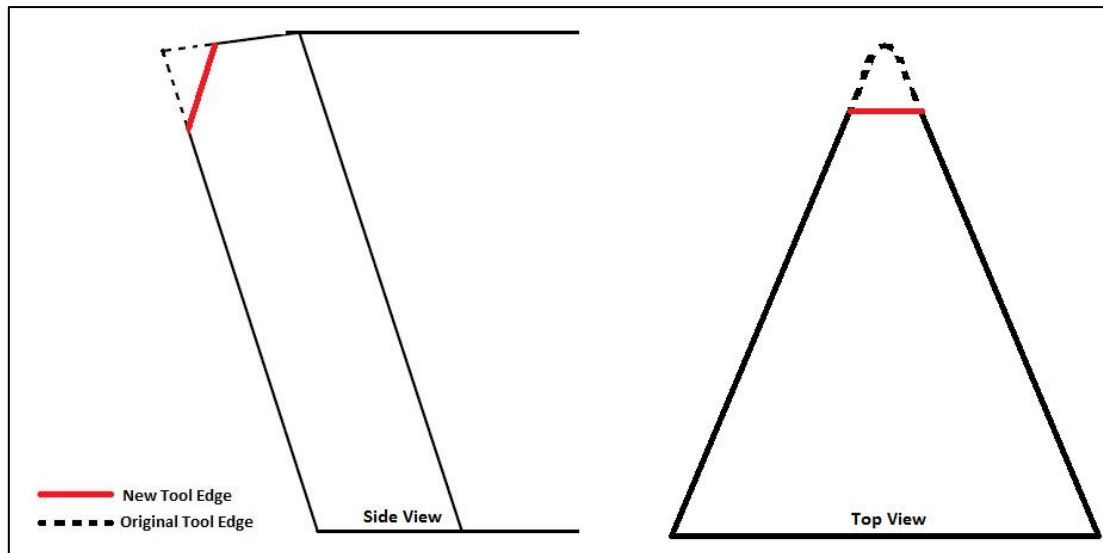


Figure 5.2: Tool tip wear

The lowest cutting speed of 500 rpm generally produced higher tool wear, with 12.2 μm being the highest measured from experiment 10. The highest cutting speed of 3000 rpm generally produced lower tool wear as seen experiments 8, 9 and 11 (3.36 μm , 3.05 μm and 2.84 μm , respectively). When comparing experiment 11 and experiment 15, where the feed rate and depth of cut was constant at 15 mm/min and 5 μm , the higher cutting speed 3000 rpm had 0.92 μm less wear than 500 rpm. This difference decreased to 0.13 μm as the cutting distance increased to 10 km, suggesting that the higher cutting speed may produce lower wear but has a higher wear rate.

Comparing experiment 1 and experiment 6, where cutting speed and depth of cut are constant at 1750 rpm and 25 μm , the higher feed rate of 25 mm/min lead to 1.36 μm more wear than the lower feed rate of 5mm/min. This was also noticed when comparing experiment 2 and experiment 13 which had the same cutting speed of 1750 rpm and depth of cut of 5 μm . Experiment 2 with the higher feed rate had 2.62 μm more tool wear. The difference in wear was maintained with increase in cutting distance. The considerable difference in wear suggested that feed rate had a significant effect on wear.

Comparing experiment 1 and experiment 2, where the cutting speed and feed rate are constant at 1750 rpm and 25 mm/min, it was seen that the smaller depth of cut (5 μm) leads to 0.3 μm less tool wear than the larger depth of cut 25 μm . This difference increasing to 3.13 μm as the distance increased to 10 km. Experiment 9 and experiment 11 also showed the smaller depth of cut having 0.21 μm less tool wear for 4 km, increasing to 2 μm less tool wear at a cutting distance 10 km. The differences in wear results between each of the two experiments suggests that depth of cut has a growing effect on tool wear with cutting distance and the wear rate is higher for deeper cuts. Additionally, depth of cut showed to have a significant effect on the length of the worn tool edge, with deeper cuts producing longer wear lands regardless of cutting speed and feed rate as there was more tool-workpiece contact.

The overall low wear could be attributed to the combination of the ultra-fine RSA microstructure and the high hardness of the diamond tool. The negative impact of some of the chemical elements contained in RSA 905 on tool wear is greatly reduced through the rapid solidification process. This meant a smoother cutting process with less of an abrasive effect between the workpiece and the diamond tool. The small grains of RSA cause less of an impact on the tool and low tool deterioration rates. Generally, a combination of higher cutting speeds, lower feed rates and smaller depth of cuts resulted in less diamond tool wear. These parameters produced finer cutting and less wear on the tool edge. This parameter combination also meant less overall cutting time for the same distance and less tool-workpiece contact time. In addition, the total number of passes required is also reduced and there is less tool-workpiece engagement reducing the impact on the tool. The highest tool wear of 12.2 μm was recorded for experiment 10 at 500 rpm cutting speed, 25 mm/min feed rate and 15 μm depth of cut. The lowest tool wear of 2.45 μm was recorded for experiment 13 at 1750 rpm cutting speed, 5 mm/min feed rate and 5 μm depth of cut.

The debris seen on the images in Figure 5.3 are a mixture of RSA 905 and the gold used to coat the tool for SEM imaging. The flattening of the tool, the nature of the wear land and scoring seen in the SEM images was evidence that the wear was mainly attributed to abrasion. Some rough cutting conditions such as experiment 12 led to chipping of the tool edge. This subsequently had adverse effects on the surface finish.

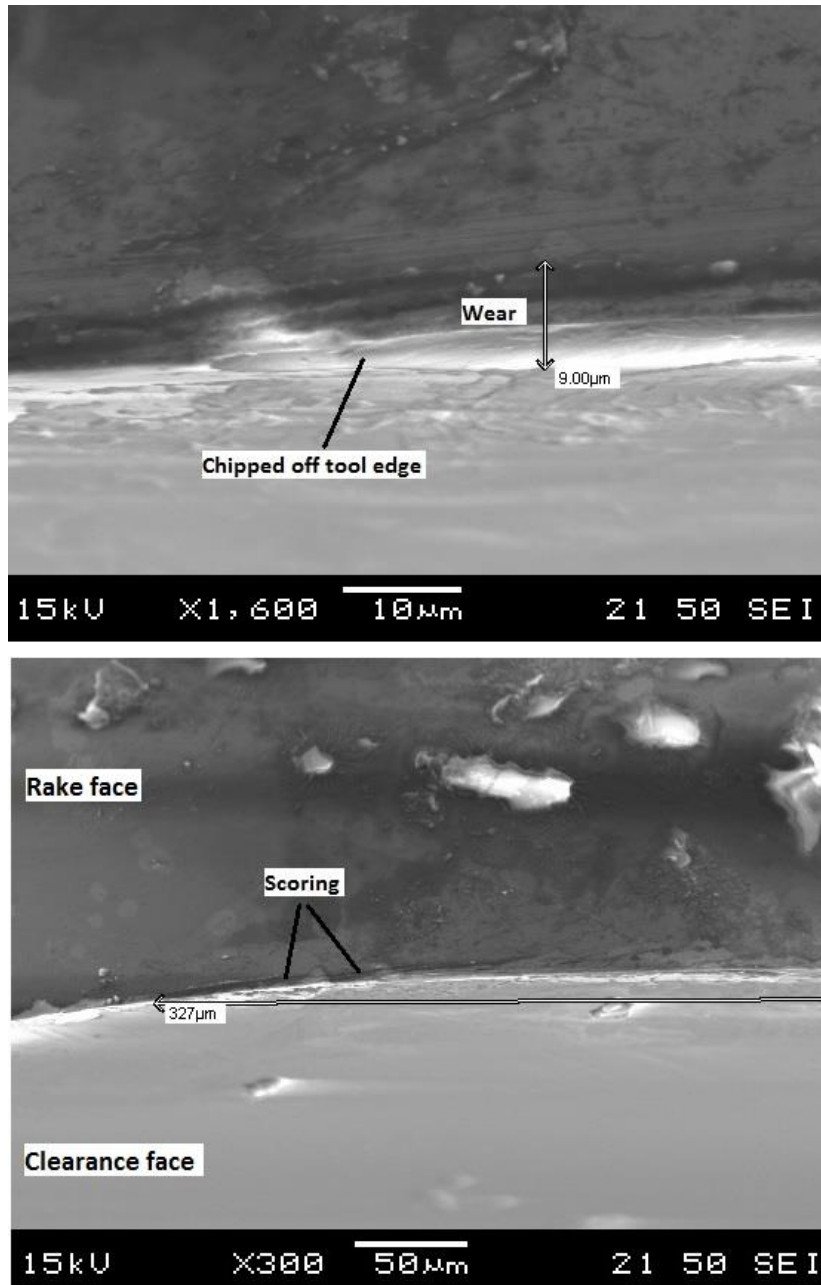


Figure 5.3: SEM image of tool edge

5.3 Tool Wear Statistical Analysis

The tool wear results from the experiments were entered into the Box Behnken design in Design Expert software and response surface method was applied to develop and evaluate the model. The selection of a suitable polynomial equation was done by performing lack of fit tests. The tool wear results ranged from 2.45 μm to 12.2 μm . The ratio of maximum to minimum was 4.98. The initial model failed the lack of fit test and had to be transformed. Based on the Box-Cox plot (Figure 5.4), an inverse transformation had to be performed to produce a model of the form

$$y' = \frac{1}{y+k} \quad (5.1)$$

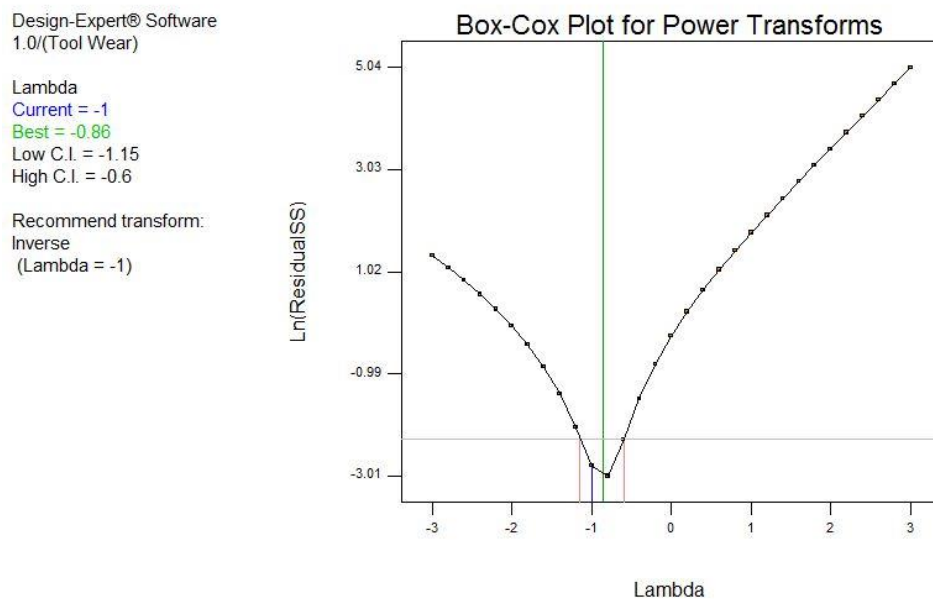


Figure 5.4: Box-Cox plot for tool wear model

The lack of fit tests produced the results shown in Table 5.2. From the table it can be seen that a quadratic model should be developed.

Table 5.2: Lack of fit tests for tool wear model

Source	Sum of Squares	DF	Mean Square	F-Value	P-Value
Linear	0.03497475	9	0.00388608	403.63947510	0.0025
2FI	0.01843856	6	0.00307309	319.19590573	0.0031
Quadratic	0.00013795	3	0.00004598	4.77620593	0.1780
Cubic	0	0			
Pure Error	0.00001926	2	0.00000963		

The adequacy of the model was evaluated through ANOVA as shown in Table 5.3. Table 5.3 revealed the relevant terms at 95% confidence level that had a significant effect (P-value < 0.05) on tool wear. The results show the model was significant and lack of fit was insignificant.

Table 5.3: Analysis of variance for tool wear model

Source	Sum of Squares	DF	Mean Square	F-Value	P-Value
Model	0.12361587	9	0.01373510	436.85152596	< 0.0001
A-Cutting Speed	0.03714852	1	0.03714852	1181.52703576	< 0.0001
B-Feed Rate	0.03760185	1	0.03760185	1195.94537039	< 0.0001
C-Depth of Cut	0.01402870	1	0.01402870	446.18981080	< 0.0001
AB	0.00767184	1	0.00767184	244.00665177	< 0.0001
AC	0.00340552	1	0.00340552	108.31416385	0.0001
BC	0.00545883	1	0.00545883	173.62077426	< 0.0001
A ²	0.00757767	1	0.00757767	241.01140255	< 0.0001
B ²	0.00528045	1	0.00528045	167.94737367	< 0.0001
C ²	0.00821279	1	0.00821279	261.21193459	< 0.0001
Residual	0.00015721	5	0.00003144		
Lack of Fit	0.00013795	3	0.00004598	4.77620593	0.1780
Pure Error	0.00001926	2	0.00000963		
Cor Total	0.12377307	14			

The insignificant terms were eliminated to produce a reduced model for tool wear. The final model to determine tool wear was thus defined as Equation 5.2.

$$T = (0.76187851 - 0.00013453v - 0.02987344f - 0.02796259a + 0.0000035vf + 0.00000233va + 0.00036942fa + 0.00000003v^2 + 0.00037817f^2 + 0.00047162a^2)^{-1} \quad (5.2)$$

where v is the cutting speed in rpm, f is the feed rate in mm/min, a is the depth of cut in μm and T is the tool wear in μm .

From the model terms, increase in cutting speed appears to decrease tool wear, but the positive square term greatly overcomes this effect leading to a decrease in tool wear as cutting speed generally has a large magnitude. The feed rate and depth of cut both cause a decrease in tool wear due to their strong negative term coefficients. The coefficients show that feed rate would have the strongest effect on the resulting tool wear followed by depth of cut then cutting speed. The presence of the squared terms suggested the factors had a curved relationship with tool wear. Further statistical analysis was carried out to determine the effects of these factors and their interaction.

The normality of residuals in Figure 5.5 verified the adequacy of the model by the close proximity to the probability line. The effect of varying each input variable on the inverse tool wear model was assessed. Figure 5.6 shows the cutting speed had a curved relationship with tool wear. As the cutting speed increased from 500 rpm to 3000 rpm, the inverse tool wear had a slow increase before rapidly increasing at approximately mid cutting speed. This meant that tool wear decreased as cutting speed increased with the higher speeds having considerably less tool wear. Figure 5.7 shows feed rate having a decreasing curve against inverse tool wear, meaning increase in feed rate led to increase in tool wear. Depth of cut had a similar effect to inverse tool wear as seen in Figure 5.8. An increase in depth of cut led to an increase in tool wear. The plots show that the three cutting parameters within their respective ranges will have a similar level of impact on the resulting tool wear. These statistical results further verify the initial findings from the assessment of Table 5.1.

Design-Expert® Software
1.0/(Tool Wear)

Color points by value of
1.0/(Tool Wear):

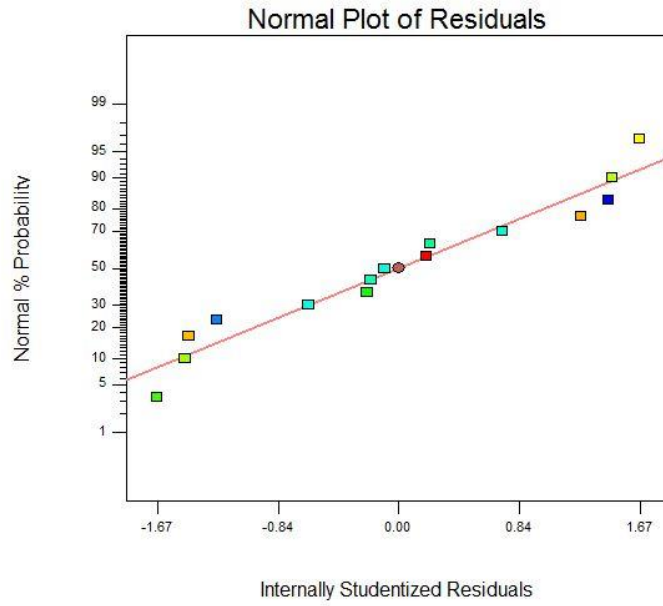


Figure 5.5: Normal probability plot for tool wear model

Design-Expert® Software
Transformed Scale
1.0/(Tool Wear)

◆ Design Points

X1 = A: Cutting Speed

Actual Factors

B: Feed Rate = 15.00

C: Depth of Cut = 15.00

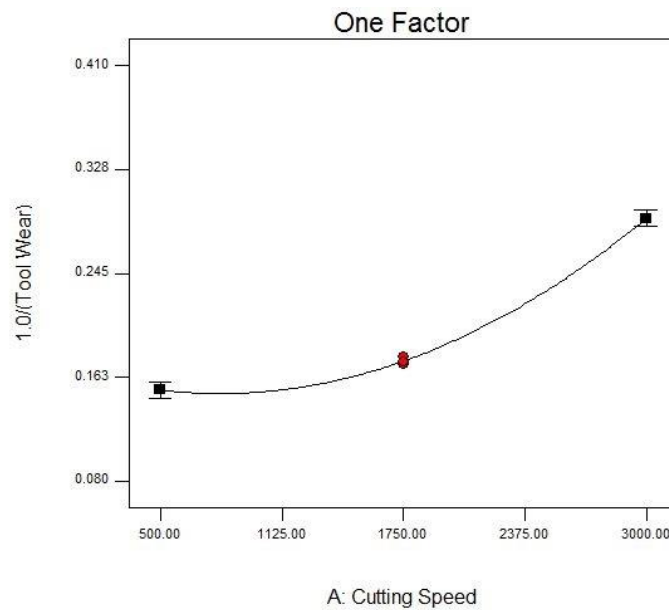


Figure 5.6: Effect of cutting speed on inverse tool wear

Design-Expert® Software
Transformed Scale
1.0/(Tool Wear)

◆ Design Points

X1 = B: Feed Rate

Actual Factors

A: Cutting Speed = 1750.00

C: Depth of Cut = 15.00

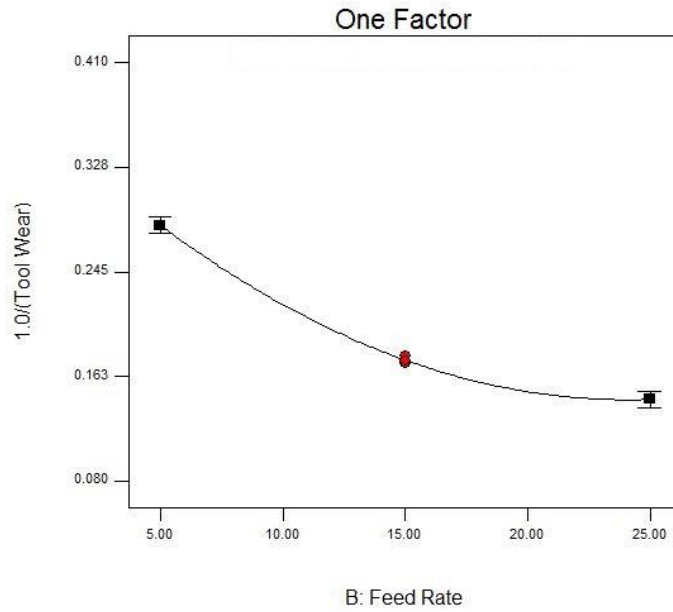


Figure 5.7: Effect of feed rate on inverse tool wear

Design-Expert® Software
Transformed Scale
1.0/(Tool Wear)

◆ Design Points

X1 = C: Depth of Cut

Actual Factors

A: Cutting Speed = 1750.00

B: Feed Rate = 15.00

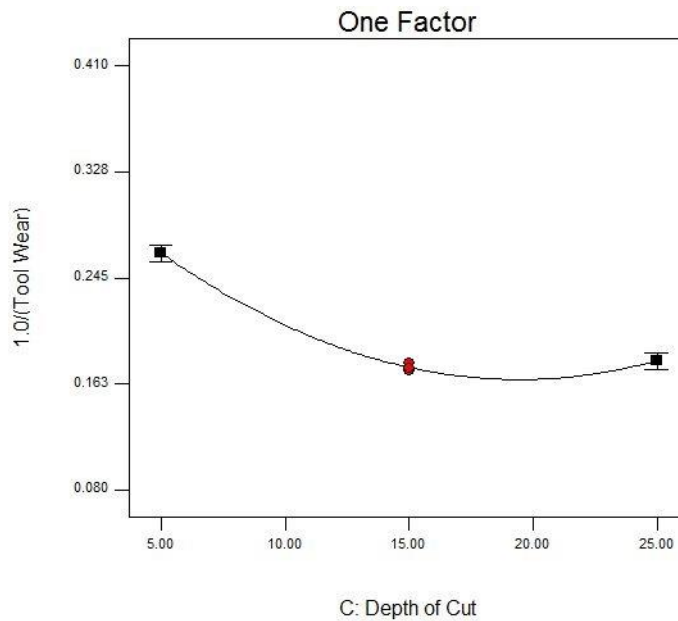


Figure 5.8: Effect of depth of cut on inverse tool wear

The developed model was used to plot contour maps of tool wear at the three levels of depth of cut. Figure 5.9-Figure 5.11 are wear maps generated from the model at 5 μm , 15 μm and 25 μm depth of cut, respectively.

Design-Expert® Software
 Transformed Scale
 1.0/(Tool Wear)
 ● Design Points
 0.0819672
 0.408163

X1 = A: Cutting Speed
 X2 = B: Feed Rate

Actual Factor
 C: Depth of Cut = 5.00

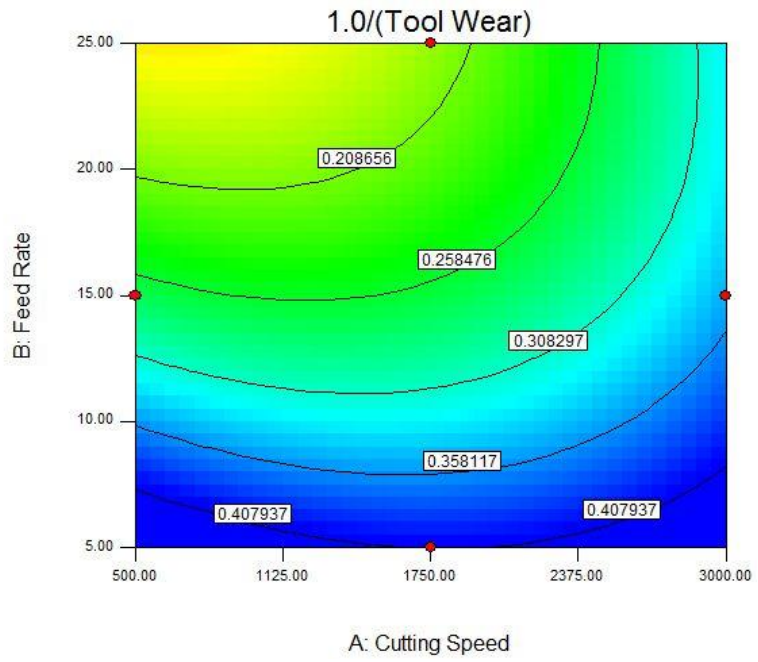


Figure 5.9: Wear map for 5 µm depth of cut

Design-Expert® Software
 Transformed Scale
 1.0/(Tool Wear)
 ● Design Points
 0.0819672
 0.408163

X1 = A: Cutting Speed
 X2 = B: Feed Rate

Actual Factor
 C: Depth of Cut = 15.00

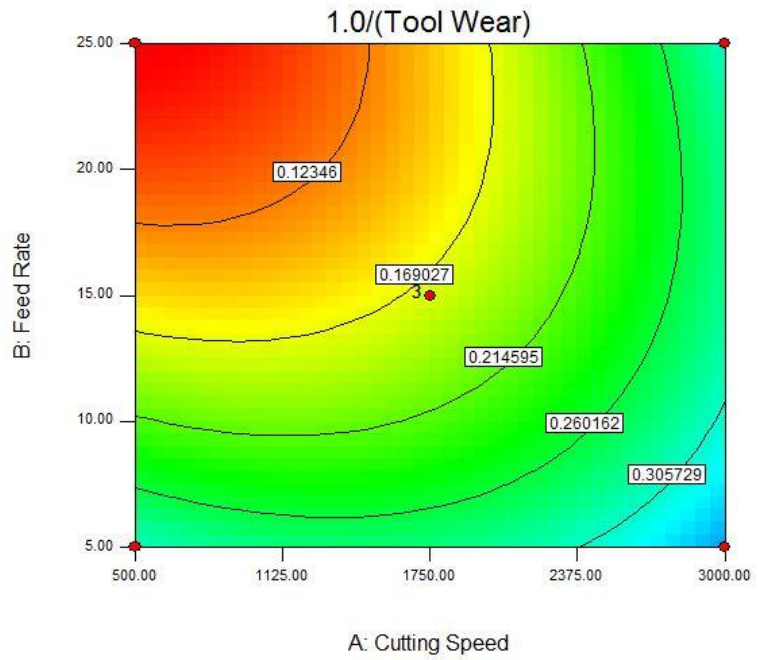


Figure 5.10: Wear map for 15 µm depth of cut

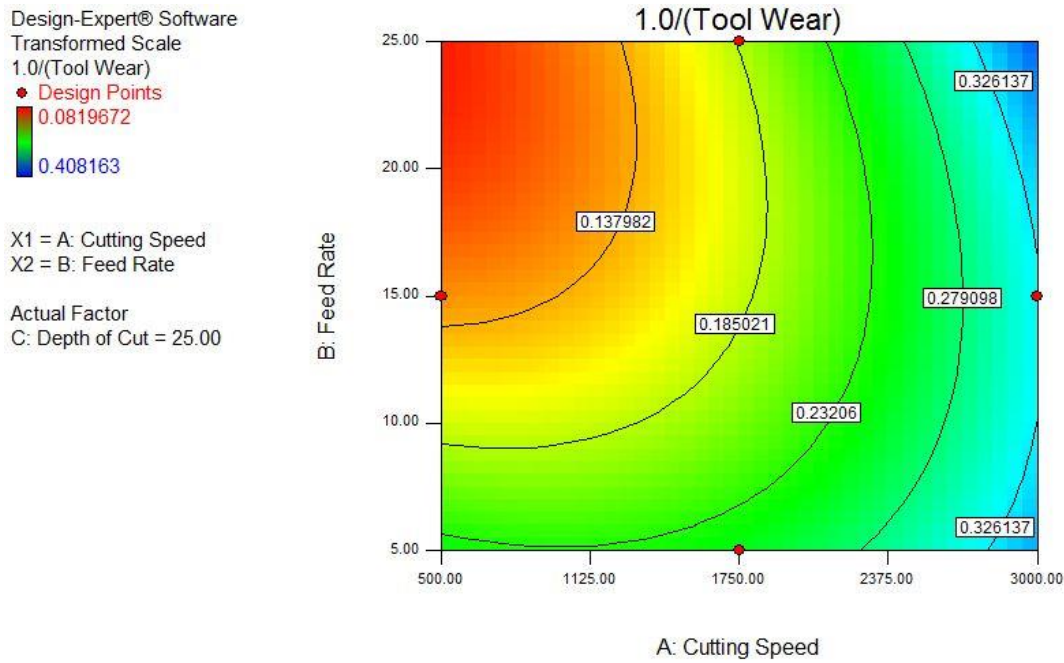


Figure 5.11: Wear map for 25 µm depth of cut

The wear maps show the lowest wear was largely associated with the smaller depth of cut. This can be seen by the 5 µm wear map having a wider area of low wear (blue zone) in comparison to 15 µm and 25 µm. The lower wear area was concentrated at the high cutting speed and low feed rate regions. These parameters are prevalent with smoother material removal and cutting resulting in less impact on the tool. As depth of cut increased, the low wear area became smaller and condensed to the higher end of the cutting speed.

The tool wear model became more linear with increase in cutting distance. At 10 km, the inverse model was maintained and the lack of fit tests (Table 5.4) showed that a linear model was recommended. The 10 km tool wear model was defined as:

$$T_{10} = (0.20832832 + 0.00003122v - 0.00266079f - 0.00420725a)^{-1} \quad (5.3)$$

where v is the cutting speed in rpm, f is the feed rate in mm/min, a is the depth of cut in µm and T_{10} is the tool wear in µm after 10 km of cutting.

Table 5.4: Lack of fit tests for 10 km tool wear model

Source	Sum of Squares	DF	Mean Square	F-Value	P-Value
Linear	0.01130016	9	0.00125557	12.74891285	0.0748
2FI	0.00922233	6	0.00153705	15.60702714	0.0614
Quadratic	0.00811347	3	0.00270449	27.46100016	0.0353
Cubic	0.00000000	0			
Pure Error	0.00019697	2	0.00009848		

The ANOVA results (Table 5.5) and the normal probability plot (Figure 5.12) show the significant terms and adequacy of the model. The model was significant and the lack of fit was insignificant.

Table 5.5: Analysis of variance for 10 km tool wear model

Source	Sum of Squares	DF	Mean Square	F-Value	P-Value
Model	0.03200970	3	0.01066990	10.20853474	0.0016
A-Cutting Speed	0.01218506	1	0.01218506	11.65817854	0.0058
B-Feed Rate	0.00566384	1	0.00566384	5.41893958	0.0400
C-Depth of Cut	0.01416080	1	0.01416080	13.54848608	0.0036
Residual	0.01149713	11	0.00104519		
Lack of Fit	0.01130016	9	0.00125557	12.74891285	0.0748
Pure Error	0.00019697	2	0.00009848		
Cor Total	0.04350683	14			

The model terms show the linearity of the cutting parameters with depth of cut having the most significant effect on the tool wear at 10 km, followed by feed rate then cutting speed. As depth of cut increased, the tool wear increased as shown by the negative coefficient in the model and Figure 5.13 where depth of cut decreased with inverse tool wear. Similarly, increase in feed rate resulted in a linear increase of tool wear as seen in Figure 5.14. An increase cutting speed resulted in a linear decrease in tool wear as seen in Figure 5.15 and the positive coefficient in the model.

Design-Expert® Software
1.0/(Tool Wear 10km)

Color points by value of
1.0/(Tool Wear 10km):

0.275482
0.0578035

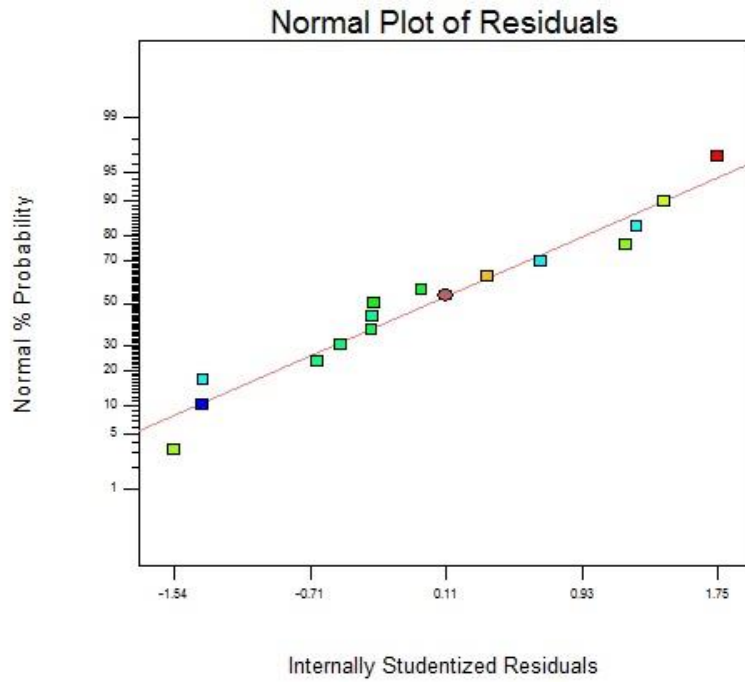


Figure 5.12: Normal probability plot for 10 km tool wear model

Design-Expert® Software
Transformed Scale
1.0/(Tool Wear 10km)

◆ Design Points

X1 = C: Depth of Cut

Actual Factors

A: Cutting Speed = 1750.00
B: Feed Rate = 15.00

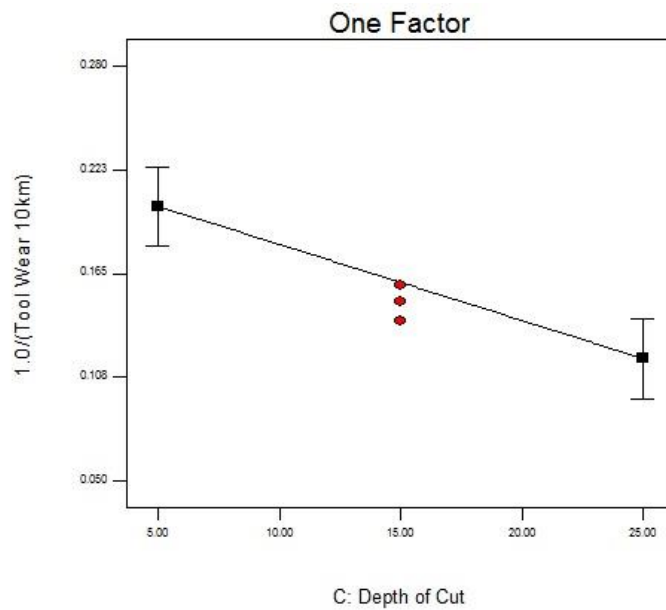


Figure 5.13: Effect of depth of cut on inverse tool wear model 10 km

Design-Expert® Software
Transformed Scale
1.0/(Tool Wear 10km)

◆ Design Points

X1 = B: Feed Rate

Actual Factors

A: Cutting Speed = 1750.00

C: Depth of Cut = 15.00

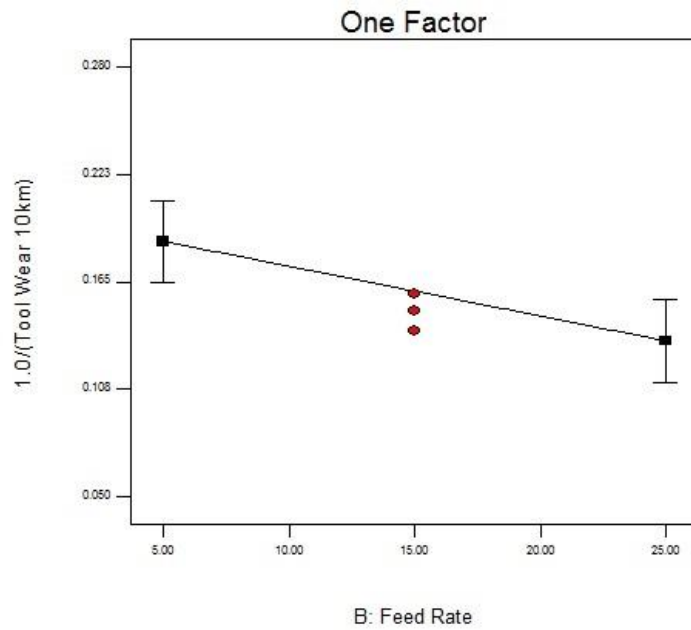


Figure 5.14: Effect of feed rate on inverse tool wear model 10 km

Design-Expert® Software
Transformed Scale
1.0/(Tool Wear 10km)

◆ Design Points

X1 = A: Cutting Speed

Actual Factors

B: Feed Rate = 15.00

C: Depth of Cut = 15.00

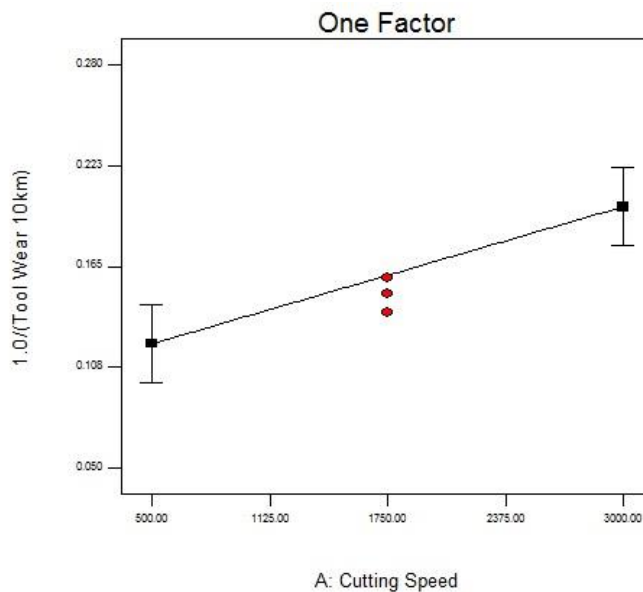


Figure 5.15: Effect of cutting speed on inverse tool wear model 10 km

These cutting parameter effects produced wear maps with linear contours that increased in wear magnitude as depth cut increased, shown in Figure 5.16-Figure 5.18. Similar to the wear maps for 4 km, the model maintained that cutting parameters of high cutting speeds, low feed rates and low depths of cut produced the least wear (blue/green zones). The trend in wear

suggested that the tool had reached the steady wear (linear) region depicted in Taylor tool life curve (Figure 2.3), while at 4 km the tool was in the initial wear region. Based on the number of experiments that experienced significant wear (and corresponding increased surface roughness), it could be suggested that this tool life stage and cutting distance may be inadequate for ultra-high precision machining depending on the level of surface quality required. Hence, cutting parameter selection becomes more stringent with increased distance.

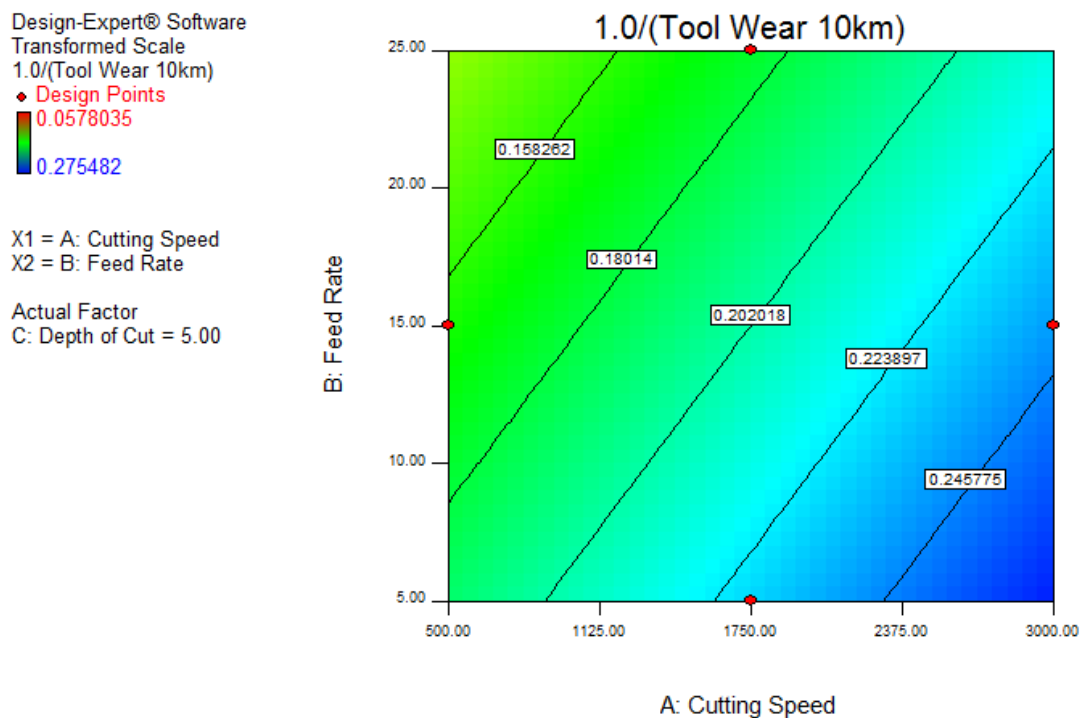


Figure 5.16: Wear map for 5 μm depth of cut at 10 km

Design-Expert® Software
 Transformed Scale
 1.0/(Tool Wear 10km)
 ♦ Design Points
 0.0578035
 0.275482

X1 = A: Cutting Speed
 X2 = B: Feed Rate

Actual Factor
 C: Depth of Cut = 15.00

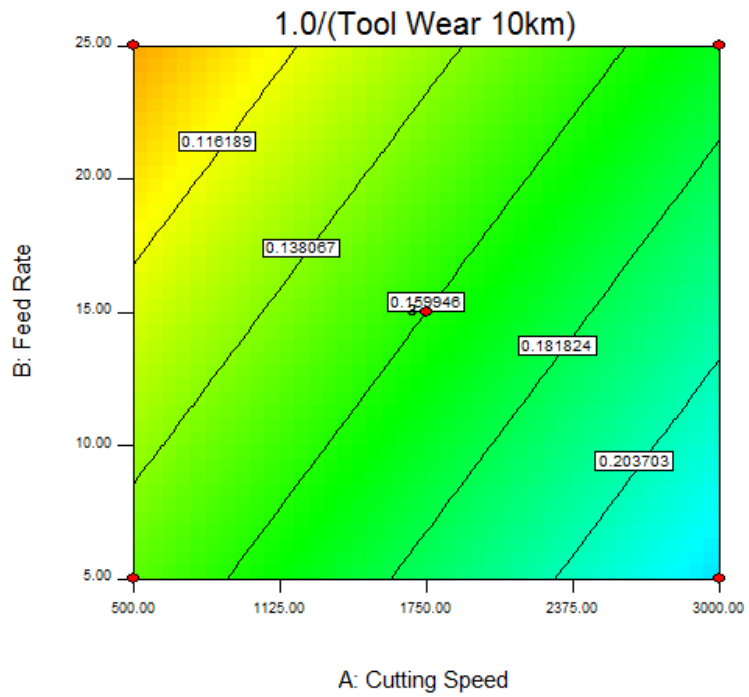


Figure 5.17: Wear map for 15 µm depth of cut at 10 km

Design-Expert® Software
 Transformed Scale
 1.0/(Tool Wear 10km)
 ♦ Design Points
 0.0578035
 0.275482

X1 = A: Cutting Speed
 X2 = B: Feed Rate

Actual Factor
 C: Depth of Cut = 25.00

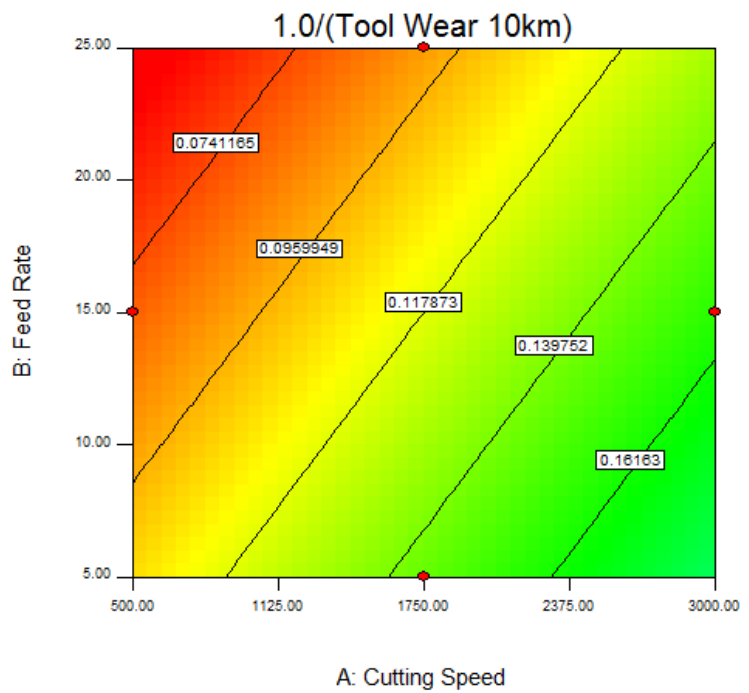


Figure 5.18: Wear map for 25 µm depth of cut at 10 km

5.4 Conclusion

The tool wear for 15 experiments developed from the Box-Behnken method were measured using SEM at a cutting distance of 4 km and 10 km. Using ANOVA, predictive models were developed using the results. The wear was generally low initially and increased considerably with increase in cutting distance towards 10 km. The 4 km model was quadratic which converted to a linear model at 10 km suggesting that the tool followed the Taylor tool life curve. Increase in cutting speed led to lower tool wear, increase in feed rate led to higher tool wear, while increase in depth of cut also led to higher tool wear. Feed rate had the most significant effect on the tool wear followed by depth of cut then cutting speed. The wear maps showed that high cutting speed (>2000 rpm), low feed rate (within 5 mm/min) and low depth of cut (within 5 μm) produced the least tool wear (within 3-5 μm). These conditions were also associated with good surface quality. The scoring and marks of the wear land from the SEM images suggest that abrasion was the dominant wear mechanism.

6. Cutting Force Analysis

6.1 Cutting Force Measurement Setup

Cutting force measurement is important in understanding the mechanism and the associated effects of the machining process. The diamond turning process can be likened to orthogonal cutting where two primary forces act on the tool and the cutting edge is perpendicular to the feed motion. The setup schematic is shown in Figure 6.1 with the cutting pictured from a side view.

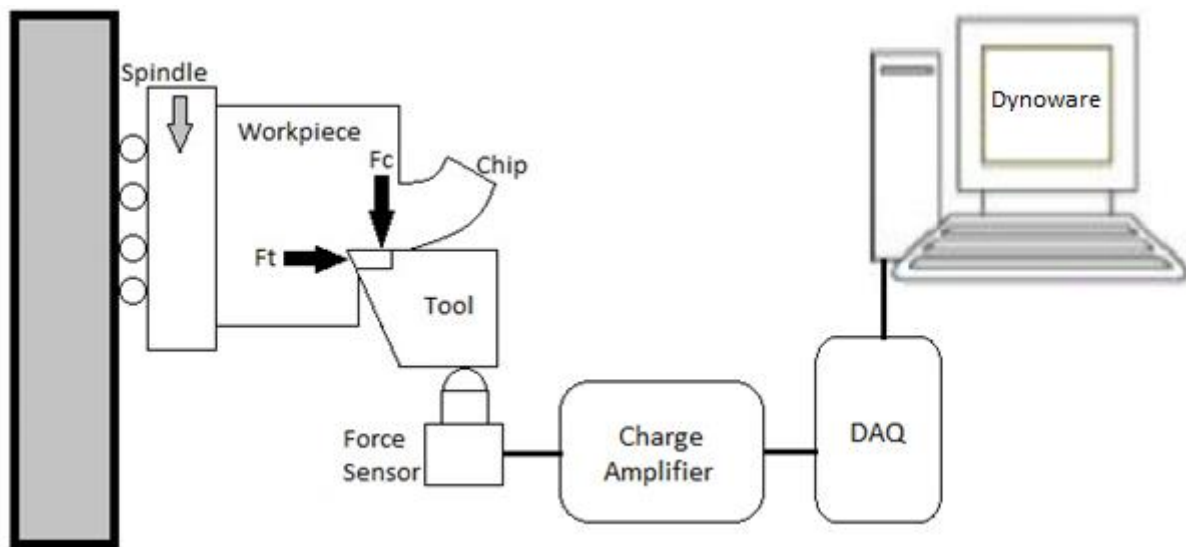


Figure 6.1: Cutting force measurement schematic

The setup (equipment pictured in Figure 6.2) consisted of a Kistler Type 9215 force sensor that was powered by a charge amplifier connected to a PC via a DAQ module. The Type 9215 is a piezoelectric force sensor with the following capabilities:

- Tensile and compression force measurement
- Dynamic measuring range from -20 – 200 N
- Highly sensitive force measurement from 1 mN
- Sensitivity -81 pC/N
- High allowable transverse force up to 90 N
- Low acceleration sensitivity

- High rigidity

The Kistler Type 5080A charge amplifier is responsible for processing the signals from the force sensor. The charge received from the force sensor is converted into voltage and processed then passed into the DAQ. The charge amplifier also provides operational assistance for the sensor enabling sensitivity, measuring range and filter adjustments. The output from the charge amplifier was received by the Kistler Type 5697A DAQ and passed to the PC loaded with the Kistler Dynoware software package.



Figure 6.2: Kistler force measurement equipment

The cutting force for each experiment was recorded during an entire pass at various distances. The data was collected through Dynoware and plotted. Figure 6.3 shows the positioning of the force sensor in the cutting setup.

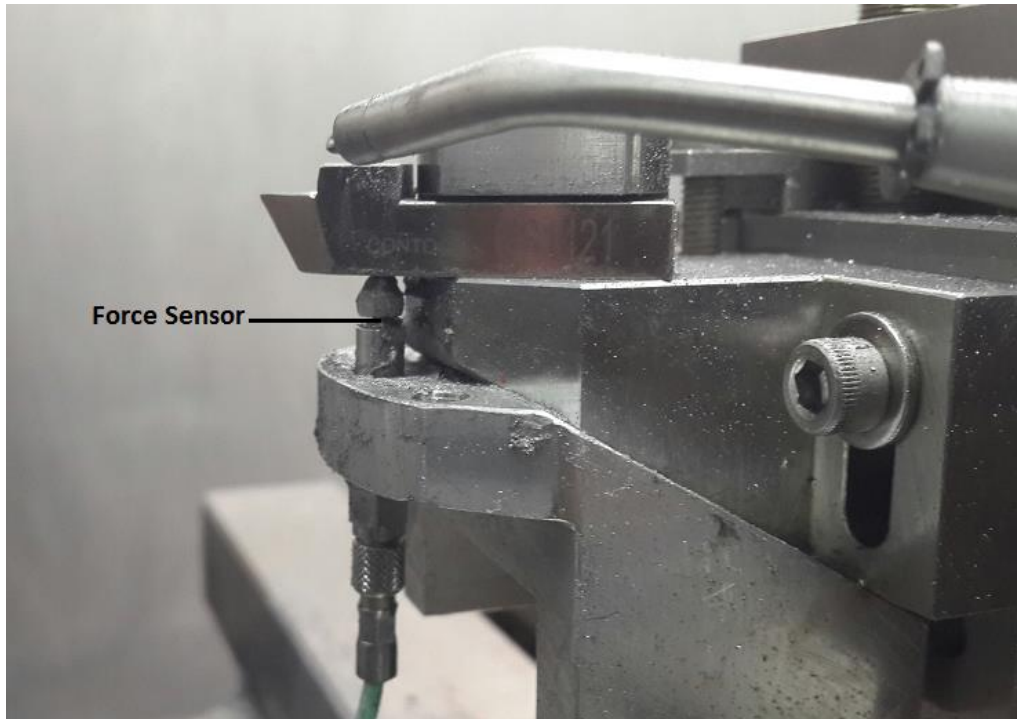


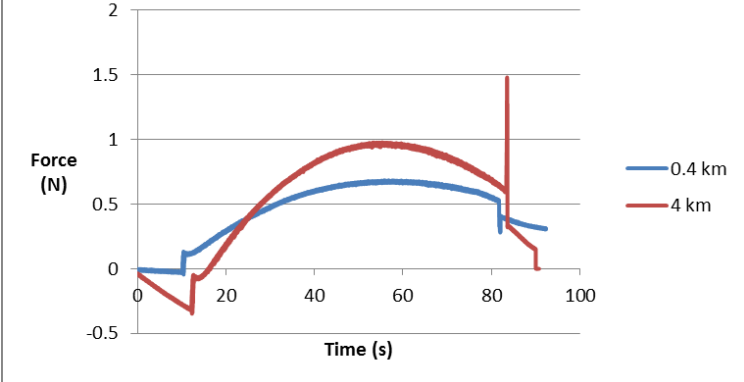
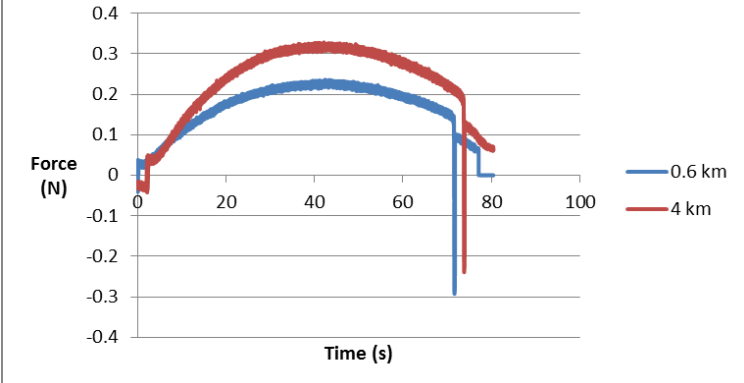
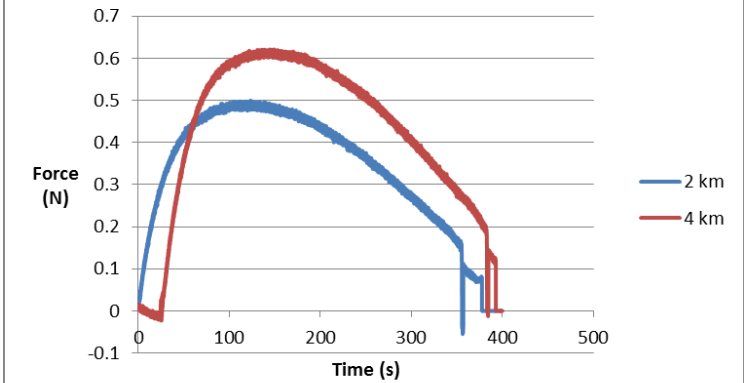
Figure 6.3: Force sensor setup

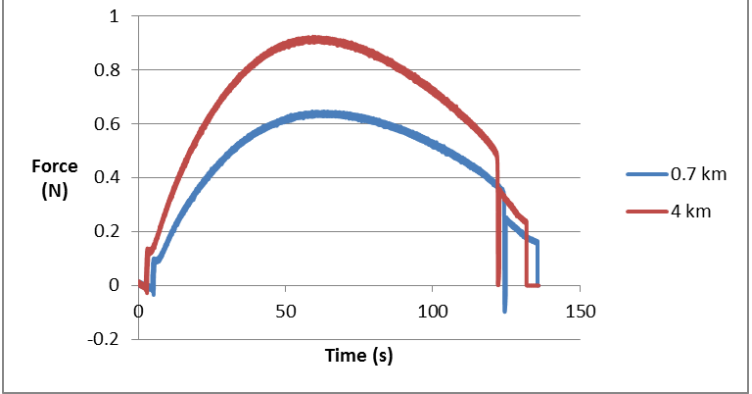
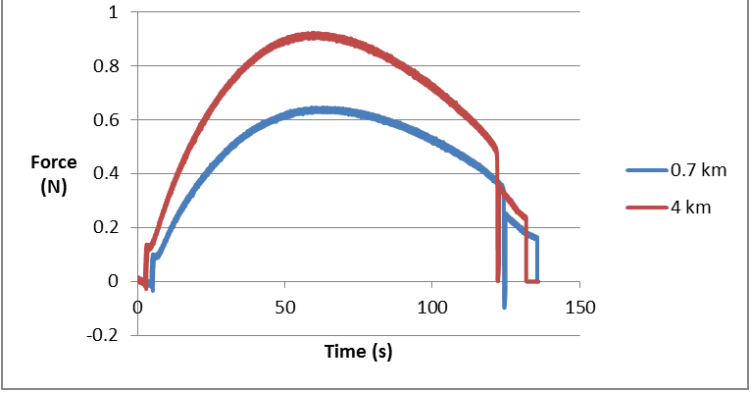
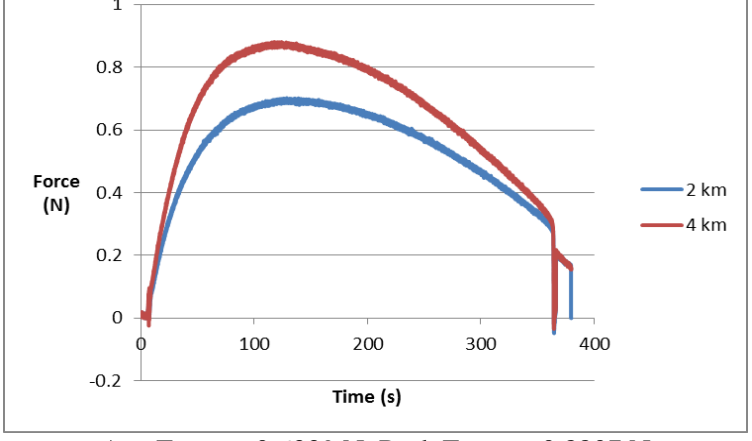
The measurement position of the force sensor under the tool meant that the measured force was an indication of the main cutting force F_c on the tool tip. Considering the small magnitude of force and the short and limited underside length of the tool holder, the positioning of the sensor along the available length showed no significant differences and the cantilever effect was disregarded. A fixed position was used for the sensor adapter as shown in Figure 6.3. The cutting force was recorded during the initial pass and the 4 km pass for each experiment.

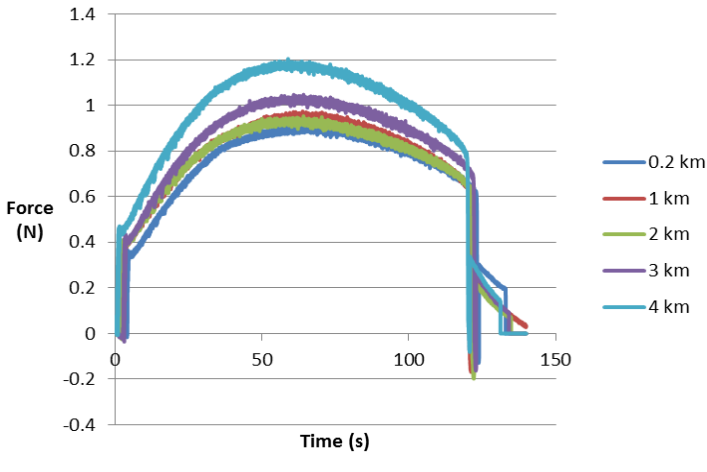
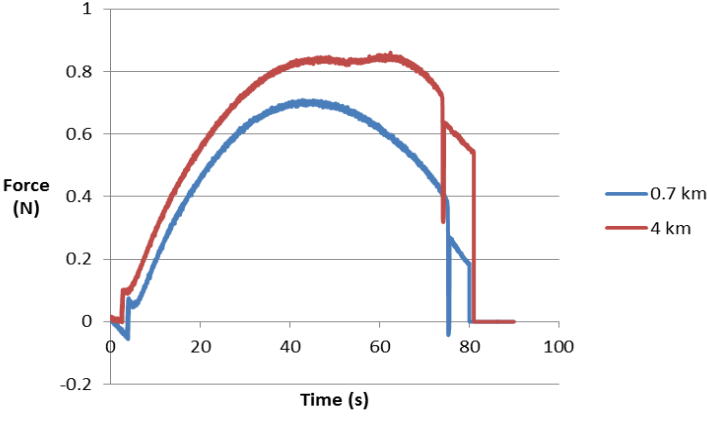
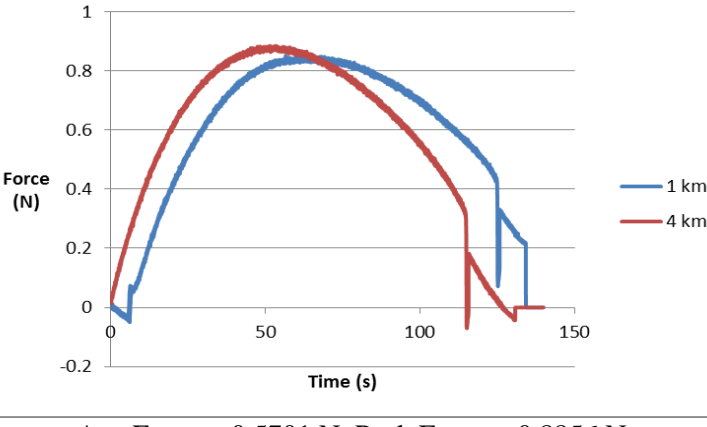
6.2 Cutting Force Results

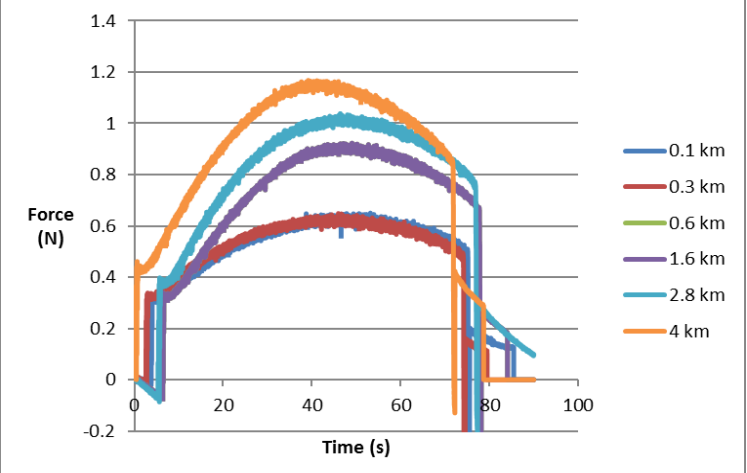
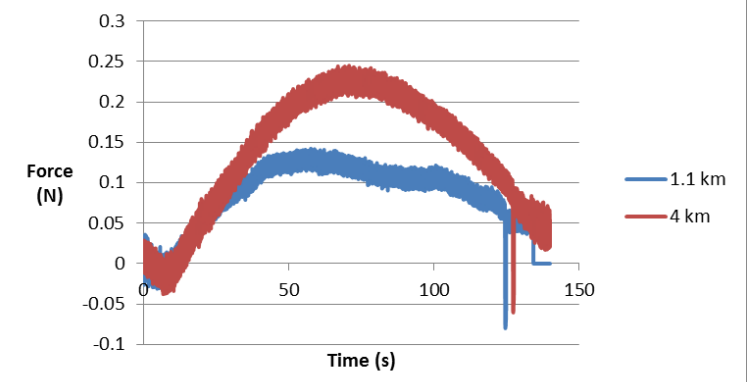
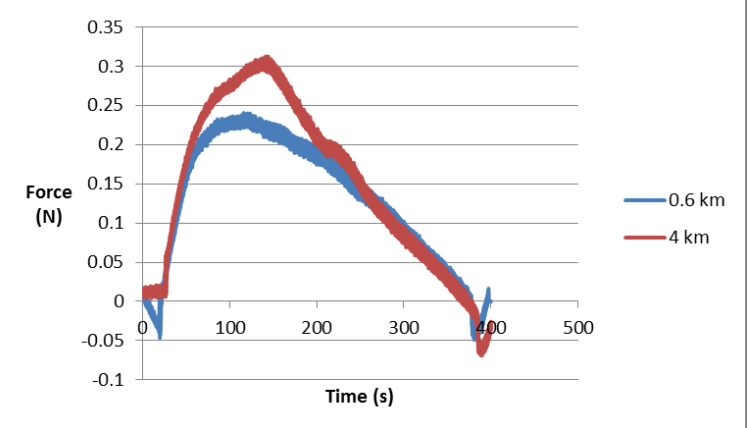
The cutting force plots for each experiment are shown in Table 6.1 with the average force and peak force at 4 km indicated below each plot.

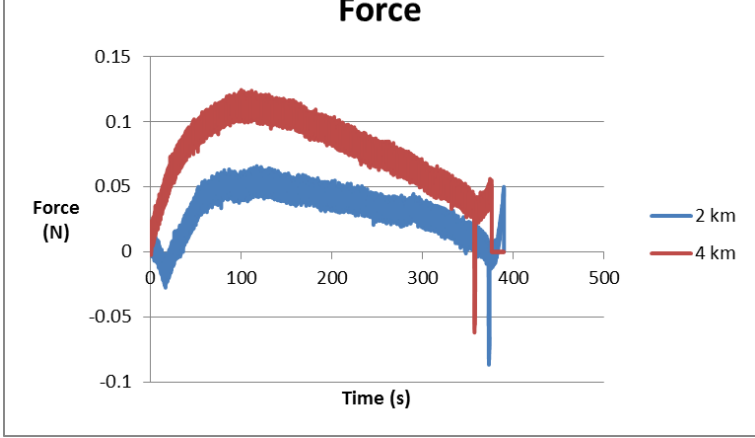
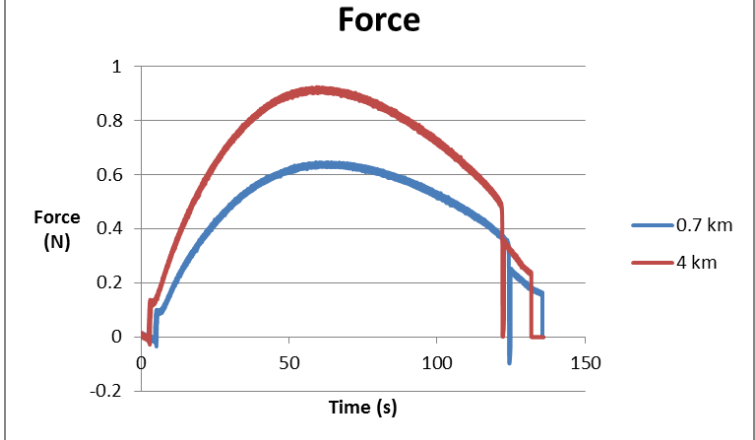
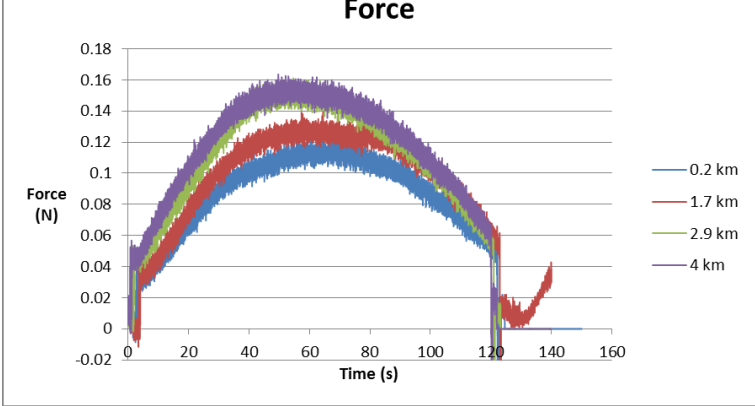
Table 6.1: Cutting force results

No.	v (rpm)	f (mm/min)	a (μm)	Results
1	1750	25	25	<p style="text-align: center;">Force</p>  <p style="text-align: center;">Ave Force = 0.7498 N, Peak Force = 0.9741 N</p>
2	1750	25	5	<p style="text-align: center;">Force</p>  <p style="text-align: center;">Ave Force = 0.2329 N, Peak Force = 0.3253 N</p>
3	3000	5	15	<p style="text-align: center;">Force</p>  <p style="text-align: center;">Ave Force = 0.4449 N, Peak Force = 0.6213 N</p>

4	1750	15	15	<p style="text-align: center;">Force</p>  <p style="text-align: center;">Ave Force = 0.6436 N, Peak Force = 0.9241 N</p>
5	1750	15	15	<p style="text-align: center;">Force</p>  <p style="text-align: center;">Ave Force = 0.6436 N, Peak Force = 0.9241 N</p>
6	1750	5	25	<p style="text-align: center;">Force</p>  <p style="text-align: center;">Ave Force = 0.6339 N, Peak Force = 0.8807 N</p>

7	500	15	25	<p style="text-align: center;">Force</p>  <p style="text-align: center;">Ave Force = 0.8584 N, Peak Force = 1.2036 N</p>
8	3000	25	15	<p style="text-align: center;">Force</p>  <p style="text-align: center;">Ave Force = 0.4737 N, Peak Force = 0.8612 N</p>
9	3000	15	25	<p style="text-align: center;">Force</p>  <p style="text-align: center;">Ave Force = 0.5701 N, Peak Force = 0.8856 N</p>

10	500	25	15	<p style="text-align: center;">Force</p>  <p style="text-align: center;">Ave Force = 0.9379 N, Peak Force = 1.0382 N</p>
11	3000	15	5	<p style="text-align: center;">Force</p>  <p style="text-align: center;">Ave Force = 0.1363 N, Peak Force = 0.2441 N</p>
12	500	5	15	<p style="text-align: center;">Force</p>  <p style="text-align: center;">Ave Force = 0.1489 N, Peak Force = 0.3125 N</p>

13	1750	5	5	<p style="text-align: center;">Force</p>  <p style="text-align: center;">Ave Force = 0.0757 N, Peak Force = 0.1215 N</p>
14	1750	15	15	<p style="text-align: center;">Force</p>  <p style="text-align: center;">Ave Force = 0.6436 N, Peak Force = 0.9241 N</p>
15	500	15	5	<p style="text-align: center;">Force</p>  <p style="text-align: center;">Ave Force = 0.1003 N, Peak Force = 0.1636 N</p>

The cutting force measured from the various experiments was generally very small, approximately below 1 N. The force plots from each experiment showed a similar pattern for each pass. The force profile increased and peaked as cutting began at the workpiece end-radius. Force then gradually decreased as the tool approached the centre of the workpiece to

complete cutting. The sharp rise in the cutting force was due to the initial impact of the tool during engagement and chip build-up. The steady decline in force was due to the decrease in cutting speed experienced in face turning when the cutting radius decreases as the tool moves towards the centre of the workpiece. The magnitude of cutting force showed an increase with increasing cutting distance. This increase between 4 km and 10 km was proportional to the magnitude, where experiments with higher forces had larger increases with distance.

At constant feed rate and depth of cut, higher forces and higher changes in forces were experienced with lower cutting speeds. Experiment 7 and experiment 9 both at a feed rate of 15 mm/min and depth of cut of 25 μm show higher forces at 500 rpm than at 3000 rpm. Similarly, experiment 10 (at 500 rpm) had higher force values than experiment 8 (at 3000 rpm), both with the same feed rate of 25 mm/min and depth of cut of 15 μm .

Comparing experiment 1 and experiment 6, where cutting speed and depth of cut are constant at 1750 rpm and 25 μm , the higher feed rate of 25 mm/min exhibited higher forces and higher changes in force compared to the lower feed rate of 5 mm/min. Similarly, experiment 10 (25 mm/min) had higher force values than experiment 12 (5 mm/min) where both experiments had cutting speed 500 rpm and depth of cut 15 μm .

With cutting speed and feed rate constant while varying depth of cut, it was seen that higher forces and higher changes in force with distance occurred with deeper cuts. Experiment 1 at 25 μm depth of cut had higher forces than experiment 2 at 5 μm , while both had 1750 rpm cutting speed and 25 mm/min feed rate. Similarly, experiment 6 (25 μm depth of cut) had higher force values than experiment 13 (5 μm depth of cut) at the same cutting speed of 500 rpm and feed rate of 15 mm/min.

Generally, rough cutting conditions (low cutting speeds, high feed rates and high depths of cut) produced higher cutting forces and higher increases in force with distance. The higher

forces were linked to more tool engagement into the workpiece along with larger and longer chips. More abrasive wear and built up edge, and the consequential poorer surface quality under these conditions produce the higher forces. The RSA microstructure also attributed to the very low forces recorded as the tool easily penetrates the workpiece. Cutting conditions that produce lower forces would be more desirable as the adverse effects on the tool and surface would be reduced.

6.3 Cutting Force Statistical Analysis

The response surface method was utilised in the Design Expert software to develop a model for cutting force. The responses were in the range of 0.0757-0.9379 N and the ratio of maximum to minimum was 12.3897. The lack of fit tests in Table 6.2 suggested that the model should be quadratic as this had the most insignificant result.

Table 6.2: Lack of fit tests for cutting force model

Source	Sum of Squares	DF	Mean Square	F-Value	P-Value
Linear	0.3100	9	0.0350	12.0900	0.0787
2FI	0.1400	6	0.0240	8.2700	0.1118
Quadratic	0.0400	3	0.0130	4.5700	0.1847
Cubic	0.0000	0			
Pure Error	0.0058	2	0.0029		

Table 6.3: Analysis of variance for cutting force model

Source	Sum of Squares	DF	Mean Square	F-Value	P-Value
Model	1.0300	5	0.2100	17.9300	0.0002
A-Spindle Speed	0.0220	1	0.0220	1.9200	0.1989
B-Feed Rate	0.1500	1	0.1500	12.9400	0.0058
C-Depth of Cut	0.6400	1	0.6400	55.8900	< 0.0001
AB	0.1400	1	0.1400	12.5700	0.0063
C^2	0.0730	1	0.0730	6.3200	0.0331
Residual	0.1000	9	0.0110		
Lack of Fit	0.0980	7	0.0140	4.8200	0.1825
Pure Error	0.0058	2	0.0029		
Cor Total	1.1300	14			

The adequacy of the model was evaluated through ANOVA as shown in Table 6.3. The results show the model was significant and lack of fit was insignificant. The insignificant terms were eliminated to produce a reduced model for cutting force.

The reduced cutting force model was described as:

$$F = -0.70978 + 0.000186v + 0.040243f + 0.070178a - 0.0000152vf - 0.00139468a^2 \quad (6.1)$$

where v is the cutting speed in rpm, f is the feed rate in mm/min, a is the depth of cut in μm and F is the average cutting force in N.

The model shows that increase in each cutting parameter increases the cutting force, but a considerable increase will negate this effect. From the model terms, depth of cut appears to have the most significant effect on the resulting force followed by feed rate then cutting speed. The normality of residuals in Figure 6.4 verified the adequacy of the model by the points along probability line. The effect of each parameter is shown in Figure 6.5-Figure 6.7.

Design-Expert® Software
Force

Color points by value of
Force:

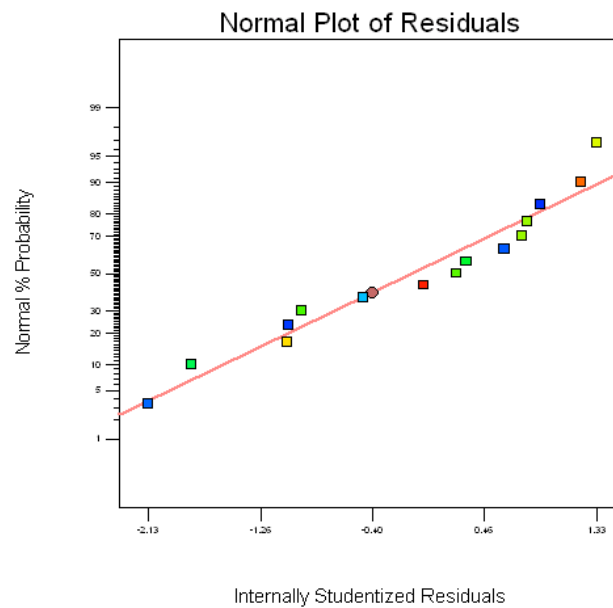


Figure 6.4: Normal probability plot for cutting force model

Change in cutting speed has a minimal effect on the cutting force as shown by the shallow gradient chart in Figure 6.5. Figure 6.6 shows that as feed rate increases, the cutting force also increases. Change in depth of cut showed to have a significant effect on cutting force. Figure 6.7 shows that increase depth of cut leads to increase in force, but at a lesser rate for high depth of cut producing the curved profile.

Design-Expert® Software

Force

● Design Points

X1 = A: Cutting Speed

Actual Factors

B: Feed Rate = 15.00

C: Depth of Cut = 15.00

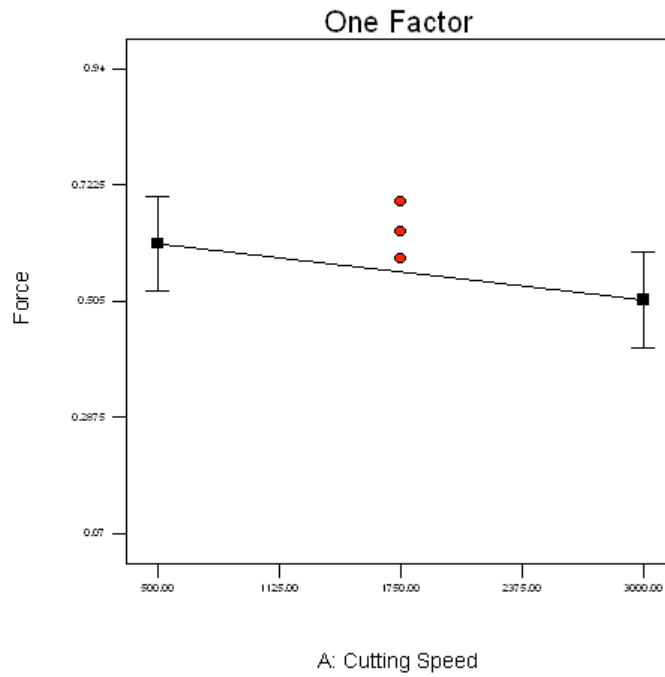


Figure 6.5: Effect of cutting speed on cutting force

Design-Expert® Software

Force

● Design Points

X1 = B: Feed Rate

Actual Factors

A: Cutting Speed = 1750.00

C: Depth of Cut = 15.00

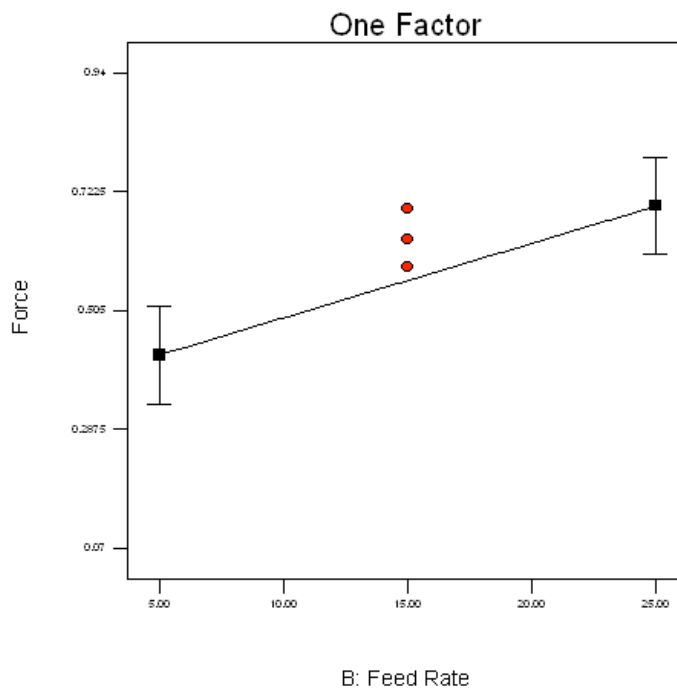


Figure 6.6: Effect of feed rate on cutting force

Design-Expert® Software

Force

● Design Points

X1 = C: Depth of Cut

Actual Factors

A: Cutting Speed = 1750.00

B: Feed Rate = 15.00

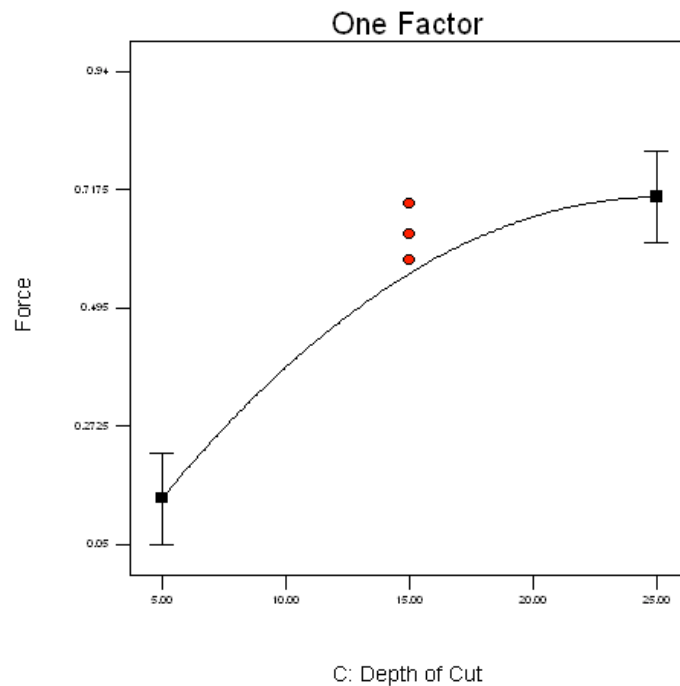


Figure 6.7: Effect of depth of cut on cutting force

The force contour plots (Figure 6.8-Figure 6.10) provide a better illustration of the interaction between cutting speed and feed rate on the cutting force at the various levels of depth of cut. The plots show that depth of cut has a significant effect with the higher force (orange/red) regions becoming considerably increased for higher depths of cut. It was also seen that the highest forces are associated with low cutting speed and high feed rate combinations along with high depth of cut. These regions are synonymous with rough cutting conditions and matches the poor surface roughness region and high tool wear region seen in their respective contour maps.

Design-Expert® Software

Force
● Design Points
0.9379
0.0757

X1 = A: Cutting Speed
X2 = B: Feed Rate

Actual Factor
C: Depth of Cut = 5.00

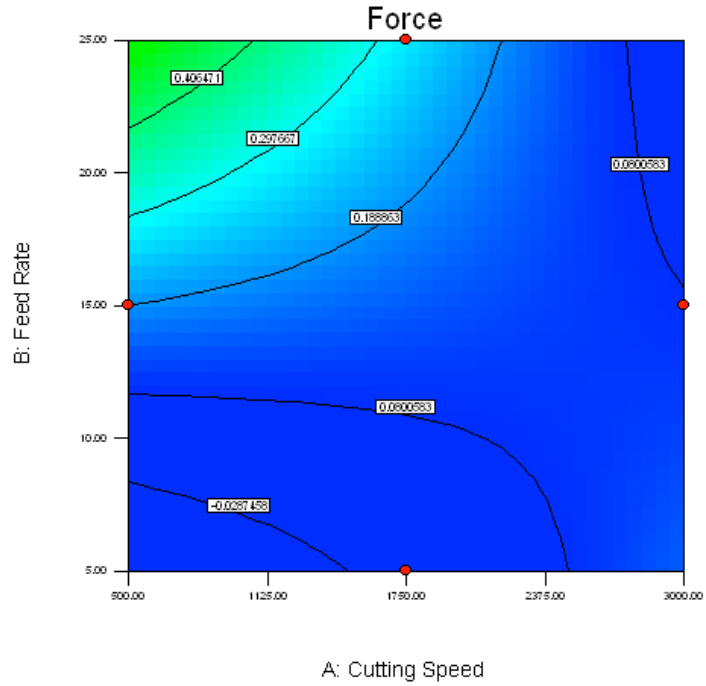


Figure 6.8: Cutting force contour map for 5 μm depth of cut

Design-Expert® Software

Force
● Design Points
0.9379
0.0757

X1 = A: Cutting Speed
X2 = B: Feed Rate

Actual Factor
C: Depth of Cut = 15.00

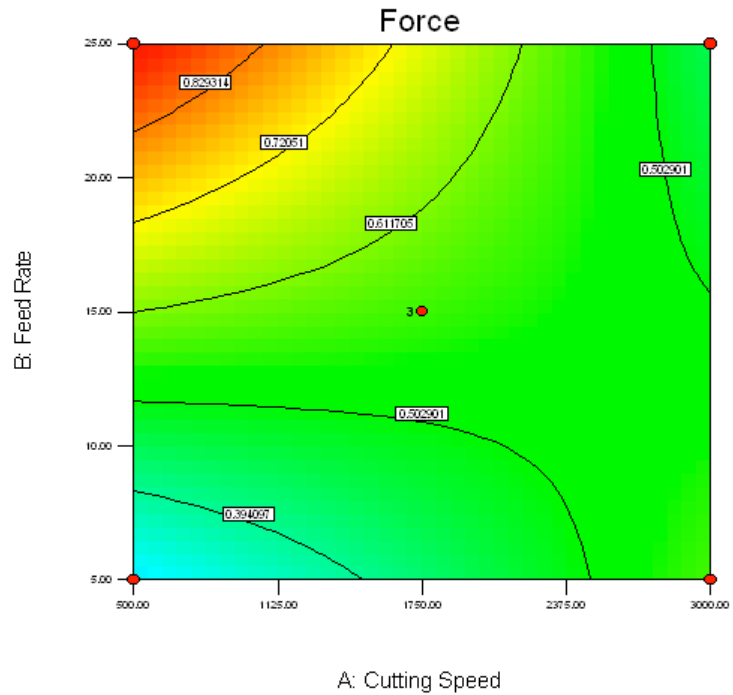


Figure 6.9: Cutting force contour map for 15 μm depth of cut

Design-Expert® Software

Force

● Design Points

0.9379

0.0757

X1 = A: Cutting Speed

X2 = B: Feed Rate

Actual Factor

C: Depth of Cut = 25.00

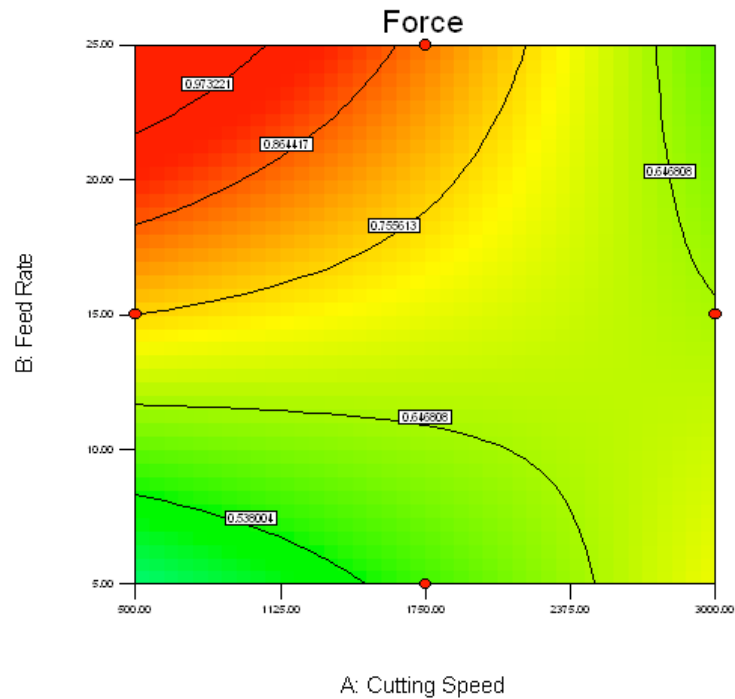


Figure 6.10: Cutting force contour map for 25 µm depth of cut

6.4 Conclusion

The cutting forces measured were generally very low, no greater 1 N. The magnitude of cutting force showed an increase with increasing cutting distance. The parameter combinations showed similar trends and force profiles of varying magnitudes. A quadratic model was developed for average cutting force using ANOVA. Analysis of the results and model showed that cutting speed had a minimal effect on the cutting force, while feed rate showed to increase cutting force. Depth of cut had the most significant effect, with an increase considerably increasing average cutting force. Higher forces were linked to more abrasive wear and built up edge, and the consequential higher surface roughness. Cutting conditions that produce lower forces would be more desirable as the adverse effects on the tool and surface would be reduced. The lowest forces were associated with high cutting speed, low feed rate and low depth of cut. The conditions also associated with high surface quality and low tool wear.

7. Acoustic Emission Analysis

7.1 Acoustic Emission Measurement Setup

Material deformation during machining produces acoustic waves whose characteristics can provide information on the cutting process. Acoustic emissions provide a means monitoring cutting tool characteristics. The Kistler Piezotron AE Sensor Type 8152B was used to measure the acoustic signals. The AE sensor consisted of a piezoelectric sensing element inside a small steel housing with a magnetic clamp for easy mounting. Figure 7.1 is a schematic of the acoustic measurement setup.

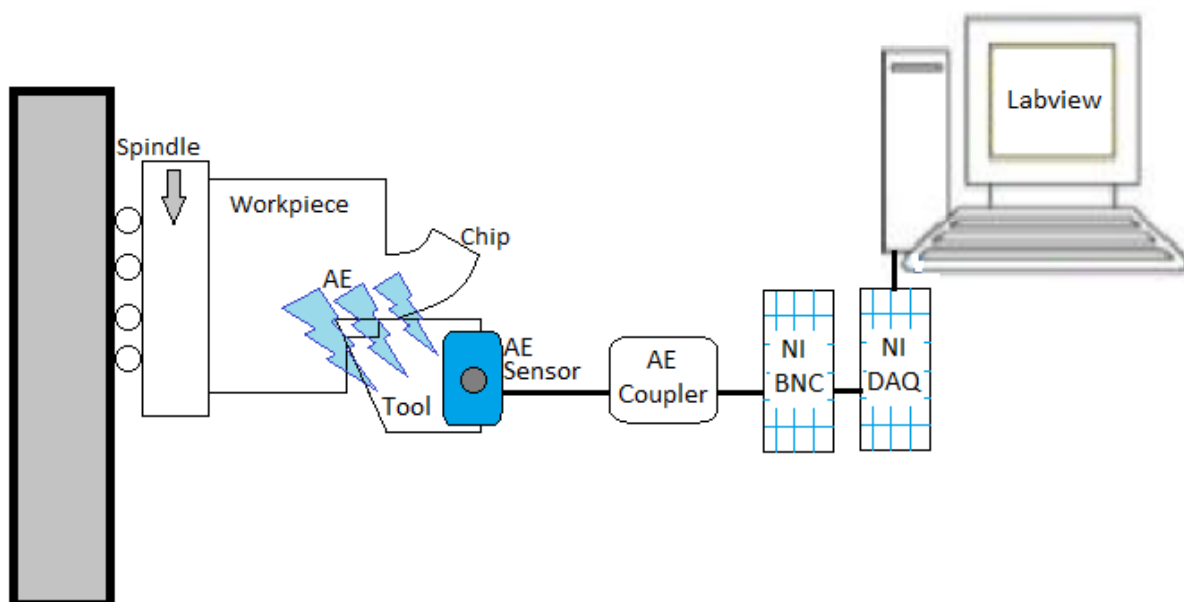


Figure 7.1: Acoustic emissions measurement schematic

The AE sensor is connected to a coupler that powers the sensor and processes the raw AE signals. The Kistler AE Piezotron Coupler Type 5125B consists of an electronic circuit with a gain amplifier, 50 kHz high-pass filter, 1000 kHz low-pass filter and RMS converter. This minimises the amount of processing required after capturing the data within software. National Instruments hardware was used for control and data acquisition. The NI BNC 2110

connector module and NI PCI 6110 DAQ card interfaced the AE sensor to the PC running NI Labview. The equipment is pictured in Figure 7.2.



Figure 7.2: Acoustic emission measurement equipment

The sensor was positioned on the tool holder as shown in Figure 7.3, and was capable of capturing high frequency signals from 50 kHz to 400 kHz. The sensor position and signal was verified during cutting run tests to ensure there was actual magnitude and frequency difference from random noise with a sample rate of up to 1 MHz for the raw signal. The RMS of the acoustic emissions AE_{RMS} for each experiment was recorded for the duration of the pass at various distances. The RMS was calculated from the raw signal to provide a good representation of the signal energy of the cutting process. A time domain analysis was selected to observe how the signal reacts along the duration of each cutting pass. The AE data was processed using NI Labview software (Figure 7.4) and plotted. The AE signal was recorded during the initial pass and the 4 km pass for each experiment.

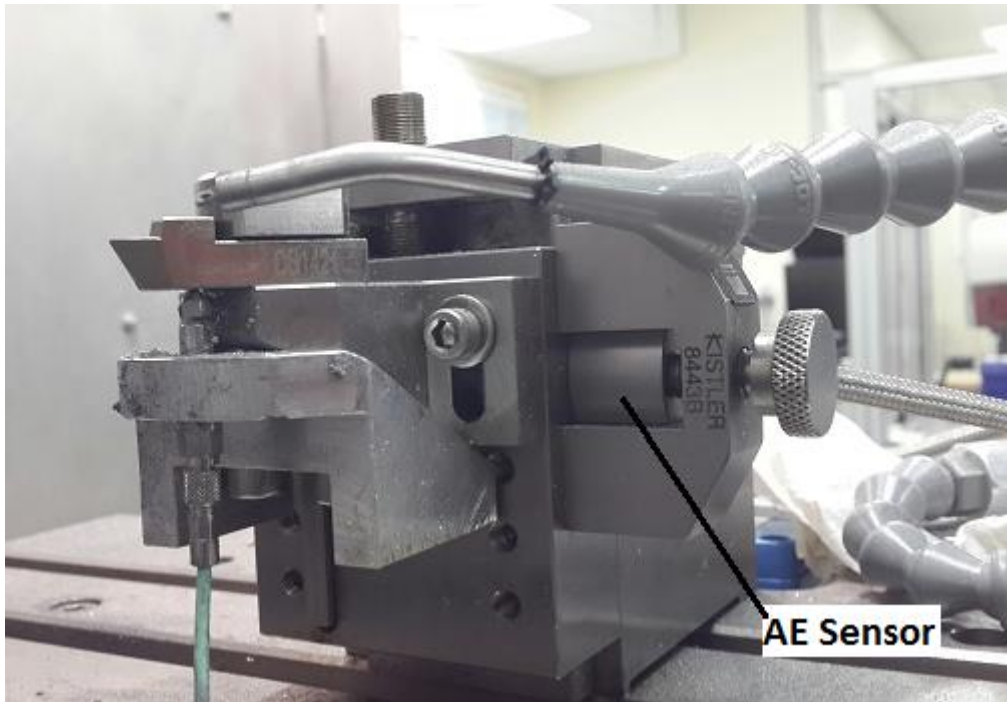


Figure 7.3: AE sensor setup

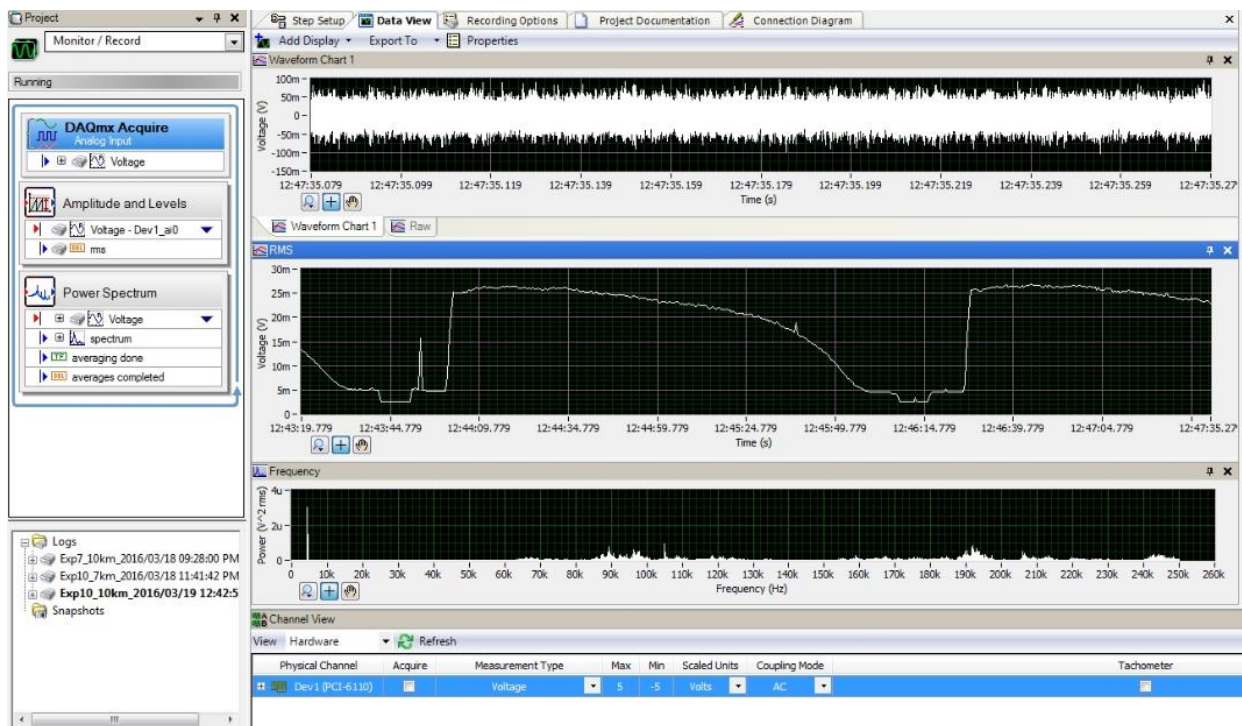


Figure 7.4: Labview acoustic data acquisition program display

7.2 Acoustic Emission Results

The plots from the acoustic measurements are shown in Table 7.1 with the average AE voltage and peak AE voltage for a cutting distance of 4 km below each plot. Figure 7.5 shows the raw AE signals for experiment 7 and experiment 11 which were converted to RMS in the table. The signal profile consists of three regions, the engagement region, the steady cutting region and the disengagement region. A large magnitude and spike was initially seen which indicates the tool engaging into the workpiece. The AE signal then maintained a steady magnitude during cutting before rapidly decreasing as the tool completed its pass and disengaged the workpiece. Spikes seen during the cutting were indicators of surface imperfections or deep grooves. Comparing the raw signals, it was seen that experiment 11 has a more even signal prevalent with smoother consistent cutting.

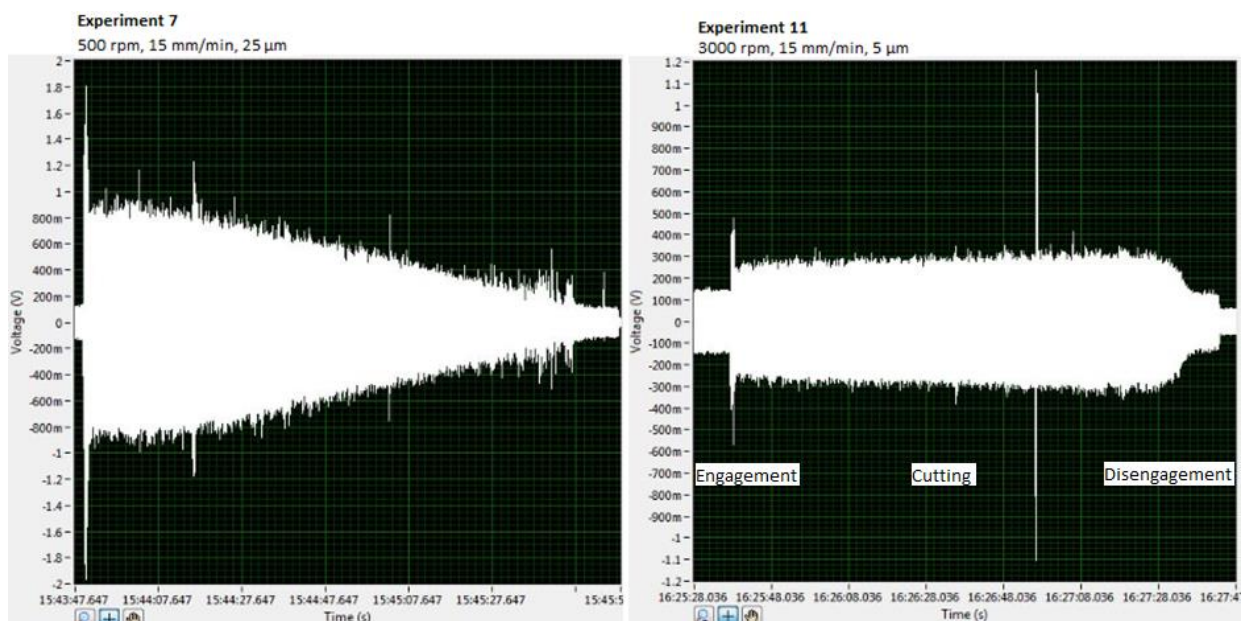
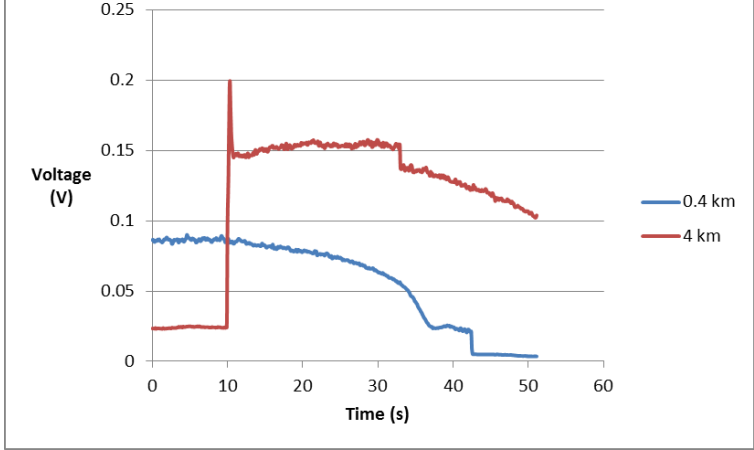
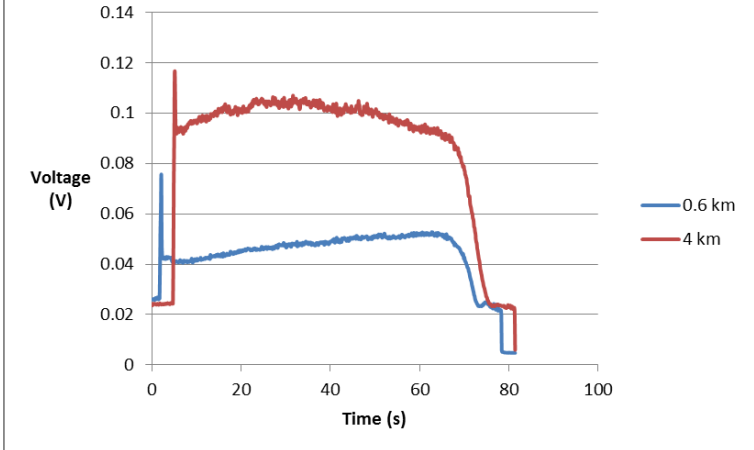
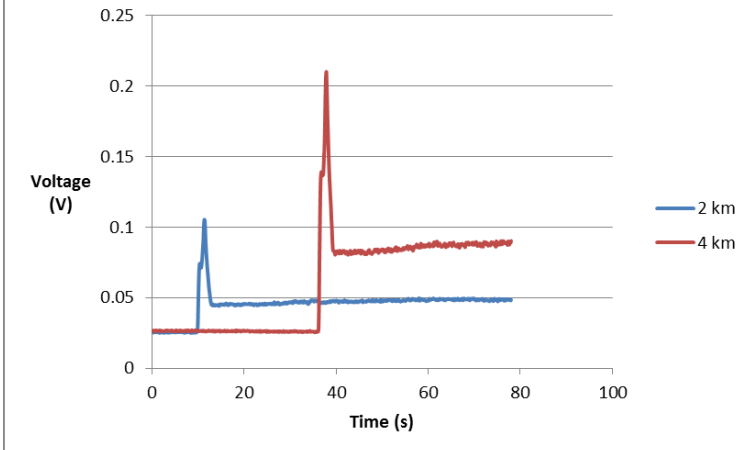
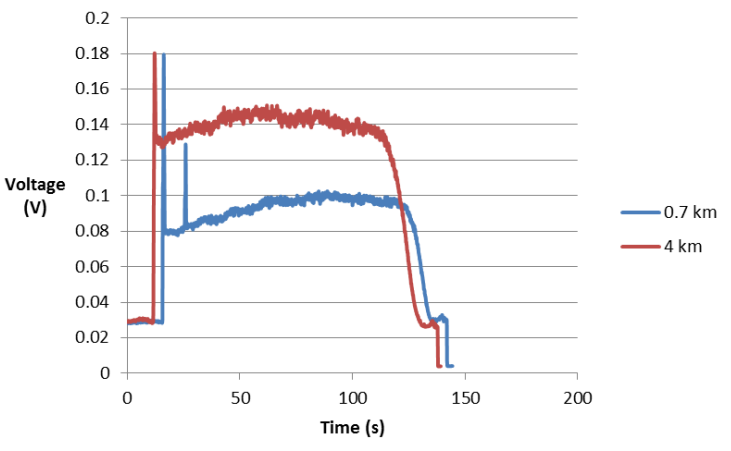
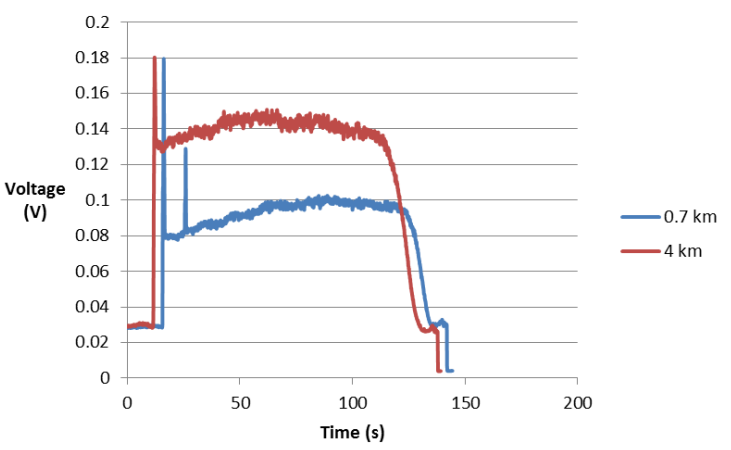
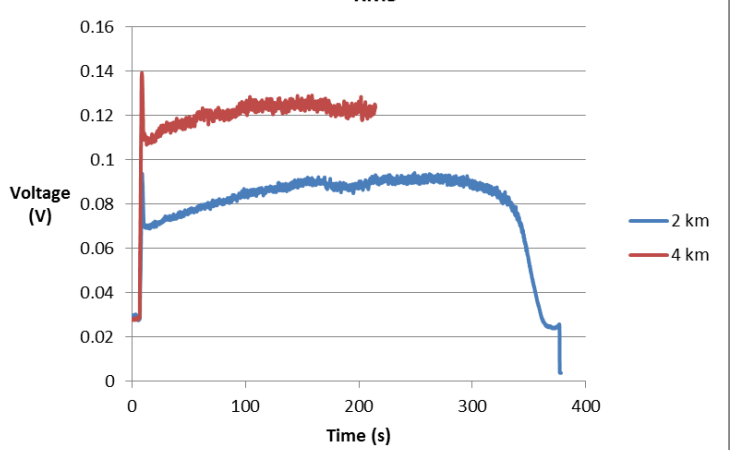
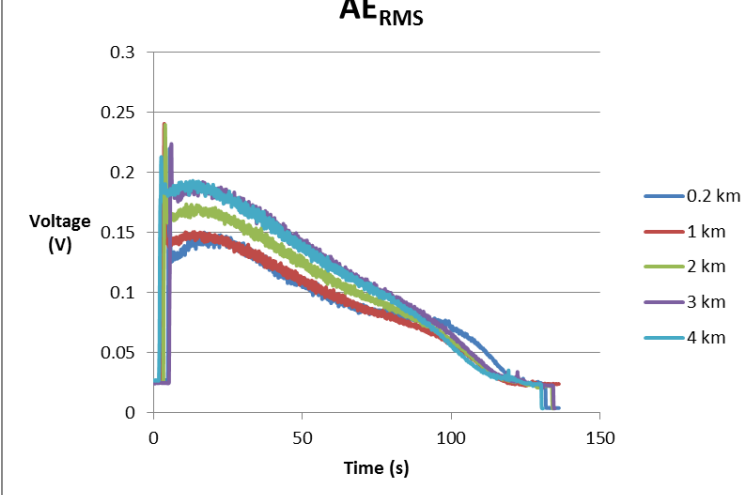
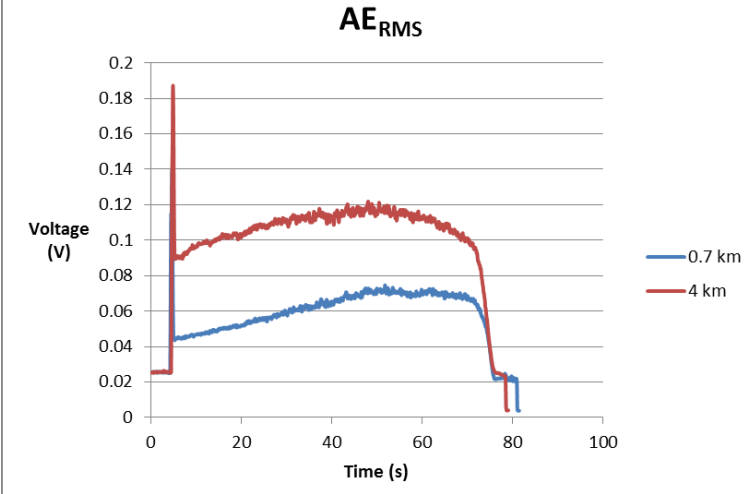
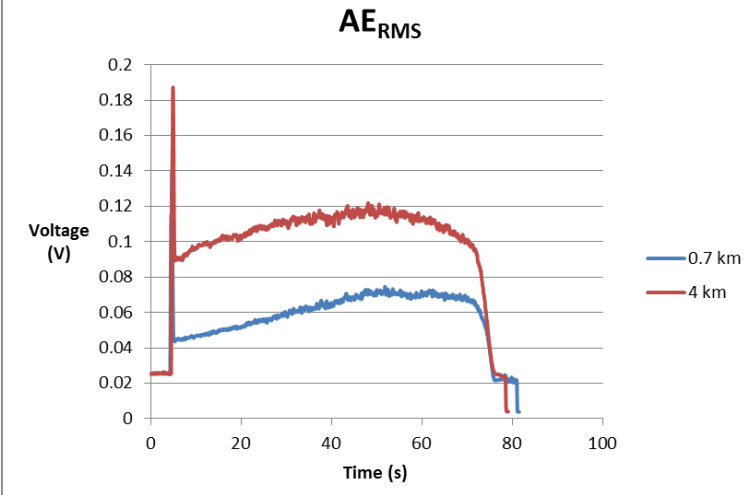


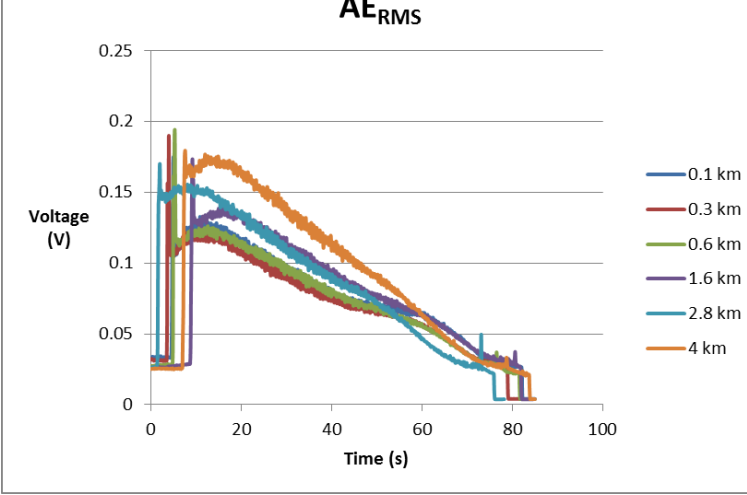
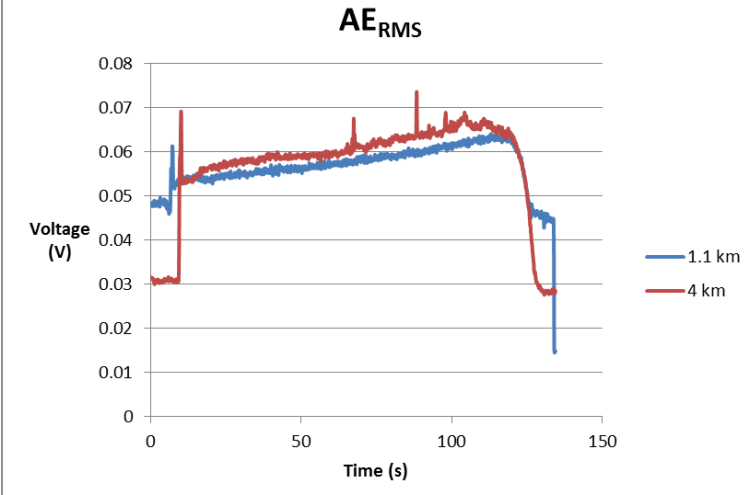
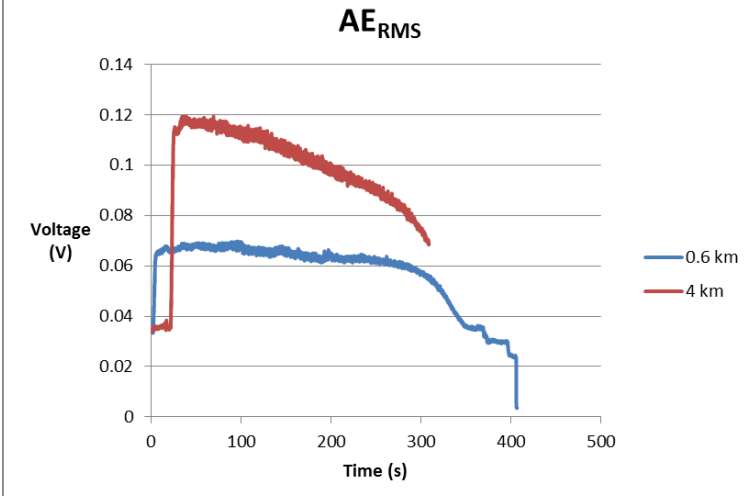
Figure 7.5: Raw AE signals for experiment 7 and experiment 11

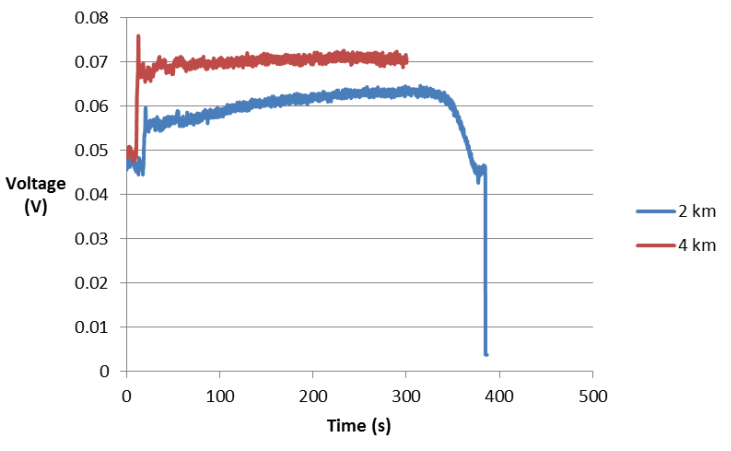
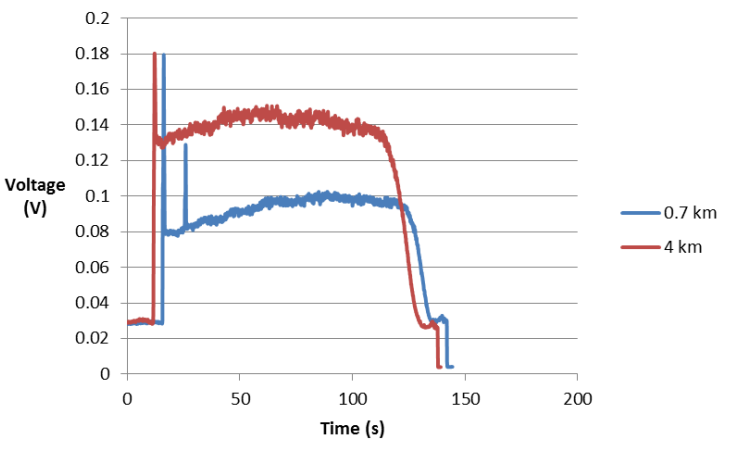
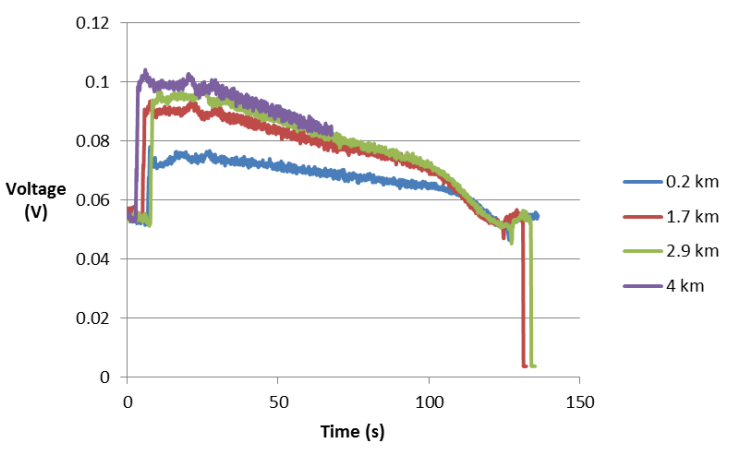
Table 7.1: Acoustic emission results

No.	v (rpm)	f (mm/min)	a (μm)	Results
1	1750	25	25	<p style="text-align: center;">AE_{RMS}</p>  <p style="text-align: center;">Ave AE_{RMS} = 0.1352 V, Peak AE_{RMS} = 0.1995 V</p>
2	1750	25	5	<p style="text-align: center;">AE_{RMS}</p>  <p style="text-align: center;">Ave AE_{RMS} = 0.0820 V, Peak AE_{RMS} = 0.1162 V</p>
3	3000	5	15	<p style="text-align: center;">AE_{RMS}</p>  <p style="text-align: center;">Ave AE_{RMS} = 0.0602 V, Peak AE_{RMS} = 0.2101 V</p>

4	1750	15	15	<p style="text-align: center;">AE_{RMS}</p>  <p style="text-align: center;">Ave AE_{RMS} = 0.1173 V, Peak AE_{RMS} = 0.1800 V</p>
5	1750	15	15	<p style="text-align: center;">AE_{RMS}</p>  <p style="text-align: center;">Ave AE_{RMS} = 0.1173 V, Peak AE_{RMS} = 0.1800 V</p>
6	1750	5	25	<p style="text-align: center;">AE_{RMS}</p>  <p style="text-align: center;">Ave AE_{RMS} = 0.1179 V, Peak AE_{RMS} = 0.1393 V</p>

7	500	15	25	<p style="text-align: center;">AE_{RMS}</p>  <p style="text-align: center;">Ave AE_{RMS} = 0.1330 V, Peak AE_{RMS} = 0.2130 V</p>
8	3000	25	15	<p style="text-align: center;">AE_{RMS}</p>  <p style="text-align: center;">Ave AE_{RMS} = 0.0979 V, Peak AE_{RMS} = 0.1868 V</p>
9	3000	15	25	<p style="text-align: center;">AE_{RMS}</p>  <p style="text-align: center;">Ave AE_{RMS} = 0.0947 V, Peak AE_{RMS} = 0.1038 V</p>

10	500	25	15	<p style="text-align: center;">AE_{RMS}</p>  <p style="text-align: center;">Ave AE_{RMS} = 0.1102 V, Peak AE_{RMS} = 0.1795 V</p>
11	3000	15	5	<p style="text-align: center;">AE_{RMS}</p>  <p style="text-align: center;">Ave AE_{RMS} = 0.0567 V, Peak AE_{RMS} = 0.0736 V</p>
12	500	5	15	<p style="text-align: center;">AE_{RMS}</p>  <p style="text-align: center;">Ave AE_{RMS} = 0.0965 V, Peak AE_{RMS} = 0.1195 V</p>

13	1750	5	5	<p style="text-align: center;">AE_{RMS}</p>  <p style="text-align: center;">Ave AE_{RMS} = 0.0694 V, Peak AE_{RMS} = 0.0759 V</p>
14	1750	15	15	<p style="text-align: center;">AE_{RMS}</p>  <p style="text-align: center;">Ave AE_{RMS} = 0.1173 V, Peak AE_{RMS} = 0.1800 V</p>
15	500	15	5	<p style="text-align: center;">AE_{RMS}</p>  <p style="text-align: center;">Ave AE_{RMS} = 0.0921 V, Peak AE_{RMS} = 0.1041 V</p>

The acoustic emission signals showed similar trends for the cutting parameters combinations. Similar to the raw AE signals, the RMS signal profile showed the engagement region (rapid increase and peak), the steady cutting region (constant) and the disengagement region (drop). The measured average AE signals were generally within the range of 0.06-0.14 V.

When varying the cutting speed while keeping feed rate and depth of cut constant, higher AE signals were produced with lower cutting speeds. The AE signal increase with increasing cutting distance was also higher at lower cutting speeds. Experiment 15 at 500 rpm produced stronger acoustic emissions and a wider AE change with increased cutting distance compared with experiment 11 at 3000 rpm when both were at feed rate 15 mm/min and depth of cut 5 μm . The same was observed with experiment 7 at 500 rpm with higher AE signals than experiment 9 at 3000 rpm, both at feed rate 15 mm/min and depth of cut 25 μm . It was also interestingly noted that the AE spike when the tool engaged the workpiece was sharper with higher cutting speeds.

When varying the feed rate while keeping cutting speed and depth of cut constant, the AE signals and AE difference with increasing cutting distance were higher with higher feed rates. Experiment 1 with cutting parameters 25 mm/min, 1750 rpm, 25 μm had higher AE signals and a wider AE range with increasing cutting distance than experiment 6 with cutting parameters 5 mm/min, 1750 rpm, 25 μm . Similarly, experiment 10 at feed rate 25 mm/min produced higher AE signals than experiment 12 at feed rate 5 mm/min, both at cutting speed 500 rpm and depth of cut 15 μm .

At constant cutting speed and feed rate while varying depth of cut, the larger depths of cut produced stronger acoustic emissions and wider AE ranges with increasing cutting distance. This was seen comparing experiment 6 at 25 μm depth and experiment 13 at 5 μm depth, where cutting speed of 1750 rpm and depth of cut of 5 mm/min were constant. Experiment 6

had higher AE values and a larger AE difference with increased cutting distance. Similarly, experiment 7 at 25 μm depth had higher AE compared to experiment 15 at 5 μm depth, where both had the same cutting speed of 500 rpm and feed rate of 15 mm/min.

There was a direct correlation between the level of tool wear and the corresponding AE signals. The AE signal voltage was observed to increase with increasing cutting distance. However, the peak, which occurred at tool point contact, and its difference from the steady cutting magnitude was found to decrease with distance as the tool edge flattened. Hence, the effect of the tool impact on the AE during workpiece engagement reduced. These trends were evident when comparing the experiments that experienced higher tool wear with those of lower tool wear. Generally, rough cutting conditions (low cutting speed and high feed rate and depth of cut) produced higher magnitude AE signals. Similar to the force measurements, the high acoustic emissions were linked to more tool engagement into the workpiece, larger chip sizes, and poorer surface quality with corresponding higher wear rates. These inefficient cutting conditions also showed to have an AE signal that gradually decreased right after tool engagement. This showed the inconsistency of the cutting under these conditions and hence the poor results. This held true for all the experiments, but this AE increase with distance was found to be lower with smoother surfaces that experienced less wear. Finer cutting conditions with high cutting speed, low feed rate and low depth of cut produced more consistent cutting results. Experiment 3, for example, showed smooth cutting conditions with a steady AE signal during cutting and small increase in AE with distance. This was a result of healthy tool contact and consequent low wear and superior surface quality.

7.3 Acoustic Emission Statistical Analysis

The acoustic emission responses were analysed by applying RSM in the Design Expert software to develop a model. The responses ranged from 0.0567 V to 0.1352 V and the ratio

of maximum to minimum was 2.38. The lack of fit tests in Table 7.2 suggested that the model should be in quadratic form based on the highest p-value.

Table 7.2: Lack of fit tests for AE_{RMS} model

Source	Sum of Squares	DF	Mean Square	F-Value	P-Value
Linear	0.001532	9	0.000170	3.2500	0.2574
2FI	0.001381	6	0.000230	4.3900	0.1970
Quadratic	0.000202	3	0.000067	1.2800	0.4664
Cubic	0.000000	0			
Pure Error	0.000105	2	0.000052		

The model was evaluated through ANOVA as shown in Table 7.3. The insignificant terms (with p-value > 0.1) were eliminated to reduce the model. The results show the model was significant and lack of fit was insignificant. Equation 6.1 described the resulting acoustic emission model.

$$AE_{RMS} = 0.035866 + 0.00002194v + 0.00349298f + 0.0022575a - 0.00000001v^2 - 0.00008256f^2 \quad (6.1)$$

where v is the cutting speed in rpm, f is the feed rate in mm/min, a is the depth of cut in μm and AE_{RMS} is the acoustic emission RMS in V.

Table 7.3: Analysis of variance for AE_{RMS} model

Source	Sum of Squares	DF	Mean Square	F-Value	P-Value
Model	0.0078290	5	0.0015660	24.25	< 0.0001
A-Spindle Speed	0.0018700	1	0.0018700	28.96	0.0004
B-Feed Rate	0.0008262	1	0.0008262	12.80	0.0060
C-Depth of Cut	0.0040770	1	0.0040770	63.15	< 0.0001
A ²	0.0008645	1	0.0008645	13.39	0.0052
B ²	0.0002532	1	0.0002532	3.92	0.0790
Residual	0.0005811	9	0.0000646		
Lack of Fit	0.0004763	7	0.0000680	1.30	0.5014
Pure Error	0.0001048	2	0.0000524		
Cor Total	0.0084100	14			

The normality of residuals in Figure 7.6 verified the adequacy of the model by the proximity of the points to the probability line.

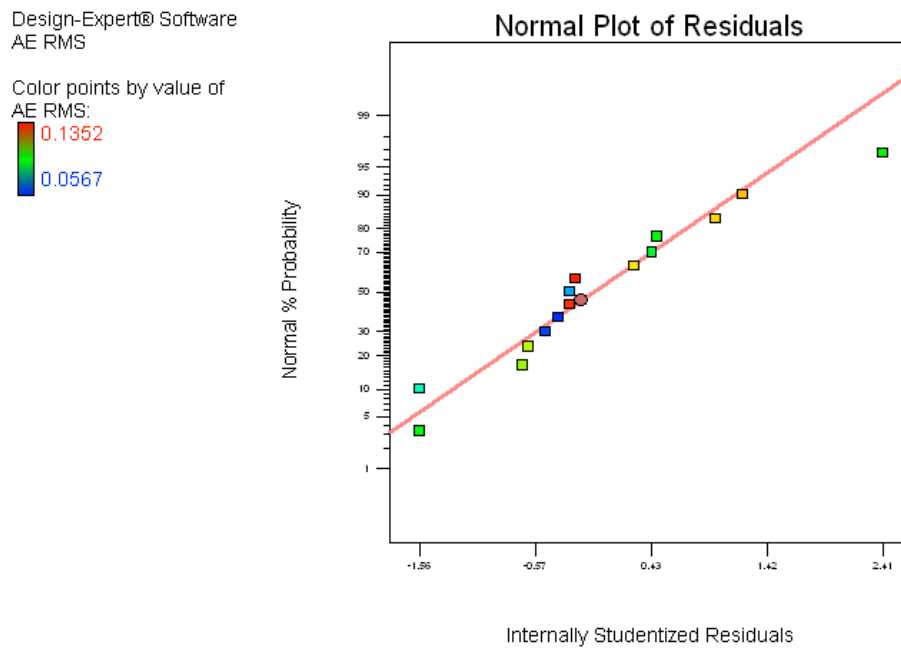


Figure 7.6: Normal probability plot for AE_{RMS} model

It is seen from the model that an increase in each cutting parameter leads to an increase in the AE response. Depth of cut has the greatest impact followed by feed rate then cutting speed. As cutting speed increases the negative square term would have a greater impact causing a decrease in the AE. Increase in feed rate causes an increase in the AE response but the negative square term slowly decreases the rate of AE increase. Increasing depth of cut leads to a steady increase in AE response.

Design-Expert® Software

AE RMS

● Design Points

X1 = A: Cutting Speed

Actual Factors
B: Feed Rate = 15.00
C: Depth of Cut = 15.00

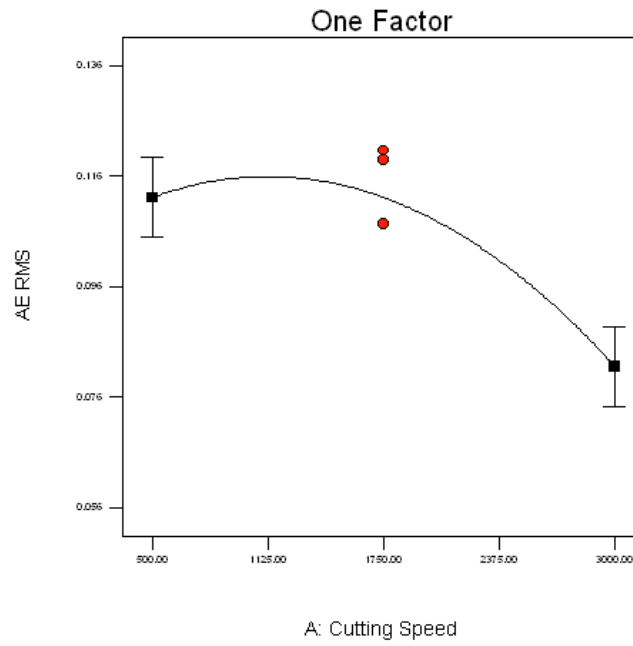


Figure 7.7: Effect of cutting speed on AE_{RMS}

Design-Expert® Software

AE RMS

● Design Points

X1 = B: Feed Rate

Actual Factors
A: Cutting Speed = 1750.00
C: Depth of Cut = 15.00

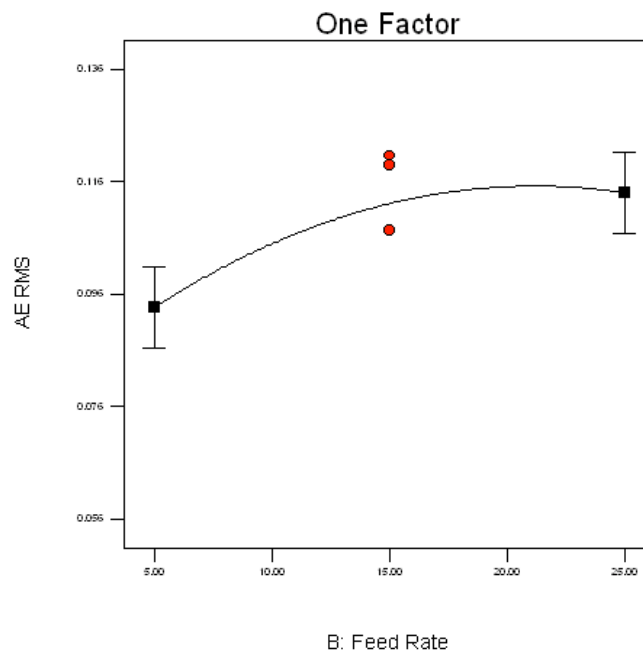


Figure 7.8: Effect of feed rate on AE_{RMS}

Design-Expert® Software

AE RMS

● Design Points

X1 = C: Depth of Cut

Actual Factors

A: Cutting Speed = 1750.00

B: Feed Rate = 15.00

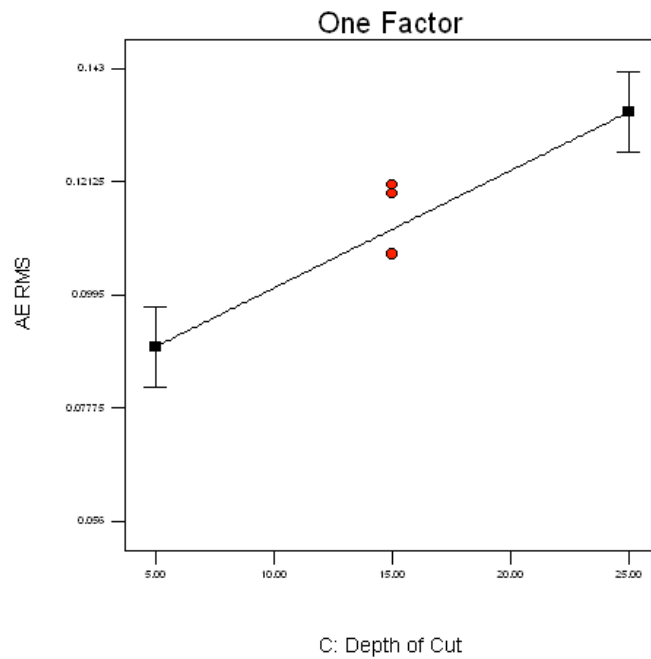


Figure 7.9: Effect of depth of cut on AE_{RMS}

The effect of each machining parameter is shown in Figure 7.7-Figure 7.9. Increase in cutting speed was seen to decrease AE response while increase in feed rate and depth of cut increased the AE response. The single factor plots show that the highest AE would be associated with low cutting speed, high feed rate and high depth of cut. The AE contour plots (Figure 7.10-Figure 7.12) further verify this by the location of the high AE regions represented by the orange/red zones. These regions also grow with increase in depth of cut. This region closely matches the poor surface roughness region and high tool wear region seen in their respective contour maps which is synonymous with rough machining.

Design-Expert® Software

AE RMS

● Design Points

0.1352

0.0567

X1 = A: Cutting Speed

X2 = B: Feed Rate

Actual Factor

C: Depth of Cut = 5.00

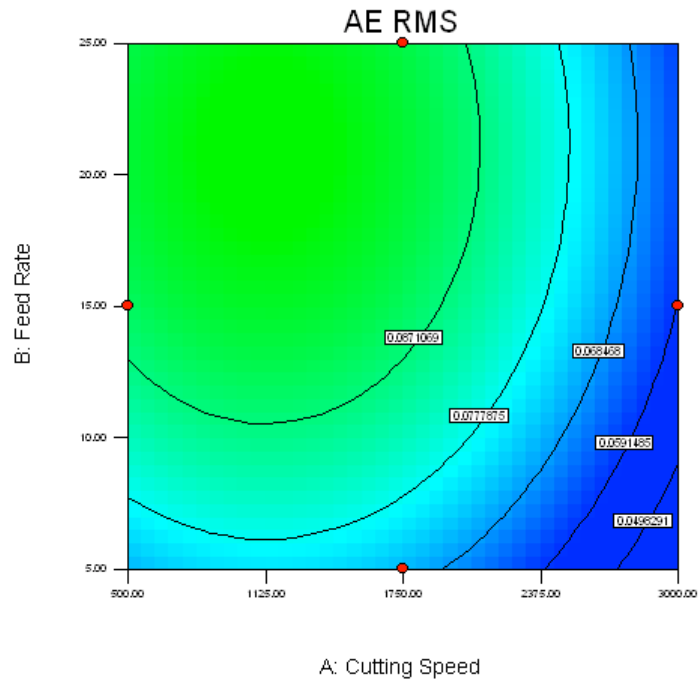


Figure 7.10: AE_{RMS} contour map for 5 μm depth of cut

Design-Expert® Software

AE RMS

● Design Points

0.1352

0.0567

X1 = A: Cutting Speed

X2 = B: Feed Rate

Actual Factor

C: Depth of Cut = 15.00

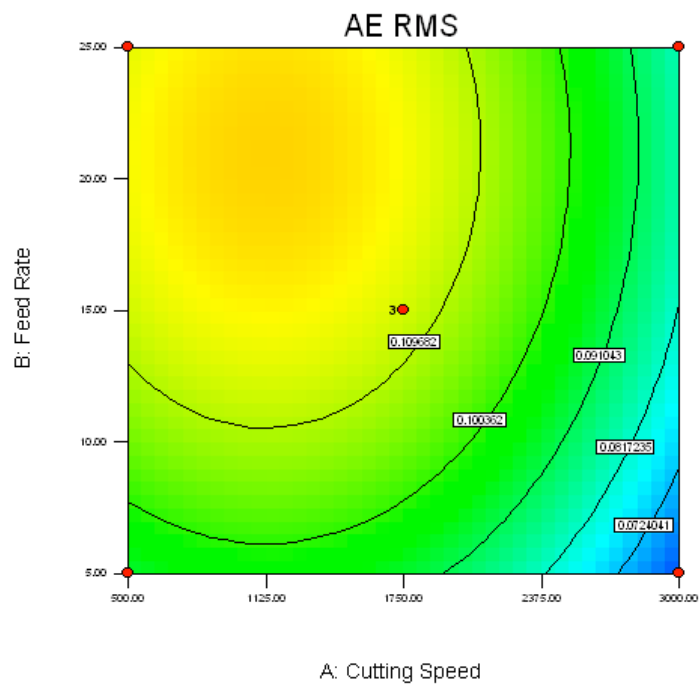


Figure 7.11: AE_{RMS} contour map for 15 μm depth of cut

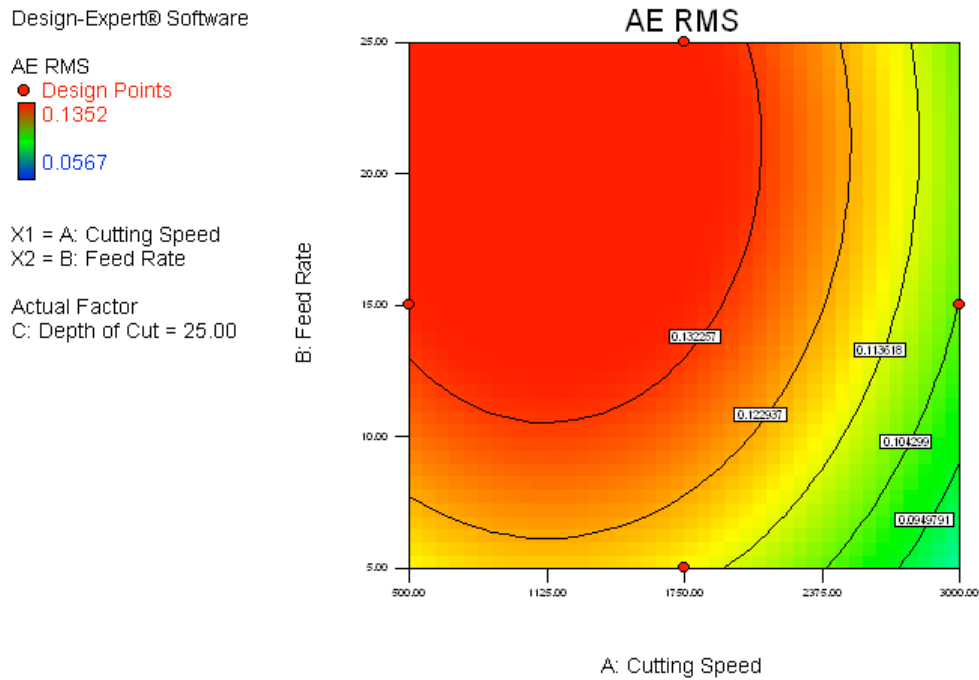


Figure 7.12: AE_{RMS} contour map for 25 μm depth of cut

7.4 Conclusion

The acoustic emissions were recorded for each of the 15 experiments and RMS results were used to create a predictive model using ANOVA. A quadratic model was developed where cutting speed had a decreasing effect on AE, while feed rate and depth of cut had an increasing effect on AE. The AE signals clearly showed the cutting progression through three regions, the engagement region, the steady cutting region and the disengagement region. A correlation was noticed between the level of tool wear and the corresponding AE signals. The AE signal voltage was observed to increase with increasing cutting distance as the wear increased. The highest AE was observed in regions with low-mid cutting speed, mid-high feed rate and high depth of cut. This closely matched regions of high wear, high cutting forces and high surface roughness. Hence, low AE would be preferred.

8. Machining Conditions Optimisation

8.1 Desirability and Numerical Optimisation

The tool wear and surface roughness are not mutually exclusive and one performance cannot be maximised without affecting the other. As tool wear increases, the resulting surface roughness also increases and thus the quality of the machined surface diminishes. Maintaining low wear rates improves machining efficiency by extending tool life while maintaining the surface quality. The tool wear models and surface roughness models predict the expected results after cutting for a given distance, hence reducing the downtime for quality checks. To reach an optimal compromise between parameters, the tool wear and surface roughness were statistically analysed to provide an understanding on their interrelationship and to provide a reference for flexibility.

The prediction models were combined with the goal of minimising tool wear and surface roughness within the parameter ranges as shown in Table 8.1. This produced the 20 possible solutions shown in

Table 8.2, ranked in order of desirability. A desirability of 1 is the target optimum result. The most optimum solution was cutting speed 2105 rpm, feed rate 5.0 mm/min, depth of cut 5.1 μm , to produce a surface roughness of 3.45 nm and tool wear 2.45 μm . These cutting parameters would produce the most efficient machining of RSA 905 allowing minimal wear while maintaining high surface quality, essentially extending cutting distance and tool life. This solution would be best for finishing cuts of small depth of cut and small material removal rate. Optimal settings can also be achieved for rough cuts which are not strongly governed by surface roughness. Solution 16 or solution 17 can be utilised for rough cuts as they exhibit higher depth of cut and higher material removal rate while substantially minimizing tool wear.

Table 8.1: Optimisation constraints

Factor	Goal	Lower Limit	Upper Limit
Cutting Speed	is in range	500	3000
Feed Rate	is in range	5	25
Depth of Cut	is in range	5	25
Surface Roughness	minimize	3.2	53.9
Tool Wear	minimize	2.45	12.2

Table 8.2: Optimum solutions

Solutions No.	Cutting Speed (rpm)	Feed Rate (mm/min)	Depth of Cut (μm)	Surface Roughness (nm)	Tool Wear (μm)	Desirability	MRR (mm^3/min)
1	2105	5.0	5.1	3.45	2.45	1	4.81
2	2118	5.0	5.1	3.46	2.45	2	4.78
3	2166	5.0	5.2	3.46	2.45	3	5.73
4	2016	5.0	5.0	3.46	2.45	4	6.09
5	2254	5.0	5.3	3.46	2.45	5	6.64
6	2164	5.0	5.6	3.41	2.49	6	7.04
7	2471	5.0	5.8	3.51	2.45	7	5.80
8	2485	5.0	5.4	3.56	2.41	8	9.52
9	2766	5.0	6.8	3.63	2.45	9	7.48
10	1344	5.0	7.1	3.51	2.65	10	12.85
11	3000	5.3	9.4	3.68	2.56	11	10.19
12	3000	5.0	13.3	3.48	2.77	12	19.92
13	2940	5.0	13.9	3.39	2.84	13	22.25
14	2996	5.0	18.7	3.50	2.95	14	23.24
15	2684	5.0	18.9	3.20	3.23	15	10.33
16	2670	5.0	19.2	3.20	3.24	16	110.46
17	3000	5.0	22.2	3.72	2.94	17	111.87
18	2916	5.2	25.0	3.91	2.96	18	102.35
19	3000	12.1	5.0	4.50	2.71	19	13.19
20	3000	20.3	23.3	4.34	3.08	20	87.79

Additionally, should surface roughness need be prioritised, solution 15 or solution 16 would be viable where surface roughness is at its lowest while keeping tool wear very low. Alternatively, should tool wear be prioritised, solution 1-5 or solution 9 are applicable. The desirability map in Figure 8.1 shows regions shaded orange/red with high desirability (closest to 1) which would produce optimum results. The map further clarifies that low feed rates and

higher cutting speeds with a small depth of cut produce the best results. The solutions table and map allows flexibility of machining parameter selection based on tool wear and surface roughness depending on the user and/or design requirements.

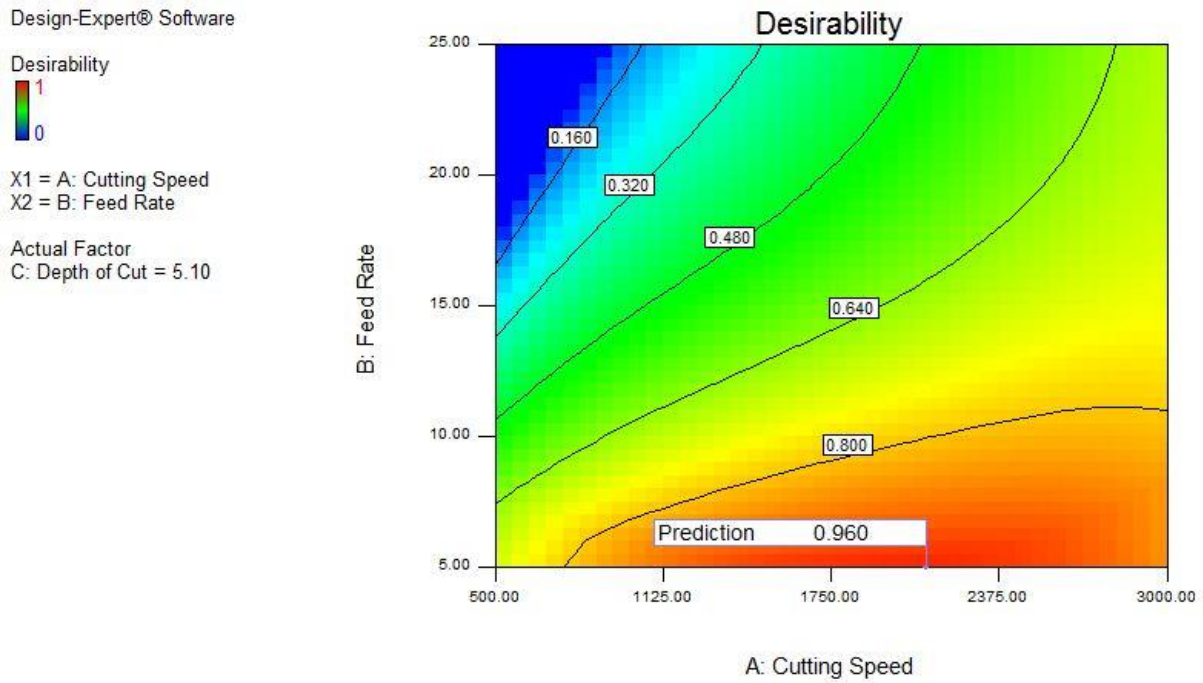


Figure 8.1: Optimum solutions desirability map

The optimal conditions also have a direct effect on the monitoring of cutting forces and acoustic emissions. Low cutting forces and low acoustic signals should be expected. The average cutting force and the average AE_{RMS} for solution 1 are predicted as 0.1319 N and 0.0669 V, respectively. During machining these initial readings will increase. Once a significant increase is observed, these monitoring parameters become good indicators for inspecting the tool and/or surface before degradation occurs. From the experiments carried out and analysis of the results, these indicative points would approximately lie at an average force of 0.6 N and an average AE_{RMS} of 0.1 V. These values are also seen on their contour maps, Figure 6.10 and Figure 7.12. Single point diamond turning requires constant monitoring and operator intervention. Quality control is usually implemented in stages and can be as often as after every pass. These results can greatly reduce this intervention through

effective monitoring and parameter selection. Quality management is thus improved, reducing the percentage of defective parts, and enhancing productivity.

8.2 Fine Tuning and Graphical Optimisation

The optimum solutions can be further narrowed down to identify a “sweet spot” that would provide a range of parameters that satisfy the optimisation criteria. Majority of the desirability results have a feed rate of 5 mm/min, hence this was held constant and the window selected provided a range for cutting speed and depth of cut that would result in surface roughness below 3.46 nm and tool wear below 2.46 μm . The overlay plot in Figure 8.2 shows this window as the region highlighted in yellow.

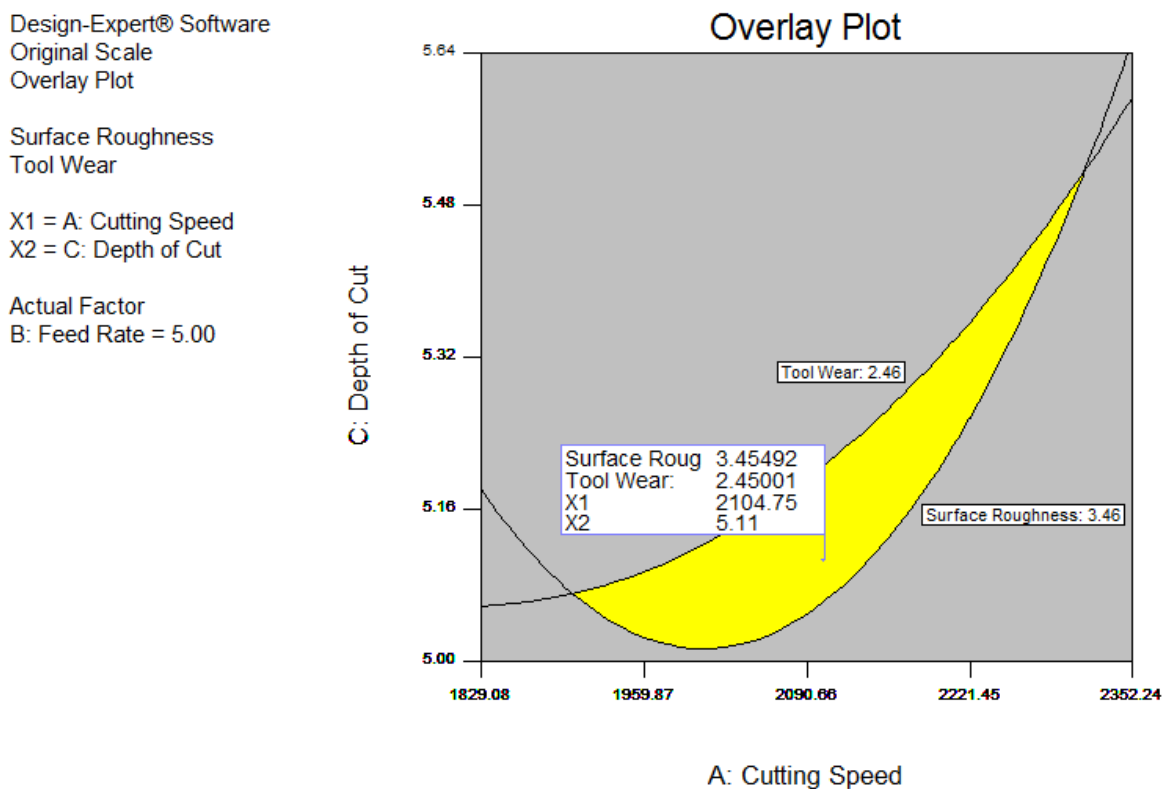


Figure 8.2: Overlay plot of optimal region

8.3 Conclusion

Optimising the cutting parameters to minimise surface roughness and tool wear greatly improves machining performance and enhances machinability of the material. Several

optimised solutions were provided to offer flexibility based on which response is more prioritised or in the event any parameter limitations exist due to the machine capability or desired cutting condition. Parameters can be selected where surface roughness is prioritised at its lowest with very low wear or vice versa, where wear is prioritised at its lowest with very low surface roughness. The solutions also provide an option to maximise material removal while keeping tool wear low. Ideally, the most optimum solution is provided where both surface roughness and tool wear are minimised. The most optimum solution was cutting speed 2105 rpm, feed rate 5.0 mm/min, depth of cut 5.1 μm , to produce a surface roughness of 3.45 nm and tool wear 2.45 μm . The average cutting force and the average AE_{RMS} for solution 1 are predicted as 0.1319 N and 0.0669 V, respectively. These values can be monitored for significant increases thus becoming indicators for inspecting the tool and/or surface before degradation occurs. Efficiency would be improved by reducing the required machining interruption through effective monitoring and performance would be improved by maintaining quality and extending tool life through parameter selection.

9. Molecular Dynamics Simulation

9.1 Microstructure Analysis

In order to approximate a model for molecular dynamics simulation, a good understanding and representation of the material structure must be obtained. The RSA 905 under investigation is known to have an ultra-fine grain structure. Thus, the use of transmission electron microscopy (TEM) was required to obtain detailed information and images of the material structure.

The TEM sample was prepared using focused ion beam (FIB) equipment to cut out a cross-sectional lamella from the RSA 905 workpiece for analysis. Figure 9.1 is a bright field TEM micrograph of the FIB lamella clearly showing the grains. The structure was seen to have ultra-fine grains approximately 0.5-1 μm in size. An area was mapped with energy dispersive spectroscopy (EDS) in the TEM to closely examine the nature and composition of the grains. Figure 9.2 is an annular dark field (ADF) of the FIB lamella showing the section that was mapped with EDS for analysis.

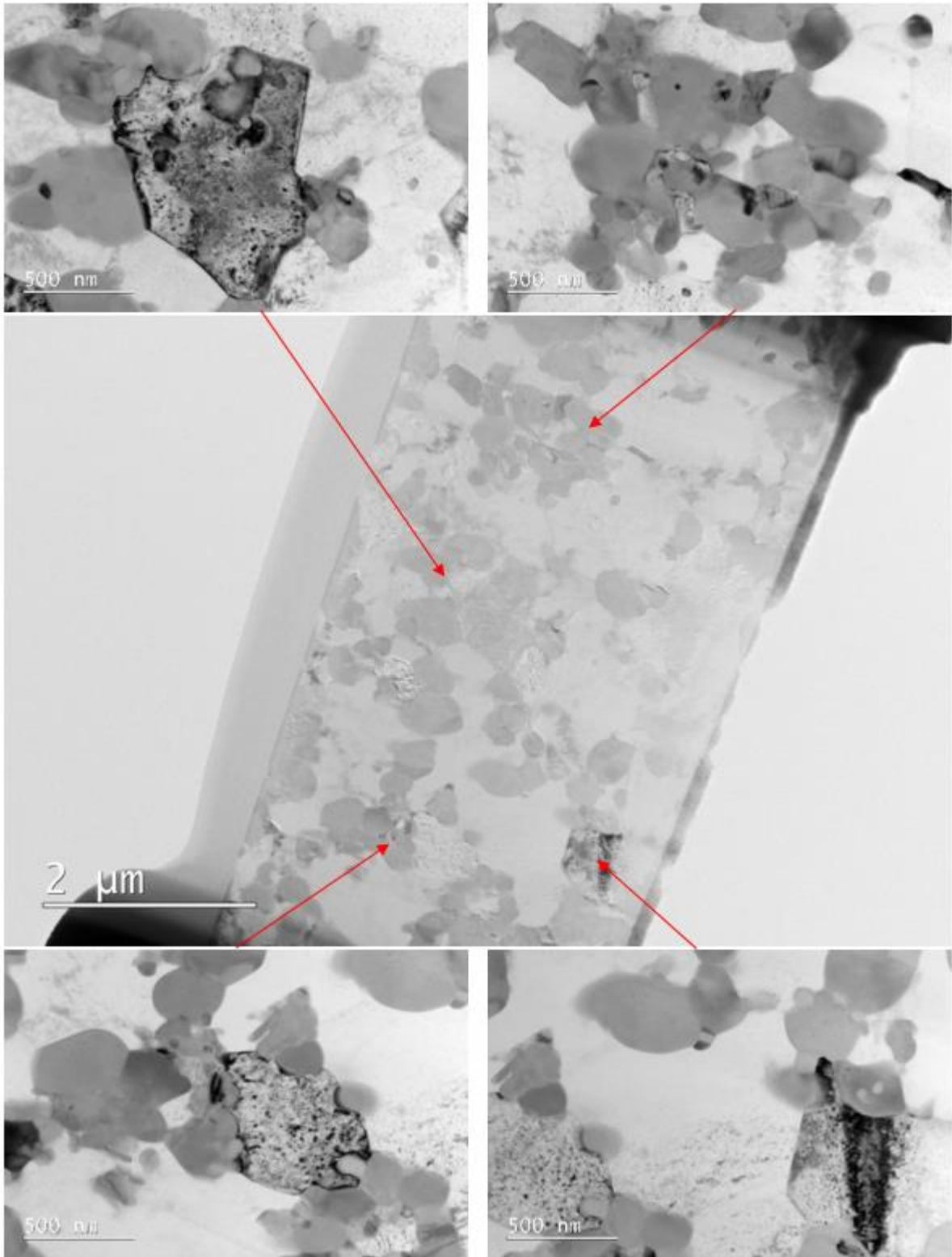


Figure 9.1: Bright field TEM of FIB lamella

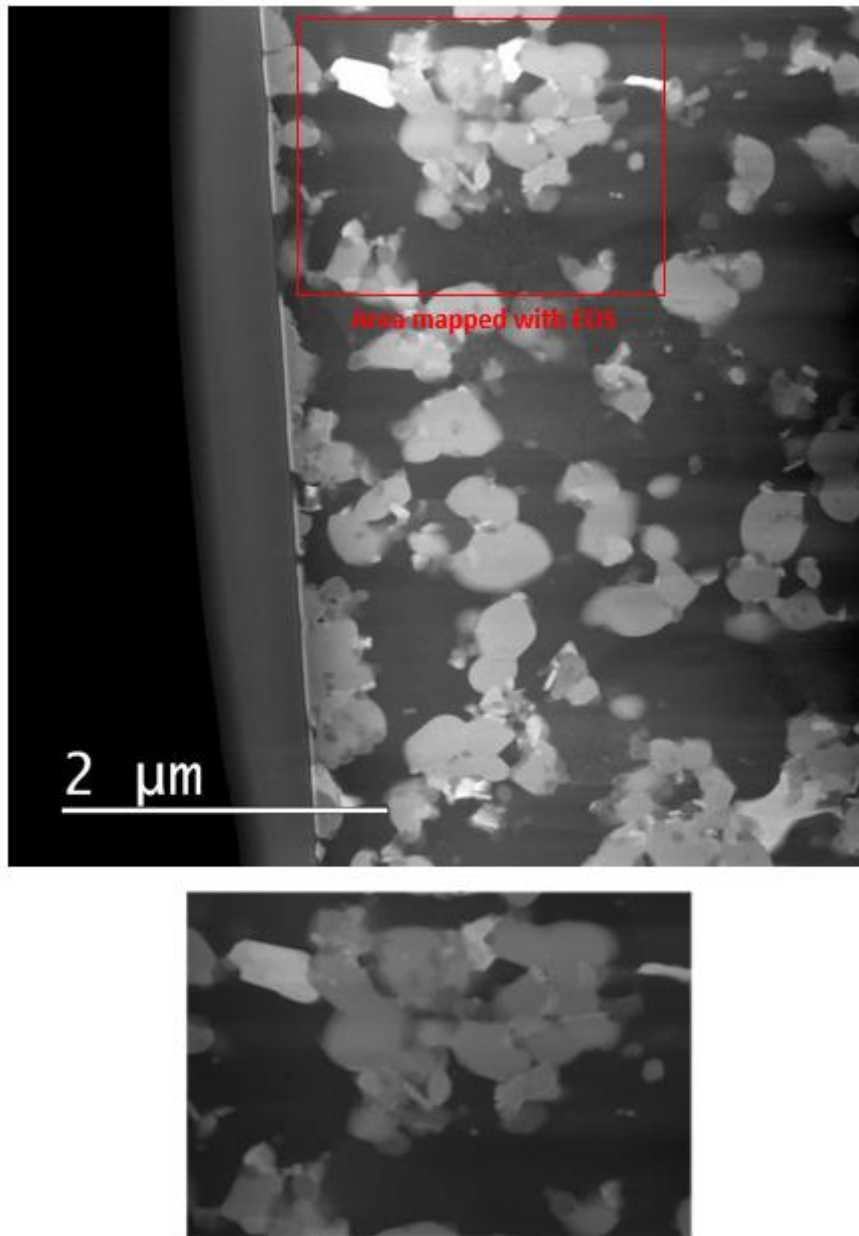


Figure 9.2: Area mapped with EDS

The mapped area showed the material is polycrystalline in nature with a random arrangement of varying grain composition. Aluminium was found throughout the sample in varying amounts from grain to grain. Figure 9.3 shows the content of various grains while Figure 9.4 is the sum spectrum of the mapped area.

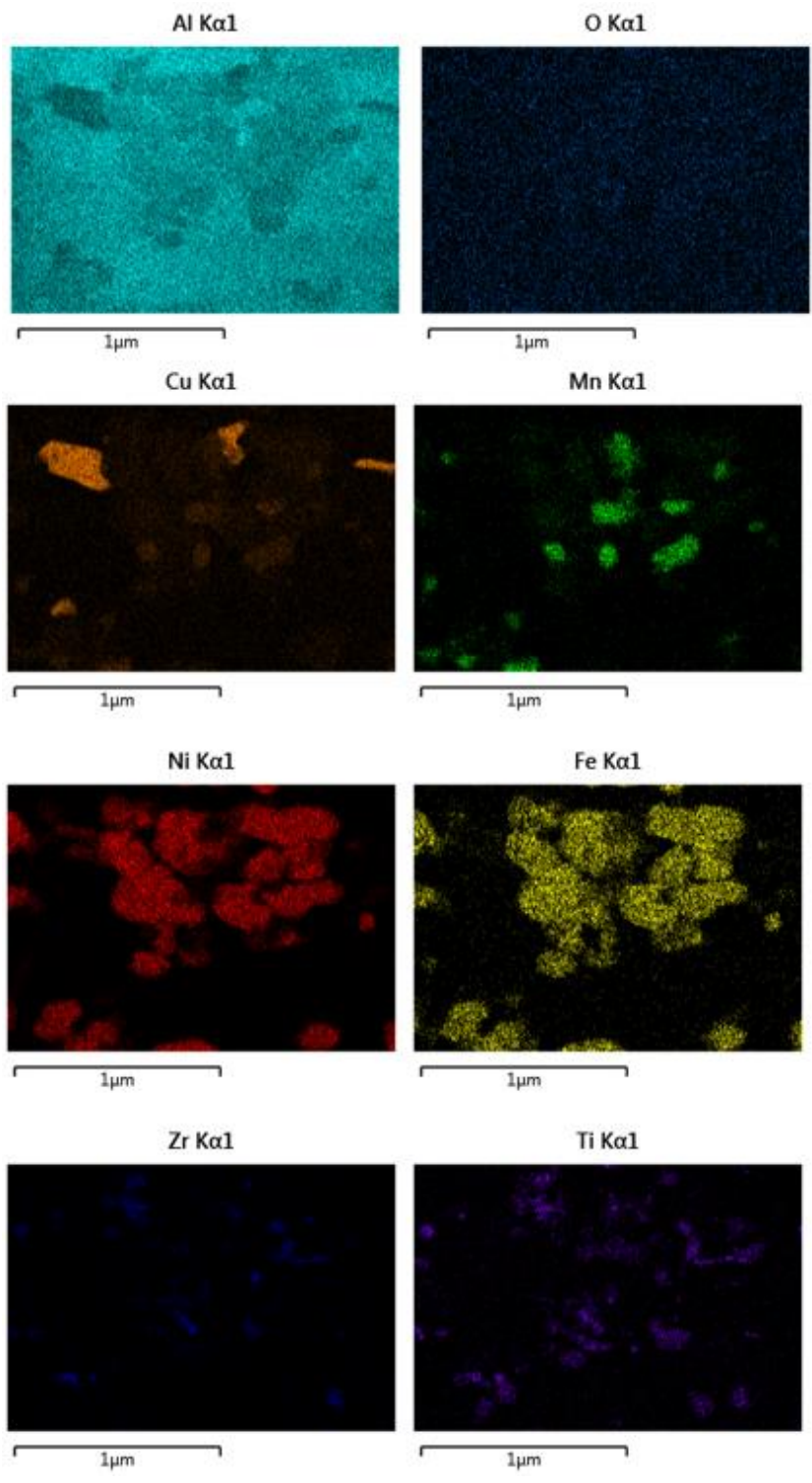


Figure 9.3: EDS results in the TEM

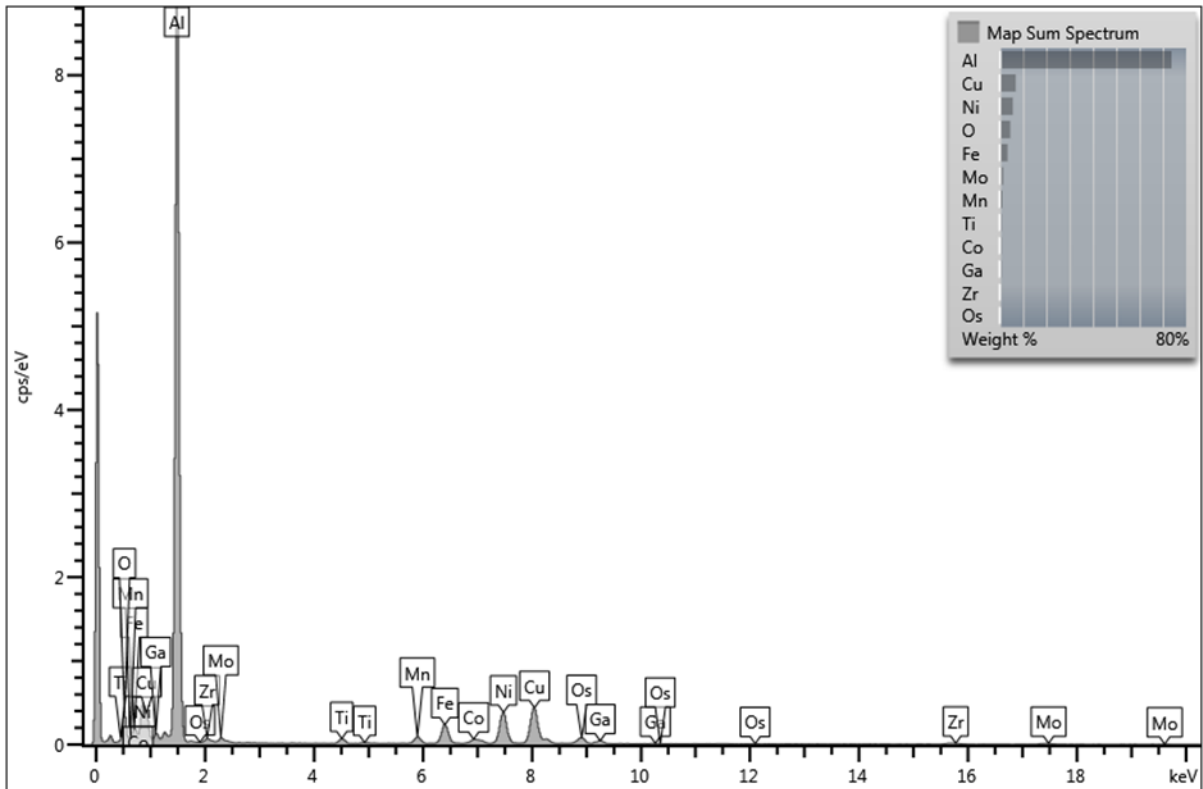


Figure 9.4: Sum spectrum for EDS mapped area

From the EDS results in the TEM, it was deduced that some grains were rich in copper (Cu) and manganese (Mn), some grains contained a combination of nickel (Ni) and iron (Fe), and others contained a combination of zirconium (Zr) and titanium (Ti). The oxygen (O) was introduced during the sample preparation and was disregarded. The EDS results obtained in the TEM were not quantitative, thus EDS was also conducted in the SEM. Table 9.1 provides an estimate of the overall composition from EDS results in the SEM.

Table 9.1: EDS results in the SEM of % wt

	Spec1	Spec2	Spec3	Spec4	Spec5	Spec6	Spec7	Spec8	Spec9
Mg	0.4	0.2	0.9	0.2	0.4	0.2	0.3	0.4	0.5
Al	85.0	85.0	73.3	72.9	85.0	85.9	93.7	74.4	84.8
Ti	0.6	0.6	1.2	-	0.7	0.5	0.4	-	0.6
Mn	1.0	1.2	1.3	1.6	0.8	1.0	0.5	1.5	1.2
Fe	2.8	2.6	4.1	8.1	2.8	3.1	1.0	6.9	2.5
Ni	5.1	5.4	8.7	13.6	5.4	5.8	1.8	12.1	5.2
Cu	3.4	3.1	7.5	2.6	3.0	2.1	1.6	3.1	3.4
Zr	1.0	0.9	1.6	-	0.9	0.8	-	0.4	0.9
Mo	0.7	0.8	1.5	0.7	0.9	0.8	0.6	1.0	0.9
Total	100	100	100	100	100	100	100	100	100
Statistics									
Max	0.9	93.7	1.2	1.6	8.1	13.6	7.5	1.6	1.5
Min	0.2	72.9	0.4	0.5	1.0	1.8	1.6	0.4	0.6
Average	0.4	82.2	0.7	1.1	3.8	7.0	3.3	0.9	0.9
Std Dev	0.2	7.1	0.3	0.3	2.3	3.7	1.7	0.4	0.3

The microstructure composition results were similar to that specified by the manufacturer datasheet, comparing Table 2.4 and Table 9.1. The microstructure results also support the machining results that were obtained. The ultra-fine grains seen in the images are testament to the superior mechanical and physical properties of RSA 905. This microstructure in combination with the chemical content results in smooth material removal and lower impact on the tool that was evident during machining, producing the nanoscale surface finish and low tool wear.

9.2 Molecular Dynamics Simulation Setup

Molecular dynamics simulation is an effective tool to investigate the underlying mechanisms of material processing at atom level. There are various software platforms available for MD simulation with their usage mostly depending on application and preference. Large-Scale Atomic/Molecular Massively Parallel Simulator (LAMMPS) software [93] was used for the

MD simulation mainly due to its versatility, compatibility with various pre and post processing software, and extensive users support forum. LAMMPS is an open source code that employs classical MD methods by computing Newton's equation of motion for interacting atoms within a system. MATLAB, a high-level numerical computing language, was utilised for the pre-processing to develop the tool and workpiece structures by generating arrays that represented the lattice atom coordinates. The MATLAB output was then read by LAMMPS to run the actual MD simulation. OVITO [94] was utilised for post processing to visualise and analyse the results.

The EDS results in the TEM/SEM for RSA 905 shows the presence of numerous elements in the material, mainly, aluminium, magnesium, nickel, copper, iron, manganese, titanium, zirconium and molybdenum. The sample was found to be an aperiodic system (no periodic unit cell) i.e. a randomly ordered alloy. Based on this information, the workpiece for the MD simulation was modelled as an aluminium lattice mixed with the appropriate fraction of these added elements to incorporate polydispersity as a representation of RSA 905. Manganese, however, was excluded due to the lack of an appropriate EAM potential to incorporate into the model. The complex structure of manganese and the existence of its various allotropes makes interatomic potential development very difficult. Currently, there is only an MEAM potential available for Mn [95] which cannot be applied or combined with the methods used for classic MD simulation.

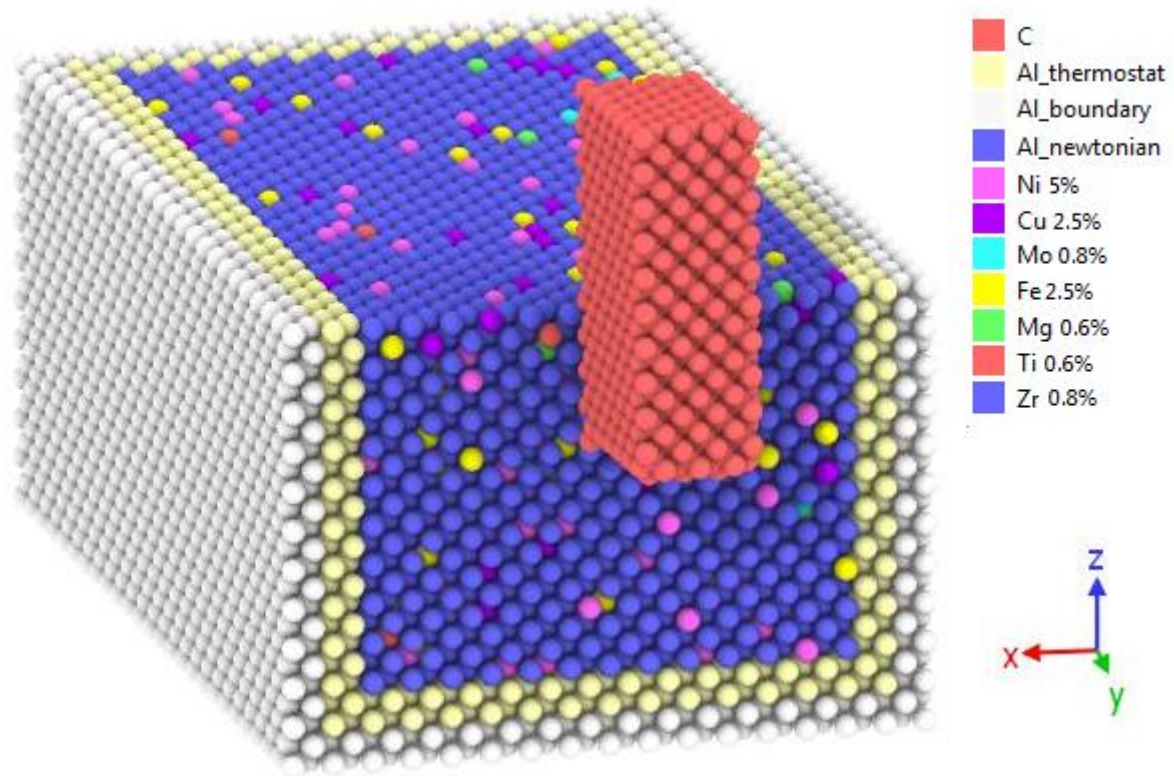


Figure 9.5: MD simulation setup

The simulation setup is illustrated in Figure 9.5 with the legend showing the fraction of the atom types added to the aluminium workpiece. The workpiece was made up of 19355 atoms grouped into boundary, thermostat and Newtonian atoms. The boundary atoms gave the workpiece shape, the thermostat atoms conducted the heat generated and the Newtonian atoms that followed Newton’s equation of motion. The workpiece lattice was based on aluminium of a face-centred cubic (FCC) structure and a lattice parameter of 4.05 Angstroms. The tool was structured as a diamond lattice made up of 1631 carbon atoms of lattice parameter 3.567 Angstroms. The diamond tool was considered as a rigid body in the simulation due to its considerably high hardness in comparison to the workpiece material. Table 9.2 lists the MD simulation conditions.

Table 9.2: MD simulation conditions for nanomachining of RSA 905

Workpiece material	RSA 905
Workpiece lattice (a_1)	0.405 nm
Workpiece dimension	$16a_1 \times 25a_1 \times 11a_1$
Tool material	Diamond
Tool lattice (a_2)	0.3567 nm
Tool dimension	$3a_2 \times 6a_2 \times 10a_2$
Tool rake angle	-2.5°
Tool clearance angle	5°
Depth of cut	0.5 - 1.5 nm
Cutting speed	5 - 15 m/s
Bulk temperature	293 K
Time steps	2 fs

The atom interactions within the simulation were modelled using three interatomic potential functions. Tersoff was implemented between the diamond tool atoms, Morse between the tool and workpiece atoms, and EAM between the workpiece atoms. These potentials were chosen due to the suitability to the respective materials. Tersoff for covalently bonded materials, EAM for metals and Morse for interactions between atoms and surface. The various atom types must be assigned to the required potential to capture all the interactions within the simulation. The silicon carbide (SiC) Tersoff potential [96] was used for the carbon atoms. The Tersoff parameters for carbon are listed in Table 9.3.

Table 9.3: Tersoff parameters for SiC [96]

Parameter	Si	C
A (eV)	1.8308×10^3	1.3936×10^3
B (eV)	4.7118×10^2	3.467×10^2
λ_1 (nm^{-1})	24.799	34.879
λ_2 (nm^{-1})	17.322	22.119
α	0.0	0.0
β	1.0999×10^{-6}	1.5724×10^{-7}
N	7.8734×10^{-1}	7.2751×10^{-1}
P	1.0039×10^5	3.8049×10^4
Q	16.218	4.384
H	-5.9826×10^{-1}	-5.7058×10^{-1}
λ_3 (nm^{-1})	17.322	22.119
R (nm)	0.285	0.18
D (nm)	0.015	0.02

The EAM potential of single elements cannot be used to model alloys. The alloy EAM potential for the workpiece was generated using the method developed by Zhou et al. [84] to

combine multiple single element EAM potentials. This process normalises EAM potentials and creates an EAM alloy model. A tool is supplied in the LAMMPS package that can be coded and edited to output the required alloy mixture potential. An EAM potential for AlCuNiFeMoMgTiZr was generated using the parameters listed in Table 9.4.

Table 9.4: EAM parameters for AlCuNiFeMoMgTiZr [84]

Parameter	Al	Cu	Ni	Fe	Mo	Mg	Ti	Zr
r_e	2.8862	2.5562	2.4887	2.4820	2.7281	3.1963	2.9339	3.2000
f_e	1.3923	1.5545	2.0070	1.8860	2.7237	0.5443	1.8632	2.2309
ρ_e	20.2265	22.1501	27.9847	20.0415	29.3541	7.1326	25.5651	30.8800
α	6.9424	7.6699	8.0296	9.8183	8.3935	10.2287	8.7754	8.5592
β	3.7026	4.0906	4.2825	5.2364	4.4766	5.4553	4.6802	4.5649
A	0.2515	0.3276	0.4397	0.3928	0.7088	0.1375	0.3736	0.4247
B	0.3134	0.4687	0.6328	0.6462	1.1204	0.2259	0.5710	0.6401
K	0.3951	0.4313	0.4134	0.1703	0.1376	0.5000	0.5000	0.5000
L	0.7903	0.8621	0.8269	0.3406	0.2753	1.0000	1.0000	1.0000
F_{n0}	-2.8068	-2.1765	-2.6940	-2.5350	-3.6929	-0.8965	-3.2038	-4.4858
F_{n1}	-0.2762	-0.1400	-0.0661	-0.0596	-0.1788	-0.0443	-0.1983	-0.2931
F_{n2}	0.8934	0.2856	0.1705	0.1931	0.3805	0.1622	0.6838	0.9901
F_{n3}	-1.6372	-1.7508	-2.4574	-2.2823	-3.1337	-0.6900	-2.3217	-3.2025
F_0	-2.8300	-2.1900	-2.7000	-2.5400	-3.7100	-0.9000	-3.2200	-4.5100
F_1	0.0000	0.0000	0.0000	0.0000	0.0000	0.0000	0.0000	0.0000
F_2	0.9295	0.7030	0.2823	0.2003	0.8759	0.1228	0.6086	0.9286
F_3	-0.6823	0.6837	0.1029	-0.1488	0.7762	-0.2260	-0.7507	-0.9819
η	0.7792	0.9212	0.5099	0.3918	0.7909	0.4314	0.5586	0.5971
F_e	-2.8294	-2.1917	-2.7005	-2.5399	-3.7121	-0.8997	-3.2192	-4.5090

The Morse potential parameters for the tool-workpiece atoms interaction were calculated using mixing rules. The Morse parameters (Table 9.5) for C, Al, Cu, Ni, Fe, Mo, Mg, Ti and Zr were obtained from literature [81,97-99] and the Lorentz-Berthelot mixing rule [100,101] was applied for each interaction with the tool C atoms. Figure 9.6 shows the Morse potential plot for C and Al individually and combined. Each element combination plot had a similar profile with their respective attraction/repulsion energies varying. The potential cutoff distance was set at 3.4 Angstroms. The following formulas estimate the Morse potential parameters D , α , r_0 for a mixed pair of atoms of material A and material B .

$$D_{A-B} = (D_A D_B)^{1/2} \quad (8.1)$$

$$\alpha_{A-B} = 1/2(\alpha_A + \alpha_B) \quad (8.2)$$

$$r_{0A-B} = (\sigma_A \sigma_B)^{1/2} + \ln(2/\alpha_{A-B}) \quad (8.3)$$

$$\sigma_{A,B} = r_{0A,B} - \ln(2/\alpha_{A,B}) \quad (8.4)$$

Table 9.5: Morse parameters for C-AlCuNiFeMoMgTiZr

	D (eV)	α (\AA^{-1})	r_0 (\AA)
C-Al	0.0944	1.7100	2.4965
C-Cu	0.1063	1.8071	2.3386
C-Ni	0.1177	1.8377	2.3028
C-Fe	0.1173	1.8220	2.3307
C-Mo	0.1627	1.8817	2.3927
C-Mg	0.0418	2.1492	2.7380
C-Ti	0.0137	1.9049	2.8673
C-Zr	0.1502	1.5463	2.4162

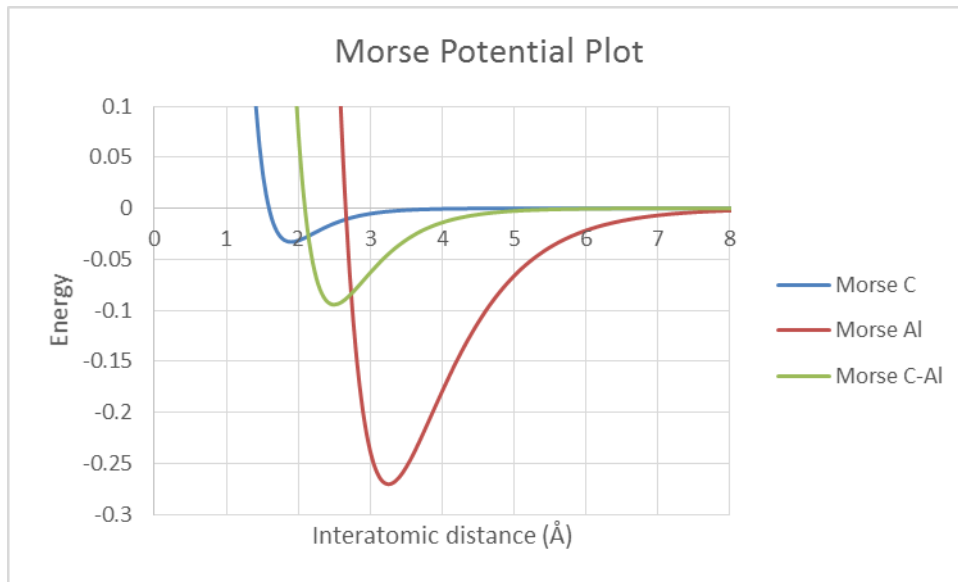


Figure 9.6: Morse potential plot for C-Al

The global simulation box was set to be non-periodic for the x and y axes, preventing atoms from interacting across the boundary, while the z axis was set to adjust as required based on atoms that moved in that direction. Prior to cutting, the model was run under constant temperature of 293K until the system relaxed allowing the atoms to reach their dynamically equilibrium states. The nanometric cutting simulation was conducted under microcanonical

ensemble (NVE). The model assumes the workpiece is without defects and the rigid tool means the effect of wear is not considered.

9.3 Molecular Dynamics Simulation Results

The simulation was run for 60000 steps and the cutting forces, temperature and energy of the system was recorded for 0.5 nm, 1.0 nm and 1.5 nm depth of cut at a cutting speed of 5 m/s.

Figure 9.7 shows the cutting process as the tool travels through the workpiece at a depth of cut of 0.5 nm and cutting speed of 5 m/s. The workpiece atoms were seen to split and flow symmetrically along the sides of the tool, some flowed under the tool, while others piled up in front of the tool to form the chip (Figure 9.8).

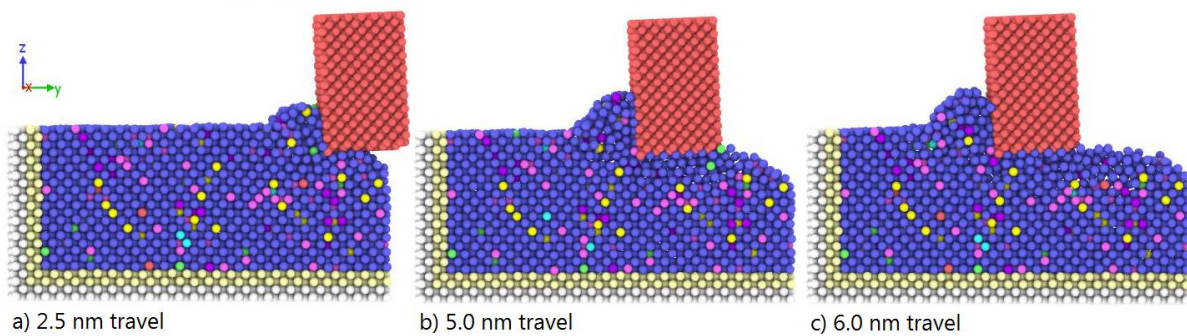


Figure 9.7: Machining simulation progression at 0.5 nm depth of cut and 5 m/s cutting speed

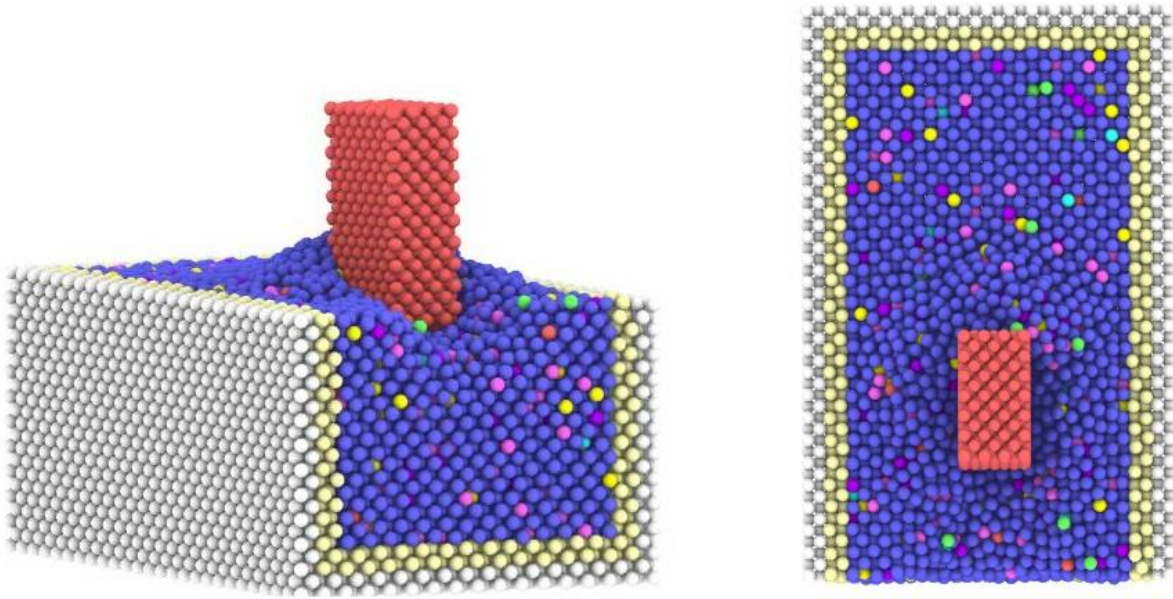


Figure 9.8: Atom distribution during cutting process

The displacement vectors in Figure 9.9 show the atoms moved in the direction of the cutting and the separation point at the tool edge. The workpiece atoms in front of the tool increasingly moved forward and upward and the chip piled up. The workpiece atoms flowing below the tool were also of interest as they form the surface left behind. Some of these atoms moved parallel with the tool while others moved downward into the workpiece. These atoms that were pushed downward penetrated the workpiece forming dislocations. Once the tool passed, these atoms moved back upward rectifying the dislocations and the machined surface is formed. This indicated that elastic deformation and some degree of ploughing occurred, which were responsible for the surface obtained after machining.

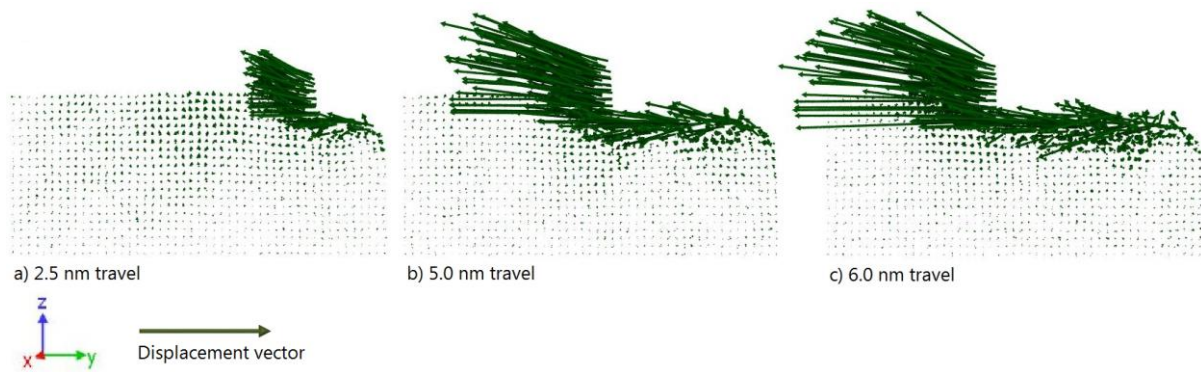


Figure 9.9: Displacement vectors of workpiece atoms on y-z plane

The shear strain of the workpiece atoms is seen in Figure 9.10. The shear strain steeply increases as the tool penetrates the workpiece. The affected atoms are concentrated around the tool and on the machined surface and subsurface layer while the rest of the workpiece atoms remain stable. This sublayer of atoms undergo compression ahead of the tool (as the chip is formed) and below the tool. As the tool travels the distribution of atoms under high shear strain increases but remains within this layer. The magnitude of the strain experienced by these atoms also increases as the cutting progresses, a result of strain rate hardening. There were no well-developed shear bands, major dislocations or structural defects within the workpiece, indicating minimal plastic deformation and a smooth cutting process. Figure 9.11 shows highlights atoms displaced/dislocated from the aluminium lattice structure and Figure 9.12 shows the bond structure of workpiece when machined. Both figures illustrate these described mechanisms.

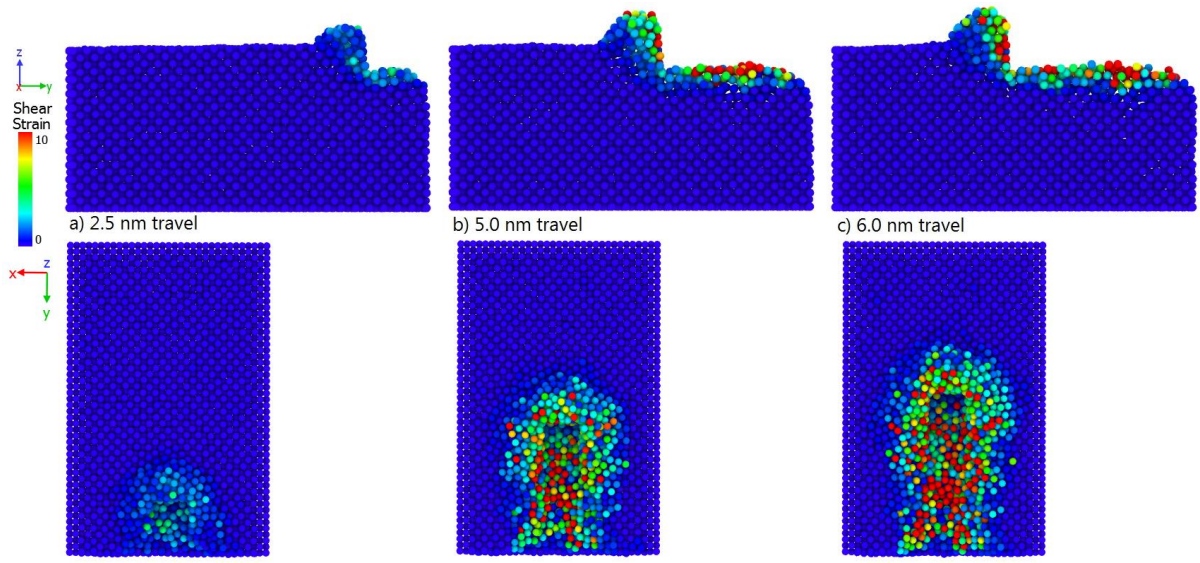


Figure 9.10: Shear strain of workpiece atoms

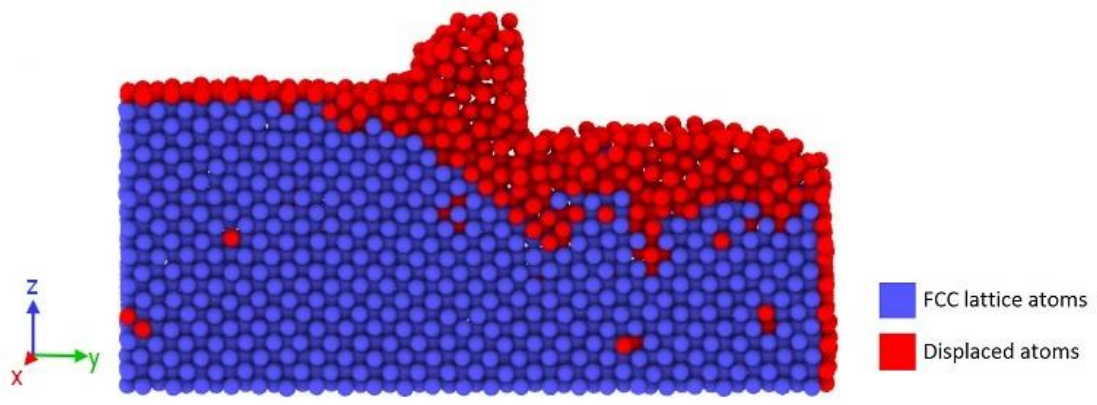


Figure 9.11: Dislocation analysis of workpiece lattice

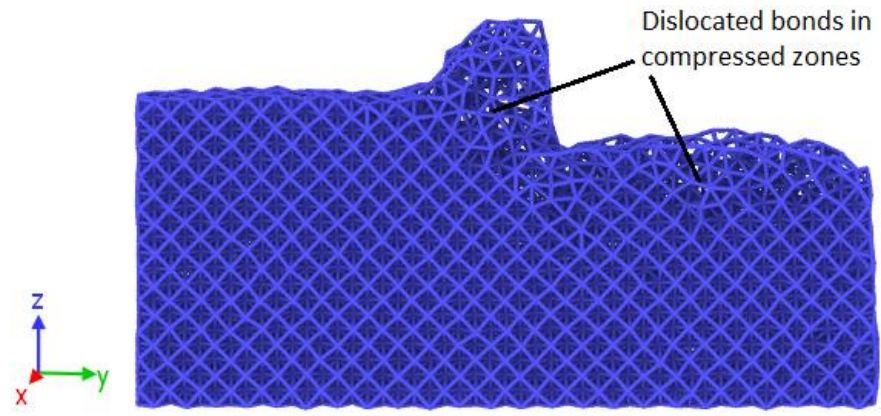


Figure 9.12: Bond representation of workpiece structure

The same atom behaviour and distribution was seen when the depth of cut was increased to 1.0 nm and 1.5 nm (Figure 9.13), but with more layers of atoms being affected and thus greater chip build-up due to increased tool-workpiece contact area.

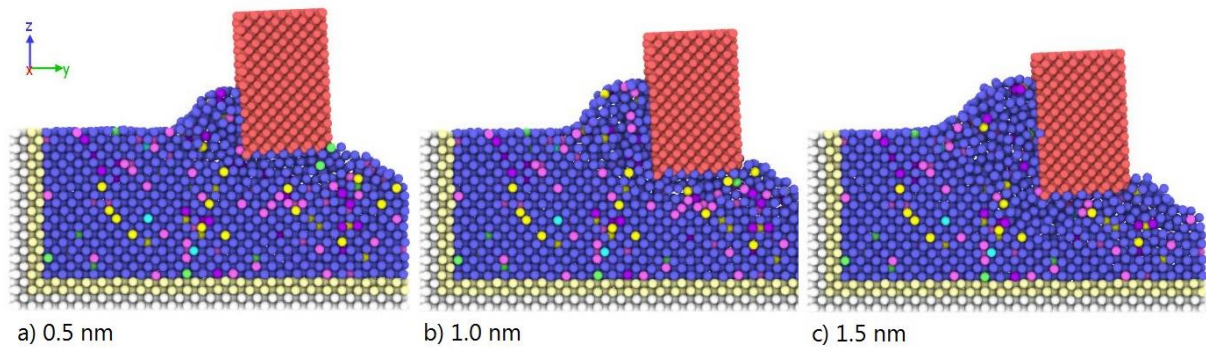


Figure 9.13: Machining simulation with increasing depth of cut at 5.0 nm tool travel

The initial relaxation was run for approximately 3000 steps. This can be seen in the total energy graph (Figure 9.14) where the energy slightly fluctuates at the start of the simulation then stabilises. The total energy remains constant and once the tool engages at approximately 0.5 nm distance, the energy increases in a stable manner during cutting. As the tool cuts through the workpiece, more energy is required for material removal. The results show a sharper increase in energy with increase in depth of cut. As depth of cut increases, more layers of atoms are affected and more energy is required for material removal. Figure 9.16 shows the total energy steadily increased at a constant rate with increase in depth of cut.

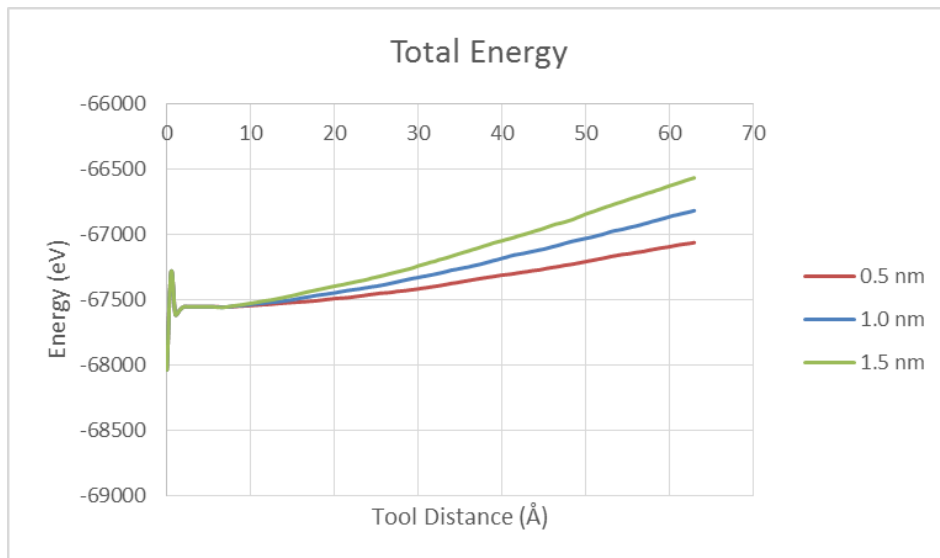


Figure 9.14: Total energy at 5 m/s cutting speed and 0.5-1.5 nm depth of cut

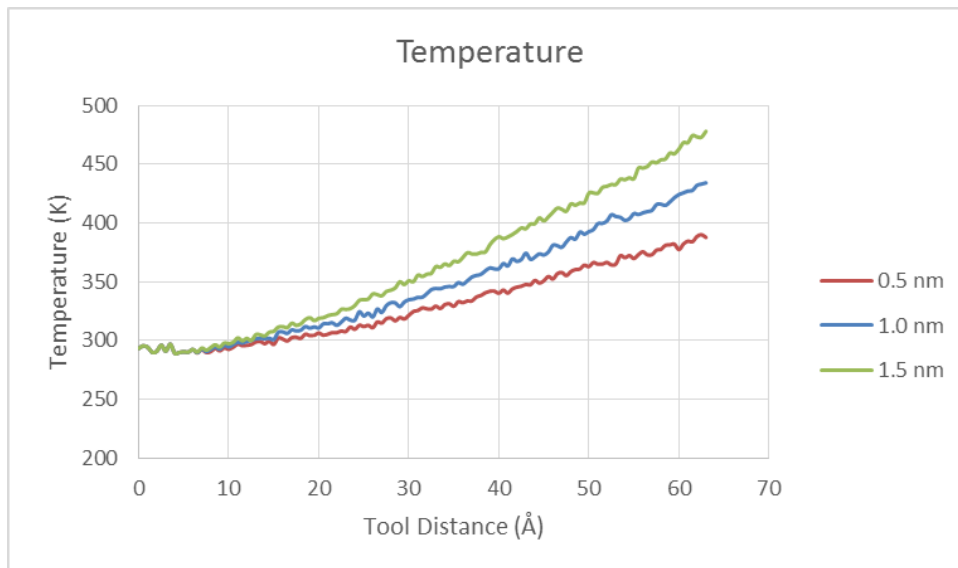


Figure 9.15: Temperature at 5 m/s cutting speed and 0.5-1.5 nm depth of cut

Similarly, the temperature chart (Figure 9.15) was seen to be stabilised at 293K and steadily increase as the tool penetrated the workpiece. The temperature showed an increase with tool travel as friction and deformation increases. This temperature increase was steeper with increase in depth of cut. After 6 nm of tool travel the temperature of the workpiece rose to 390K, 434K and 478K for 0.5 nm, 1.0 nm and 1.5 nm depth of cut, respectively. Figure 9.17 shows the steady linear increase in maximum temperature with increase in depth of cut at 6 nm tool distance.

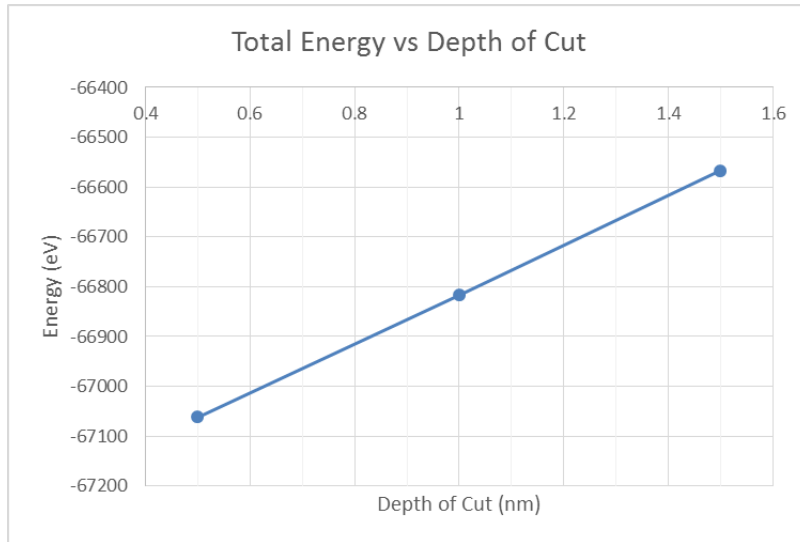


Figure 9.16: Maximum total energy vs depth of cut

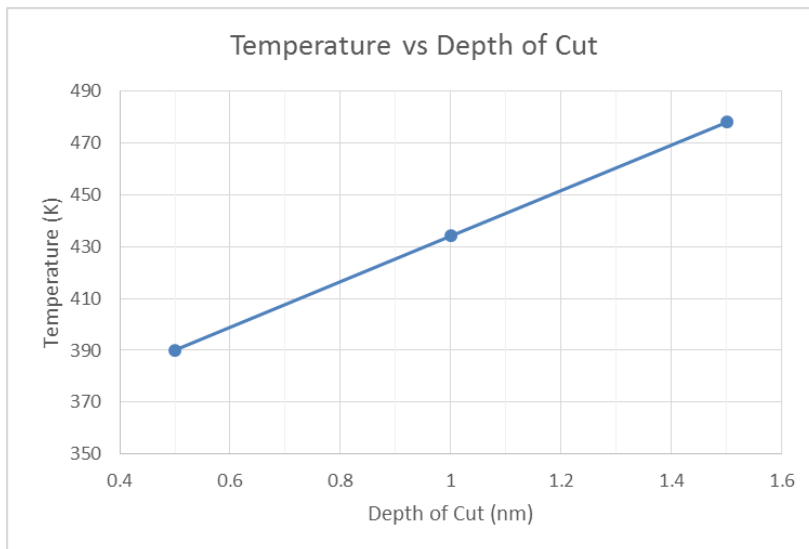


Figure 9.17: Maximum temperature vs depth of cut

The cutting forces recorded during the machining simulation showed an increase with tool travel, where F_y was the primary (tangential) cutting force and F_z was the normal force. The axial force F_x was negligible as the tool did not travel along the x-axis. The tangential force increased as the tool travelled further into the workpiece and the chip built up, then slowed to a steady magnitude as the chip maintained a fairly constant size while consistent cutting was achieved. The normal force showed the same trend as the tangential force but stabilised sooner as the layer of atoms below the tool achieved a steady flow against the clearance

angle. This lowered the normal force as the atoms moved away from the tool. Figure 9.18 shows the cutting forces for 0.5 nm depth of cut. Similar chart profiles were seen as the depth of cut was increased to 1.0 nm (Figure 9.19) and 1.5 nm (Figure 9.20), but the forces were higher as there was more tool engagement into the workpiece and larger chips were formed. The forces also stabilised sooner with smaller depths of cut. The average tangential forces were 8.7 eV/Å, 13.1 eV/Å and 17.9 eV/Å for 0.5 nm, 1.0 nm and 1.5 nm depth of cut, respectively. These tangential forces showed similar profiles and trends with those recorded during actual machining in Section 6.2 for increase in depth of cut. The average normal forces were 4.6 eV/Å, 5.6 eV/Å and 8.1 eV/Å for 0.5 nm, 1.0 nm and 1.5 nm depth of cut, respectively.

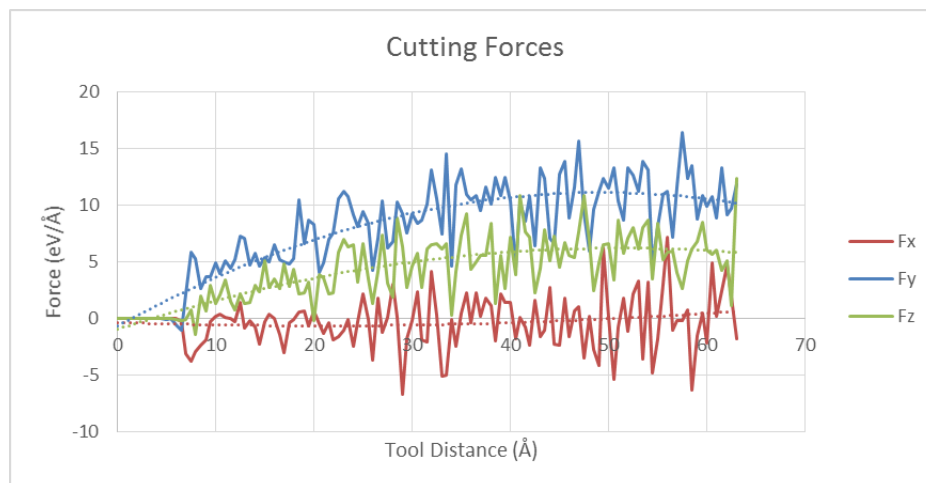


Figure 9.18: Cutting forces at 5 m/s cutting speed and 0.5 depth of cut

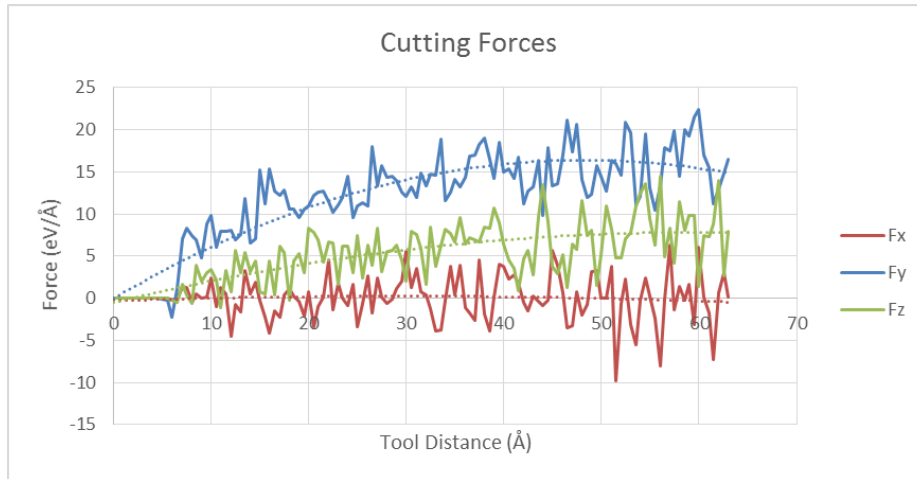


Figure 9.19: Cutting forces at 5 m/s cutting speed and 1.0 depth of cut

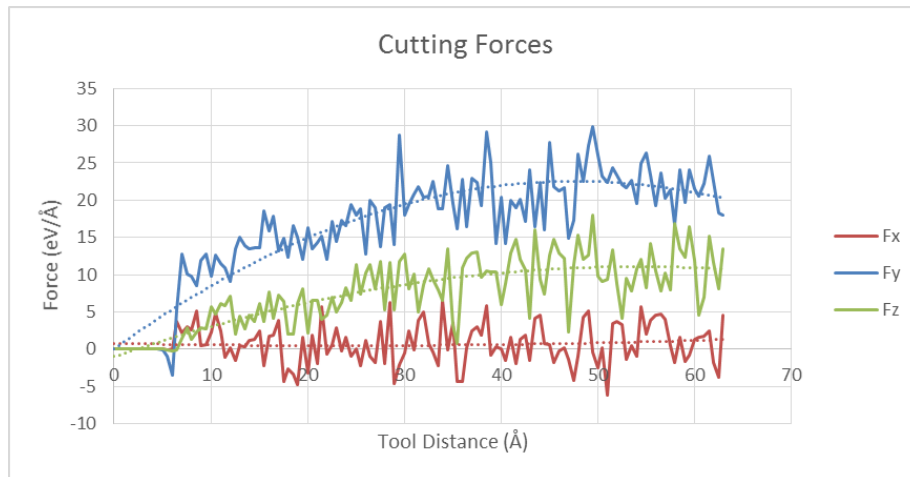


Figure 9.20: Cutting forces at 5 m/s cutting speed and 1.5 depth of cut

The friction coefficient, defined as the ratio of tangential force to normal force (F_y/F_z), was found to remain fairly constant with increase in depth of cut. Figure 9.21 plots the average forces against the depth of cut. The tangential force had a steady rate of increase as the depth of cut increased, as did the normal force. This consequently kept the friction coefficient relatively constant with changes in depth of cut. The friction coefficients were 1.9, 2.3 and 2.2 for 0.5 nm, 1.0 nm and 1.5 nm depth of cut, respectively. The results indicate that the cutting process as depth of cut increases was fairly consistent, but the increase in cutting forces as well as temperature would eventually affect tool deterioration resulting in the minimal effect on surface finish to become significant.

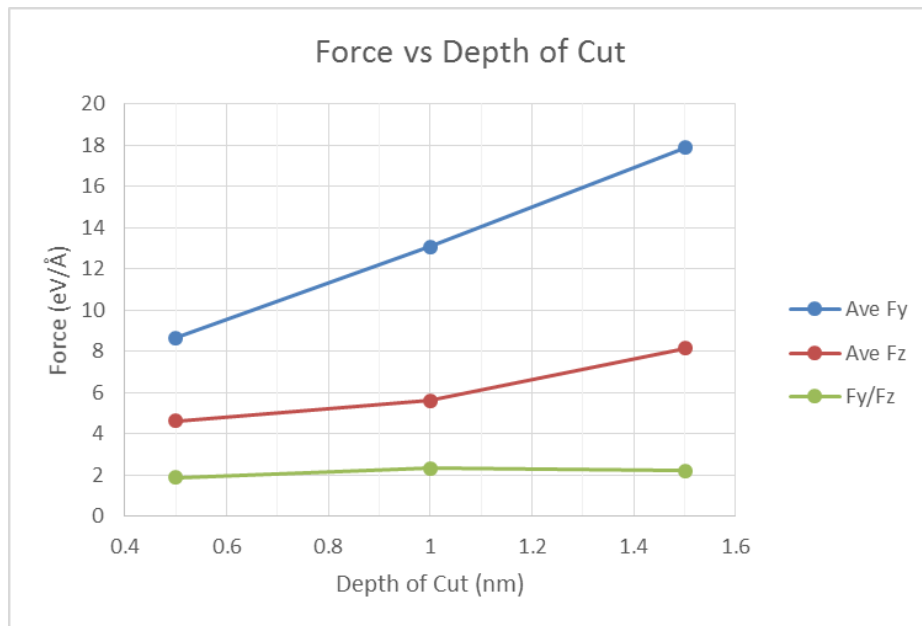


Figure 9.21: Average forces vs depth of cut

The effect of cutting speed was observed by running the simulation at 5 m/s, 10 m/s and 15 m/s with a constant depth of cut of 1.0 nm. Figure 9.22 shows the tool at a distance of 5.0 nm for the three selected cutting speed settings.

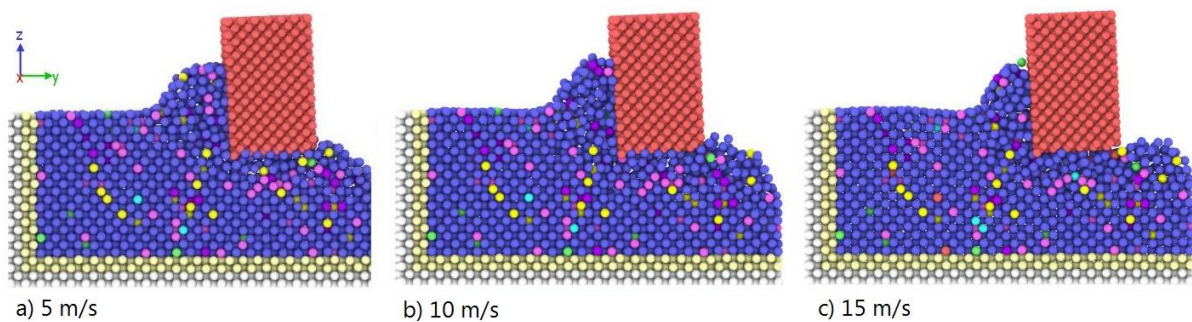


Figure 9.22: Machining simulation with increasing cutting speed at 5.0 nm tool travel

It was seen that as cutting speed increases, the tool impact causes the workpiece atoms to become more loosely bonded and the resulting chip also reduces in size. This was similar to the chips seen during the actual experimentation where the higher cutting speeds had smaller fragmented chips. The total energy increased steadily as the tool progressed (Figure 9.23). As the cutting speed increased from 5 m/s to 10 m/s the total energy showed a slight increase before evening out as the cutting speed further increased to 15 m/s (Figure 9.24).

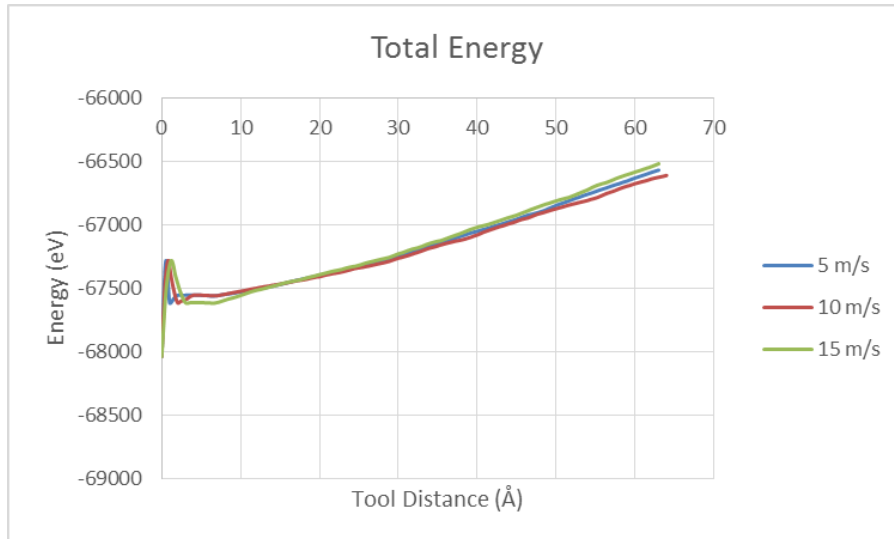


Figure 9.23: Total energy at 1.0 nm depth of cut and 5-15 m/s cutting speed

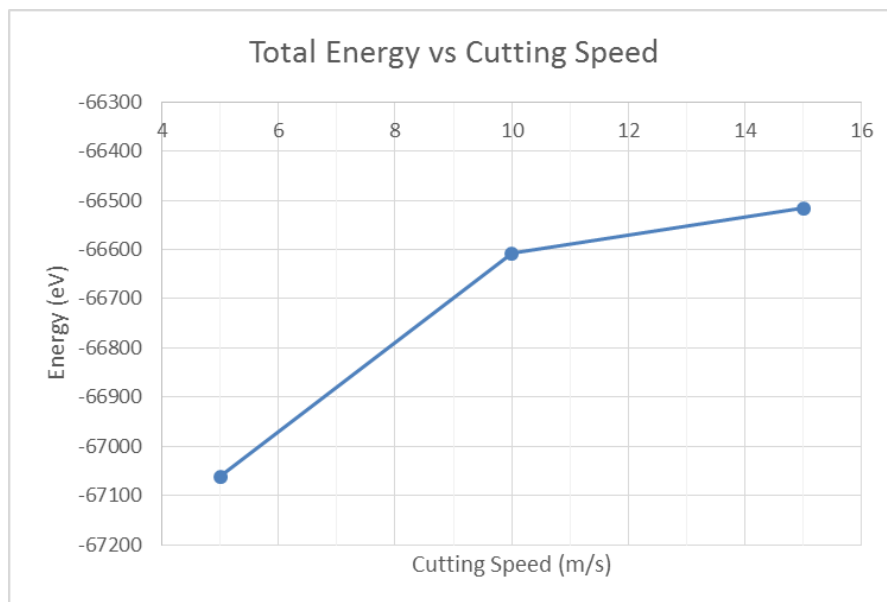


Figure 9.24: Maximum total energy vs cutting speed

Temperature showed a similar trend as seen in Figure 9.25 and Figure 9.26. The smaller chip formed and increased cutting speed led to slowing increases in temperature and energy as the workpiece atoms were loosely displaced by impact. The higher temperatures weakened the atomic bonds making the cuts smoother. This consequently resulted in finer surface finishes. The maximum temperature reached after 6 nm of tool travel was 434 K, 481 K and 515 K for

5 m/s, 10 m/s and 15 m/s cutting speed, respectively. The total energies and temperatures with increase in cutting speed were higher than that seen with increase in depth of cut.

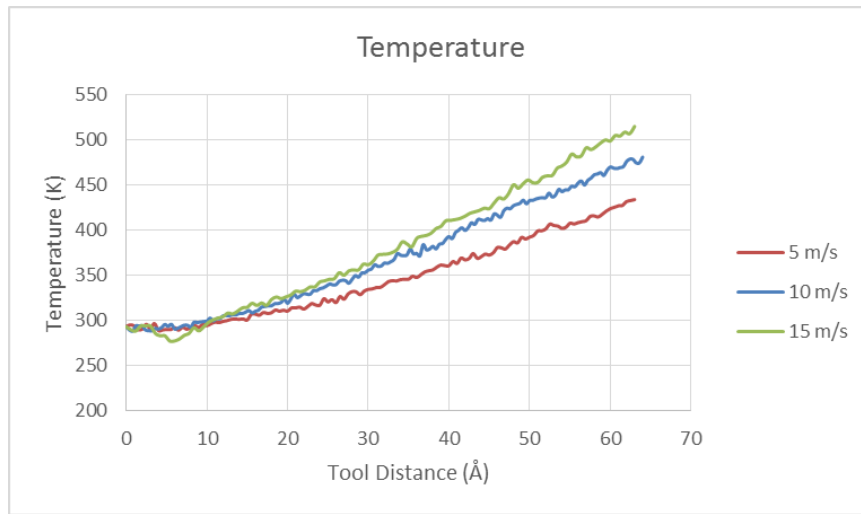


Figure 9.25: Temperature at 1.0 nm depth of cut and 5-15 m/s cutting speed

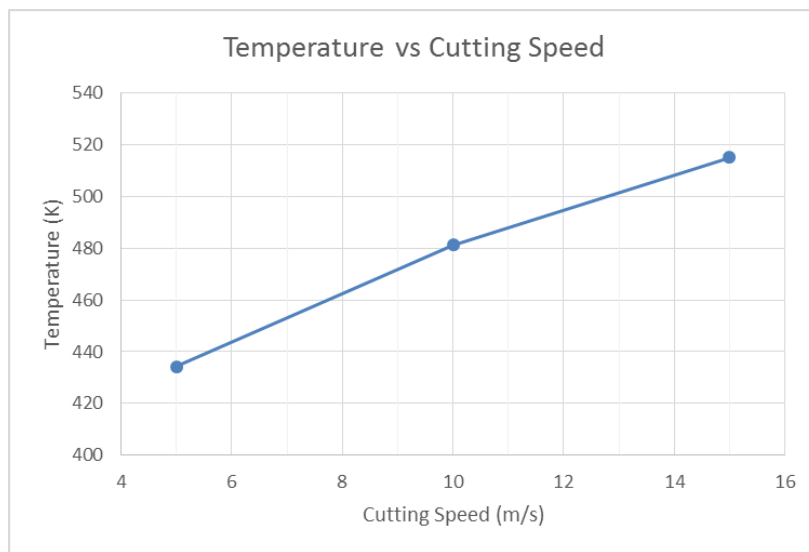


Figure 9.26: Maximum temperature vs cutting speed

The cutting forces increased with tool travel and rapidly reached a steady magnitude as seen in Figure 9.27 and Figure 9.28 for 10 m/s and 15 m/s, respectively. The cutting forces for 5 m/s was already captured in Figure 9.19. The increase in cutting force with tool travel was

steeper and stabilised faster with increase in cutting speed as there was more flow of atoms around the tool.

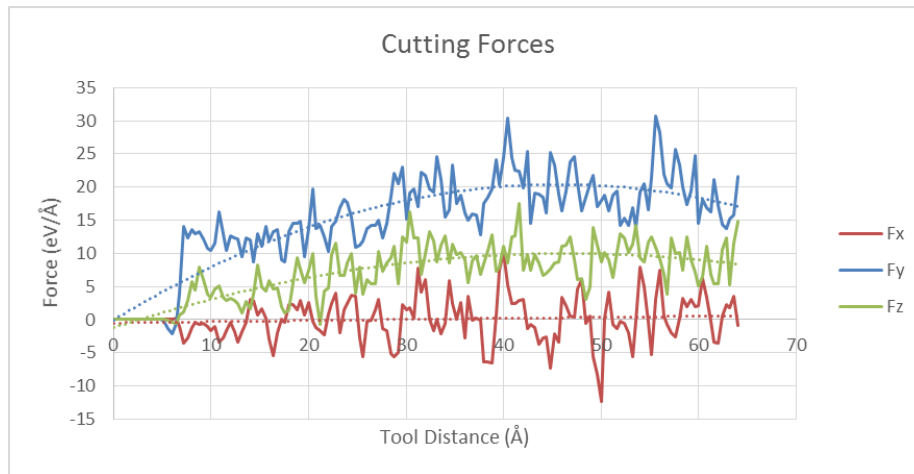


Figure 9.27: Cutting forces at 10 m/s cutting speed and 1.0 depth of cut

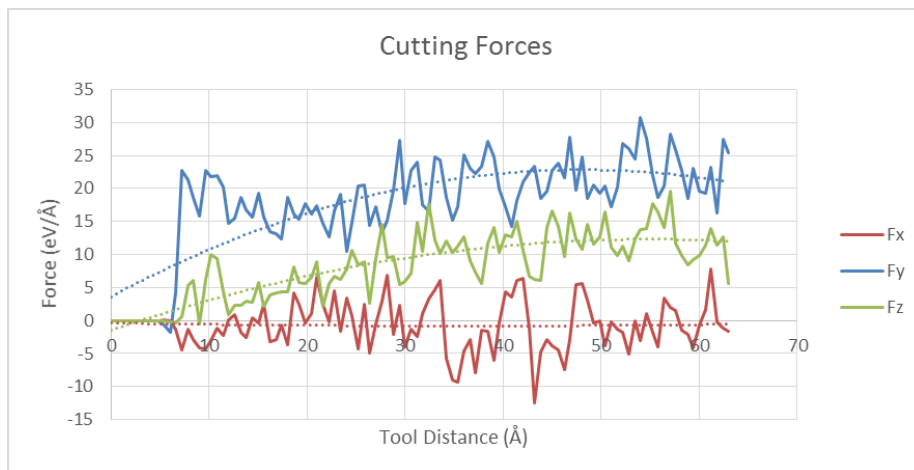


Figure 9.28: Cutting forces at 15 m/s cutting speed and 1.0 depth of cut

Figure 9.29 shows the average cutting forces with increase in cutting speed. It is seen that the average tangential force F_y initially decreased when the cutting speed was increased from 5 m/s to 10 m/s due to smaller chip. As the cutting speed increased to 15 m/s, the impact of the tool against the workpiece overcame the effect of the smaller chip leading to a rapid increase in the tangential force. The average tangential forces were 13.1 eV/Å, 11.6 eV/Å and 19.2 eV/Å for 5 m/s, 10 m/s and 15 m/s cutting speed, respectively. The normal force F_z showed a slowing increase as the workpiece atoms below the tool flowed faster relieving the pressure

exerted by the tool. The average normal forces were 5.6 eV/Å, 7.7 eV/Å and 8.9 eV/Å for 5 m/s, 10 m/s and 15 m/s cutting speed, respectively. Consequently, the friction coefficient decreased from 5 m/s to 10 m/s then increased with further increase in the cutting speed. The friction coefficient was 2.3, 1.5 and 2.1 for 5 m/s, 10 m/s and 15 m/s cutting speed, respectively.

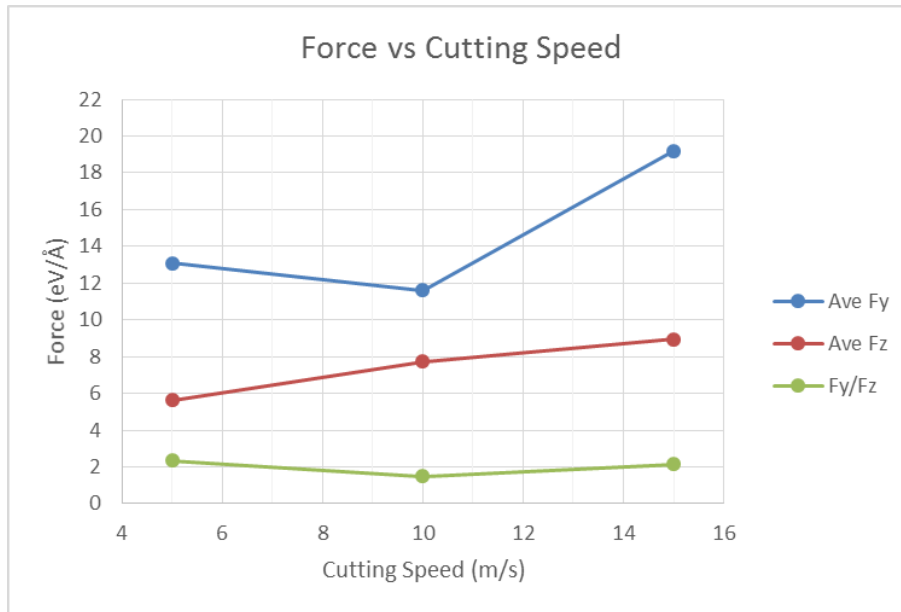


Figure 9.29: Average forces vs cutting speed

These results indicated that cutting speed played a significant role in the cutting mechanisms and machining outcomes. They suggest that there is a desired point of moderate to high cutting speeds with adequate cutting forces and temperatures that would achieve the desired machining results of good surface finishes and low tool wear.

9.4 Conclusion

The RSA microstructure under TEM shows the presence of randomly ordered ultra-fine grains of aluminium with various composition of Cu, Ni, Fe, Mn, Mo, Mg, Ti and Zr. The nanomachining simulation produced through molecular dynamics showed the smooth cutting prevalent with the rapidly solidified aluminium. There were no well-developed shear bands,

major dislocations or structural defects observed. The temperature and average cutting forces were plotted with increasing depth of cut and cutting speed. As depth of cut increased, temperature increased, cutting forces increased. The chip size increased with depth of cut as expected which contributed to the increased cutting forces. The friction coefficient was also recorded which remained constant. This showed that the cutting was consistent with increase in depth of cut resulting in consistent surface finishes. As cutting speed increased, higher temperatures and smaller chips were observed. The higher temperatures weakened the atomic bonds making the cuts smoother which would consequently attribute to finer surface finishes. This also caused a decline in cutting forces, but was soon overcome by the impact of tool as the cutting speed significantly increased leading to an increase in cutting forces. The MD simulations indicate that there was a desired point of moderate to high cutting speeds and low depth of cut with adequate cutting forces and temperature that would produce the ideal machining results. The MD results thus show a correlation with the actual machining results.

References

1. Taniguchi N (1983) Current Status in and future trends of ultra precision machining and ultra-fine processing. *Annals of the CIRP* 32 (2):573-582
2. Venkatesh VC, Izman S (2007) *Precision Engineering*. Tata McGraw-Hill Publishing Company Limited, New Delhi
3. Schaub M, Schwiegerling J, Fest E, Shepard RH (2011) *Molded Optics: Design and Manufacture*. CRC Press, London
4. Beich WS (2002) Specifying injection-molded plastic optics. *Photonics Spectra* 36 (3):127-128
5. Imran M, Mativenga P (2011) Assessment of machining performance using the wear map approach in micro-drilling. *International Journal of Advanced Manufacturing Technology* 59:119-126
6. König W (1994) *Manufacturing Strategies for the Production of Ultraprecision Parts*. UPT, Aachen
7. Yu J, Yan J Ultraprecision diamond turning of optical crystals. In: Doherty VJ (ed) *Proceedings of SPIE Advanced Optical Manufacturing and Testing IV*, San Diego, 1994. pp 51-59
8. Groover MP (1996) *Fundamentals of Modern Manufacturing: Materials, Processes, and Systems*. Prentice Hall, New Jersey
9. Krar SF, Gill AR, Smid P (2005) *Technology of Machine Tools*. McGraw Hill, New York
10. Astakhov VP (2004) The assessment of cutting tool wear. *International Journal of Machine Tools & Manufacture* 44:637-647
11. Lim CYH, Lau PPT, Lim SC (2001) The effects of work material on tool wear. *Wear* 250:344-348
12. Jaffery SI, Mativenga PT (2009) Assessment of the machinability of Ti-6Al-4V alloy using the wear map approach. *International Journal of Advanced Manufacturing Technology* 40:687-696
13. Abou-El-Hossein K, Olufayo O (2014) Diamond machining of rapidly solidified aluminium for optical mould inserts. *Materials Science* 6:1077-1082
14. Lane B, Shi M, Dow T, Scattergood R (2010) Diamond tool wear when machining Al6061 and 1215 steel. *Wear* 268 (11):1434-1441
15. Paul E, Evans CJ, Mangamelli A, McGlaufflin ML, R. S. Polvani (1996) Chemical aspects of tool wear in single point diamond turning. *Precision Engineering* 18 (1):4-19

16. Oomen JM, Eisses J (1992) Wear of monocrystalline diamond tools during ultraprecision machining of nonferrous metals. *Precision Engineering* 14 (4):206-218
17. Gubbels GPH, Beek GJFTvd, Hoep AL, Delbressine FLM, Halewijn Hv (2004) Diamond tool wear when cutting amorphous polymers. *Annals of the CIRP* 53 (1):447-450
18. Lim SC (1998) Recent developments in wear-mechanism maps. *Tribology International* 31:87-97
19. Lim SC (1993) Wear maps for uncoated high-speed steel cutting tools. *Wear* 170 (1):137-144
20. Davim JP (2011) *Tribology for Engineers: A Practical Guide*. Woodhead Publishing, Cambridge
21. Shaw MC (1986) *Metal Cutting Principles*. Oxford University Press Inc, New York
22. Whitehouse DJ (1994) *Handbook of Surface Metrology*. Institute of Physics, Bristol
23. *Surface Finish Metrology* (2003). Taylor Hobson Ltd,
24. Mu YH, Hung NP, Ngoi KA (2000) Monitoring a sub-newton cutting force for ultra-precision machining. *International Journal of Advanced Manufacturing Technology* 16:229-232
25. Gao W, Hocken RJ, Patten JA, Lovingood J (2000) Force measurement in a nanomachining instrument. *Review of Scientific Instruments* 71:4325-4329
26. Arcona C, Dow TA (1998) An empirical tool force model for precision machining. *Journal of Manufacturing Science and Engineering* 120 (4):700-707
27. Bailey JA, Boothroyd G (1968) Critical review of some previous work on the mechanics of the metal-cutting process. *Journal of Engineering for Industry* 90 (1):54-62
28. Marinov V (2011) *Manufacturing Technology*. Eastern Mennonite University, Virginia
29. Oluwajobi AO (2012) *Nanomachining Technology Development*. University of Huddersfield, West Yorkshire
30. Nakayama K, Tamura K (1968) Size effect in metal-cutting force. *Journal of Engineering for Industry* 90:119-126
31. Backer WR, Marshall ER, Shaw MC (1952) The size effect in metal cutting. *Transactions of ASME* 74:61-72
32. Standard definitions of terms relating to acoustic emission (1982). STM E610-82. American Society for the Testing Materials,
33. Varkey G (2003) Online processing of acoustic emission signals. Paper presented at the Awareness Seminar on Digital Signal Processing,

34. Giriraj B, Raja VP, Gandhinadhan R, Ganeshkumar R (2006) Prediction of tool wear in high speed machining using acoustic emission technique and neural network. *Indian Journal of Engineering & Material Sciences* 13:275-280
35. Childs T, Maekawa K, Obikawa T, Yamane Y (2000) *Metal Machining Theory and Applications*. Arnold, London
36. Lan M, Dornfeld D (1984) In process tool fracture detection. *Journal of Engineering Materials and Technology* 106 (2):111-118
37. Emel E, Kannatey-Asibu E Characterisation of tool wear and breakage by pattern recognition of AE signals. In: *Proceedings of 14th NAMRAC Conference, 1988*. pp 266-272
38. Inasaki I, Yonetsu S In process detection of cutting tool damage by acoustic emission measurements. In: *22nd International Machine Tool Design and Research Conference, 1986*. pp 261-268
39. Lee JM, Choi DK, Chu CN (1994) Real-time tool breakage monitoring for NC turning and drilling. *Annals of the CIRP* 43 (1):81-84
40. Min S, Lidde J, Raue N, Dornfeld D (2011) Acoustic emission based tool contact detection for ultra-precision machining. *Manufacturing Technology* 60:141-144
41. Gubbels GPH, Venrooy BWHv, Bosch AJ, Senden R Rapidly solidified aluminium for optical applications. In: *Advanced Optical and Mechanical Technologies in Telescopes and Instrumentation, Proceedings of the SPIE Vol. 7018, Marseille, France, 2008*. pp 70183-70192
42. Asai S, Kobayashi A (1990) Observations of chip producing behaviour in ultra-precision diamond machining and study on mirror-like surface generating mechanism. *Precision Engineering* 12 (3):137-143
43. Shi M, Lane B, Mooney C, Dow T, Scattergood R (2010) Diamond tool wear measurement by electron-beam-induced deposition. *Precision Engineering* 34 (4):718-721
44. Tribastone C, Peck W (2010) *An Introduction to the Design, Manufacture and Application of Plastic Optics*. Opkor Inc.,
45. Karaköse E, Keskin M (2011) Structural investigations of mechanical properties of Al based rapidly solidified alloys. *Materials & Design* 32 (10):4970-4979

46. Guofa MI, Yalin MO, Kuangfei W (2009) Microstructure and mechanical properties of rapidly solidified Al-Cr alloys. *Journal of Wuhan University of Technology Materials Science* 24 (3):424-427
47. Salehi M, Dehghani K (2008) Structure and properties of nanostructured aluminum A413 produced by melt spinning compared with ingot microstructure. *Journal of Alloys and Compounds* 457 (1):357-361
48. Zhang L, Jiang Y, Ma Z, Shan S, Jia Y, Fan C, Wang W (2008) Effect of cooling rate on solidified microstructure and mechanical properties of aluminium-A356 alloy. *Journal of Materials Processing Technology* 207 (1):107-111
49. Anantharaman TR, Suryanarayana C (1987) *Rapidly Solidified Metals: A Technological Overview*. Trans Tech Publications, Uetikon-Zurich
50. Bosch AJ, Senden R, Gubbels GPH, vanVenrooy BWH Optimisation strategy for aluminium optics using the meltspinning technology. In: SPIE Conference OPTIFAB, Rochester, USA, 2009. RSP Technology,
51. Tash M, Samuel F, Mucciardi F, Doty H, Valtierra S (2006) Effect of metallurgical parameters on the machinability of heat-treated 356 and 319 aluminum alloys. *Materials Science and Engineering A* 434 (1):207-217
52. To S, Lee W, Cheung C (2003) Orientation changes of aluminium single crystals in ultra-precision diamond turning. *Journal of Materials Processing Technology* 140 (1):346-351
53. Rana RS, Purohit R, Das S (2012) Reviews on the influences of alloying elements on the microstructure and mechanical properties of aluminum alloys and aluminum alloy composites. *International Journal of Scientific and Research Publications* 2 (6):1-7
54. RS Alloys Overview. RSP Technology. www.rsp-technology.com. 2015
55. Aluminium Alloy 6082 - T6~T651. Aalco Metals Ltd. www.aalco.co.uk. 2015
56. Aluminium Alloy 6061 - T6. Aalco Metals Ltd. www.aalco.co.uk. 2015
57. Zhong Z, Leong M, Liu X (2011) The wear rates and performance of three mold insert materials. *Materials & Design* 32 (2):643-648
58. Vancoliie E, Xiangdong L, Ling Y, Annergren I (2000) *Materials Selection for Durable Optical Inserts Used in Plastic Lens Moulding*. SIMTech, Singapore
59. Furushiro N, Tanaka H, Higuchi M, Yamaguchi T, Shimada S (2010) Suppression mechanism of tool wear by phosphorous addition in diamond turning of electroless nickel deposits. *CIRP Annals Manufacturing Technology* 59 (1):105-108

60. Pramanik A, Neo K, Rahman M, Li X, Sawa M, Maeda Y (2003) Cutting performance of diamond tools during ultra-precision turning of electroless-nickel plated die materials. *Journal of Materials Processing Technology* 140 (1):308-313
61. Yamaguchi T, Higuchi M, Shimada S, Kaneeda T (2007) Tool life monitoring during the diamond turning of electroless Ni–P. *Precision Engineering* 31 (3):196-201
62. Gubbels G, Tegelaers L, Senden R Melt spun aluminium alloys for moulding optics. In: *Proceedings of the SPIE Optifab, Rochester, 2013.*
63. Strenkowski JS, Carroll JT (1985) A finite element model of orthogonal metal cutting. *ASME Journal of Engineering for Industry* 107:349-354
64. Strenkowski JS, Carroll JT (1988) Finite element models of orthogonal cutting with application to single point diamond turning. *International Journal of Mechanical Science* 30:899-920
65. Luo X, Cheng K, Guo X, Holt R (2003) An investigation on the mechanics of nanometric cutting and the development of its test-bed. *International Journal of Production Research* 41 (7):1149-1165
66. Rapaport DC (2004) *The Art of Molecular Dynamics Simulation.* Cambridge University Press, UK
67. Wang L (2012) *Molecular Dynamics: Studies of Synthetic and Biological Macromolecules.* InTech, USA
68. Jastrzebski ZD (1976) *The Nature and Properties of Engineering Materials.* Wiley, New York
69. Shimada S, Ikawa N, Tanaka H, Ohmori G, Uchikoshi J (1993) Feasibility study on ultimate accuracy in microcutting using molecular dynamics simulation. *Annals of the CIRP* 42 (1):91-94
70. Cheong WCD, Zhang L, Tanaka H (2001) Some essentials of simulating nano-surface processes using the molecular dynamics method. *Key Engineering Materials* 196:31-42
71. Jackson MJ (2008) Micro and nanomachining. In: Davim JP (ed) *Machining: Fundamentals and Recent Advances.* Springer, London, pp 271-297
72. Komanduri R, Raff LM (2001) A review on the molecular dynamics simulation of machining at the atomic scale. *Proceedings of the Institution of Mechanical Engineers* 215:1639-1672
73. Belak J, Boercker DB, Stower IF (1993) Simulation of nanometer scale deformation of metallic and ceramic surfaces. *MRS Bulletin* 18:55-60

74. Promyoo R, El-Mounayri H, Yang X (2010) Molecular dynamics simulation of nanometric cutting. *Machining Science and Technology: An International Journal* 14 (4):423-439
75. Komanduri R, Lee M, Raff LM (2004) The significance of normal rake in oblique machining. *International Journal of Machine Tools & Manufacture* 44 (10):1115-1124
76. Komanduri R, Chandrasekaran N, Raff LM (2001) MD simulation of exit failure in nanometric cutting. *Materials Science and Engineering A* 311 (1):1-12
77. Huang Y, Zong W (2014) Molecular dynamic simulation for nanometric cutting of single-crystal face-centered cubic metals. *Nanoscale Research Letters* 9 (1):622-631
78. Cheng K, Luo X, Ward R, Holt R (2003) Modeling and simulation of the tool wear in nanometric cutting. *Wear* 255 (7):1427-1432
79. Narulkara R, Bukkapatnamb S, Raffc LM, Komanduria R (2009) Graphitization as a precursor to wear of diamond in machining pure iron: a molecular dynamics investigation. *Computational Materials Science* 45 (2):358-366
80. Shi J, Verma M (2011) Comparing atomistic machining of monocrystalline and polycrystalline copper structures. *Materials and Manufacturing Processes* 26 (8):1004-1010
81. Shi J, Wang Y, Yang X (2013) Nano-scale machining of polycrystalline coppers - effects of grain size and machining parameters. *Nanoscale Research Letters* 8 (1):500
82. Becker CA, Tavazza F, Trautt ZT, Macedo RABd (2013) Considerations for choosing and using force fields and interatomic potentials in materials science and engineering. *Current Opinion in Solid State and Materials Science* 17:277-283
83. Ward L, Agrawal A, Flores KM, Windl W (2012) Rapid Production of Accurate Embedded-Atom Method Potentials for Metal Alloys. ARXIV 1209.0619
84. Zhou XW, Johnson RA, Wadley HNG (2004) Misfit-energy-increasing dislocations in vapor-deposited CoFe/NiFe multilayers. *Physical Review B* 69 (14):144113
85. Zhou XW, Wadley HNG (1998) Atomistic simulations of the vapor deposition of Ni/Cu/Ni multilayers: The effects of adatom incident energy. *Journal of Applied Physics* 84:2301
86. Zhou XW, Wadley HNG, Johnson RA, Larson DJ, Tabat N, Cerezo A, Petford-Long AK, Smith GDW, Clifton PH, Martens RL, Kelly TF (2001) Atomic scale structure of sputtered metal multilayers. *Acta Materialia* 49:4005-4015

87. Liu K, Wu H, Liu P, Shaw KC (2011) Ultra-precision machining of aluminium alloy surfaces for optical applications. *International Journal of Nanomanufacturing* 7 (2):116-125
88. Revel P, Khanfir H, Fillit RY (2006) Surface characterization of aluminum alloys after diamond turning. *Journal of Materials Processing Technology* 178 (1):154-161
89. Wang S, To S, Chan C, Cheung C, Lee W (2010) A study of the cutting-induced heating effect on the machined surface in ultra-precision raster milling of 6061 Al alloy. *International Journal of Advanced Manufacturing Technology* 51 (1):69-78
90. Zhou M, Ngoi B, Wang X (2003) Tool wear in ultra-precision diamond cutting of non-ferrous metals with a round-nose tool. *Tribology Letters* 15 (3):211-216
91. Horst Rt, Haan Md, Gubbels G, Senden R, Venrooy Bv, Hoogstrate A Diamond turning and polishing tests on new RSP aluminium alloys. In: *Modern Technologies in Space and Ground Based Telescopes and Instrumentation II, Proceedings of the SPIE Vol. 8450*, Amsterdam, Netherlands, 2012.
92. Ferreira SLC, Bruns RE, Ferreira HS, Matos GD, David JM, Branda GC, Silva EGPd, Portugal LA, Reis PSd, Souza AS, Santos WNLd (2007) Box-Behnken design: An alternative for the optimization of analytical methods. *Analytica Chimica Acta* 597:179-186
93. Plimpton S (1995) Fast parallel algorithms for short-range molecular dynamics. *Journal of Computational Physics* 117:1-19
94. Stukowski A (2009) Visualization and analysis of atomistic simulation data with OVITO - the Open Visualization Tool. *Modelling and Simulation in Materials Science and Engineering* 18 (1)
95. Kim Y-M, Shin Y-H, Lee B-J (2009) Modified embedded-atom method interatomic potentials for pure Mn and Fe-Mn system. *Acta Materialia* 57:474-482
96. Tersoff J (1989) Modeling solid-state chemistry: Interatomic potentials for multicomponent systems. *Physical Review B* 39:5566
97. Girifalco LA, Weizer VG (1959) Application of the morse potential function to cubic metals. *Physical Review* 114 (3):687-690
98. Teik-Chang L (2004) Relationship and discrepancies among typical interatomic potential functions. *Chinese Physics Letters* 21 (11):2167-2170
99. Baranov MA, Dubov EA (2005) Definition of elastic modules of ordered hexagonal crystals. *Eurasian Physical Technical Journal* 1:28-33

100. Chen SJ, Huang HL (1981) Diffusion activation energies in face-centered cubic metals using the morse potential function. *Chinese Journal of Physics* 19 (4):106-112
101. Fang T, Wu J (2008) Molecular dynamics simulations on nanoindentation mechanisms of multilayered films. *Computational Materials Science* 43:785-790

Publications

1. Cheng YC, Hsu WY, Abou-El-Hossein K, Olufayo O, Otieno T (2014) Investigation of diamond turning: of rapidly solidified aluminum alloys. Proceedings of SPIE 9192, Current Developments in Lens Design and Optical Engineering XV, 919214. DOI: 10.1117/12.2060176
2. Otieno T, Abou-El-Hossein K, Hsu WY, Cheng YC, Mkoko Z (2015) Surface roughness when diamond turning RSA 905 optical aluminium. Proceedings of SPIE 9575, Optical Manufacturing and Testing XI, 957509. DOI: 10.1117/12.2185470
3. Cheng YC, Hsu WY, Kuo CH, Abou-El-Hossein K, Otieno T (2015) Investigation of rapidly solidified aluminum by using diamond turning and a magnetorheological finishing process. Proceedings of SPIE 9575, Optical Manufacturing and Testing XI, 957519. DOI: 10.1117/12.2186725
4. Otieno T, Abou-El-Hossein K (2016) Effect of cutting parameters on tool wear in diamond turning of new optical aluminium grade. Chinese Optics 9 (5):579-587. DOI: 10.3788/CO.20160905.0579
5. Otieno T, Abou-El-Hossein K (2017) Surface Roughness Analysis when Diamond Turning Optical Grade Rapidly Solidified Aluminium RSA 905. Journal of Optics 46 (4):446-455. DOI: 10.1007/s12596-017-0405-2
6. Otieno T, Abou-El-Hossein K (2018) Molecular dynamics analysis of nanomachining rapidly solidified aluminium. International Journal of Advanced Manufacturing Technology 94(1):121-131. DOI: 10.1007/s00170-017-0853-5
7. Otieno T, Abou-El-Hossein K (2018) Cutting forces and acoustic emissions in the diamond turning of rapidly solidified aluminium. The Journal of the British Institute of Non-Destructive Testing (Accepted, pending publication).
8. Otieno T, Abou-El-Hossein K (2018) Tool wear analysis and model for diamond turning of rapidly solidified aluminium. Manufacturing Technology Journal (Submitted).